AD-A080 592 STANFORD UNIV CALIF STANFORD ELECTRONICS LABS F/G 4/2
RAPID-SCANNING MEASUREMENTS OF WIND-PRODUCED DOPPLER ON AN ASYM--ETC(U)
JUN 79 R D FLEMING N00014-75-C-0601
UNCLASSIFIED SU-SEL-79-016 NL

1 OF 2
AD
A080592

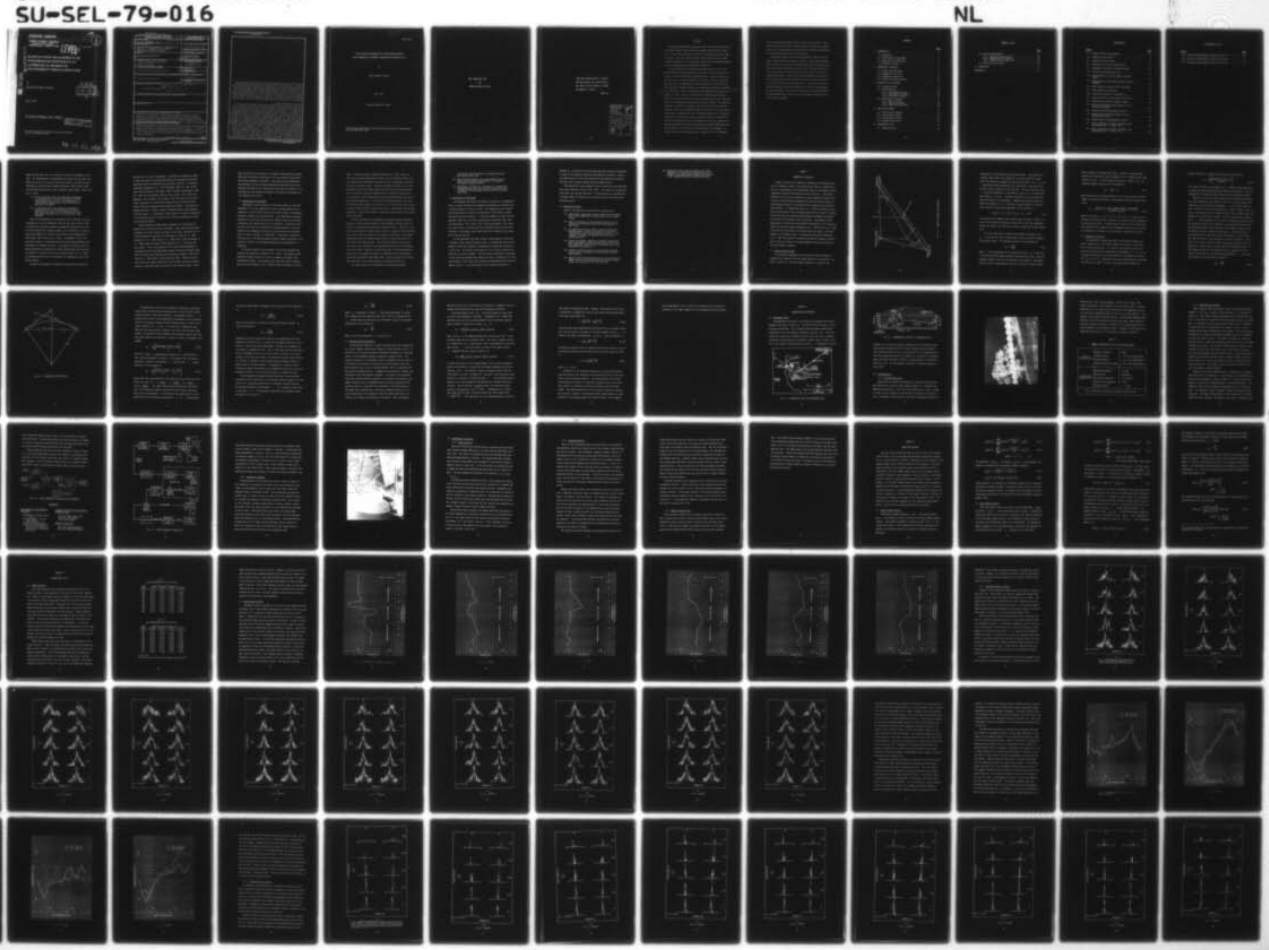

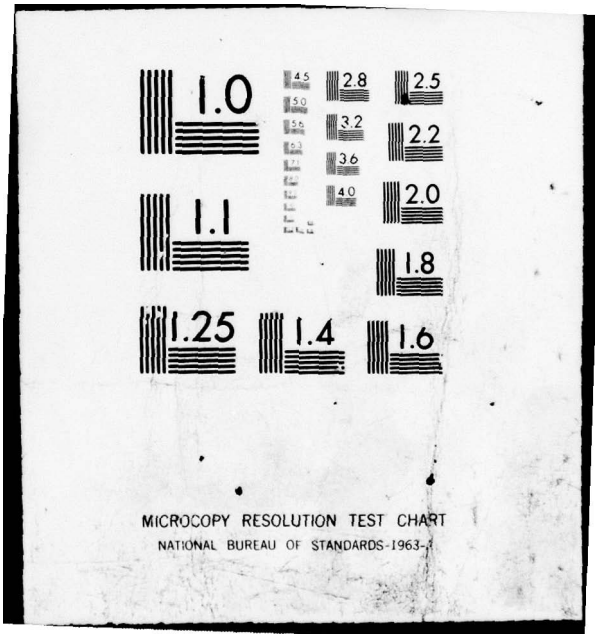
1.0
1.1
1.25
1.4
1.6
1.8
2.0
2.2
2.5
2.8
3.2
3.6
4.0
4.5
5.0
5.6
MICROCOPY RESOLUTION TEST CHART
NATIONAL BUREAU OF STANDARDS-1963-A

RADIOSCIENCE LABORATORY

STANFORD ELECTRONICS LABORATORIES
DEPARTMENT OF ELECTRICAL ENGINEERING
STANFORD UNIVERSITY · STANFORD, CA 94305

SEL-79-016

RAPID-SCANNING MEASUREMENTS OF WIND-PRODUCED DOPPLER ON AN ASYMMETRICAL MICROWAVE TRANSHORIZON PROPAGATION PATH

by

Ronald Douglas Fleming

June 1979

Technical Report No. 4504-1

This work was supported by the Joint Services Electronics Program under Contract N00014-75-C-0601.

UNCLASSIFIED

SECURITY CLASSIFICATION OF THIS PAGE (When Data Entered)

REPORT DOCUMENTATION PAGE

READ INSTRUCTIONS BEFORE COMPLETING FORM

1. REPORT NUMBER: Technical Report No. 4504-1
2. GOVT ACCESSION NO.:
3. RECIPIENT'S CATALOG NUMBER:

4. TITLE (and Subtitle): RAPID-SCANNING MEASUREMENTS OF WIND-PRODUCED DOPPLER ON AN ASYMMETRICAL MICROWAVE TRANSHORIZON PROPAGATION PATH

5. TYPE OF REPORT & PERIOD COVERED: Technical Report, 6/79

6. PERFORMING ORG. REPORT NUMBER: SEL-79-016

7. AUTHOR(s): Ronald Douglas Fleming

8. CONTRACT OR GRANT NUMBER(s): JSEP Contract No. N00014-75-C-0601

9. PERFORMING ORGANIZATION NAME AND ADDRESS:
Stanford Electronics Laboratories
Stanford University
Stanford, California 94305

10. PROGRAM ELEMENT, PROJECT, TASK AREA & WORK UNIT NUMBERS: 143

11. CONTROLLING OFFICE NAME AND ADDRESS:
Joint Services Electronics Program

12. REPORT DATE: June 1979

13. NUMBER OF PAGES: 122

14. MONITORING AGENCY NAME & ADDRESS (if different from Controlling Office):
Office of Naval Research

15. SECURITY CLASS. (of this report): Unclassified

15a. DECLASSIFICATION/DOWNGRADING SCHEDULE:

16. DISTRIBUTION STATEMENT (of this Report):
Distribution Unlimited

SU-SEL-79-016,
TR-4504-1

17. DISTRIBUTION STATEMENT (of the abstract entered in Block 20, if different from Report):

18. SUPPLEMENTARY NOTES:

19. KEY WORDS (Continue on reverse side if necessary and identify by block number):
Tropospheric Propagation, Transhorizon Microwave Propagation, Doppler Spectra, Angle-of-Arrival, Phased Arrays, Aircraft Trailing Vorticies, Atmospheric Remote Probing, Wind Velocity Structure, Low-Altitude Winds, Wind-Produced Doppler, Rapid Scanning Arrays, Rapid Data-Gathering System, Spectral Signatures, Aircraft-Induced Doppler

20. ABSTRACT (Continue on reverse side if necessary and identify by block number):
Concentional methods for monitoring winds aloft have inherent spatial and/or temporal limitations that severely restrict their usefulness. An alternate solution is the use of transhorizon bistatic radio techniques. By using a phase-coherent system with some form of beam-swinging capability, it is possible to measure the wind-produced Doppler shifts associated with moving off-path scatterers.

(continued) 332400 JCB

DD FORM 1 JAN 73 1473 EDITION OF 1 NOV 65 IS OBSOLETE
S/N 0102-LF-014-6601

UNCLASSIFIED

SECURITY CLASSIFICATION OF THIS PAGE (When Data Entered)

In this experiment a rapid data-gathering system is used to remotely probe the wind-field velocity structure in the common volume region of a 164-km trans-horizon propagation path. The phase-stable system operates at 3.2 GHz and employs a 12-element horizontal receiving antenna array. The amplitudes and relative phases of the output signals from the individual elements are sequentially sampled and recorded at a 40-Hz rate. Off-line processing of the amplitude and phase data samples is used to "scan" in azimuth a 0.3° wide fan beam through a 3.88° sector and to obtain virtual simultaneous Doppler spectra measurements at a continuum of angles within the sector scanned. An algorithm developed to identify the apparent source direction of each spectral component permits an appropriate weighting to be applied to the spectra on the basis of angle-of-arrival. The average Doppler shift (spectrum centroid) as a function of the array pointing angle is interpreted in terms of the average transverse wind speed and direction. Doppler relations applicable to previous experiments are modified to account for the influence of differences in the longitudinal path geometry. An analytical expression employing a path asymmetry factor is developed for the wind-produced Doppler from a single scatterer model. Wind velocities inferred from the average Doppler shift data are compared with in situ wind observation data obtained by optically tracking pilot balloons released into the common volume.

Measurement results show the average Doppler shifts to have an almost linear dependence on angle-of-arrival. Wind-produced Doppler shifts resulting from average transverse velocities up to about 5 m/s have been measured and found consistent both in magnitude and direction with the prevailing winds observed in the lower strata of the common volume region. On numerous occasions, Doppler measurement results reflected much higher average velocities (~40 m/s) than could be attributed to normal low-altitude winds. Time-spatial analyses of these anomalous spectra are indicative of aircraft-induced atmospheric disturbances. The spectral signatures of these disturbances may provide additional insight into the generation and decay of aircraft trailing vortices.

SEL-79-016

RAPID-SCANNING MEASUREMENTS OF WIND-PRODUCED DOPPLER ON AN ASYMMETRICAL MICROWAVE TRANSHORIZON PROPAGATION PATH

by

Ronald Douglas Fleming

June 1979

Technical Report No. 4504-1

This work was supported by the Joint Services Electronics Program under Contract N00014-75-C-0601.

"The wind bloweth where it listeth,

and thou hearest the sound thereof,

but canst not tell whence it cometh,

and whither it goeth . . ."

John 3:8

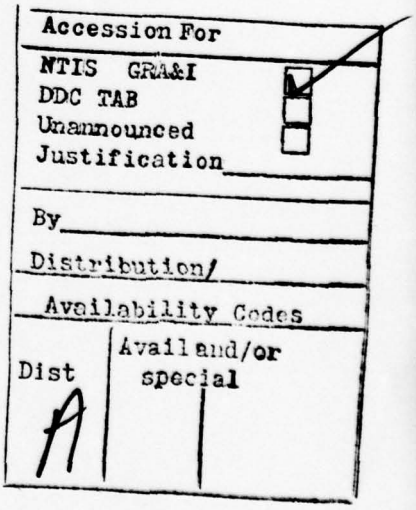

ABSTRACT

Conventional methods for monitoring winds aloft have inherent spatial and/or temporal limitations that severely restrict their usefulness. An alternate solution is the use of transhorizon bistatic radio techniques. By using a phase-coherent system with some form of beam-swinging capability, it is possible to measure the wind-produced Doppler shifts associated with moving off-path scatterers.

In this experiment a rapid data-gathering system is used to remotely probe the wind-field velocity structure in the common volume region of a 164-km transhorizon propagation path. The phase-stable system operates at 3.2 GHz and employs a 12-element horizontal receiving antenna array. The amplitudes and relative phases of the output signals from the individual elements are sequentially sampled and recorded at a 40-Hz rate. Off-line processing of the amplitude and phase data samples is used to "scan" in azimuth a 0.3° wide fan beam through a 3.88° sector and to obtain virtual simultaneous Doppler spectra measurements at a continuum of angles within the sector scanned. An algorithm developed to identify the apparent source direction of each spectral component permits an appropriate weighting to be applied to the spectra on the basis of angle-of-arrival. The average Doppler shift (spectrum centroid) as a function of the array pointing angle is interpreted in terms of the average transverse wind speed and direction. Doppler relations applicable to previous experiments are modified to account for the influence of differences in the longitudinal path geometry. An analytical expression employing a path asymmetry factor is developed

for the wind-produced Doppler from a single scatterer model. Wind velocities inferred from the average Doppler shift data are compared with in situ wind observation data obtained by optically tracking pilot balloons released into the common volume.

Measurement results show the average Doppler shifts to have an almost linear dependence on angle-of-arrival. Wind-produced Doppler shifts resulting from average transverse velocities up to about 5 m/s have been measured and found consistent both in magnitude and direction with the prevailing winds observed in the lower strata of the common volume region. On numerous occasions Doppler measurement results reflected much higher average velocities (~40 m/s) than could be attributed to normal low-altitude winds. Time-spatial analyses of these anomalous spectra are indicative of aircraft-induced atmospheric disturbances. The spectral signatures of these disturbances may provide additional insight into the generation and decay of aircraft trailing vortices.

CONTENTS

		Page
1.	INTRODUCTION	1
	1.1 Background	1
	1.2 Significance of Experiment	4
	1.3 Description of Experiment	6
	1.4 Summary of Results	7
2.	THEORETICAL DISCUSSION	9
	2.1 Single Scatterer Model	9
	2.2 Symmetrical Path Case	12
	2.3 Asymmetrical Path Case	15
	2.4 Multiple Scattering Effects	19
3.	DESCRIPTION OF EXPERIMENT	23
	3.1 Propagation Path	23
	3.2 Instrumentation	24
	3.2.1 Data-Gathering Array	24
	3.2.2 Array-Receiver Channels	27
	3.2.3 Transmitter Assembly	31
	3.3 Experimental Procedures	34
	3.3.1 Data Collection	34
	3.3.2 System Calibration	35
	3.3.3 PIBAL Wind Monitoring	36
4.	ANALYTICAL METHODS	39
	4.1 Single Element Spectra	39
	4.2 Array Angular Spectra	40
	4.3 Average Doppler Shift	43
	4.4 Average Wind Velocity	43
5.	DISCUSSION OF DATA	45
	5.1 PIBAL Wind Data	45

CONTENTS (Cont)

	Page
5.2 Wind-Produced Doppler	47
5.2.1 Unweighted Angular Spectra	54
5.2.2 Weighted Angular Spectra	75
5.2.3 Comparisons with PIBAL Data	95
5.3 Aircraft-Induced Doppler	106
6. CONCLUSIONS	117
REFERENCES	119

ILLUSTRATIONS

Figure		Page
2.1	Single scatterer path geometry	10
2.2	Symmetrical path profile	14
2.3	Asymmetrical path profile	16
3.1	Propagation path and surrounding area	23
3.2	Topographical profile of propagation path	24
3.3	Horizontal data-gathering array	25
3.4	Block diagram of an array element receiving channel	28
3.5	Block diagram of amplitude and phase-sampling equipment	29
3.6	Block diagram of data-collection equipment	30
3.7	Block diagram of transmitter	32
3.8	Transmitting antenna and equipment van	33
5.1	Vertical profile of cross-path wind velocity	48
5.2	Unweighted wind-produced Doppler spectra	55
5.3	Measured unweighted average Doppler shift vs array pointing angle	69
5.4	Weighted wind-produced Doppler spectra	76
5.5	Measured weighted average Doppler shift vs array pointing angle	89
5.6	Hourly Doppler wind-measurement results	98
5.7	Hourly comparisons of PIBAL vs Doppler wind-measurement data - 21 April 1978	100
5.8	Hourly comparisons of PIBAL vs Doppler wind-measurement data - 22 April 1978	103

ILLUSTRATIONS (Cont)

Figure		Page
5.9	Aircraft-induced Doppler spectra at 0111:11.2	108
5.10	Aircraft-induced Doppler spectra at 0111:20.8	110
5.11	Aircraft-induced Doppler spectra at 0111:30.4	112

TABLES

Number		Page
3.1	Summary characteristics of data-gathering array	26
5.1	PIBAL wind-measurement data on 21 April 1978	46
5.2	PIBAL wind-measurement data on 22 April 1978	46
5.3	Doppler wind-measurement data on 21 April 1978	97
5.4	Doppler wind-measurement data on 22 April 1978	97
5.5	Spectral analysis results of aircraft-induced disturbance	114
5.6	Aircraft transit-time analysis data	114

Chapter 1

INTRODUCTION

This dissertation describes the results of a microwave transhorizon experiment in which a rapid data-gathering antenna array is used as a remote sensing probe of low-altitude tropospheric winds.

1.1 Background

The initial transhorizon propagation of an ultrahigh frequency signal was reported by Marconi in 1932 after he successfully transmitted a 500-MHz signal over a distance of 168 miles (270 km). The underlying physical principles involved in transhorizon propagation subsequently became a subject of discussion and some controversy among researchers. The smooth-earth diffraction theory (Watson, 1918 and 1919; Van der Pol and Bremmer, 1937, 1938, and 1939), which suggests an exponential decrease in the received power with distance, was the generally accepted explanation for transhorizon propagation in the early 1940s. With the advent of high-power transmitters and sensitive receivers during the war, signal reception far beyond the horizon became more frequent (Bullington, 1955). The received signal levels, however, were consistently found to be far above the levels predicted by the diffraction theories. Concerted efforts were made by investigators in the late 1940s to find a plausible explanation for the transhorizon signal observations. Pekeris (1947) suggested the signals, based on their appearance, were a result of some scattering process from refractive-index variations in the atmosphere. As a consequence, several theoretical propagation

models evolved that took into account the prevailing atmospheric structure. The preponderance of experimental data taken over the years supports the validity of two basic theoretical models, one derived from a turbulence scattering theory (Booker and Gordon, 1950; Staras, 1952) and the other derived from a layer reflection theory (Bauer, 1956; Friis et al., 1957):

(1) In the turbulence theory the propagation phenomena is characterized as a scattering process resulting from turbulent conditions in the atmosphere that cause random irregularities in the refractive properties of the medium.

(2) In the layer theory the propagation phenomena is characterized as a reflection process resulting from stratified layers in the atmosphere that produce sharp discontinuities in the refractive index gradient.

Much of the experimental and theoretical work conducted since the introduction of the two fundamental theories has dealt with the study of the physical mechanisms supporting propagation beyond the horizon. The early experimental research, however, was influenced to a large extent by the demands for reliable long-distance radio communications (Bullington, 1950; Mellen et al., 1955). Consequently, one of the principal concerns of researchers was the signal fading problems often experienced on transhorizon paths. The cumulative results of the numerous experiments conducted up to about 1960 provided sufficient data to establish a statistical basis for predicting (Baris et al., 1962) the average expected level of performance of transhorizon radio transmission systems.

By 1960 the tropospheric propagation characteristics beyond the

horizon were fairly well understood. Investigators subsequently began to look into ways of distinguishing between the propagation mechanisms associated with the turbulence and layer model theories. At Stanford researchers (Waterman et al., 1957; Waterman, 1958; Lee, 1961; Strohbehn, 1963; Waterman and Strohbehn, 1963; Strohbehn and Waterman, 1966; Cox, 1967; Cox and Waterman, 1969 and 1971; Cianos, 1971; Cianos and Waterman, 1973; Waterman, 1973; Cianos, 1978) have used various experimental techniques to differentiate between the two prevailing atmospheric structures suggested by the theoretical models. These empirical methods provided in effect a means of remotely probing the atmosphere with radio waves -- a technique in which analyses of specific parameters of the received signal are used to infer certain characteristics about the intervening medium.

Several important meteorological parameters can be measured remotely using transhorizon radio techniques. Among the many measureable parameters, the wind velocity structure in the lower atmosphere has received considerable attention by investigators (Atlas et al., 1968; Birkemeier et al., 1968; Atlas et al., 1969; Atlas, 1969; Birkemeier et al., 1969; Lammers and Olsen, 1973; Chadwick et al., 1975) over the past decade. Early investigations of the signal fading phenomena on transhorizon paths have demonstrated marked correlations between signal fade rates and local transverse wind conditions (Laaspere, 1958; Crawford et al., 1959; Doherty, 1959; Gjessing, 1964). Refractive structures within the common volume drift with the mean wind velocity which results in stochastic phase variations in the received signal. These

phase variations are reflected in the Doppler spectrum and are dependent upon the spatial distribution, size, and relative velocities of the moving atmospheric structures. The analytical and experimental work performed in this area have provided the motivation for the experiment described in this dissertation which seeks to further our understanding of the spatial and temporal variations of atmospheric motion produced by the wind.

1.2 Significance of Experiment

Knowledge of wind information in localized regions of the lower atmosphere is of vital importance not only to meteorologists but to researchers in such diverse areas as air-traffic safety, environmental pollution, energy, and even agriculture. The conventional rawinsonde technique of monitoring winds aloft has inherent spatial and temporal limitations that severely restrict its usefulness. Situations requiring near real-time wind information in selected regions of the atmosphere are not adequately served by the widely spaced and infrequent (every 12 hours) launches of rawinsondes. A reduction in either the time interval or the spacing between launches becomes economically prohibitive in terms of the increased manpower and instrumentation requirements.

An alternate means of wind sounding in the lower atmosphere has recently been proposed by Chadwick et al. (1975). The remote probing technique proposed involves the use of a network of bistatic radio transmission systems. The proposal stems from the results of experimental work by Birkemeier et al. (1968 and 1969) and Lammers and Olsen

(1973). Analyses by Atlas (1969) and Atlas et al. (1965, 1968, and 1969) have provided considerable insight into the elementary theory and have enabled the experimental observations to be interpreted in meteorologically significant terms. Observed systematic increases in the average Doppler shift with offset angle from the great-circle bearing have been attributed to the wind-produced drift of refractive structures in the atmosphere. By incorporating narrow-beam antennas with some form of beam-swinging capability, it is possible to remotely monitor the transverse (cross-path) component of the wind over a wide spatial extent using a bistatic phase-coherent transhorizon system. Aligning two such systems orthogonal to one another permits a complete characterization of the horizontal wind-field.

Previous experiments have employed synchronously offset steerable antennas to probe selected regions in the atmosphere and have been conducted on longitudinally symmetrical propagation paths. These are transhorizon paths where the common volume region is symmetrical about the mid-path plane between the receiver and transmitter terminals. Over highly asymmetrical paths the common volume region is skewed significantly to one side of the mid-path plane. The resultant Doppler relations must then reflect the influence of the longitudinal position of the dominant scattering region. Analytical results applicable to both longitudinally symmetrical and asymmetrical paths are presented in this dissertation along with experimental measurement data. Unique features of the experiment pertinent to the remote probing of tropospheric winds are

(1) Angle-of-arrival measurements of wind-produced Doppler

are derived from processing array-sampled amplitude and relative phase data.

(2) Rapid sampling features of the data-gathering array permit the simultaneous measurement of the upwind and downwind Doppler spectra.

(3) Measurements are made on a longitudinally asymmetrical propagation path where the principal scattering region is centrally located between the receiver and the mid-path plane.

1.3 Description of Experiment

To investigate the spatial and temporal variations of tropospheric winds, a 42-hour transhorizon propagation experiment was conducted over a 164-km asymmetrical path at 3.2 GHz. The propagation path extended from Jackson Butte, California (transmitter) to the foothills behind Stanford University (receiver). A rapid data-gathering system (Cox and Waterman, 1969) used in previous transhorizon experiments (Cox, 1967; Cox and Waterman, 1971; Cianos, 1971; Cianos and Waterman, 1973; Waterman, 1973; Cianos, 1978) was modified to remotely probe the wind-field structure in the common volume region above the Livermore Valley about 40 km from the receiver.

In this experiment the phase-coherent system employs a horizontal 12-element linear receiving antenna array. The amplitudes and relative phases of individual elements are sequentially sampled and recorded at a 40-Hz rate. An effective scan period of 5 ms is used to acquire the data from all twelve elements. Off-line signal processing is performed on the amplitude and phase data samples to "scan" in azimuth a 0.3° wide beam through a 3.88° sector and to obtain corresponding angle-of-arrival Doppler spectra. The average Doppler shift (spectrum centroid) is

computed as a function of the array pointing angle and then interpreted in terms of the average transverse wind speed and direction. Results are compared with in-situ wind observation data obtained by optically tracking pilot balloons released into the common volume.

The experimental data presented in this dissertation were obtained from tests conducted on April 21-22, 1978. Ten minutes of transhorizon radio data were recorded each hour. A pilot balloon was launched hourly between 0800 and 1800 hours in the middle of every 10-minute data recording period.

1.4 Summary of Results

Some of the significant results of this research are:

(1) Wind-Doppler measurement results compare most favorably with in-situ PIBAL data in lower strata of the common volume.

(2) Spectral broadening of wind-produced spectra are observed during afternoon hours when the atmosphere is well mixed.

(3) At symmetrical off-axis angles, measured upwind and downwind Doppler spectra are observed to be nearly antisymmetric about the zero-Doppler frequency. This suggests some degree of spatial uniformity in the transverse winds.

(4) On-axis the Doppler spectra are generally symmetrical about zero-Doppler suggesting the absence of vertical wind components and/or spatial non-uniformities in the transverse wind velocity.

(5) Aircraft trailing vorticies produce spectral broadening and spatial asymmetries in the ambient wind produced spectra.

(6) Spectral and transit-time analyses of aircraft-induced Doppler permit a determination of the spatial extent, range, and velocity of trailing vorticies.

(7) Analytical results show the Doppler shift for a scatterer at a fixed cross-path position to be greater on a longitudinally asymmetrical path vis a vis a symmetrical path of equal path length.

Chapter 2

THEORETICAL DISCUSSION

Signals received via transhorizon tropospheric scattering processes are frequently subject to rapid fading and spectral instabilities. This is a consequence of the interference nature of the Doppler-shifted components associated with moving off-path scatterers. Interference patterns are set up at the receiver by signal components scattered off refractive eddy structures transported by the wind through regions of the atmosphere mutually illuminated by the transmitting and receiving antenna beams. As suggested by Atlas et al. (1969), atmospheric structures on the upwind side of the beam produce positive Doppler frequency shifts that beat with negative-shifted Doppler components associated with eddies on the downwind side of the beam. These Doppler shifts progressively increase with the off-path displacement of the scattering region and have been shown (Birkemeier et al., 1968; Atlas et al., 1969) to be directly proportional to the cross-path wind speed in the lower segments of the common volume. A single-scatterer model (Birkemeier et al., 1968) can be used to illustrate the physical concepts involved and to show the influence of the path geometry and source position on the basic Doppler relations.

2.1 Single Scatterer Model

In the analysis presented in this section a single scatterer is assumed to be responsible for the signal observed at the receiver. As shown in Figure 2.1, the point source scatterer is located at the

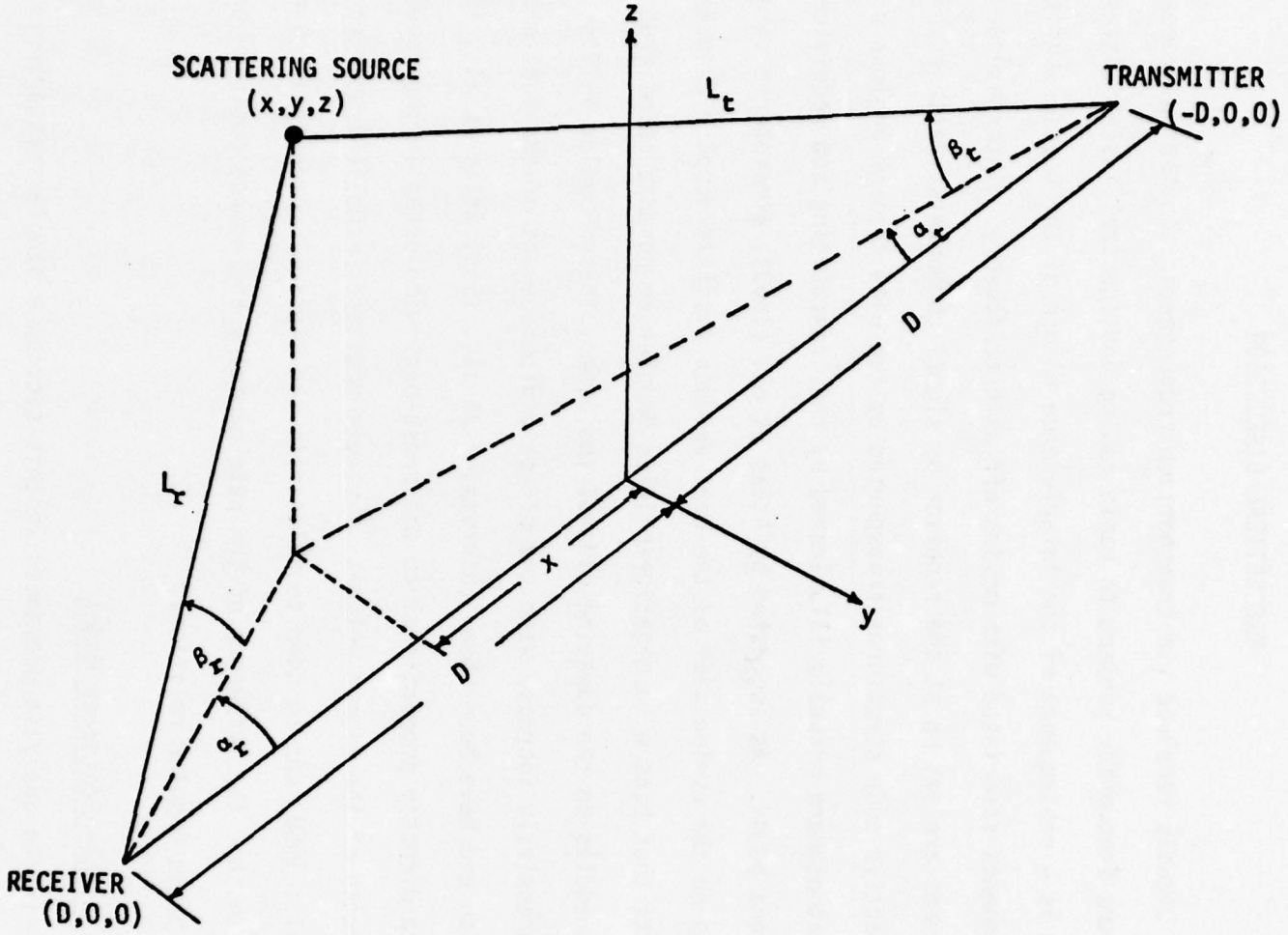

Fig. 2.1. SINGLE SCATTERER PATH GEOMETRY.

intersection of two perfectly narrow antenna beams. The Cartesian coordinate system used in this model has its origin centrally located along the chordal axis between the two radio terminals. The x, y, and z coordinates define respectively the longitudinal, transverse, and vertical spatial positions of the scatterer. The total ray-path length, L, from the transmitter to the receiver is the sum of the respective path lengths, L_t and L_r, from the transmitter to the scatterer and from the receiver to the scatterer. Denoting the chordal distance between the terminals as $2D$, the total ray-path length can be expressed in terms of the position coordinates of the scatterer as

$$L = [(D+x)^2 + y^2 + z^2]^{\frac{1}{2}} + [(D-x)^2 + y^2 + z^2]^{\frac{1}{2}} \qquad (2.1)$$

If we assume a 4/3 effective earth radius (Bean and Dutton, 1966) to account for the refractive bending of radio rays in the lower atmosphere, we may use straight lines for the ray paths in applying the above expression.

It is well known that a moving source produces a Doppler shift, f_d, at the receiver that is proportional to the time rate of change of the ray-path length. This Doppler principle can be expressed as

$$f_d = -\frac{1}{\lambda}\frac{dL}{dt} \qquad (2.2)$$

where λ is the wavelength of the transmitted signal. It is seen that if the effective path length decreases (increases) with time, a positive (negative) Doppler shift will be observed at the receiver. The Doppler shift can also be interpreted as the rate at which the scatterer moves

across surfaces of constant path length. Contours of constant path length are ellipsoidal surfaces (Birkemeier et al., 1968) with the radio terminals as foci. If the scatterer moves with a velocity, $\overline{V}_s$, an equivalent Doppler expression can be written as

$$f_d = -\frac{1}{\lambda}\overline{V}_s \cdot \nabla L \tag{2.3}$$

Upon substituting the expression given in (2.1) for the total ray-path length, the Doppler shift from a single moving scatterer becomes expressed as

$$f_d = -\frac{1}{\lambda}\left\{\frac{[ux + vy + wz]L + uD[(\gamma^2-2xD)^{\frac{1}{2}} - (\gamma^2+2xD)^{\frac{1}{2}}]}{(\gamma^2+2xD)^{\frac{1}{2}}\,(\gamma^2-2xD)^{\frac{1}{2}}}\right\} \tag{2.4}$$

where in the above $\gamma^2 = [x^2 + y^2 + z^2 + D^2]$ and u, v, and w are respectively the longitudinal, transverse, and vertical velocity components of the moving scatterer. From the general result in (2.4) specific Doppler expressions for symmetrical and asymmetrical paths will be derived to illustrate the influence of the scatterer's longitudinal position.

2.2 Symmetrical Path Case

On longitudinally symmetrical paths, the scattering regions primarily responsible for the received signal are located in close proximity of the mid-path plane. As a result, a moving point-source scatterer has relatively small longitudinal displacements, i.e. $x \ll D$ and is generally confined to scattering regions in the common volume where $D^2 \gg [x^2 + y^2 + z^2]$. Applying a first-order approximation to the terms $(\gamma^2+2xD)^{\frac{1}{2}}$ and $(\gamma^2-2xD)^{\frac{1}{2}}$ in (2.4), the Doppler shift produced by a

moving scatterer on a symmetrical path becomes expressible as

$$f_d = -\frac{4}{\lambda L}\left[\frac{ux(1-4D^2/L^2) + vy + wz}{1 - 16x^2D^2/L^4}\right] \qquad (2.5)$$

This result arrived at by Birkemeier et al. (1968) has been applicable to previously reported transhorizon wind-sensing experiments since such experiments have heretofore been conducted on near-symmetrical paths.

Equation (2.5) can be further simplified by considering the geometry of the symmetrical path profile in Figure 2.2 and the relative contributions of the wind velocity components. It can be shown that the term $(1-4D^2/L^2)$ is small and equivalent to $4z_m^2/L^2 = 4h_m^2/D^2$ where z_m and h_m are respectively the mid-path heights of the scatterer above the chordal axis and the earth's surface. Since the longitudinal displacement, x, of the scatterer is also small, the Doppler contribution from the longitudinal wind can be neglected. the longitudinal motion produces negligible Doppler effects because of the elongated shapes of the ellipsoidal surfaces of constant path length. A scatterer moving in the longitudinal direction cuts across the surfaces at a much slower rate than one moving in the transverse or vertical directions. The effect of the vertical wind can in most instances be neglected since its magnitude is normally much less than that of the horizontal wind. It then becomes evident that the Doppler shift on a symmetrical path is linearly proportional to the cross-path displacement, y, of the moving scatterer and may be explicitly given as

$$f_d = -\frac{4vy}{\lambda L} \qquad (2.6)$$

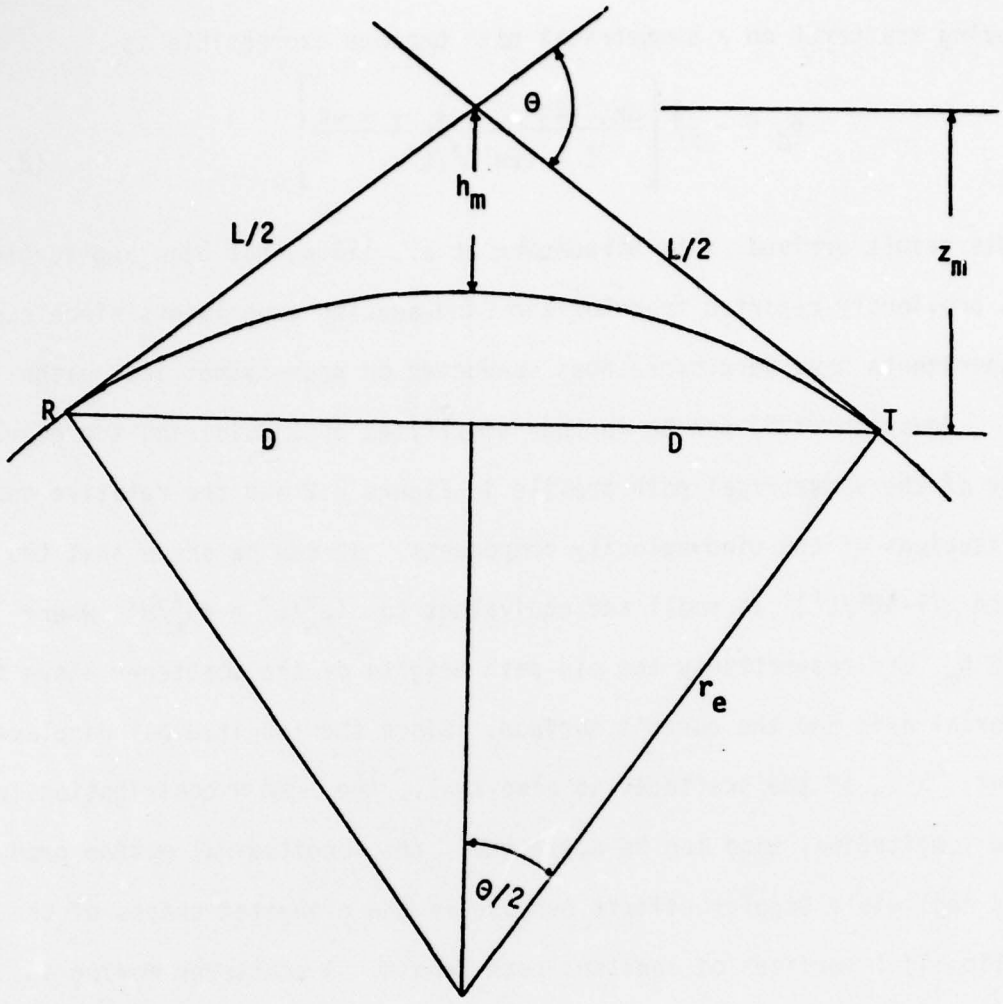

Fig. 2.2. SYMMETRICAL PATH PROFILE.

The Doppler shift may also be expressed in terms of the azimuthal angular position, α , of the scatterer. The Doppler relationship is then written as

$$f_d = - \frac{2v}{\lambda} \sin(\alpha) \tag{2.7}$$

which, for small angles, can be approximated with negligible error as

$$f_d = - \frac{2v\alpha}{\lambda} \tag{2.8}$$

2.3 Asymmetrical Path Case

Consider now the path profile shown in Figure 2.3 where the principal scattering region in the common volume is skewed significantly to one side of the mid-path plane. We begin this treatise by again looking at the terms $(\gamma^2+2xD)^{\frac{1}{2}}$ and $(\gamma^2-2xD)^{\frac{1}{2}}$ in the general Doppler shift expression given in (2.4) but view them from the standpoint of an asymmetrical path. For this situation, it is assumed that the longitudinal displacement, x , is such that $(D-x)^2 >> y^2 + z^2$ for all values of x , y , and z within the common volume. With this constraint, a first-order approximation to the terms, $(\gamma^2+2xD)^{\frac{1}{2}}$ and $(\gamma^2-2xD)^{\frac{1}{2}}$, results in a Doppler shift on an asymmetrical path that can be expressed as

$$f_d = - \frac{L}{\lambda D^2} \left[\frac{2ux(1-2D/L) + vy + wz}{1 - x^2/D^2} \right] \tag{2.9}$$

This result reduces to that for the symmetrical path case when $x << D$. Hence, the Doppler shift expression given in (2.9) is a more general result that is applicable to both symmetric and asymmetric path geometries.

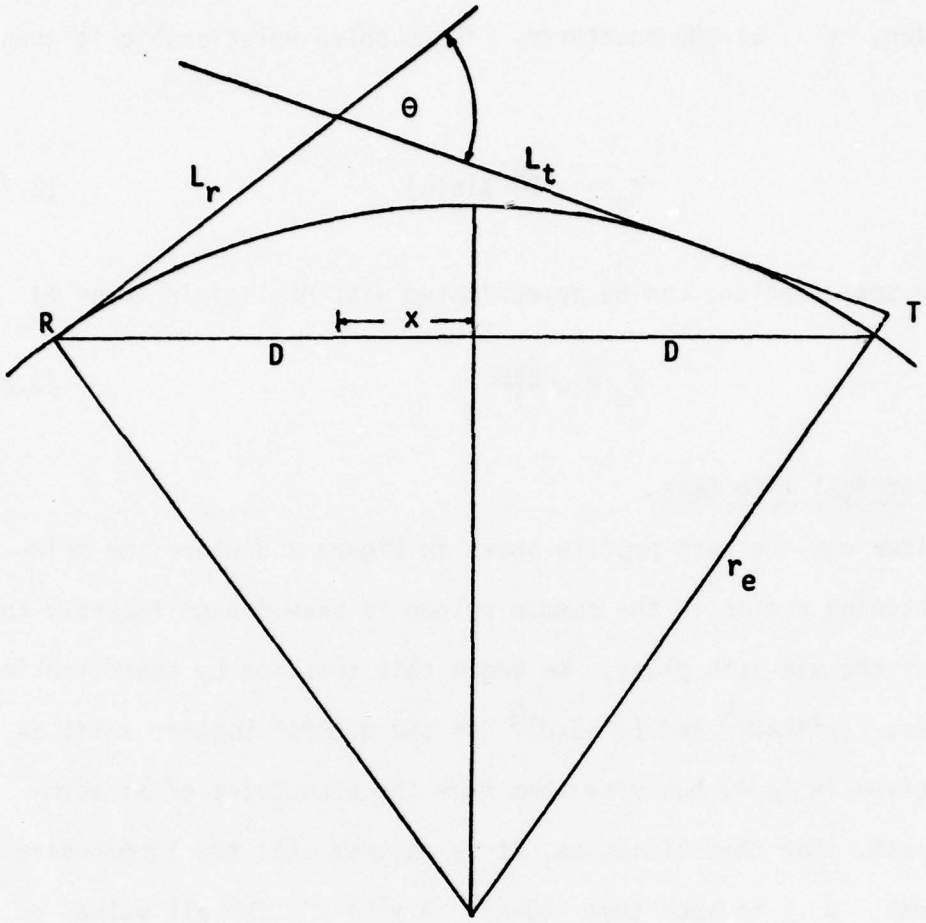

Fig. 2.3. ASYMMETRICAL PATH PROFILE

A simplification of (2.9) can be made by introducing a path asymmetry factor resulting from the terrain profile along the path and the relative heights of the radio terminals. The asymmetry factor, s, is defined as the ratio of the longitudinal displacement of the scattering source to the chordal distance from the mid-path plane to either of the radio terminals, i.e. $s \equiv x/D$. It is zero for a symmetrical path. When the scattering region is skewed to one side of the mid-path plane, however, the magnitude of the asymmetry factor becomes greater than zero but always remains less than unity. Using this factor, the Doppler shift becomes

$$f_d = - \frac{L}{\lambda D} \left[\frac{2us(1-2D/L) + vy/D + wz/D}{1 - s^2} \right] \tag{2.10}$$

The term $(1-2D/L)$ is approximately equivalent to $(y^2+z^2)/2(D^2-x^2)$. Thus, using the geometry in Figure 2.1, the Doppler shift can then be expressed in terms of the azimuthal, α, and vertical, β, angular positions of the scatterer as

$$f_d = - \frac{L}{\lambda D} \left[\frac{us(\alpha_r\alpha_t + \beta_r\beta_t)}{1 - s^2} + \frac{v\alpha_r + w\beta_r}{1 + s} \right] \tag{2.11}$$

where small angle approximations with respect to the receiver and transmitter are used, i.e. $\alpha_r \simeq \frac{y}{D(1-s)}$, $\alpha_t \simeq \frac{y}{D(1+s)}$, $\beta_r \simeq \frac{z}{D(1-s)}$, and $\beta_t \simeq \frac{z}{D(1+s)}$. For equal transverse and longitudinal wind velocities, the longitudinal Doppler contribution again remains relatively small and can be neglected. If the vertical wind contribution is also neglected and the first-order approximation, $L \simeq 2D$, is substituted

for the ray-path length, the Doppler shift expression (2.10) simplifies to

$$f_d = - \frac{2vy}{\lambda D(1-s^2)} \qquad (2.12)$$

which can be rewritten in terms of the azimuthal angular offset, α_r , from the receiver as

$$f_d = - \frac{2v\alpha_r}{\lambda(1+s)} \qquad (2.13)$$

Comparing the above results with those for the symmetrical path case, equations (2.6) and (2.8), it is seen that the Doppler shift for a scatterer at a given cross-path displacement is greater on an asymmetrical path than on a symmetrical path. This is consistent with the interpretation of the Doppler shift as the rate at which a scatterer cuts across surfaces of constant path length. The separation between these ellipsoidal surfaces is greatest in the mid-path plane and becomes smaller towards either of the two terminals. Consequently, a scatterer moving through the common volume region on an asymmetrical path cuts across the equiphase surfaces at a more rapid rate than on a symmetrical path.

On the asymmetrical Jackson-Stanford path used in the experiment discussed in this dissertation, the principal scattering region is in the vicinity of a transverse plane about 40 kilometers from the receiver. The average longitudinal displacement, x , of a scatterer on this path is such that $s \simeq \frac{1}{2}$. The analytical expression for the Doppler shift applicable to this path is

$$f_d = - \frac{4v\alpha_r}{3\lambda} \tag{2.14}$$

where α_r is measured in radians. If the angle measurement is converted to degrees and the numerical value (9.4×10^{-2}m) is substituted for λ, a more simplified expression for the Doppler shift on the Jackson-Stanford path can be written as

$$f_d = - \frac{v\alpha_r}{4} \tag{2.15}$$

where in the above expression v is units of m/s.

2.4 Multiple Scattering Effects

In the previous sections, a single scattering source was assumed and as a result, Doppler effects were limited to single frequency shifts. A multiplicity of scatterers randomly distributed throughout an illuminated region in the atmosphere produces a spectrum of Doppler shifts. The spectral composition of the Doppler shifts is dependent upon the spatial distribution and the relative velocities of the individual scatterers. Each scatterer gives rise to a discrete Doppler shift in accordance with the analysis developed earlier. A number of the scatterers, however, may contribute to the same spectral component. The extent of the contributions from the many off-path scatterers is reflected in the shape of the Doppler spectrum, which is dependent upon the relative strength of the received signal as a function of the scatterers' cross-path positions. The signal power received from a particular azimuthal direction is directly proportional to the product of the net antenna gain and the reflectivity or scatter cross-section of the medium. Thus, the Doppler

spectrum arising from a distribution of scatterers is dependent upon the antenna beam configuration and the basic propagation mechanism.

An average Doppler shift, $\overline{f}_d$, can be attributed to a mean flow or drift of the atmospheric scatterers. Birkemeier et al. (1968) have specified analytically the average Doppler shift for antennas synchronously aligned in azimuth at an angle, α_a , as

$$\overline{f}_d = -\frac{2v}{\lambda}\int \alpha G(\alpha-\alpha_a)W(\alpha)d\alpha \Big/ \int G(\alpha-\alpha_a)W(\alpha)d\alpha \qquad (2.16)$$

where $G(\alpha-\alpha_a)$ is the combined antenna gain function and $W(\alpha)$ is the scattered power per unit azimuthal angle. this result, however, applies to a symmetrical path. A more general result incorporates the path asymmetry factor, s , and can be given in terms of the angular offset, α_r , measured from the receiver location, as

$$\overline{f}_d = \frac{2v}{\lambda(1+s)}\int \alpha G(\alpha-\alpha_r)W(\alpha)d\alpha \Big/ \int G(\alpha-\alpha_r)W(\alpha)d\alpha \qquad (2.17)$$

In these expressions for the average Doppler shift, various atmospheric models can be applied to account for the angular-dependence scattering function, $W(\alpha)$. The classical isotropic turbulence model (Tatarski, 1961) predicts a minus 11/3 power-law variation in the scattering cross-section as a function of scattering angle, θ . The scattering angle is defined as the angle between the transmitted and received ray-path directions. For the isotropic turbulence model, the scattering cross-section is proportional to $\sin^{-\frac{11}{3}}(\theta/2)$. Birkemeier et al. (1977) have shown that for small scattering angles near the mid-path plane $\theta \simeq 2\sqrt{\alpha^2 + \beta^2}$. This expression for the scattering angle is valid for

near-symmetric propagation paths. However, a more general result that is applicable to asymmetrical paths as well shows the scattering angle to be given approximately as

$$\theta \simeq \sqrt{\alpha_r^2 + \beta_r^2} + \sqrt{\alpha_t^2 + \beta_t^2} \tag{2.18}$$

Using the small angle approximations developed earlier, the above expression can be written as a function of the path asymmetry factor, s, in terms of the angular displacements, α_r and β_r, from the receiver as

$$\theta \simeq \frac{2}{1+s} \sqrt{\alpha^2{}_r + \beta_r^2} \tag{2.19}$$

An equivalent expression for the Jackson-Stanford path, which has a minimum scattering angle of 0.84° occurring at an elevation angle of 0.25°, is

$$\theta \simeq 0.5 + \frac{4}{3} \sqrt{\alpha_r^2 + \beta_r^2} \tag{2.20}$$

where $\beta_r \geq 0.25°$.

In addition to the azimuthal variations, the above relationships show the extent of the influence of the vertical positions of the scatterers on the scattering function. The average Doppler shift from a given azimuthal direction is a spatially averaged result of the transverse motions of scatterers at various altitudes within the common volume. The wind-produced drift of the scatterers generally increases with altitude. However, the turbulence model assumed produces a rapid decrease in the scattered power with elevation angle. This suggests

the average Doppler shift is primarily associated with the motion of scatterers in the lower segments of the illuminated scattering region.

Chapter 3

DESCRIPTION OF EXPERIMENT

3.1 Propagation Path

The experiment described in this report was conducted over the propagation path shown in Figure 3.1. The 164-km (102 miles) path is aligned along a SW-NE (230° - 50°) azimuthal bearing between Jackson Butte (transmitter site) and Stanford, California (receiver site). The transmitter was situated on a 725-meter (2375 ft) peak just east of Jackson, California and the receiver was located 110 meters (360 ft) above sea level in the foothills behind Stanford University. A topographical profile

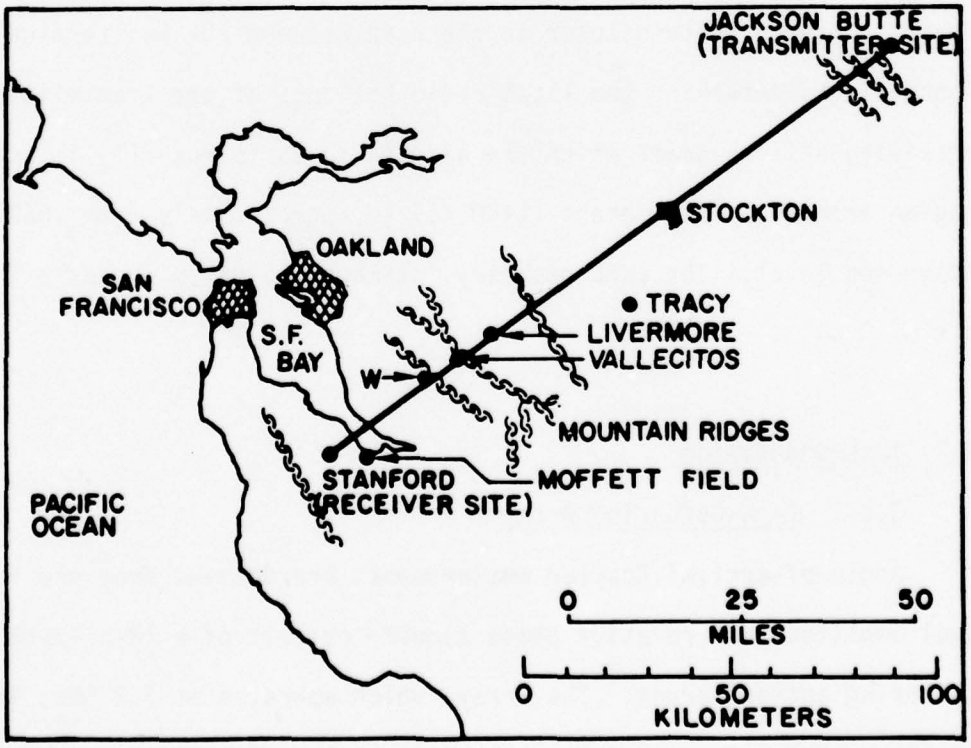

Fig. 3.1. PROPAGATION PATH AND SURROUNDING AREA.

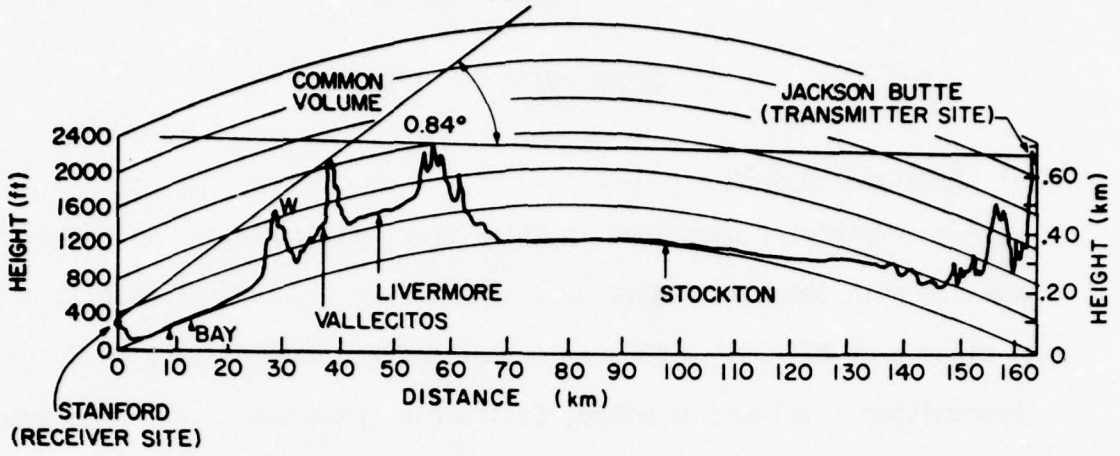

Fig. 3.2. TOPOGRAPHICAL PROFILE OF PROPAGATION PATH.

(Figure 3.2) of the path shows the existence of three mountain ridges that are nearly perpendicular to the path between the two terminals. These ridges determine the local radio horizons of the transmitting and receiving antenna beams which are aligned so as to mutually illuminate a region from about 425 meters (1400 ft) to approximately 2 km (6600 ft) above sea level. The path geometry introduces a minimum scattering angle of 0.84°

3.2 Instrumentation

3.2.1 Data-Gathering Array

Angle-of-arrival Doppler measurements are derived from the individual amplitude and relative phase sampled outputs of a 12-element data gathering antenna array. The array, which operates at 3.2 GHz, is shown in Figure 3.3 and, except for the horizontal orientation and polarization, is identical to the vertical array used in previous experiments at

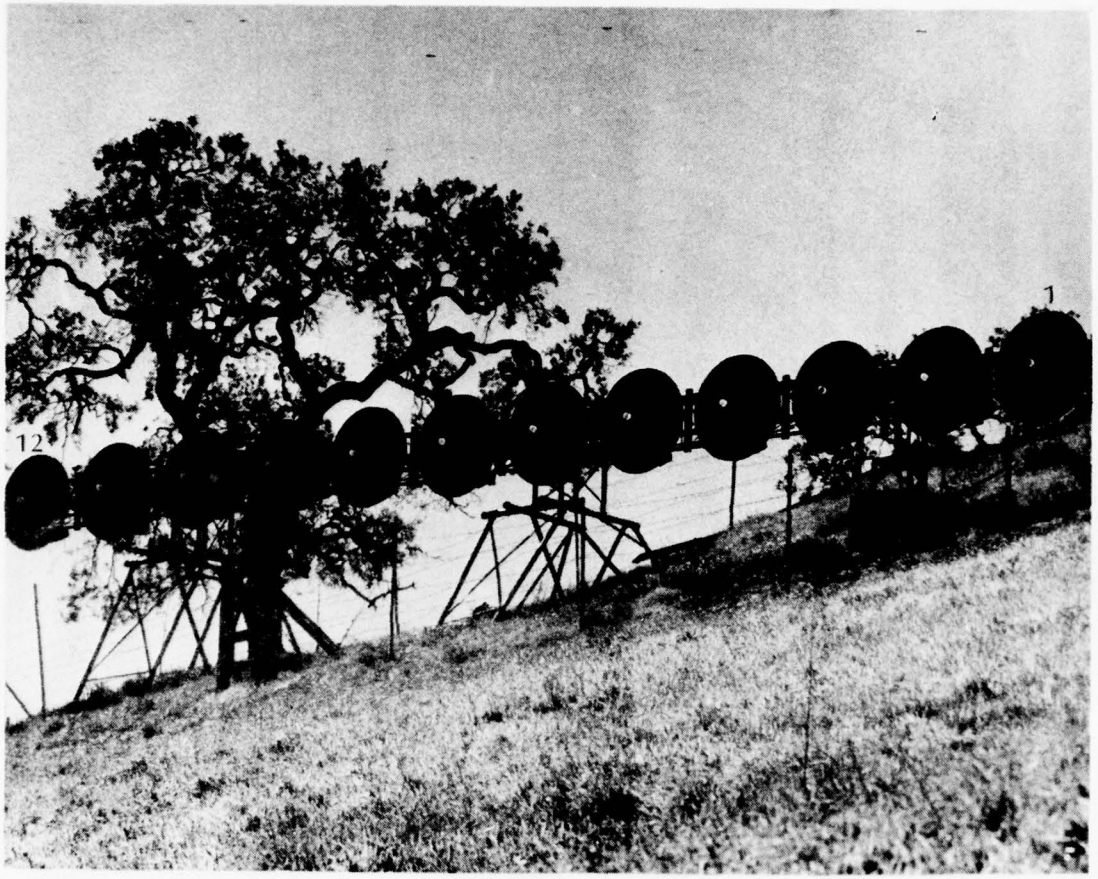

Fig. 3.3. HORIZONTAL DATA-GATHERING ARRAY.

Stanford (Cox, 1967; Cox and Waterman, 1969 and 1971; Cianos, 1971; Cianos and Waterman, 1973; Waterman, 1973; and Cianos, 1978). The data-gathering array is aligned nearly broadside to the propagation path and is structurally supported beneath the 2nd, 6th, and 10th elements. Each element is horizontally polarized and has a 5° half-power beamwidth which determines the vertical extent of the array fan beam. When uniformly illuminated, the array produces in azimuth a 0.3° wide beam which can be scanned through a 3.88° azimuthal sector. A summary of the physical and operational characteristics of the array is outlined in Table 3.1.

Table 3.1

SUMMARY CHARACTERISTICS OF DATA-GATHERING ARRAY

Physical Characteristics	Number of elements	Twelve
	Element spacing	1.4 m (14.8 wavelengths)
	Element diameter	1.2 m (13.0 wavelengths)
	Effective aperture length	15.2 m (162.5 wavelengths)
Operational Characteristics	Operating frequency	3.2 GHz
	Polarization	Horizontal
	Half-power beamwidth*	0.3° AZ/5° EL
	Grating lobe separation*	3.88°
	Sidelobe levels*	< - 13 dB
* for a uniformly illuminated conventional additive array		

3.2.2 Array-Receiver Channels

Twelve separate receiving channels connect to the twelve separate elements in the array. A typical receiving channel is illustrated in Figure 3.4. Each channel receives simultaneously the transhorizon signal at 3.2001 GHz and a stable line-of-sight reference signal at 3.2000 GHz. A 3.2300-GHz local oscillator signal (common to all 12 channels) is mixed with both the transhorizon and reference signals in mixer-preamps mounted directly behind each array element. The down-converted transhorizon (29.9-MHz) and reference (30.0-MHz) signals are separated by 2-kHz wide crystal filters. The 30-MHz IF reference is amplified and then used as a second local oscillator which mixes with the 29.9-MHz transhorizon IF signal. The resultant 100-kHz second IF signal is narrow-band filtered with a 23-Hz wide crystal filter which effectively sets the noise bandwidth of the receiving channel. After further amplification the narrow-band 100-kHz signal is passed through a variable phase shifter and a variable gain amplifier which are adjusted and set during calibration. This signal is then continuously available from each array-element receiving channel.

Sampling of the twelve 100-kHz signals is performed by a computer-controlled electronic commutator. A block diagram of the amplitude and phase sampling equipment is shown in Figure 3.5. Every 25 ms the commutator is sequentially stepped through all 12-element positions. The commutator takes five milliseconds to completely scan all twelve elements. The commutator output is bandpass filtered to reduce switching transients. The sample 100-kHz output is phase compared with a stable 100-kHz reference standard. Additionally, the signal is applied to two

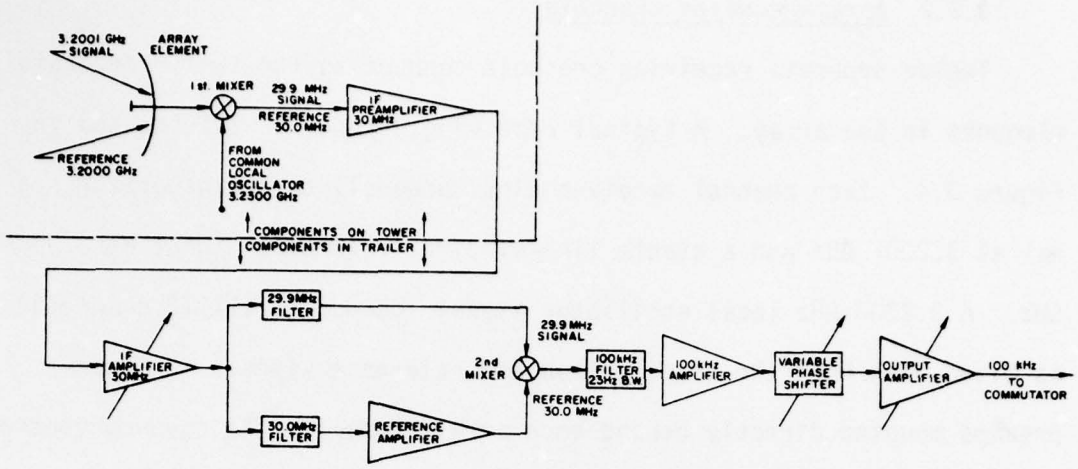

Fig. 3.4. BLOCK DIAGRAM OF AN ARRAY ELEMENT RECEIVING CHANNEL.

Parameters

1st Mixers (part of LEL type SBC-6

Noise figure: 9 to 10 dB (depends on unit)

30-MHz IF Preamplifiers (part of LEL type SBC-6)

Gain: 25 to 30 dB RF to IF (depends on unit)

30-MHz IF Amplifiers (LEL type ITA-1)

Adjustable gain: 20 to 70 dB
Bandwidth: 3 MHz

29.9-MHz and 30.0-MHz Filters (Hughes special design)

Bandwidth: 2 kHz
Quartz crystals

2nd Mixers

Balanced diodes for LO (reference signal)
Noise Suppression

100-kHz Filters (Blackhawk Networks Corporation)

Bandwidth: 23 Hz
Quartz Crystals

Phase Shifters (Nilsen V42-01 Variogon)

Adjustable 0° to 360° continuously
Loss independent of phase setting

100-kHz Output Amplifiers

Low output impedance: 5 to 10 Ω
Phase shift independent of gain setting
Gain adjustable 0 to 20 dB

All active circuit elements are solid-state devices

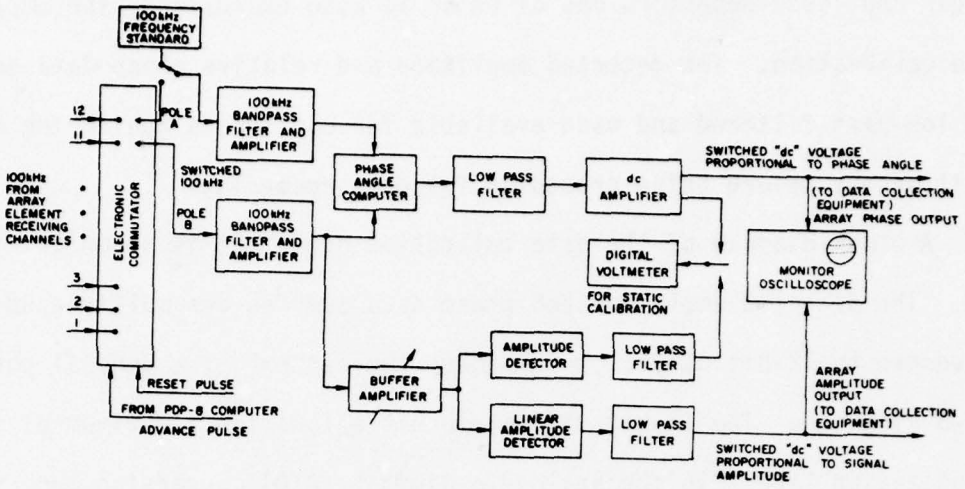

Fig. 3.5. BLOCK DIAGRAM OF AMPLITUDE AND PHASE-SAMPLING EQUIPMENT.

Parameters

Electronic Commutator

2-pole 12-position switch
Scans array at 100 scans (over 12 elements)/sec
Settling time: << 0.3 msec

100-kHz Bandpass Filters

Bandwidth: 30 kHz

Phase-Angle Computer (Wiltron Model 351)

Measures phase to 1° or better over 60 dB signal variation in either or both channels

Lowpass Filters

Active 2-pole filter using RC feedback around an operational amplifier
RC feedback set to optimize rise time at switch rate used
dc offset: < 1 mV

Linear Amplitude Detector

Linear to 1% of full scale over dynamic range > 40 dB

dc Amplifiers

dc offset: < 1 mV
Feedback around operational amplifier for good linearity

Frequency Standard (James Knight FS-1100T

100 kHz output
Aging rate of 1 to 2 parts in 10^{10}/day (1 to $2 \cdot 10^{-5}$ Hz/day at 100 kHz)

linear amplitude detectors one of which is used exclusively for amplitude calibration. The detected amplitude and relative phase data samples are low-pass filtered and made available for continuous monitoring on an oscilloscope before being processed for data recording.

A block diagram of the data collection equipment is shown in Figure 3.6. The detected amplitude and phase data samples are multiplexed and converted to 12-bit digital words under the control of a general purpose PDP-8 computer. The 12-bit digital format allows for a maximum of 4096 quantization levels in the analog-to-digital (A/D) conversion process.

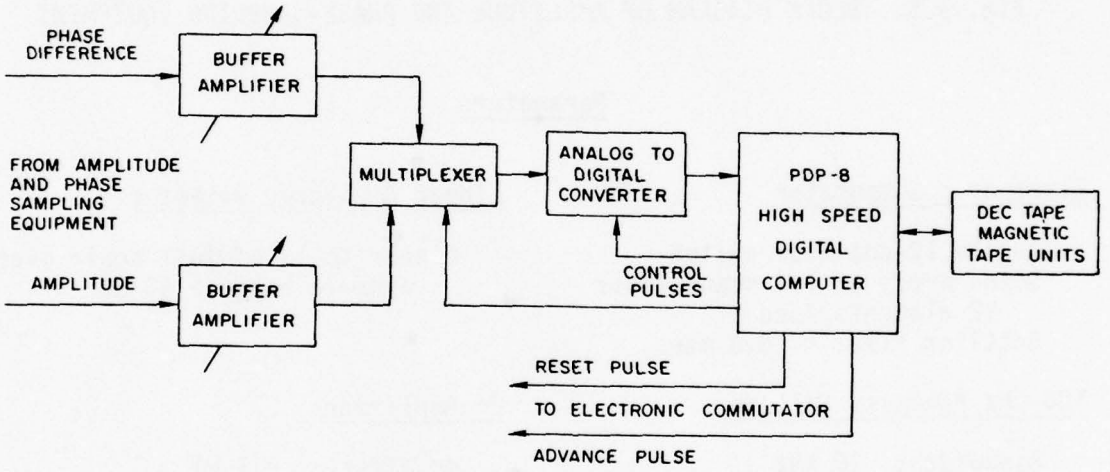

Fig. 3.6. BLOCK DIAGRAM OF DATA-COLLECTION EQUIPMENT.

Parameters

A/D Converter and Multiplexer (DEC AF01)

Multiplexer switching speed: < 2 μsec
A-D word length: 12 bits (3096 levels)
35 μsec conversion time
±0.25% max switching point error for ±1/2 least significant bit of quantization error

Computer (DEC PDP-8) with Hardware Arithmetic Unit

1.5 μsec memory cycle time
4096 word fast memory
12-bit word length

Magnetic Tape Units

DEC TU-20 (IBM Compatible)
DEC TU-55 (Program DECtape)

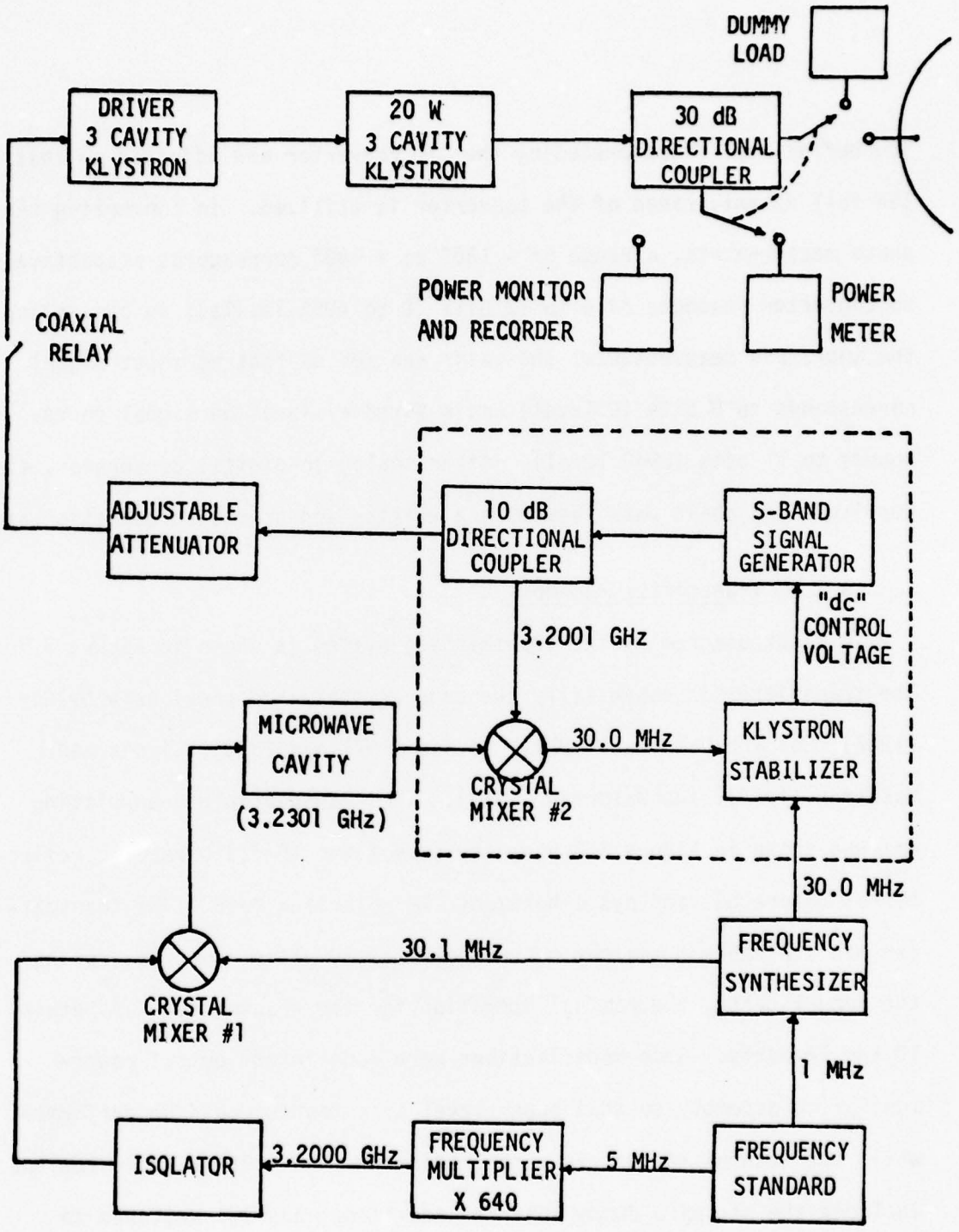

Fig. 3.7. BLOCK DIAGRAM OF TRANSMITTER

The buffer amplifiers preceding the A/D converter are adjusted so that the full dynamic range of the converter is utilized. In converting the phase measurements, a range of - 180° to + 180° corresponds respectively to converter readouts of 0 to 12 bits (0 to 4095 levels); in converting the amplitude measurements, the gains are set so that no input signal corresponds to 0 bits (0 level) and a fixed calibration signal corresponds to 11 bits (2048 level). After analog-to-digital conversion, the amplitude and phase data samples are written and stored on magnetic tape.

3.2.3 Transmitter Assembly

A block diagram of the transmitting system is shown in Figure 3.7. The transmitter is essentially the same as that used previously by Cox (1967), Cox and Waterman (1971), Cianos (1971 and 1978), Cianos and Waterman (1973), and Waterman (1973). The transportable transmitting antenna shown in Figure 3.8 uses the same 2.4-m (8-ft) parabolic reflector as before but employs a horizontally polarized feed. The transmitter has available a maximum output power of 20 watts; however, during the actual tests, the nominal operation for the transmitter was between 10 and 12 watts. Some modifications were made in the output power-monitoring assembly so that power level adjustments could be performed while the transmitter was in a non-radiating mode. These modifications included the use of a dummy load and additional coaxial switches to permit the transmitter signal to be monitored under loaded non-radiating conditions during calibration and alignment periods.

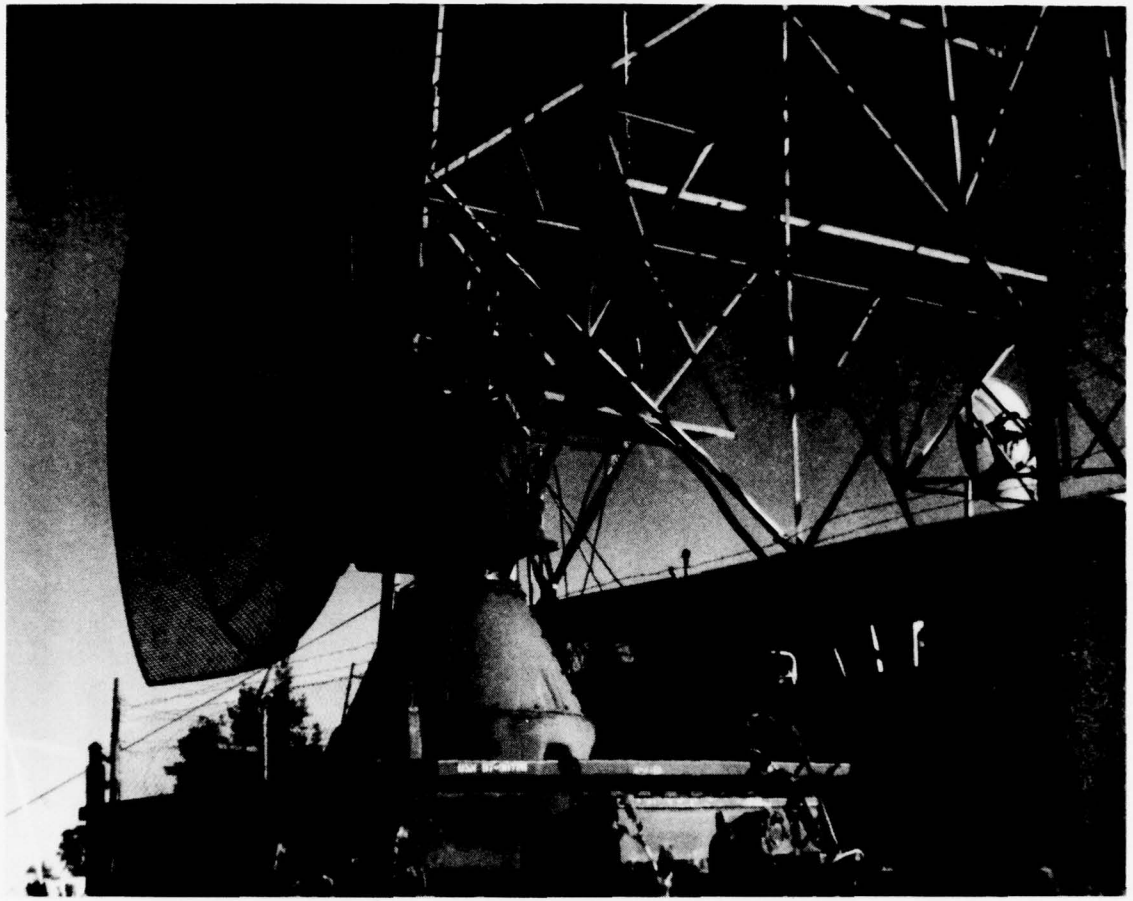

Fig. 3.8. TRANSMITTING ANTENNA AND EQUIPMENT VAN.

3.3 Experimental Procedures

3.3.1 Data Collection

Data was collected and recorded during a continuous 42-hour experiment conducted between 0000 hours on 21 April 1978 and 1830 hours on 22 April 1978. Ten minutes of transhorizon data were recorded every hour beginning approximately on the hour. The sampled amplitude and phase data from each array element were recorded in 12-bit digital format on magnetic tape at a 40-Hz rate. A five millisecond scan period was used to sample and record the amplitude and phase data from all twelve elements. The data samples were recorded in the sequence $a_1,\phi_1; a_2,\phi_2; \ldots a_{12},\phi_{12}$.

A calibration signal transmitted from a line-of-sight source about a mile from the receiver along the path was recorded for 1.6 seconds (64 scans) before every ten-minute data recording period. Immediately following the recording of transhorizon data, the transmitter was turned off and the calibration signal again turned on. The amplitude and phase calibration levels of each array element were then monitored with the digital voltmeter (Figure 3.5) and read into the log while the commutator was manually stepped through all twelve element positions.

During actual data recording, the sampled amplitudes and phases of all twelve elements were continuously monitored on an oscilloscope (Figure 3.5). Any signal anomalies that could be attributed to aircraft, interference, etc. were noted in the log. Visual sightings of aircraft in the vicinity of the common volume were logged at the transmitter, receiver, and PIBAL launch sites.

3.3.2 System Calibration

Prior to each transhorizon data recording period, the transmitter was completely checked and aligned; and all array element receiving channels were calibrated. The transmitter frequency standard (Figure 3.5) was adjusted each day during the quiet early morning hours and set to within 2 parts in 10^{11} (0.064 Hz at 3.2 GHz) of the frequency standard used to generate the reference and calibration signals. In the calibration and alignment of the individual receiving channels, a number of critical checks were made to ensure proper operation during the data-gathering portions of the experiment. The mixer currents, the amplifier gains, and the phase-lock loop status of the receiving system were routinely checked and if necessary, adjusted before each data recording period.

During calibration periods, the transhorizon signal was turned off and a 3.2001-GHz calibration signal was transmitted from a stable source about 1.6 kilometers from the receiver. This signal was remotely controlled from the receiving site and was used to properly set the variable 100-kHz amplifiers and phase-shifters in each receiving channel. With the calibration signal on, the commutator was manually advanced through all twelve element positions and the detected amplitude and adjacent element phase-difference signals were monitored with the digital voltmeter. The variable phase-shifters and amplifiers were then adjusted on an element by element basis for predetermined calibration readings on the digital voltmeter.

The predetermined phase-difference and amplitude calibration set-

tings were obtained from the results of a series of line-of-sight (LOS) tests in which the transmitter was placed at selected azimuthal positions about 15 kilometers from the receiving array. With the calibration signal off and the transmitter on (at reduced power), the individual amplitudes were set uniformly across the array by adjusting the gains of the 100-kHz amplifiers. Adjacent element phase-differences were set with the variable phase-shifters to values calculated from the signal's known angle-of-arrival. After the phase and amplitude adjustments were made, the transmitter was turned off and the LOS calibration source turned on. Phase and amplitude readings were then obtained for all twelve elements using the digital voltmeter.

The above procedures were repeated for three different line-of-sight transmitter positions. Results from two of the azimuthal positions were averaged and used to obtain the final amplitude and phase-difference calibration settings. The maximum variation in the adjacent element phase-differences observed between the two locations was 14° and the rms variation was 7°. In the amplitude readings, the maximum variation was 2 dB and the rms variation was 0.7 dB.

3.3.3 PIBAL Wind Monitoring

Pilot balloons released into the common volume from a launch site near Livermore were optically tracked during daylight hours with a single theodolite system to obtain vertical profiles of the horizontal windfield. A pilot balloon (PIBAL) was launched every hour at five minutes past the hour between 0805 and 1805 on each of the two data recording

days. The balloons were released by members of the San Jose State University Meteorology Department from a position beneath the common volume about 0.9° SE of the great-circle bearing and 165 meters (540 ft) above mean sea level. The PIBAL ascent rate was approximately 200 meters (650 ft) per minute. Azimuth and elevation position readings were taken every 30 seconds and each PIBAL was tracked to an altitude of approximately 2.4 km (7870 ft) above sea level. An algorithm used by the meteorology group reduced the PIBAL azimuth and elevation information to horizontal wind velocity profiles.

Chapter 4

ANALYTICAL METHODS

Two basic signal processing steps are used to obtain the angle-of-arrival Doppler spectra from measured amplitude and phase data samples. First, a digital Fourier transform is performed in the time domain on the sampled output signals from the individual array elements. The amplitudes and phases of the resultant spectra are preserved and used to characterize the array element output signals in the frequency domain. A spatial transform is then performed in the array plane on the element spectra to obtain an angular Doppler spectrum for the array. In this process, the individual element spectra are combined using conventional additive array techniques to maximize the output spectra for a particular angle-of-arrival. An average Doppler frequency shift (spectrum centroid) is computed as a function of the angular "pointing" direction of the array with respect to the great-circle (zero-Doppler) plane. The apparent source direction together with the computed average Doppler shift is used to infer an average transverse wind velocity.

4.1 Single Element Spectra

The measured element amplitude, $a_n(k)$, and relative phase, $\phi_n(k)$, data samples are used to construct the single element Doppler spectra. Each spectral component is evaluated from a set of K contiguous data samples. The in-phase and out-of-phase quadrature components of the element spectra are computed in accordance with the following

$$S_{XK}(n,f_i) = \sum_{k=1}^{K} a_n(k)\cos\left[\frac{2\pi f_i(k-1)}{40} - \phi_n(k)\right] \qquad (4.1)$$

$$S_{YK}(n,f_i) = \sum_{k=1}^{K} a_n(k)\sin\left[\frac{2\pi f_i(k-1)}{40} - \phi_n(k)\right] \qquad (4.2)$$

where: $n = 1, 2, \ldots, 12$

The amplitudes, $A_{nK}(f_i)$, and phases, $\Psi_{nK}(f_i)$, of the spectral components are computed from the quadrature phasor components

$$A_{nK}(f_i) = \sqrt{S_{XK}^2(n,f_i) + S_{YK}^2(n,f_i)} \qquad (4.3)$$

$$\Psi_{nK}(f_i) = \tan^{-1}\left[S_{YK}(n,f_i)/S_{XK}(n,f_i)\right] \qquad (4.4)$$

These parameters are obtained for 100 Doppler frequencies in a preselected spectral observation window. The spectral window, which is less than the receiver bandwidth (23 Hz), is centered about zero Doppler to permit simultaneous observation of the upwind (positive) and downwind (negative) Doppler shifts.

4.2 Array Angular Spectra

The array angular spectra are derived from the amplitudes, $A_{nK}(f_i)$, and phases, $\Psi_{nK}(f_i)$, of the individual element spectra. A progressive linear phase-shift across the array is applied to the spectral components of the individual element spectra. Each component is phase-shifted in accordance with conventional additive array techniques. The quadrature phasor components of the resultant angular spectra are then computed for selected beam-pointing angles, α_r , between $\pm$ 1.94° as follows

$$S_{XK}(\alpha_r, f_i) = \sum_{n=1}^{12} A_{nK}(f_i)\cos\left[\Psi_{nK}(f_i) - (n-1)\gamma\alpha_r\right] \qquad (4.5)$$

$$S_{YK}(\alpha_r, f_i) = \sum_{n=1}^{12} A_{nK}(f_i)\sin\left[\Psi_{nK}(f_i) - (n-1)\gamma\alpha_r\right] \qquad (4.6)$$

where: γ = phase shift constant

= 92.71 phase degrees/beam angle degree

A positive (negative) angular direction corresponds to a SE (NW) angle-of-arrival with respect to the great-circle bearing. The Doppler or power spectra, $P(\alpha_r, f_i)$, are computed for a particular angular direction by summing the squares of the quadrature phasor components, i.e.

$$P(\alpha_r, f_i) = S_{XK}^2(\alpha_r, f_i) + S_{YK}^2(\alpha_r, f_i) \qquad (4.7)$$

These angular spectra are essentially unweighted since each spectral component is evaluated from the same set of element amplitudes irrespective of its source direction. The Doppler spectra, however, can be weighted to account for the angle-of-arrival variations arising from the scattering mechanism and the antenna patterns. We define the direction to the source in terms of an angle, α_i , viewed from the receiver. The weighted Doppler spectra, $P_w(\alpha_r, f_i)$, are then determined by applying a normalized angular scattering function, $W_\beta(\alpha_i)$, and a combined receiver-transmitter antenna gain function, $G_c(\alpha_i - \alpha_r)$, to the unweighted spectra, i.e.

$$P_w(\alpha_r, f_i) = P(\alpha_r, f_i)\, W_\beta(\alpha_i)\, G_c(\alpha_i - \alpha_r) \qquad (4.8)$$

Each Doppler frequency is converted to an apparent angular source direction through use of the Doppler relation in (2.15), which for a uniform transverse wind velocity*, v_o , yields

$$\alpha_i = - \frac{4f_i}{v_o} \tag{4.9}$$

On the basis of the computed angular source direction, each spectral component is weighted in accordance with the classical isotropic turbulence model, a $\sin(x)/x$ receiving array pattern, and a Gaussian transmitting pattern. The normalized scattering function is evaluated for a given elevation angle, β , using the following expression with the numerator obtained from equation 2.20

$$W_\beta(\alpha_i) = \left[\frac{0.51 + \frac{4}{3}\sqrt{\alpha_i^2 + \beta^2}}{0.84} \right]^{-m} \tag{4.10}$$

where: $m = 11/3$

$\beta \geq 0.25°$

The combined antenna gain for the assumed patterns is evaluated for each source direction from the following

$$G_c(\alpha_i - \alpha_r) = \left[\frac{\sin[a(\alpha_i - \alpha_r)]}{a\pi(\alpha_i - \alpha_r)/180} \right]^2 \exp[- b\alpha_i^2] \tag{4.11}$$

where: $a = 549.900$

$b = 0.03429$

---

*The sign convention for the wind velocity is negative for a SE wind and positive for a NW wind.

The beam constants a and b are determined for half-power beamwidths of 0.29° and 3°, respectively. The transmitting beam constant, b , includes the path geometry scaling factor which permits angular measurements to be referenced to the receiver.

4.3 Average Doppler Shift

The average Doppler shift is obtained by computing the first moment (spectrum centroid) of the angular Doppler spectra. For the unweighted spectra, the average is given by

$$\bar{f} = \frac{\sum_{i=1}^{100} f_i P(\alpha_r, f_i)}{\sum_{i=1}^{100} P(\alpha_r, f_i)} \tag{4.12}$$

Similarly, for the weighted spectra

$$\bar{f}_w = \frac{\sum_{i=1}^{100} f_i P_w(\alpha_r, f_i)}{\sum_{i=1}^{100} P_w(\alpha_r, f_i)} \tag{4.13}$$

4.4 Average Wind Velocity

The average transverse wind velocity is determined using the results of averaging the unweighted and weighted Doppler spectra. An unweighted average velocity, $\bar{v}$, is obtained directly from the measured unweighted average Doppler shift, $\bar{f}$, by using equation 2.15, i.e.

$$\bar{v} = -\frac{4\bar{f}}{\alpha_r} \tag{4.14}$$

A weighted average wind velocity, $\bar{v}_w$, is computed to include corrections for the effects of the scattering mechanism and the antenna patterns. This result is obtained from a linear interpolation of the measured weighted average Doppler shift, $\bar{f}_w$, (for uniform wind v_o) and the measured unweighted average Doppler shift

$$\bar{v}_w = \frac{\bar{f}}{\bar{f}_w} v_o \tag{4.15}$$

In these expressions, the wind speed is measured in meters per second and all angles are measured in degrees.

Chapter 5

DISCUSSION OF DATA

5.1 PIBAL Wind Data

Local wind conditions were influenced during the tests by a low pressure weather system centered off the coast of the state of Washington. About six hours before the onset (0100 April 21) of the experiment, a low pressure frontal system moved through the area with slight precipitation and some gusty winds. During the two 11-hour periods between 0800 and 1800 when pilot balloons (PIBALS) were launched, the measured cross-path winds were generally from the southeast. Steady southeasterly winds prevailed at nearly all altitudes on the first day of the experiment. The winds were moderate and progressively increased during the day reaching maximum velocities in mid-afternoon. In contrast, light variable winds persisted throughout the second day when wind speeds rarely exceeded two meters per second. Typical transverse winds on this day were less than one meter per second and on occasions wind direction changes were observed between SE and NW.

PIBAL readings were taken every 30 seconds at approximately 100-m height intervals. PIBAL data above the radio horizon were averaged over 400-m vertical segments for comparison with inferred results from radio Doppler measurements. Successive averages were taken throughout the vertical extent (1600 meters) of the common volume region. Average transverse wind velocities in the four vertical segments of the common volume are tabulated in Tables 5.1 and 5.2 for the PIBAL wind soundings

Table 5.1

PIBAL WIND-MEASUREMENT DATA ON 21 APRIL 1978*

PIBAL Release	Average Transverse Wind Velocity (m/s) 1st 400-m	2nd 400-m	3rd 400-m	4th 400-m
0805	1.93 SE	3.58 SE	5.69 SE	7.12 SE
0905	1.06 SE	3.37 SE	5.61 SE	6.85 SE
1005	1.16 SE	2.73 SE	5.19 SE	5.86 SE
1105	1.84 SE	1.96 SE	3.96 SE	5.12 SE
1205	4.10 SE	4.49 SE	1.68 SE	4.19 SE
1305	3.95 SE	4.18 SE	4.55 SE	4.02 SE
1405	3.21 SE	3.95 SE	4.81 SE	4.01 SE
1505	1.98 SE	1.08 SE	3.51 SE	4.51 SE
1605	3.52 SE	4.32 SE	4.74 SE	4.65 SE
1705	4.96 SE	4.65 SE	2.51 SE	3.55 SE
1805	3.15 SE	2.40 SE	2.92 SE	3.69 SE

Table 5.2

PIBAL WIND-MEASUREMENT DATA ON 22 APRIL 1978*

PIBAL Release	Average Transverse Wind Velocity (m/s) 1st 400-m	2nd 400-m	3rd 400-m	4th 400-m
0805	0.10 NW	0.92 NW	0.48 SE	2.82 SE
0905	0.12 NW	1.49 NW	0.14 SE	1.76 SE
1005	0.34 SE	0.09 SE	0.53 NW	0.98 SE
1105	0.54 NW	0.14 NW	1.00 NW	0.08 SE
1205	0.43 NW	0.78 SE	0.99 NW	1.13 NW
1305	0.09 SE	0.29 SE	2.17 NW	0.40 NW
1405	0.53 SE	1.88 SE	0.56 NW	2.25 NW
1505	1.45 SE	0.73 SE	1.07 NW	0.09 NW
1605	1.01 SE	0.72 SE	0.98 NW	0.52 NW
1705	0.45 SE	0.22 SE	0.70 NW	2.72 NW
1805	0.89 NW	0.18 NW	2.17 NW	1.02 NW

*Average transverse wind in 400-m vertical segments above radio horizon.

taken respectively on April 21 and 22. Examples of vertical profiles of the cross-path wind component observed on the two days are shown in Figure 5.1 [(a) thru (f)]. Data from the 0805 launch on April 21 (Figure 5.1a) reflected a fairly strong wind shear between the 1300 and 1600-meter elevations. Within this 300-meter vertical range, the wind changed from 0.8 m/s NW to 12 m/s SE. This shear dissipated by the next wind sounding one hour later. No other anomalous wind conditions were observed for the duration of the experiment.

5.2 Wind-Produced Doppler

The Doppler spectra presented in this section are computed from 600 contiguous sets of data samples representing 15 seconds of real-time data. Each data set is comprised of twelve amplitudes and twelve relative phases. Computations are made from the same data sets for a sequence of array pointing angles about the great-circle bearing. In order to simultaneously measure upwind and downwind Doppler shifts, spectral observation windows are centered about the zero-Doppler frequency. Observation windows used in the spectrum analysis are narrower than the system noise bandwidth (23 Hz) but are broad enough to encompass the ambient wind-produced Doppler shifts. For the wind conditions experienced during the tests, an 8 to 10-Hz wide observation window was found to be sufficient to completely envelop the wind-produced Doppler spectrum. Outside the selected observation windows, the Doppler spectra have relatively low power spectral densities. Each computed spectrum contains 100 Doppler frequencies spaced from about 0.08 to 0.10 Hz apart depending upon the width of the spectral observation window. The spectral resolution

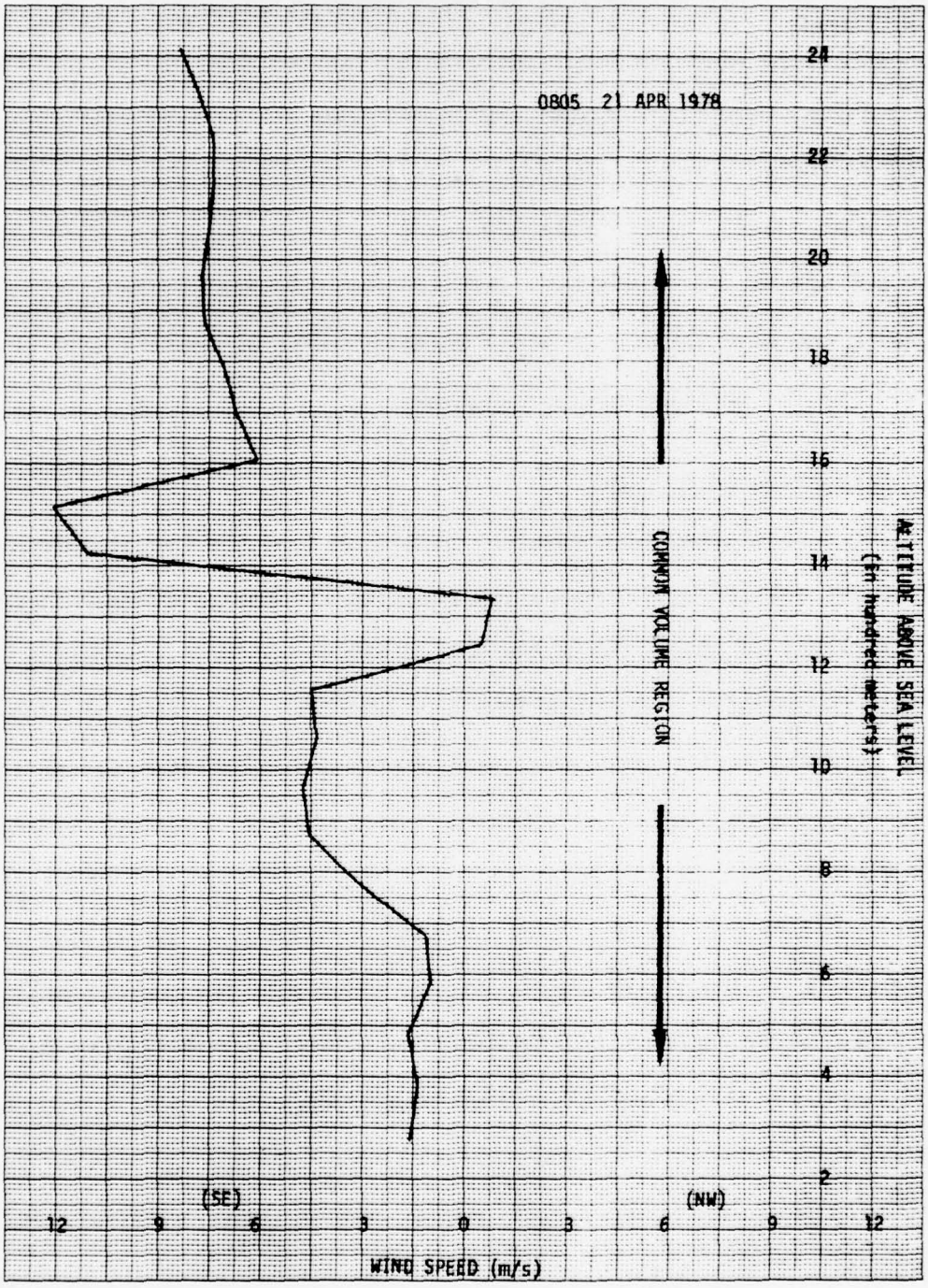

(a)

Fig. 5.1. VERTICAL PROFILE OF CROSS-PATH WIND VELOCITY

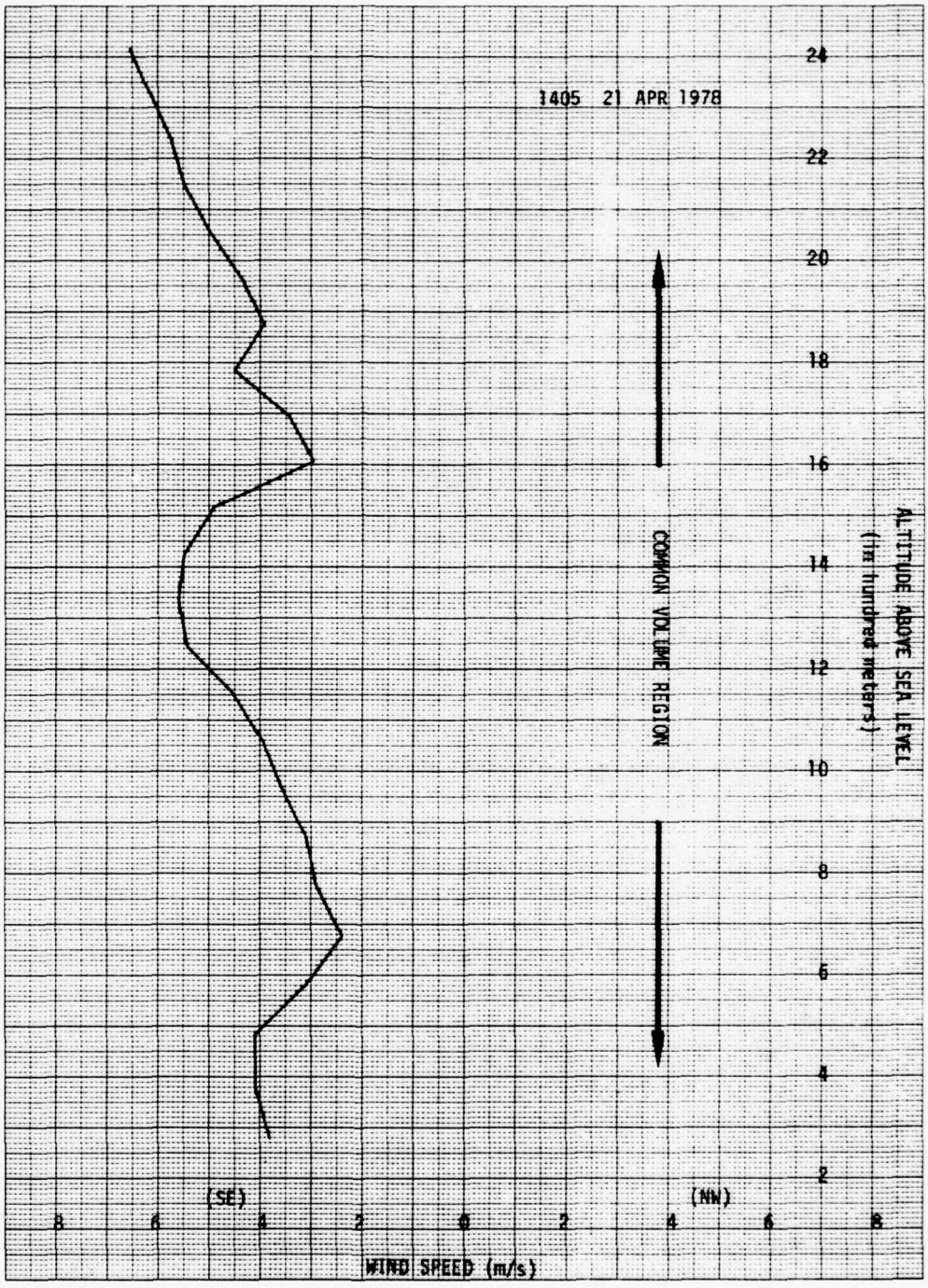

(b)

Fig. 5.1. CONTINUED.

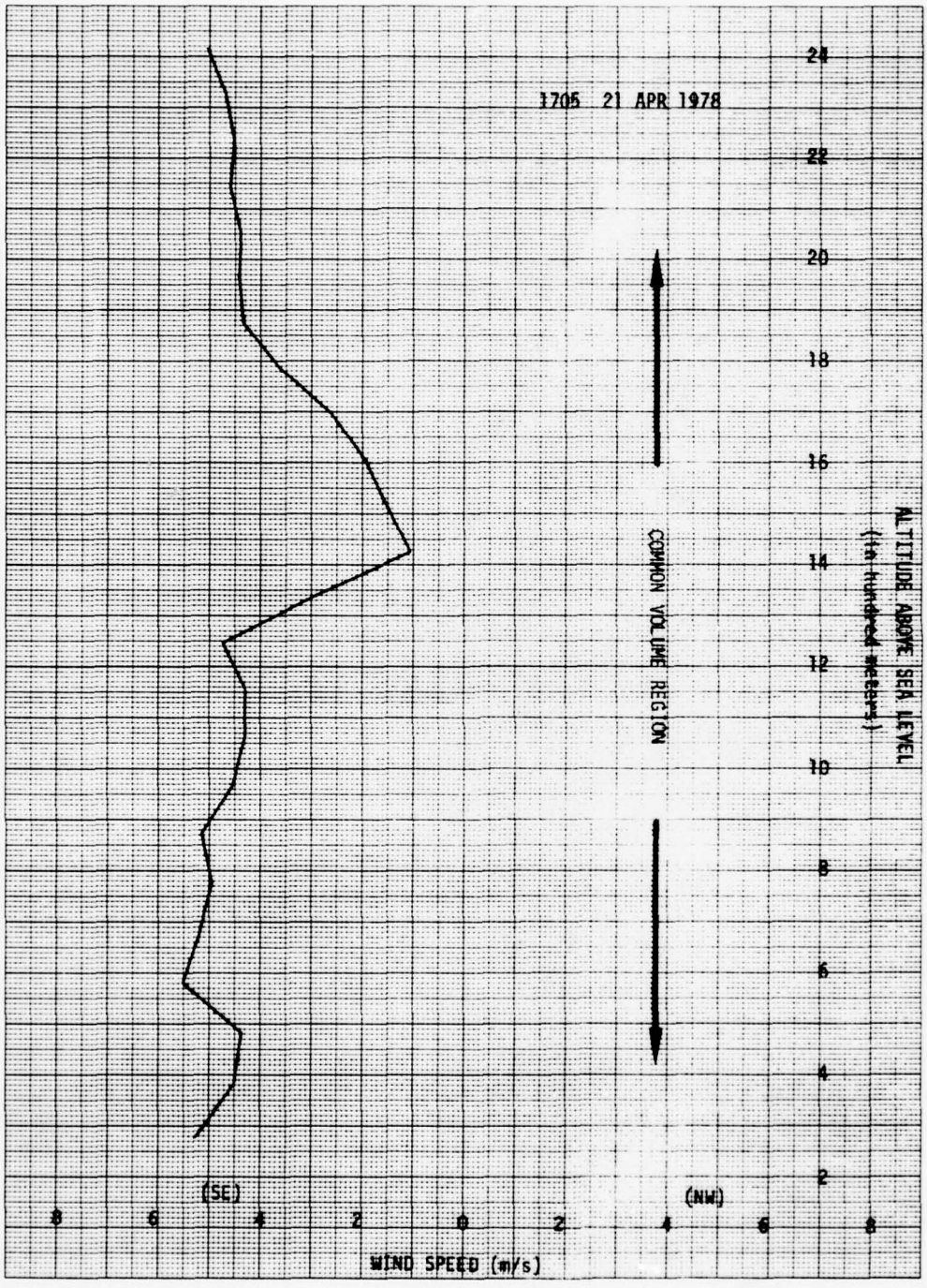

(c)

Fig. 5.1. CONTINUED.

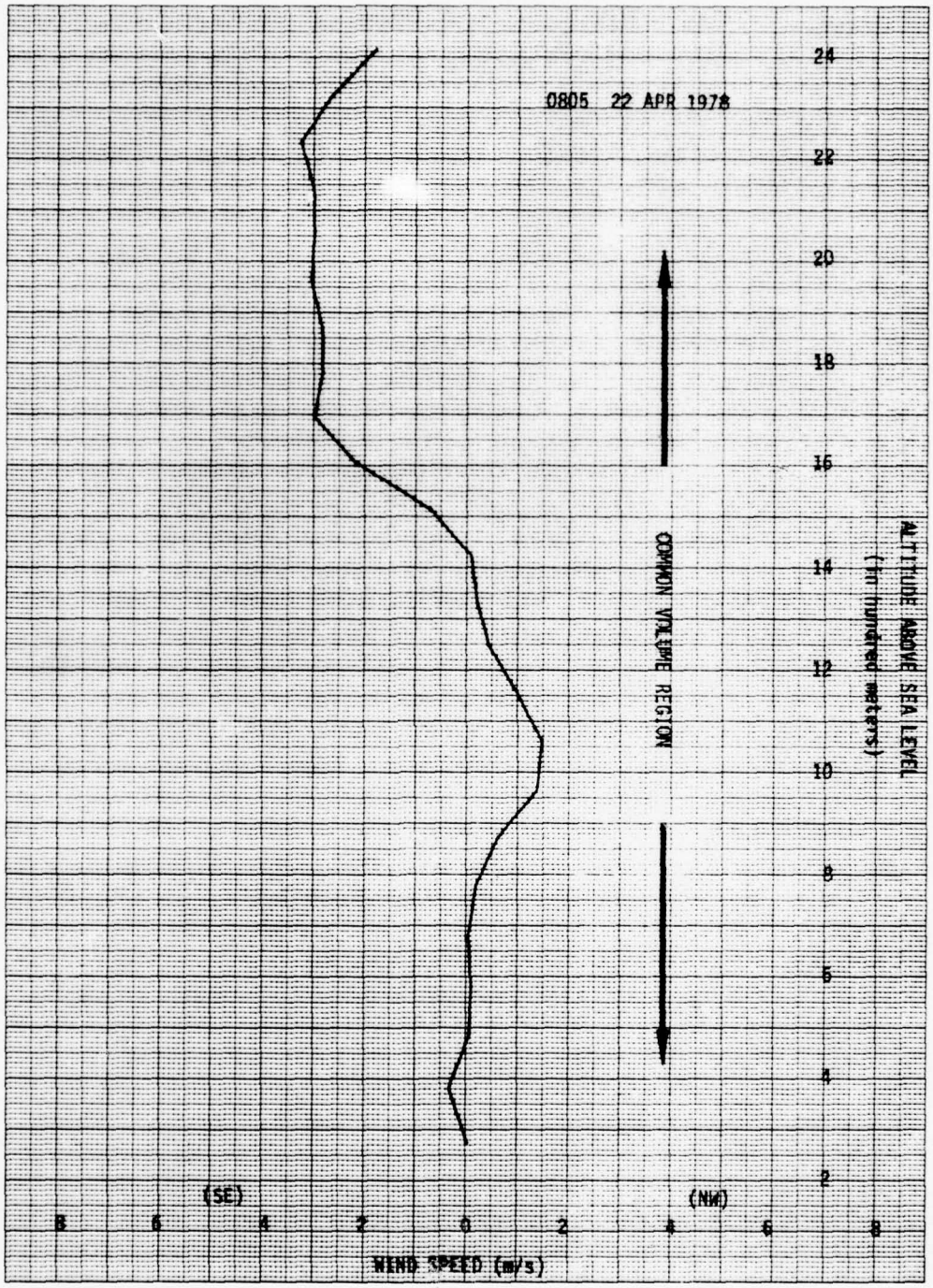

(d)

Fig. 5.1. CONTINUED.

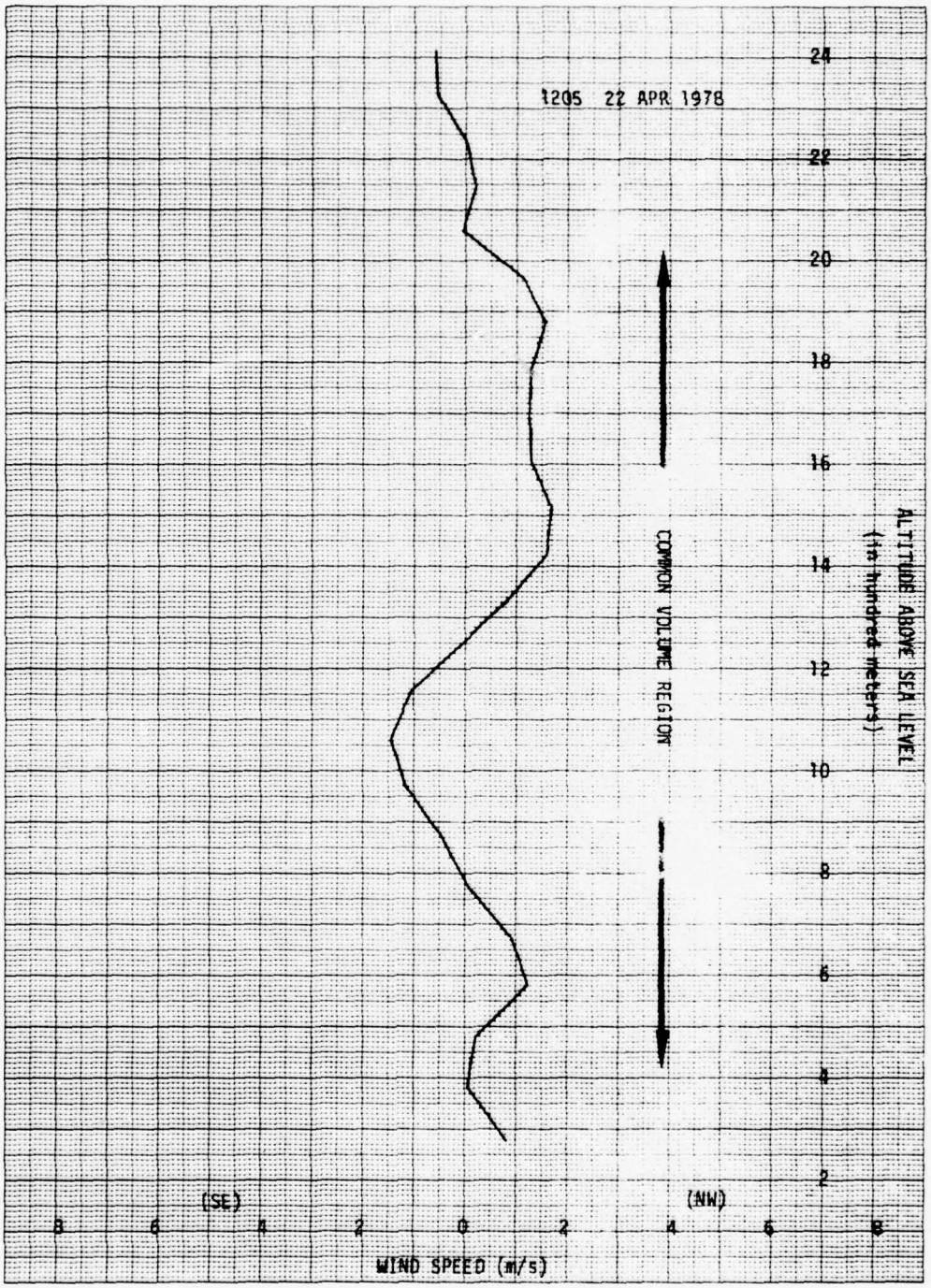

(e)

Fig. 5.1. CONTINUED.

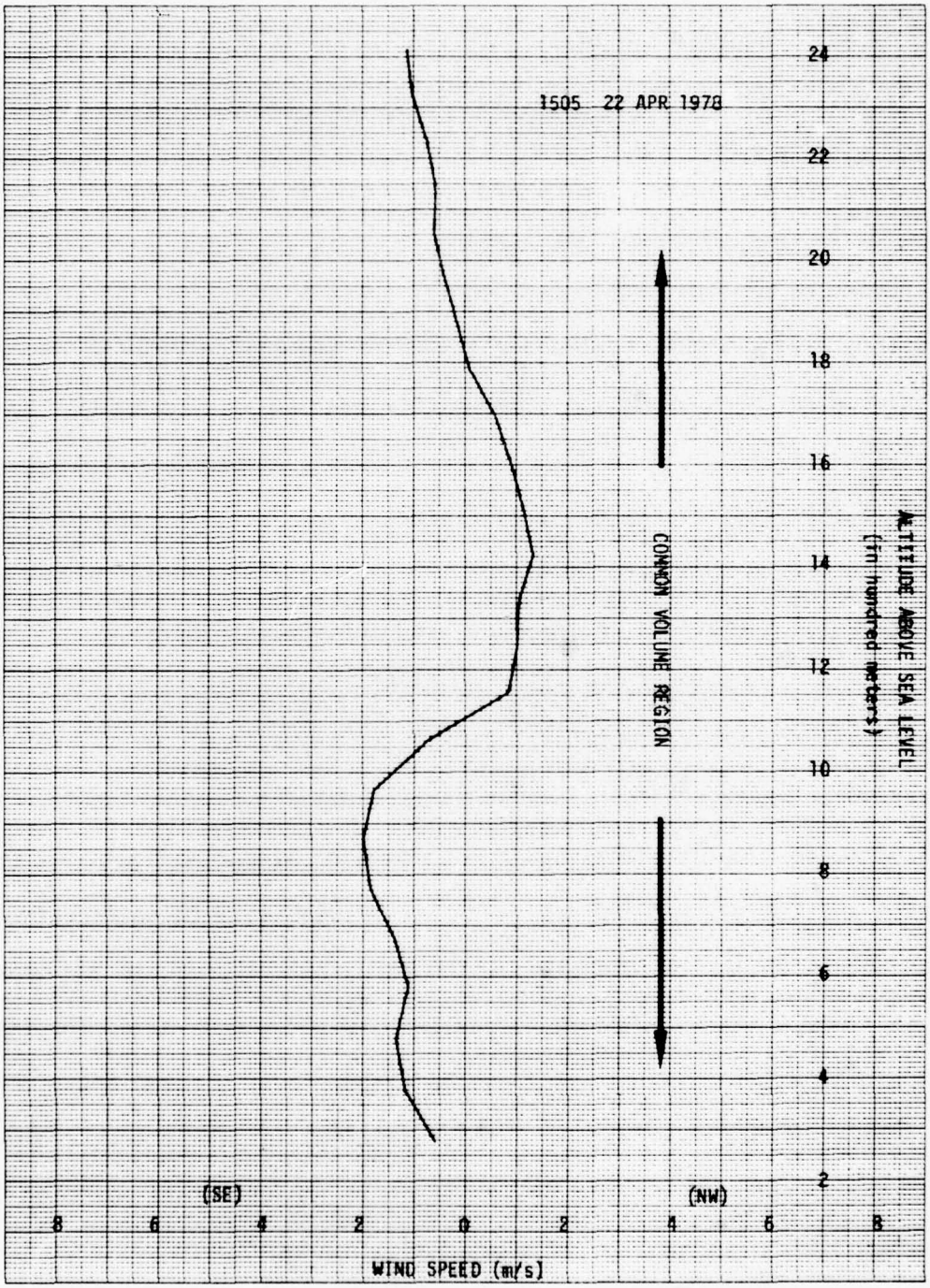

(f)

Fig. 5.1. CONTINUED.

attainable in the coherent integration process of the 600 data samples is 0.07 Hz. However, the realizable resolution is more on the order of 0.1 Hz due to the short-term instabilities (1.5 parts in 10^{11}) of the quartz oscillators.

5.2.1 Unweighted Angular Spectra

Examples of some unweighted Doppler spectra are shown in Figure 5.2 [(a) thru (l)]. These spectra are taken for symmetrical (NW/SE) beam pointing directions about the great-circle bearing at 0° azimuth. The spectra are plotted over a 40-dB range in 0.25° increments out to one degree either side of the great-circle bearing. Two 15-second samples taken one minute apart are presented for each hourly example in order to show temporal variations in the wind-produced Doppler shifts.

Initial observations of the high-resolution spectra show the presence of a coherent stationary source with a very narrow spectral width at zero-Doppler frequency. This spectral component is most likely a result of knife-edge diffraction over one or more of the mountain ridges between the transmitter and receiver. It is seen that the diffracted component increases in intensity as the array scan approaches the great-circle. Occasionally, when the array beam is pointed on-axis, the level of the diffracted component exceeds the 40-dB plotting range and a linear foldover (overshoot) occurs. Aside from its intensity level, the diffraction component is totally invariant to the azimuthal pointing direction of the array.

In contrast, the wind-produced Doppler shifts show systematic variations with the array pointing direction. A qualitative analysis of the

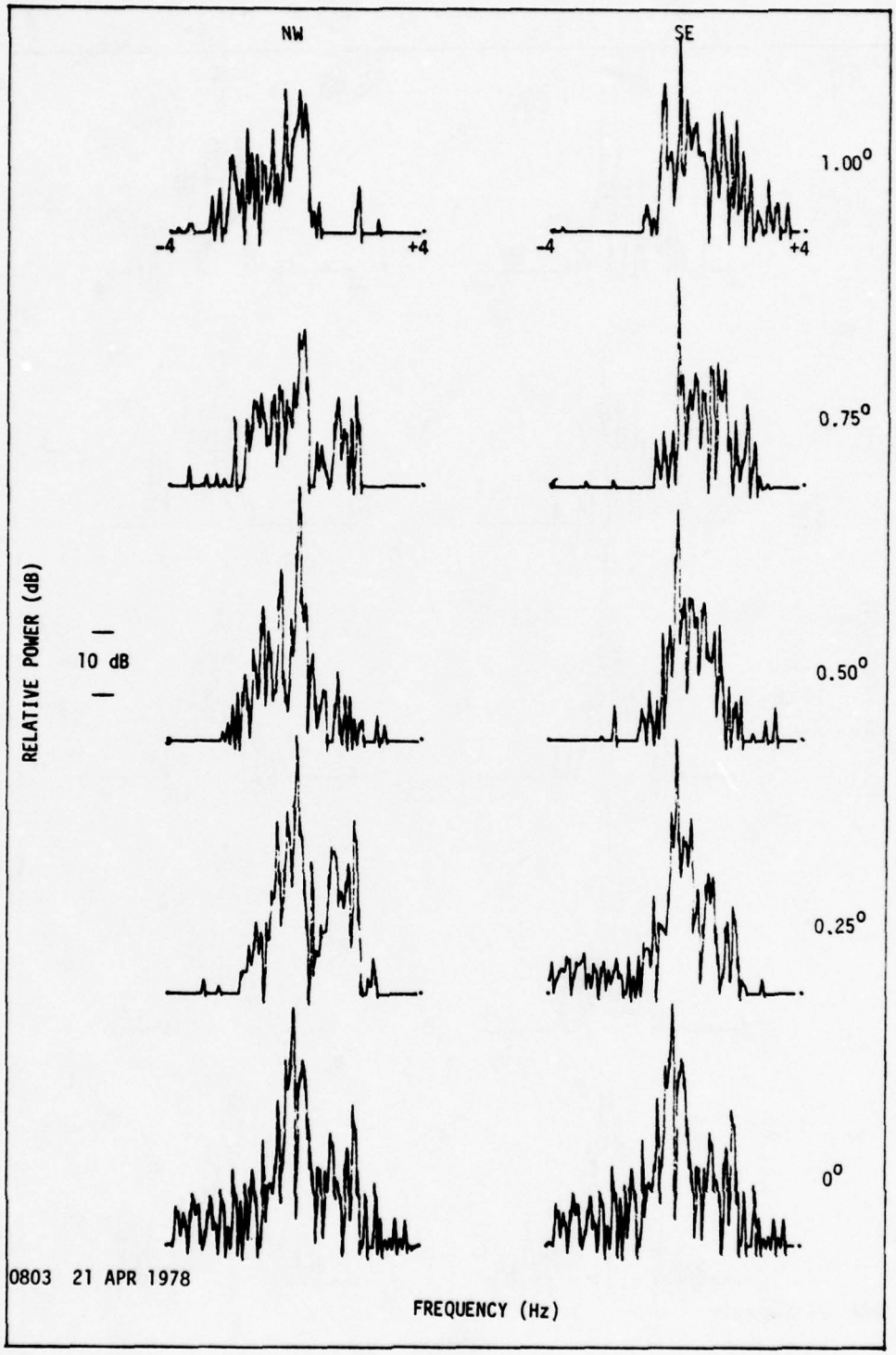

(a)

Fig. 5.2. UNWEIGHTED WIND-PRODUCED DOPPLER SPECTRA. Angle-of-arrival spectra are computed from the coherent integration of 600 (15-sec) data samples.

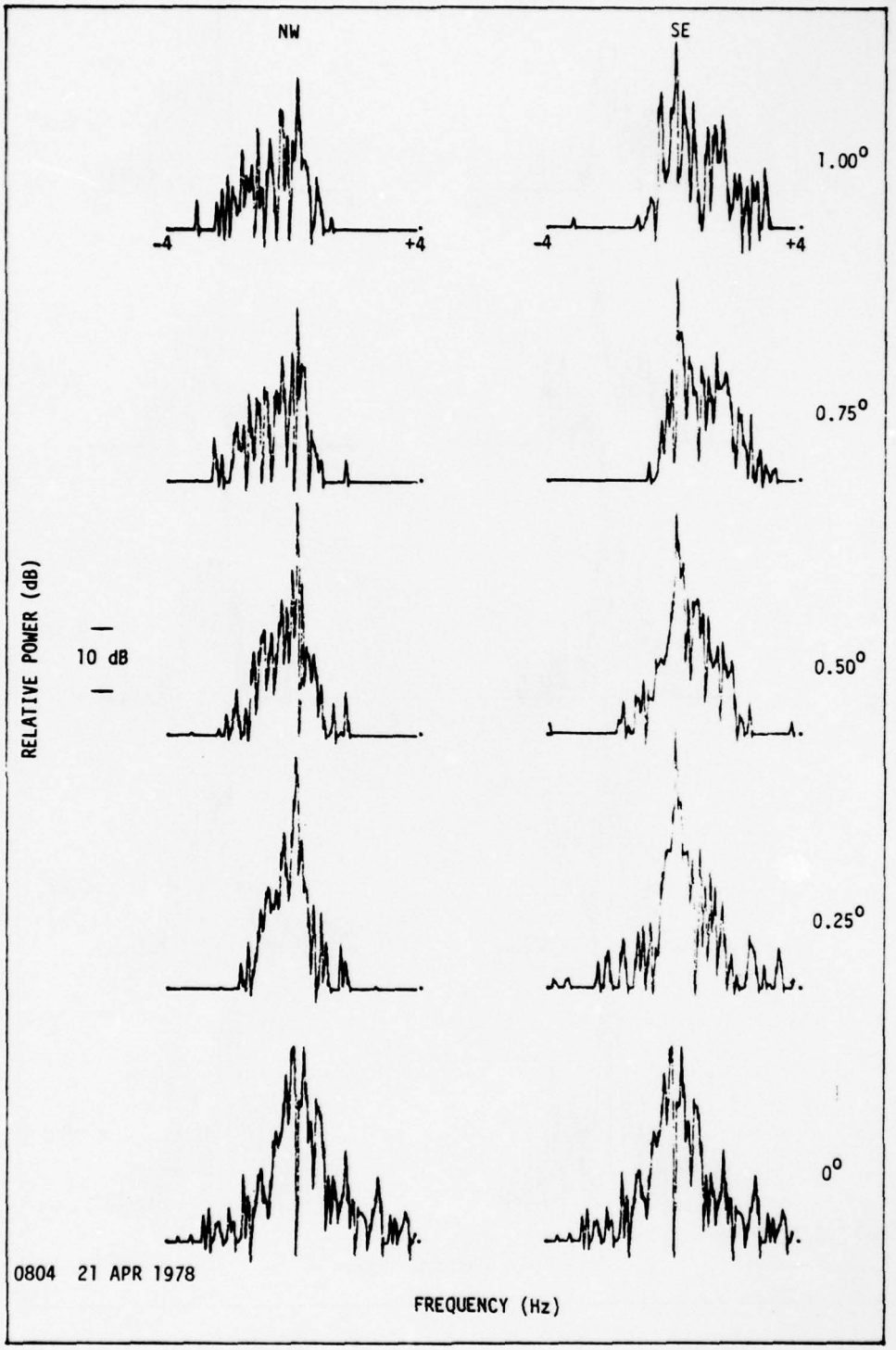

(b)

Fig. 5.2. CONTINUED.

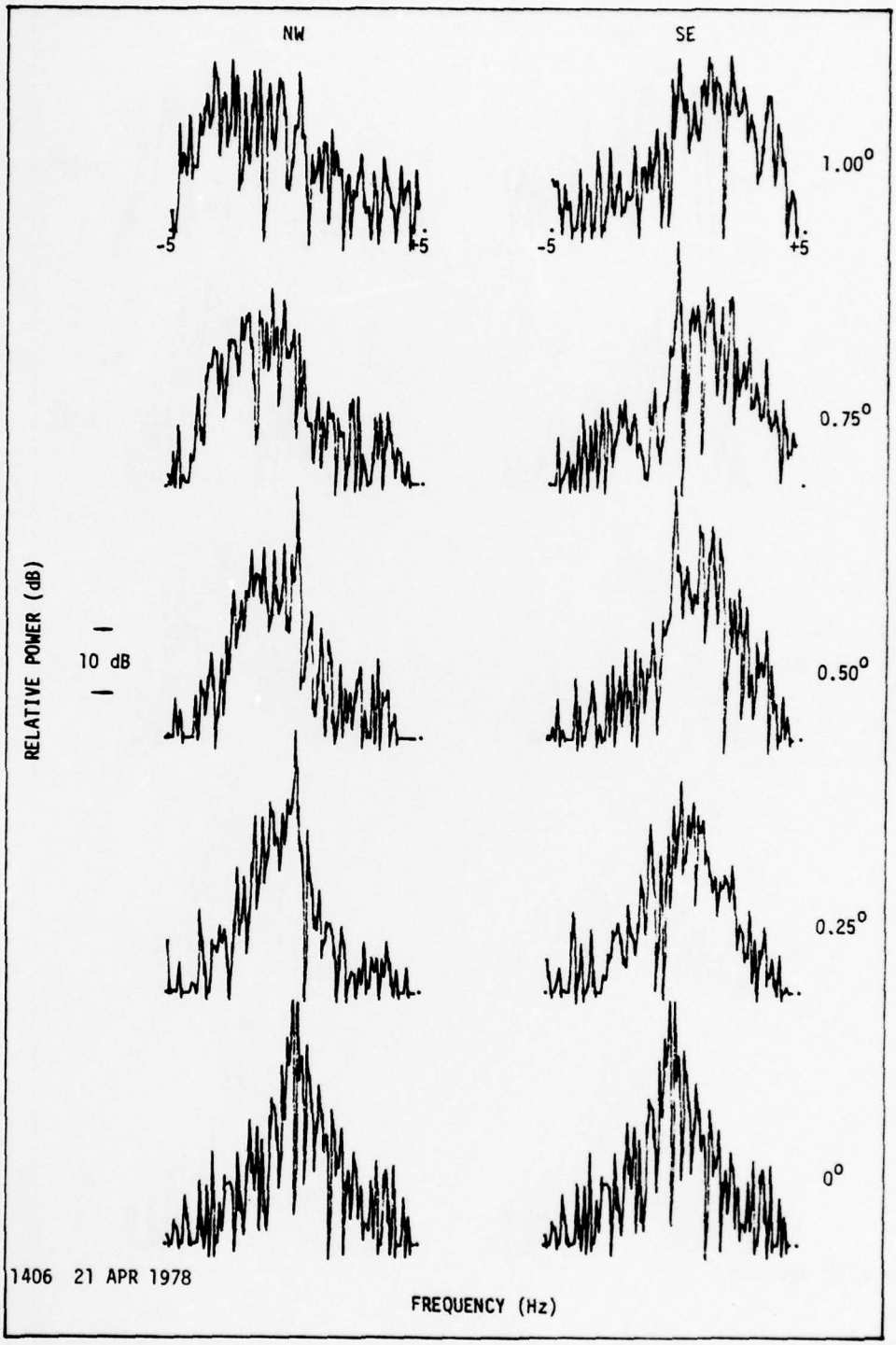

(c)

Fig. 5.2. CONTINUED.

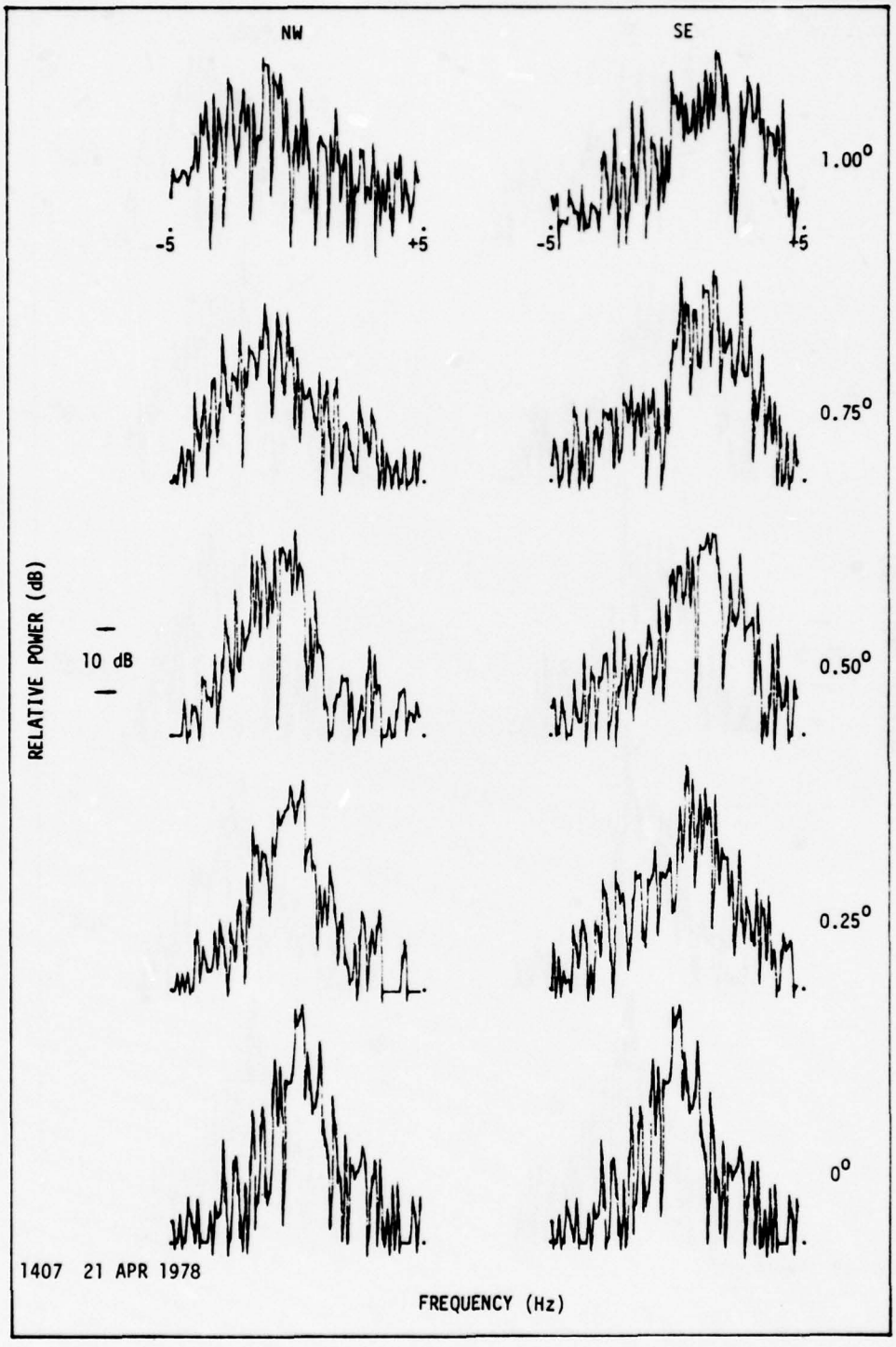

(d)

Fig. 5.2. CONTINUED.

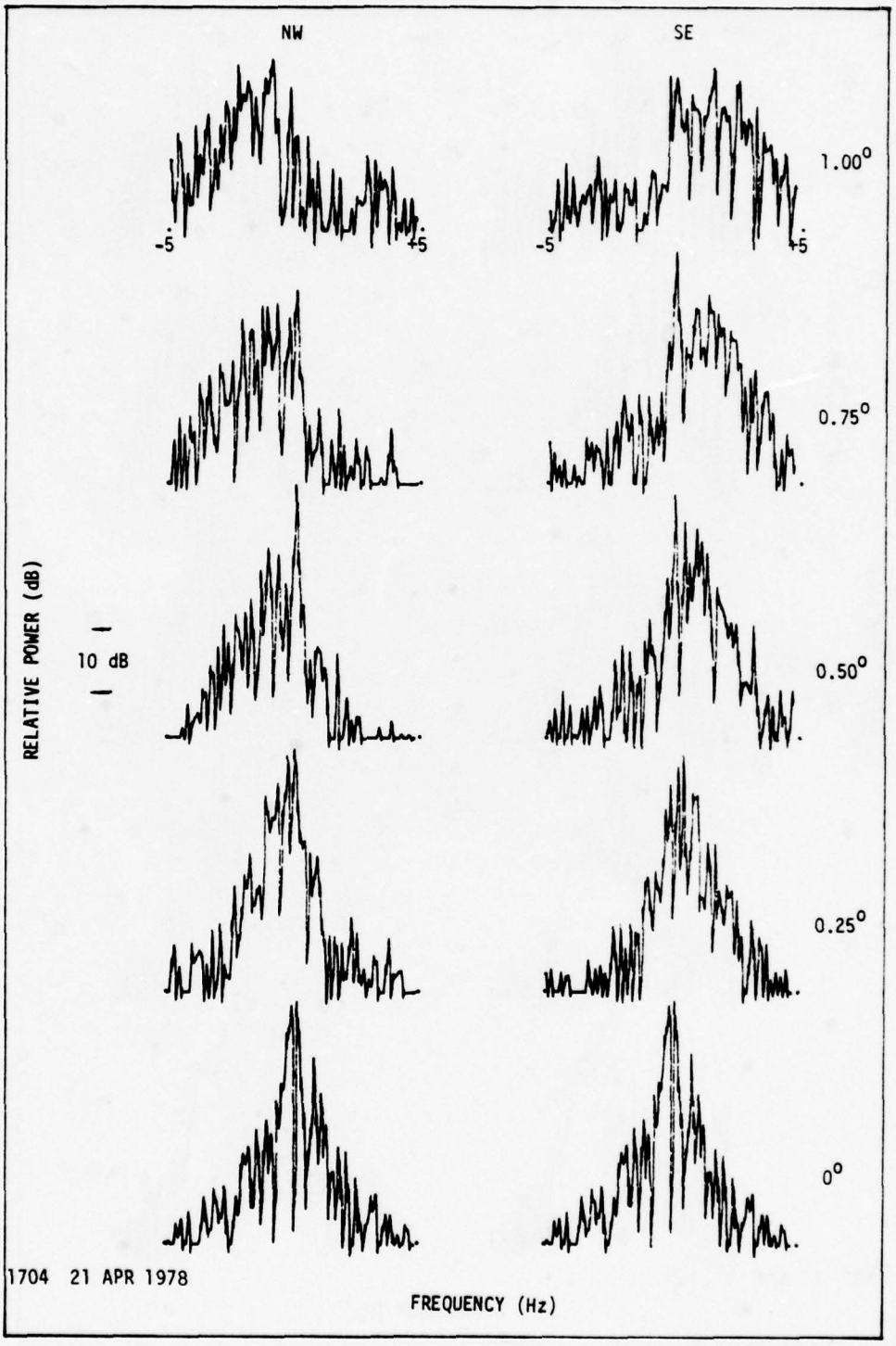

(e)

Fig. 5.2. CONTINUED.

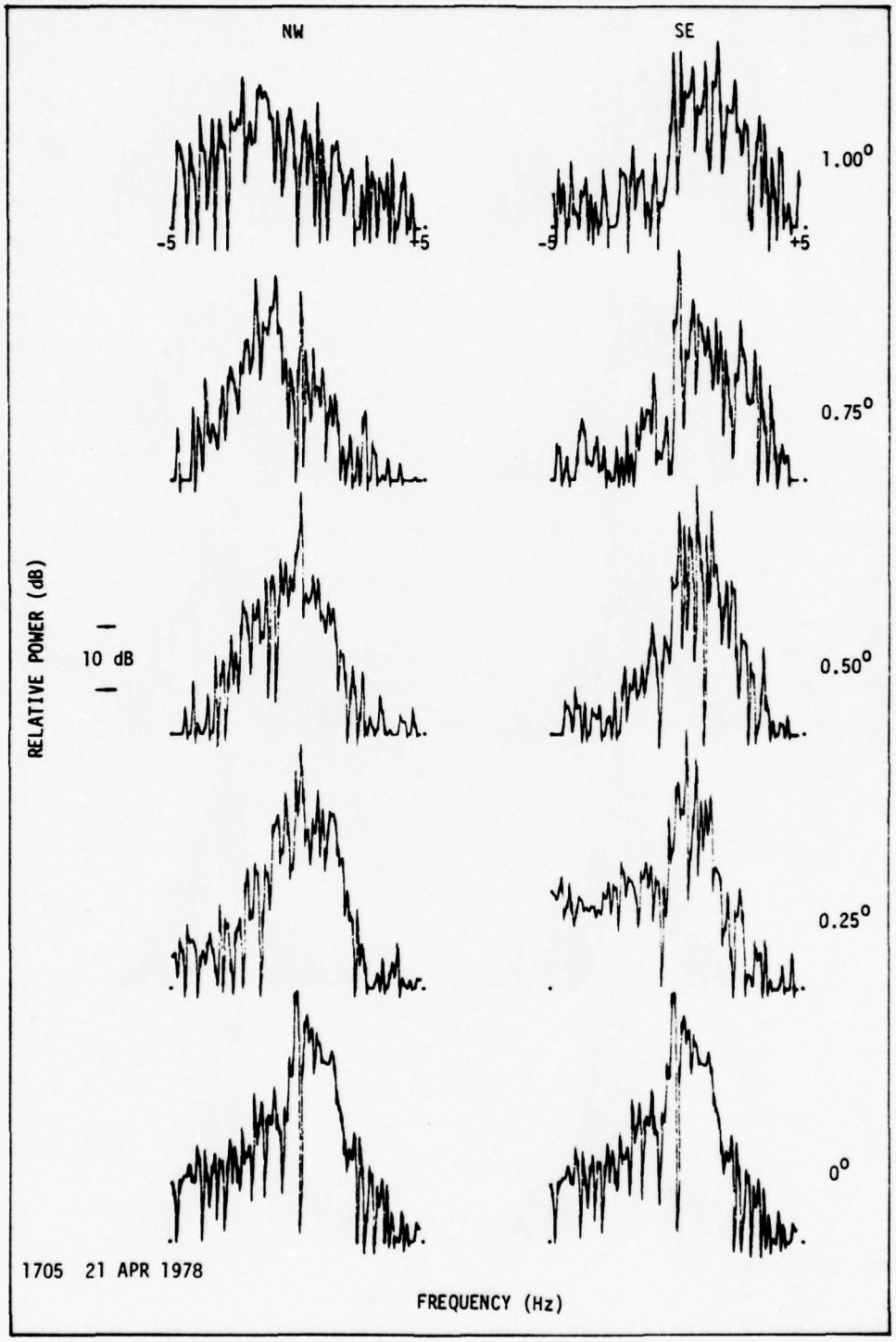

(f)

Fig. 5.2. CONTINUED.

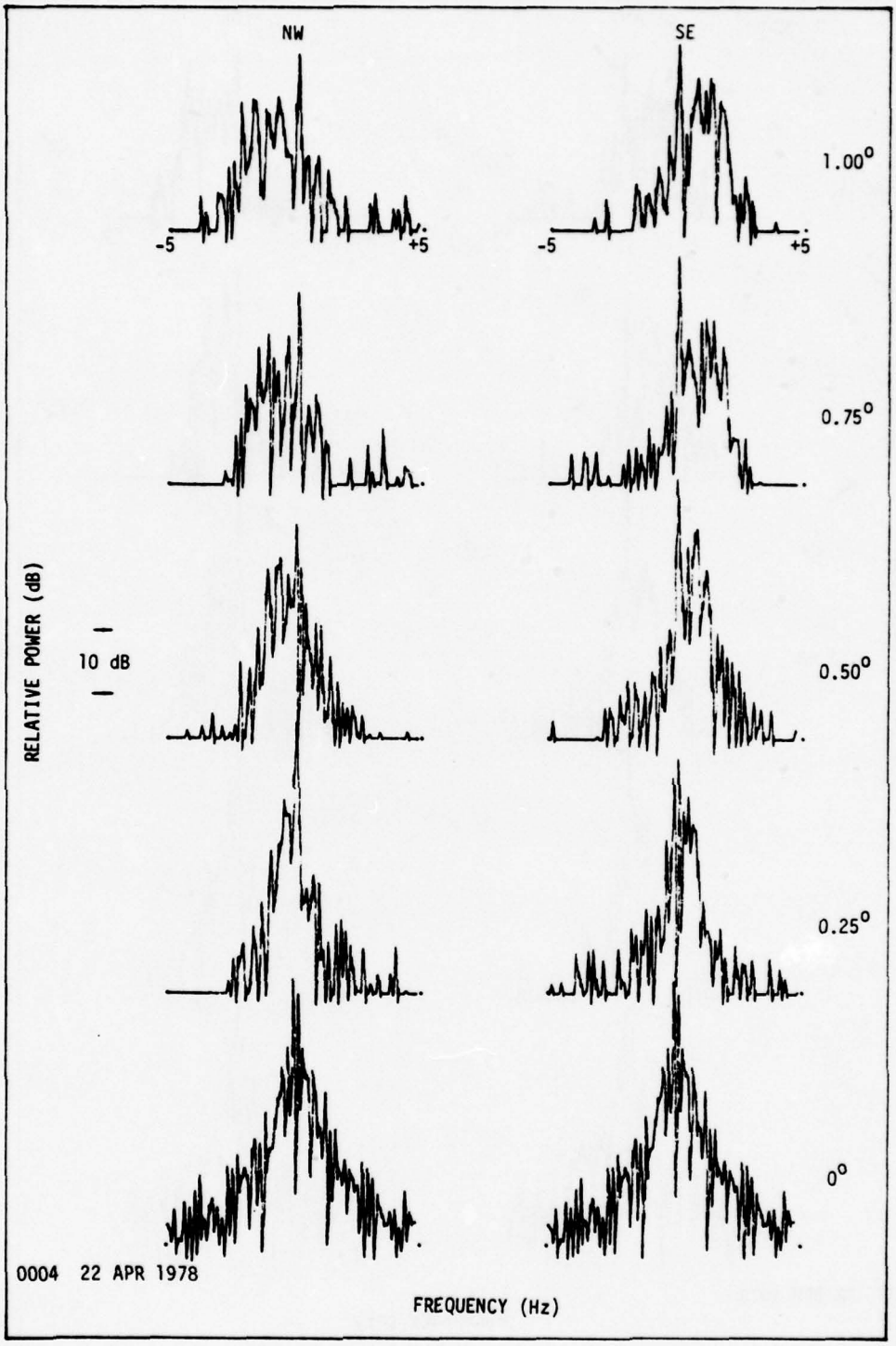

(g)

Fig. 5.2. CONTINUED.

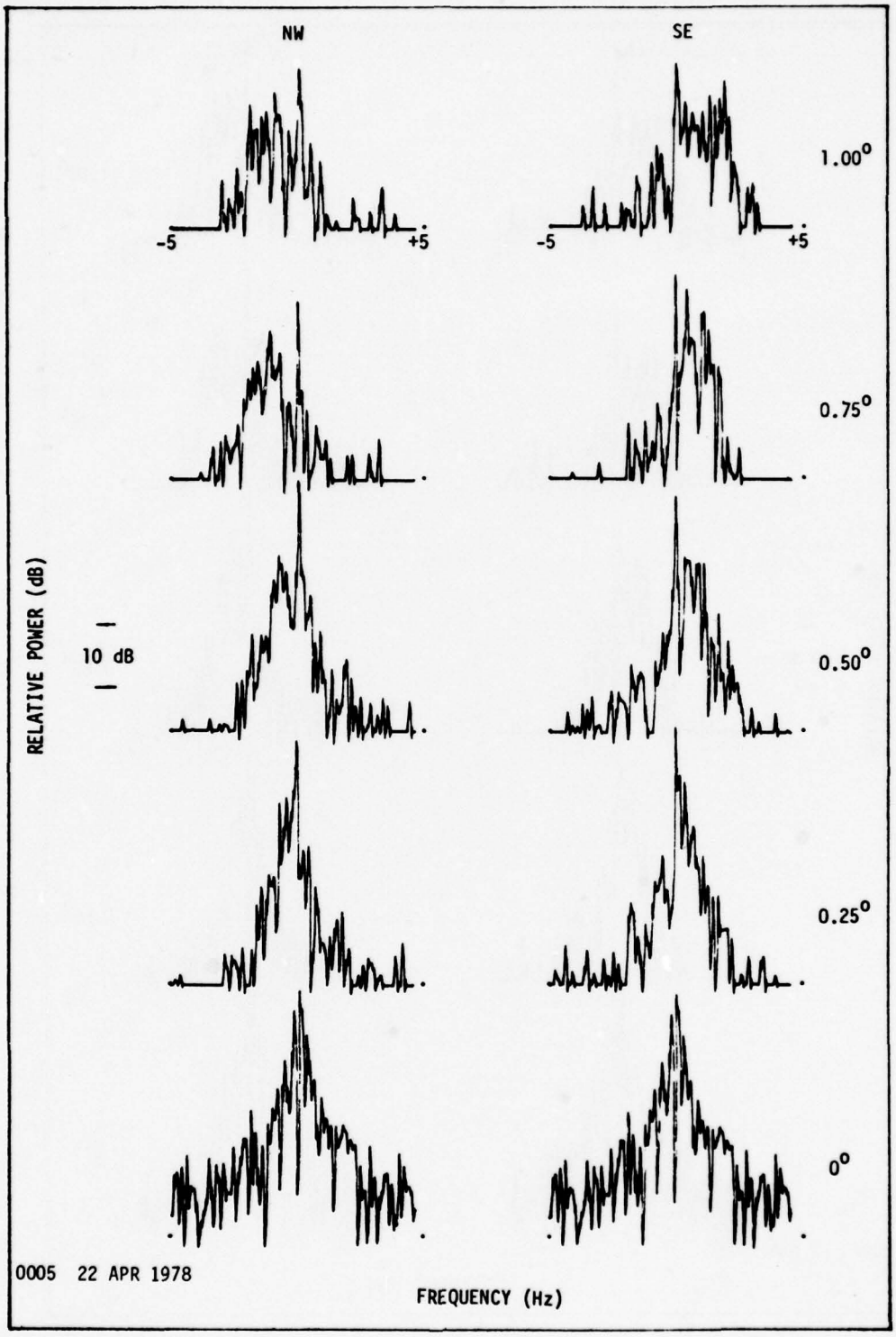

(h)

Fig. 5.2. CONTINUED.

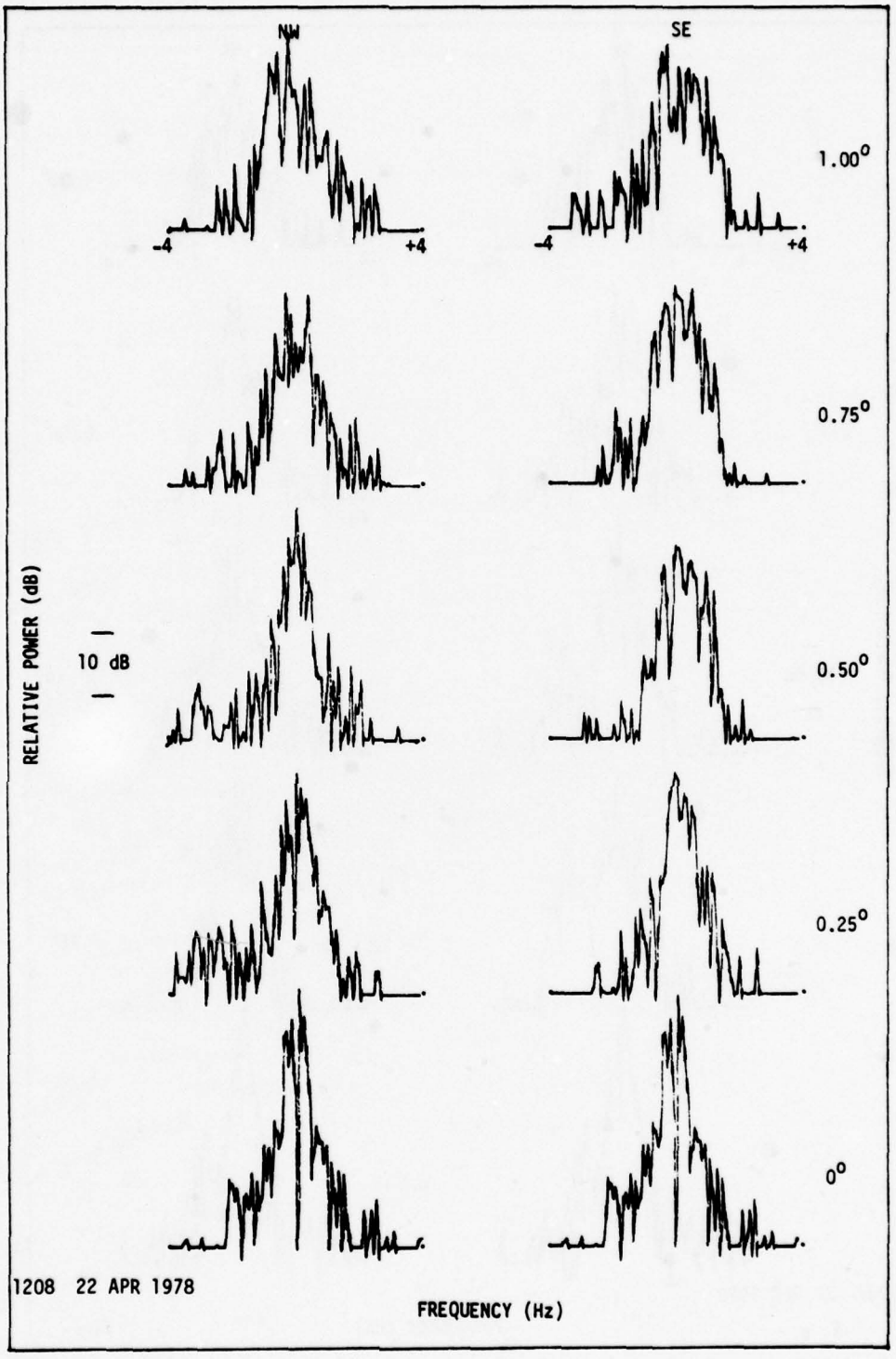

(i)

Fig. 5.2. CONTINUED.

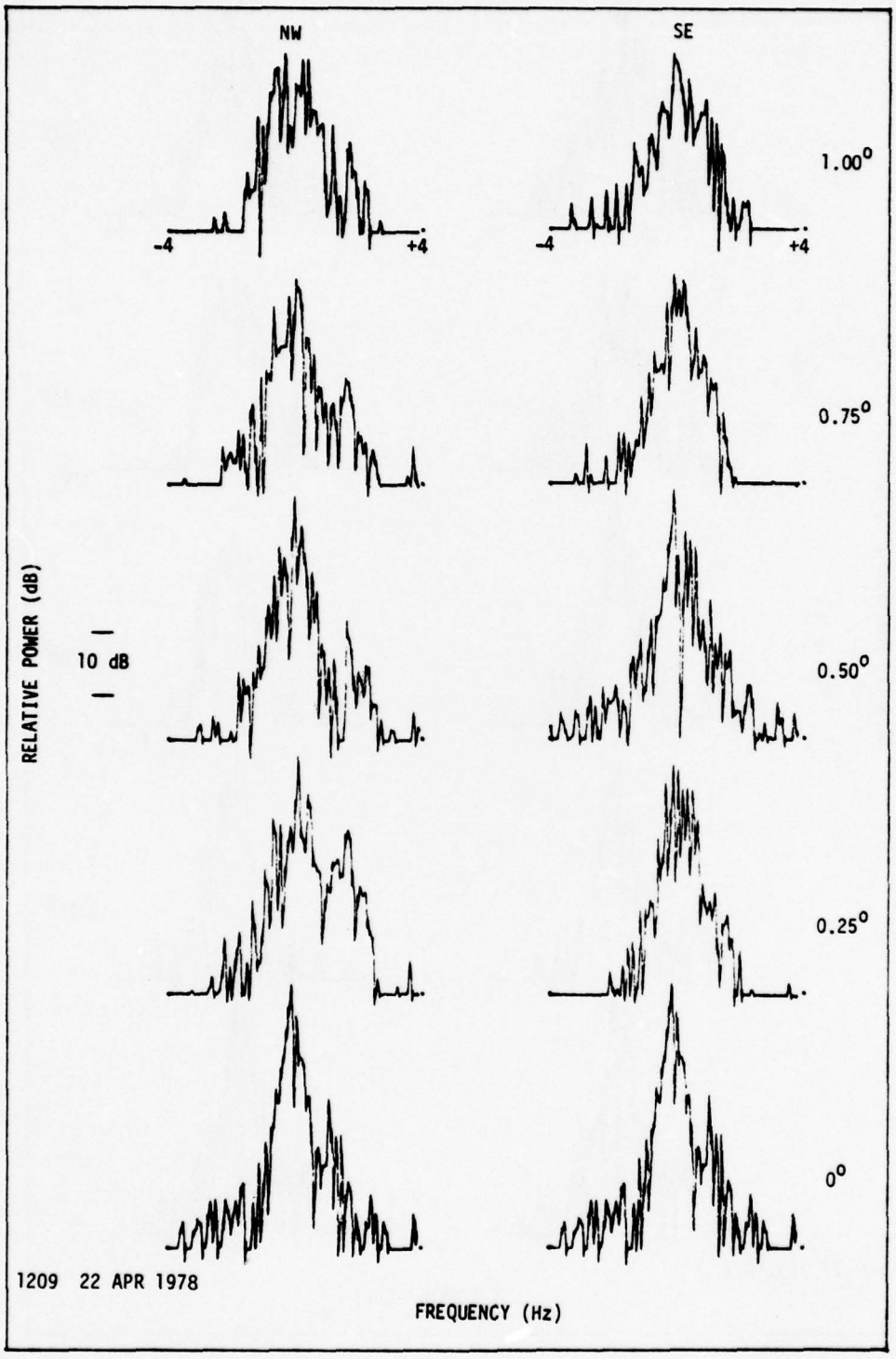

(j)

Fig. 5.2. CONTINUED.

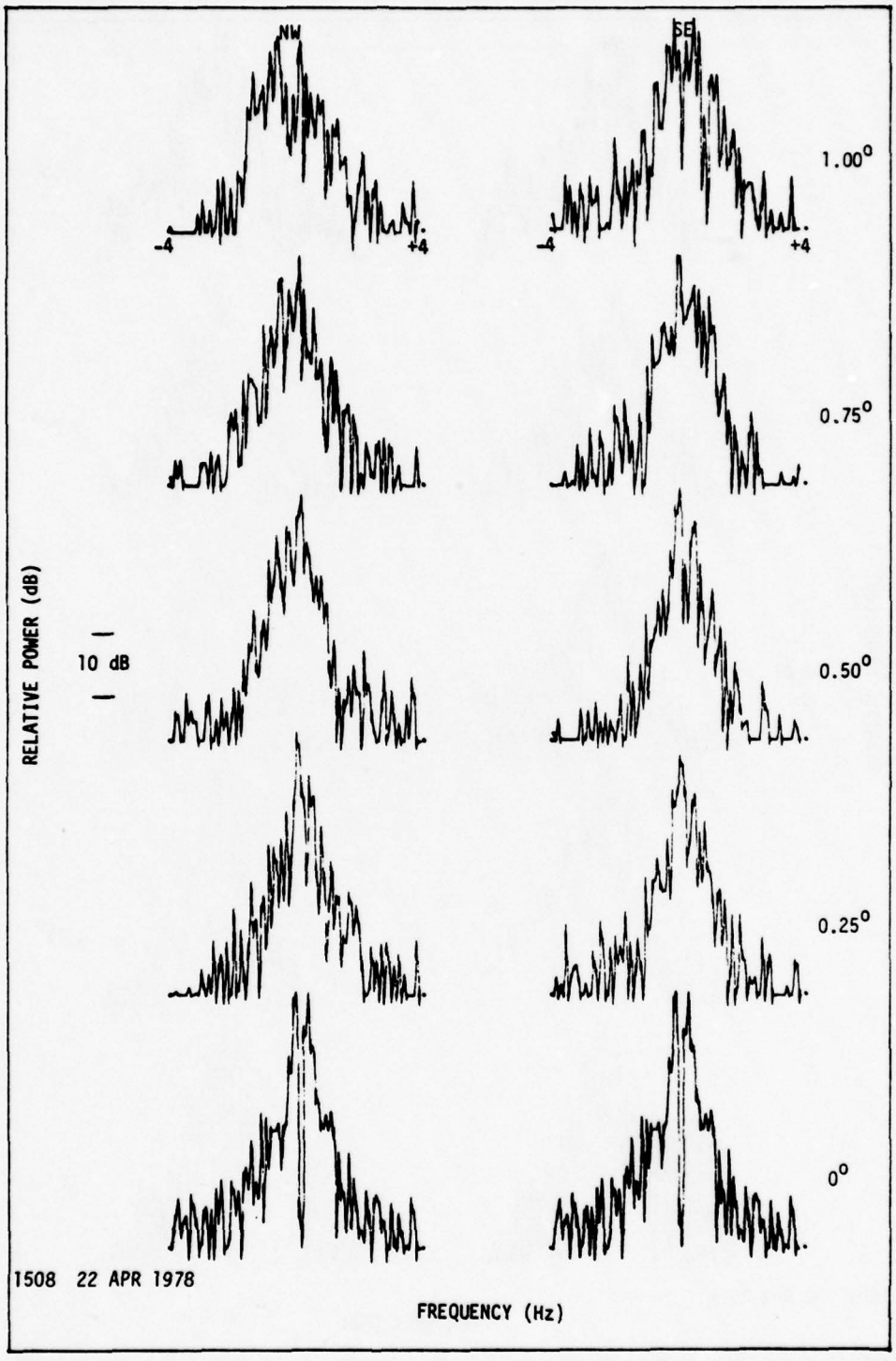

(k)

Fig. 5.2. CONTINUED.

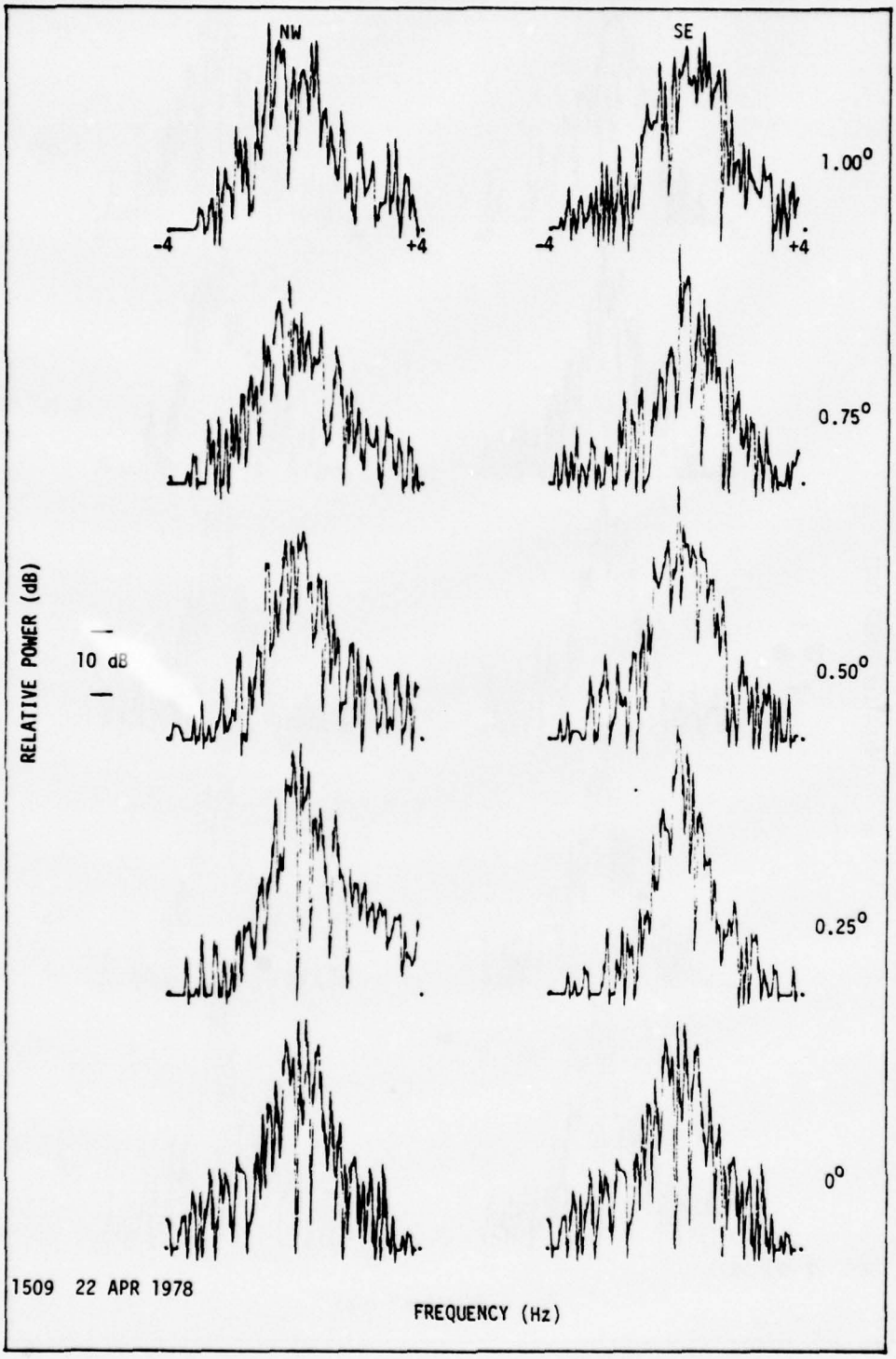

(1)

Fig. 5.2. CONTINUED.

wind-produced spectra shows progressive increases in the average Doppler shift as the array is pointed off-axis. For the examples shown in Figure 5.2, SE winds are apparent at all angles. Doppler shifts are generally positive for array pointing angles in the SE (upwind) direction and negative for angles in the NW (downwind) direction. At most off-axis angles, the upwind and downwind Doppler spectra are nearly antisymmetric about the zero-Doppler frequency which suggests some degree of spatial uniformity in the transverse winds. On-axis the Doppler spectra are generally symmetrical about zero Doppler. Any asymmetries appearing in the spectra when the array beam is aligned along the great-circle can either be attributed to a vertical wind component or to spatial non-uniformities in the transverse wind. Birkemeier et al (1977) point out that such spectral asymmetries also result from the misalignment of the transmitting and receiving antennas. Misalignment errors, however, are eliminated when using a phased-array.

Although no quantitative analysis is presented, other observations from Figure 5.2 reveal definite spectral broadening during afternoon periods when the atmosphere is fairly well mixed. This is a logical consequence of diffuse (turbulent) scattering processes which produce wide variations in the signal's angle-of-arrival. On the other hand, in the morning hours, the atmosphere is relatively stable and is more likely to be partially stratified. In such situations, a quasi-coherent signal is received that arrives via a number of specular reflection points distributed over a small angular region near the great-circle

bearing. As a result of the narrow range of angles-of-arrival, the signal spectra are not nearly as broad as the spectra produced by signals propagating through a turbulent atmosphere. The spectra are also seen to be somewhat broader on the first day [Figure 5.2 (a) thru (f)] of the experiment than on the second day [Figure 5.2 (g) thru (l)]. This variance appears directly attributable to the contrasting wind conditions on the two days.

The short-term variability of the wind can be observed from temporal changes in the Doppler spectra. Of particular importance in this regard are the temporal changes in the average Doppler shift as a function of the array pointing angle. Figure 5.3 [(a) thru (f)] shows the measured average Doppler shifts for the spectra given in Figure 5.2. Average Doppler shifts are computed in accordance with equation 4.12 for 21 equally-spaced (0.15°) pointing angles between 1.5° NW and 1.5° SE. The slopes of these curves are directly proportional to the prevailing wind speeds. Averages taken one minute apart are shown on the same plot for comparative analysis of short-term variations. The 15-second samples are generally in close agreement from one minute to the next. This suggests reasonably good correlation of wind conditions within one minute intervals. As evidenced by the near linearity of the Doppler shift curves, there is some apparent uniformity in the wind structure over the spatial regions probed. Occasionally, however, there are noticeable departures from this linear trend that may be attributable to variable wind conditions. For example, in Figure 5.3a at 0803 on 21 April a definite change in the polarity of the average Doppler shift is

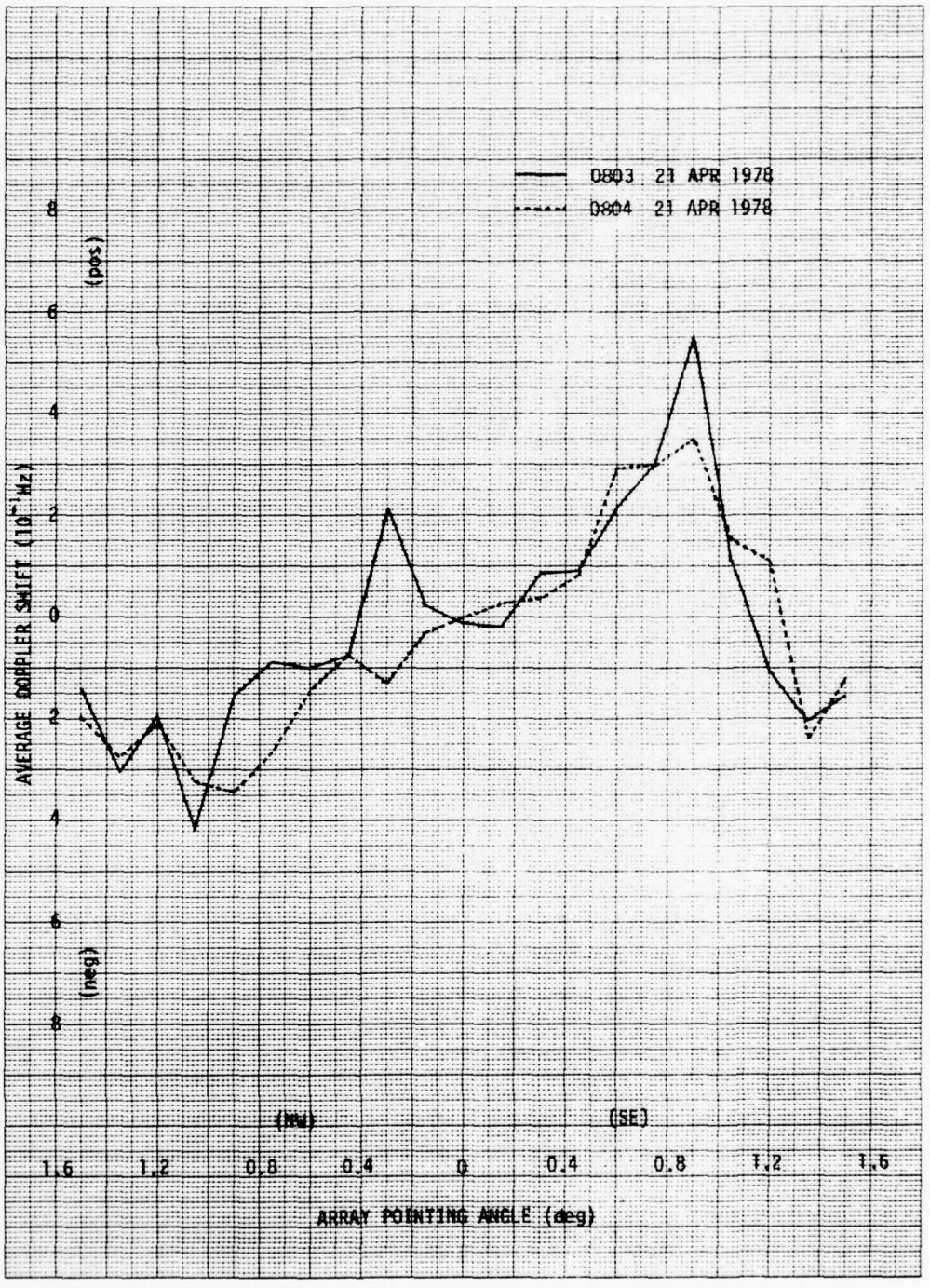

(a)

Fig. 5.3. MEASURED UNWEIGHTED AVERAGE DOPPLER SHIFT VS ARRAY POINTING ANGLE.

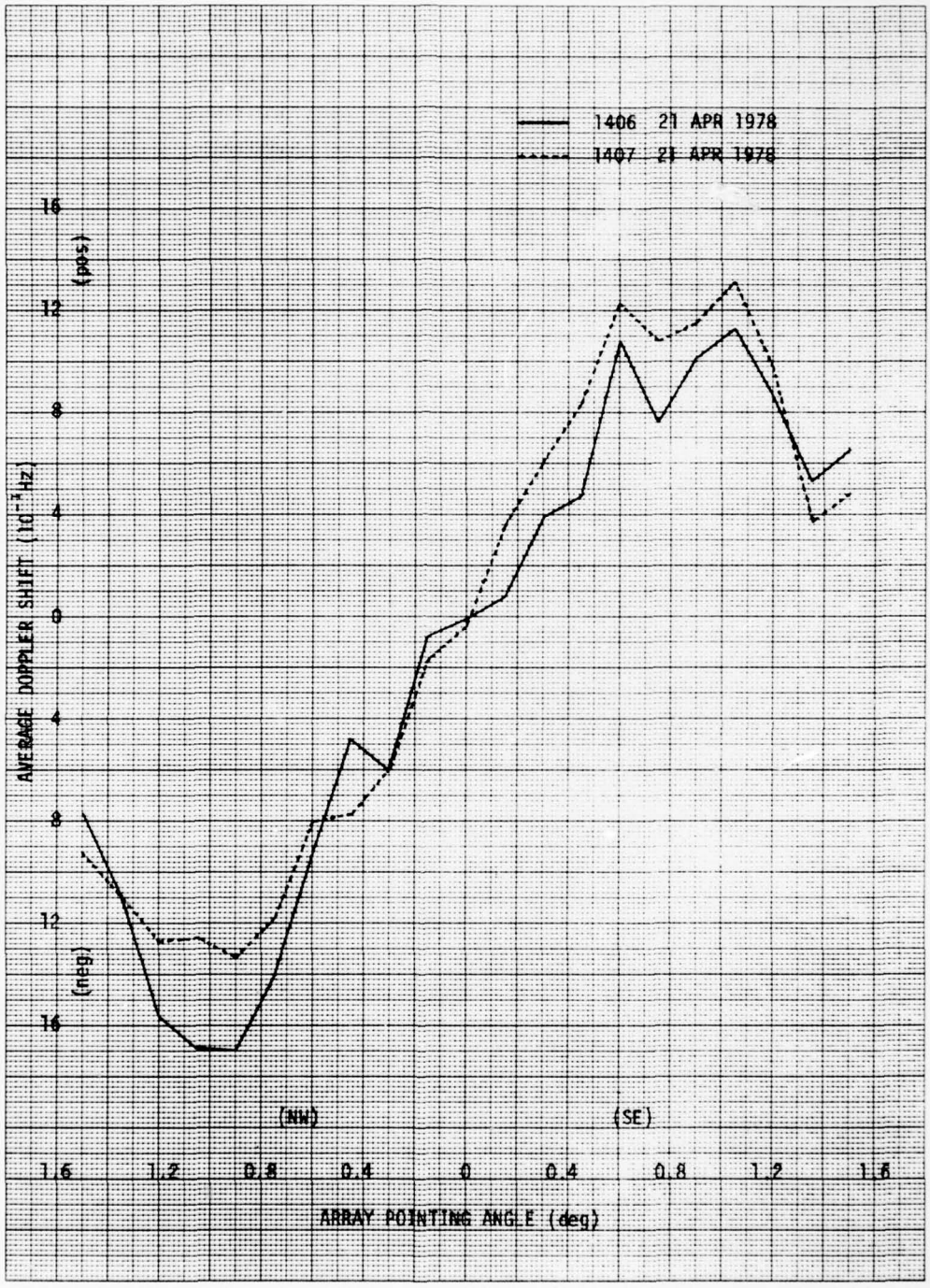

(b)

Fig. 5.3. CONTINUED.

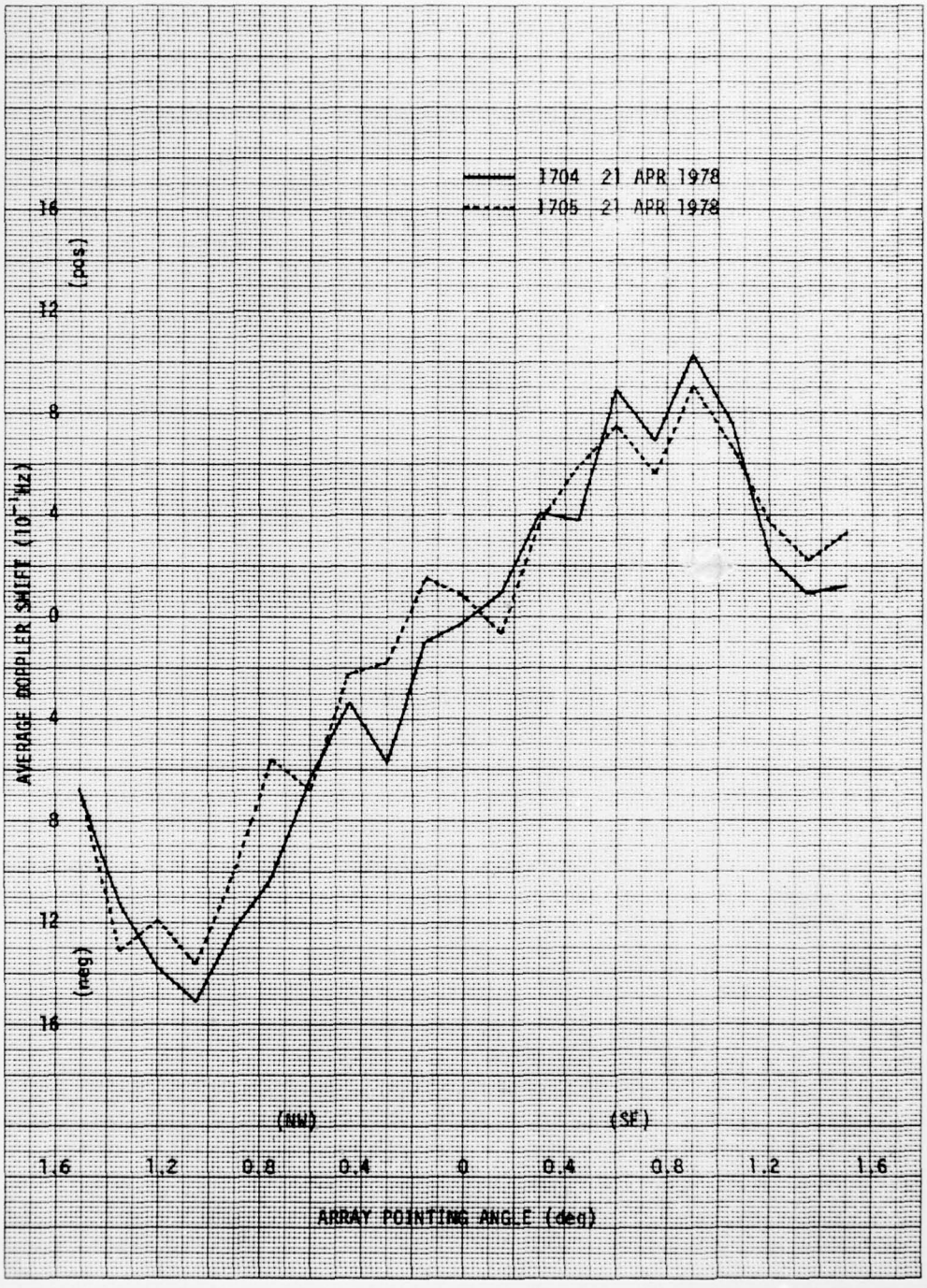

(c)

Fig. 5.3. CONTINUED.

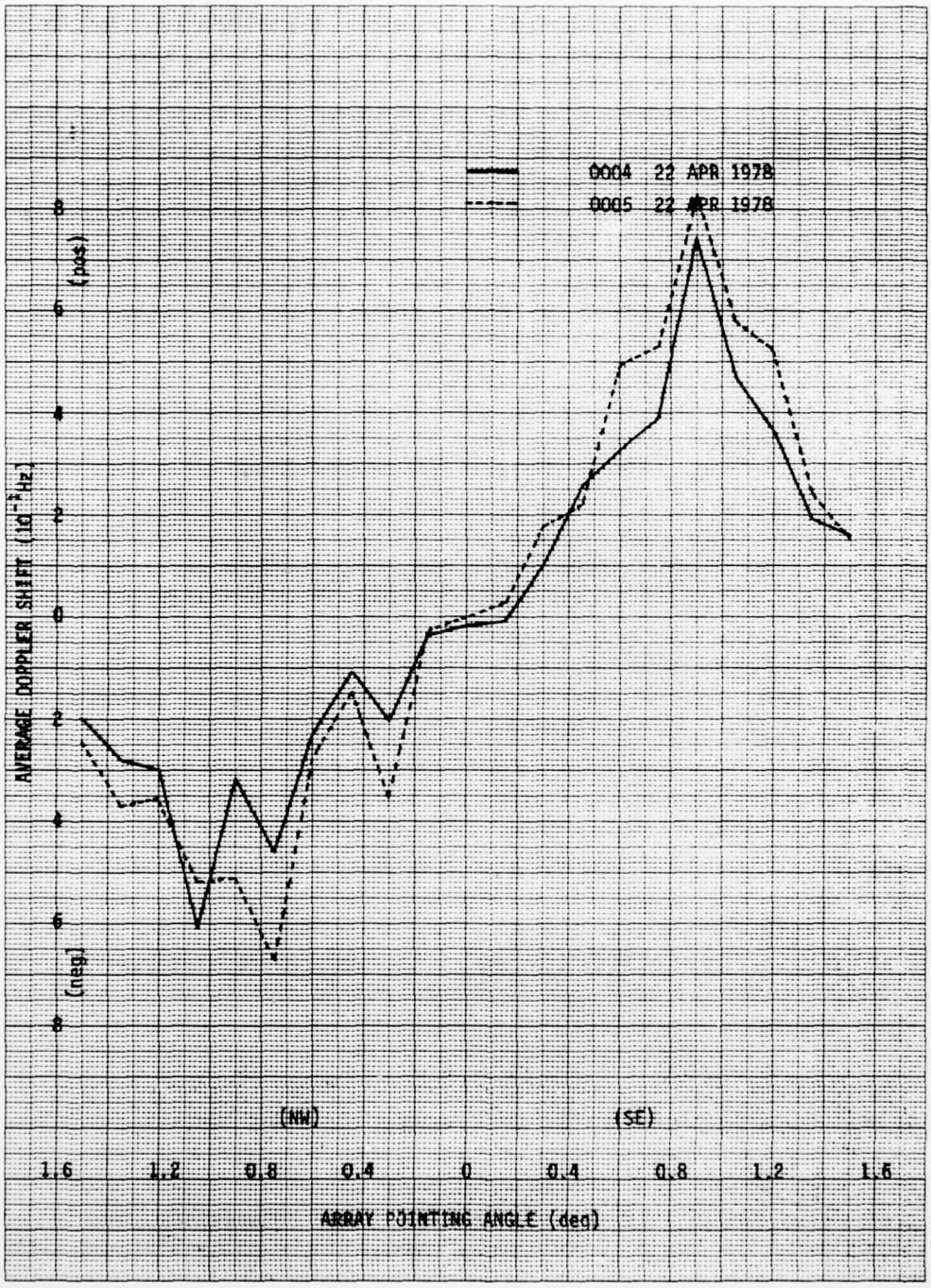

(d)

Fig. 5.3. CONTINUED.

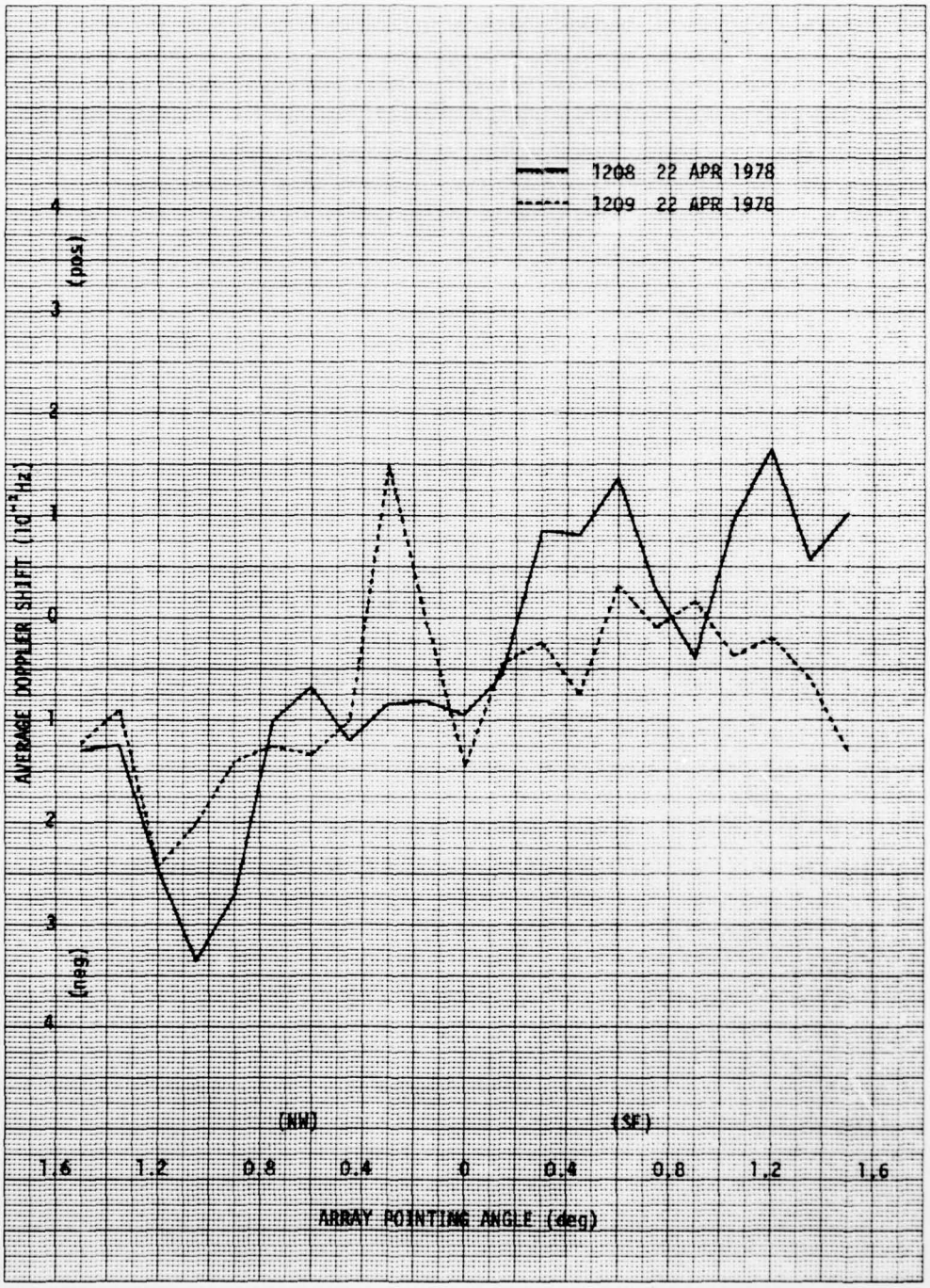

(e)

Fig. 5.3. CONTINUED.

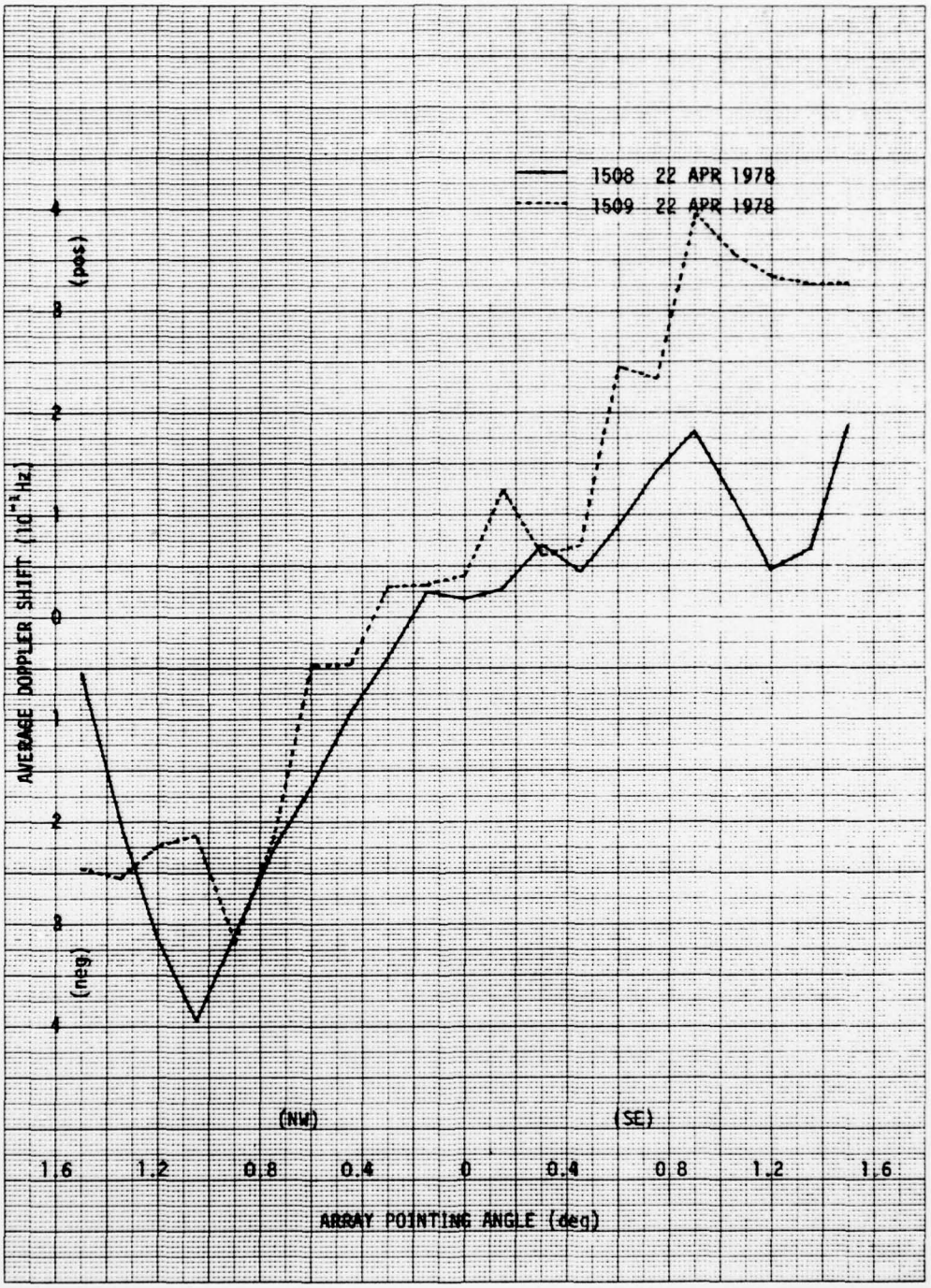

(f)

Fig. 5.3. CONTINUED.

observed when the array is pointed in the vicinity of 0.3° NW. An off-axis polarity change such as this is reflective of a corresponding wind direction change. Supporting this are the wind-shear conditions reflected in the PIBAL measurement data (Figure 5.1a) at the same hour. There are nonlinearities in the average Doppler shift curves that are not necessarily associated with the wind. These nonlinearities occur near the extremities of the array sector scan and are most likely due to the combined off-axis effects of atmospheric scattering and secondary grating lobes. Effects of the scattering mechanism can be taken into account by weighting the Doppler spectra in accordance with an appropriate atmospheric scattering model. The data results from this effort are discussed in the following section.

5.2.2 Weighted Angular Spectra

The Doppler spectra presented in the previous section are essentially unweighted in that the spectral components are derived from data samples that are uniformly weighted over the angular range scanned by the array. Here we take into account the apparent source direction of each spectral component and the angular scattering properties of the atmosphere. Weighting factors based on angle-of-arrival scattering variations are then applied to the individual spectral components in accordance with procedures outlined in section 4.2.

Figure 5.4 [(a) thru (l)] shows the results of applying a normalized Tatarski scattering model to the unweighted spectral data in Figure 5.2. These spectra are obtained for an assumed uniform wind and a turbulent scattering region situated at an elevation angle of 0.25°.

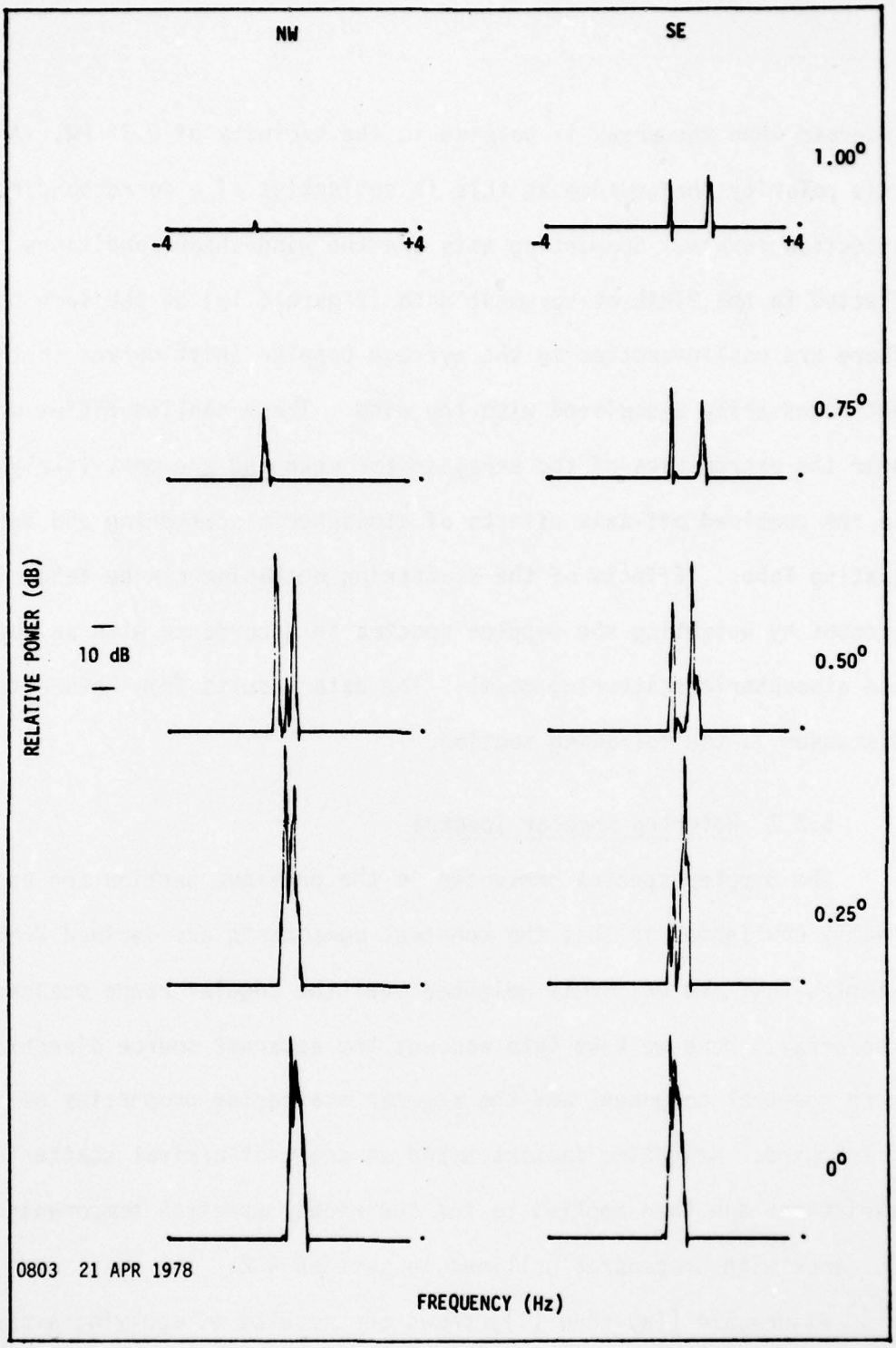

(a)

Fig. 5.4. WEIGHTED WIND-PRODUCED DOPPLER SPECTRA. Angle-of-arrival spectra are weighted in accordance with (1) a normalized Tatarski scattering model, (2) a sin(x)/x receiving array pattern, and (3) a Gaussian transmitting pattern under the assumption of a uniform wind and a source elevation angle, $\beta = 0.25°$.

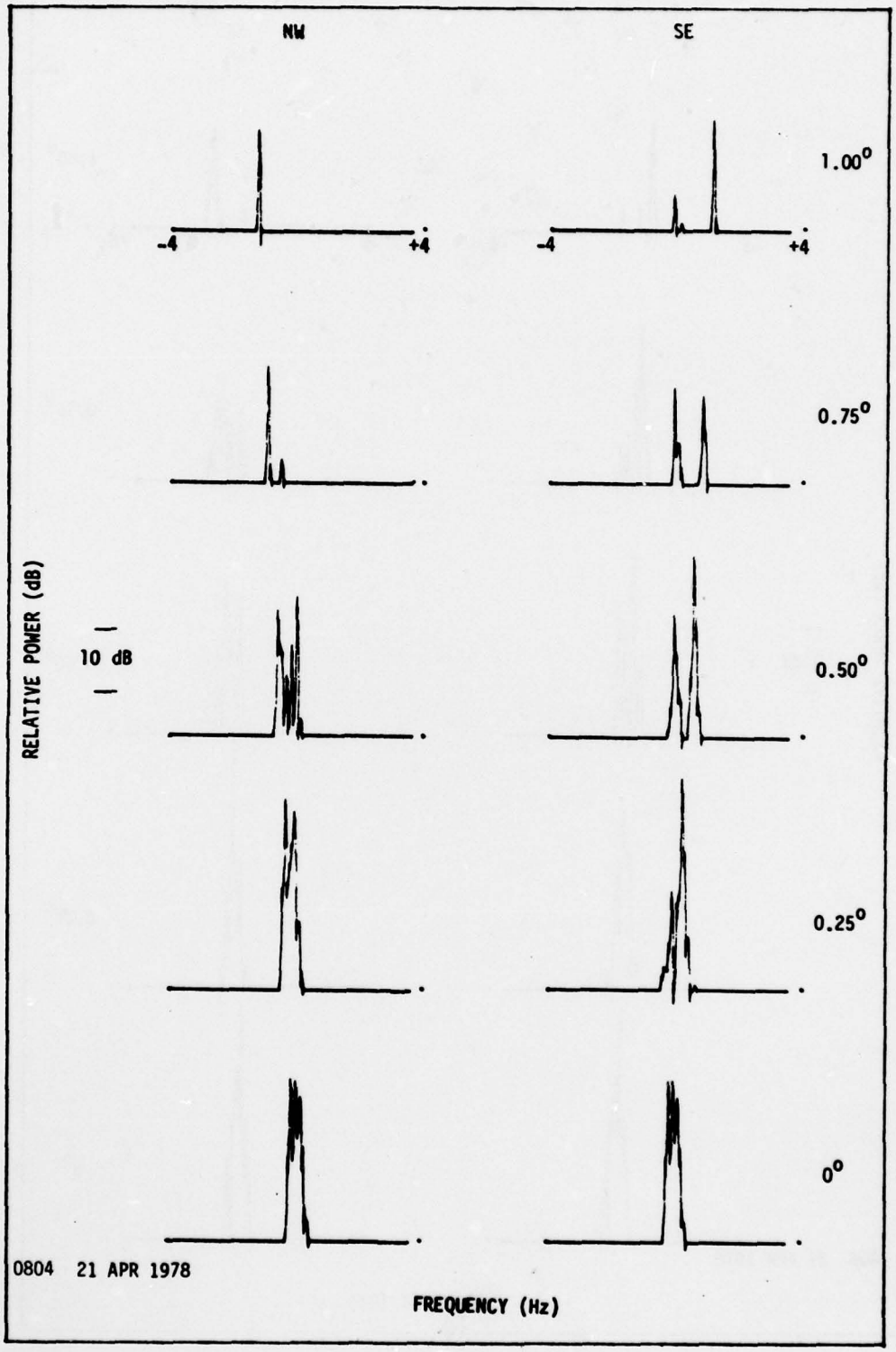

(b)

Fig. 5.4. CONTINUED.

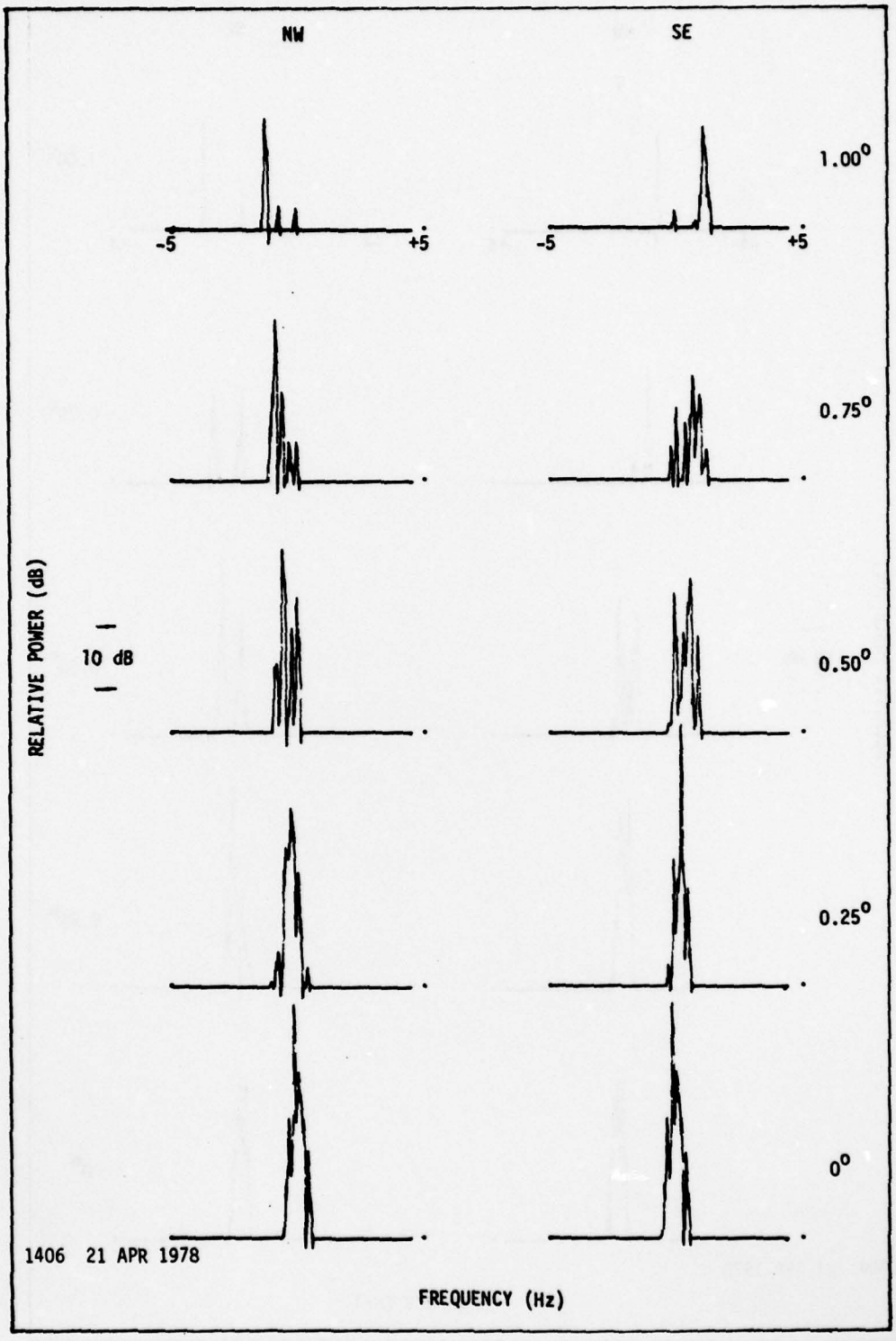

(c)

Fig. 5.4. CONTINUED.

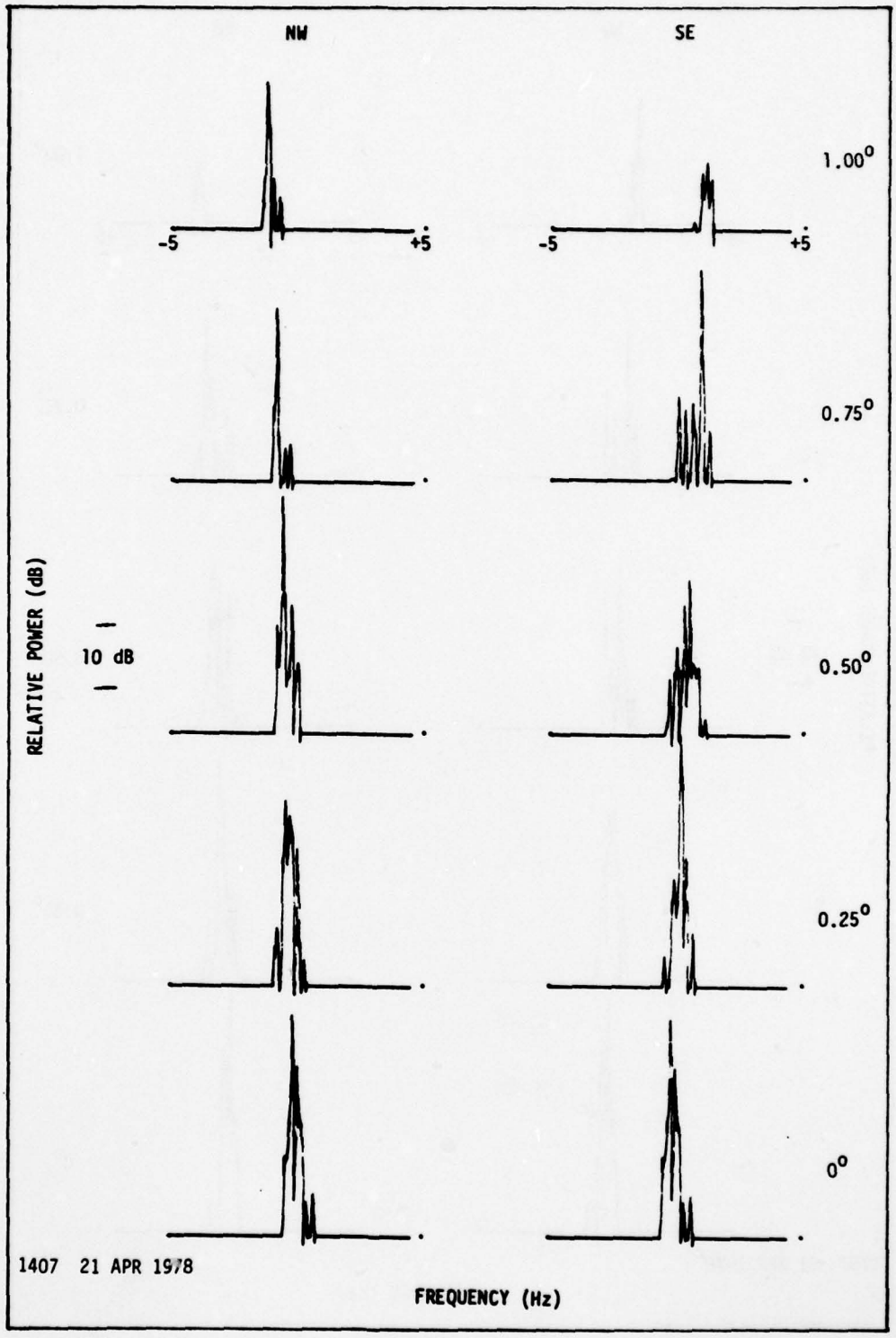

(d)

Fig. 5.4. CONTINUED.

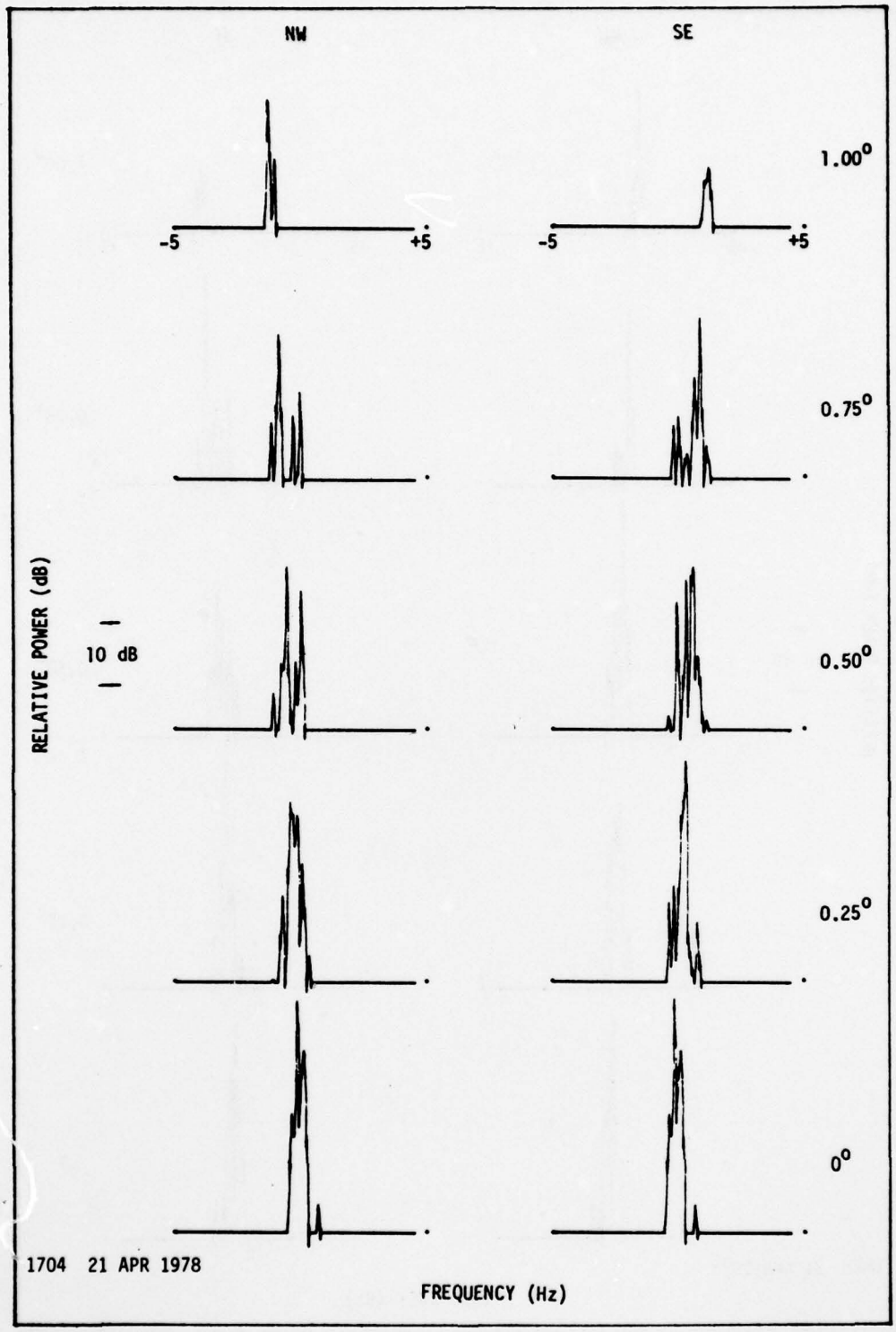

(e)

Fig. 5.4. CONTINUED.

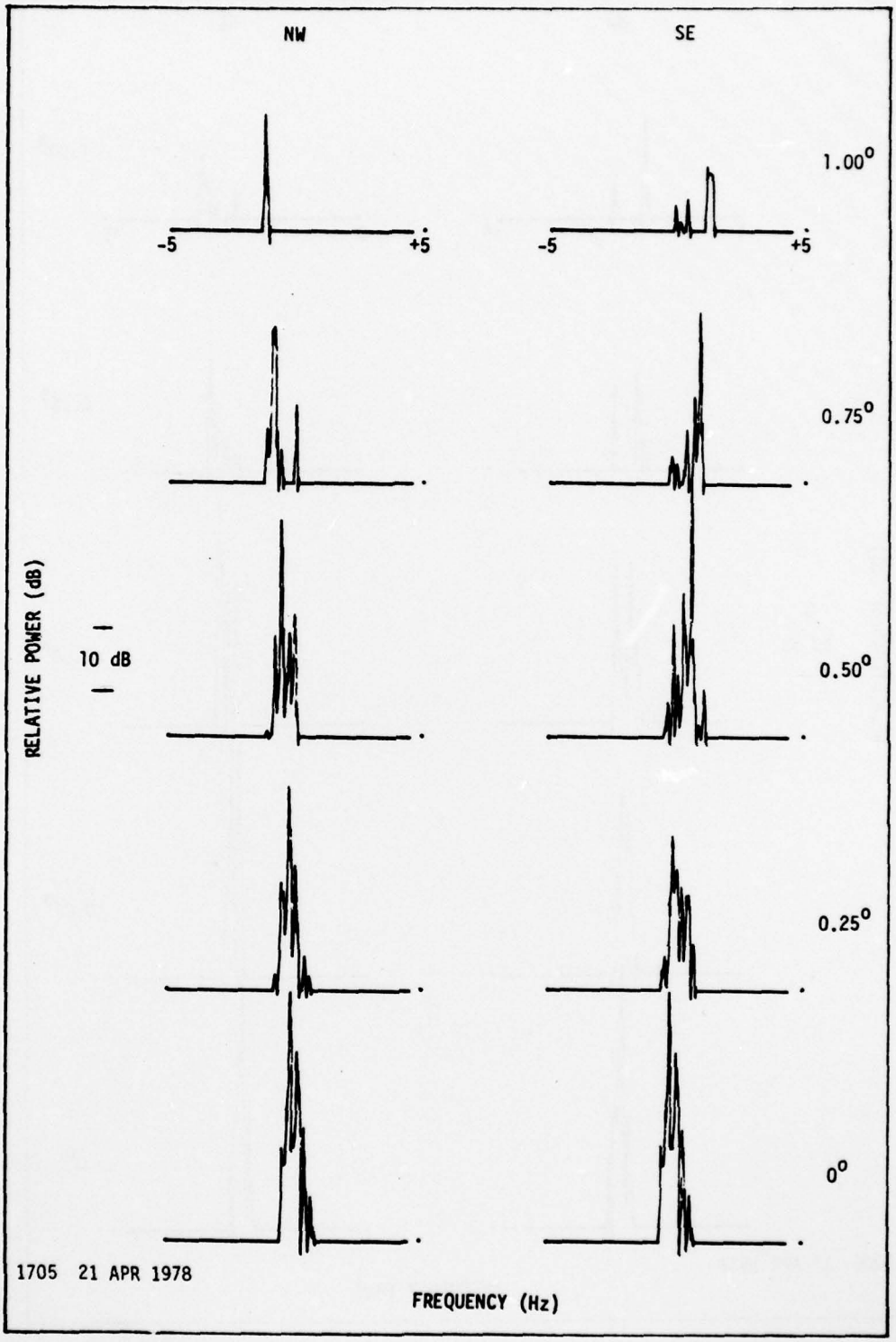

(f)

Fig. 5.4. CONTINUED.

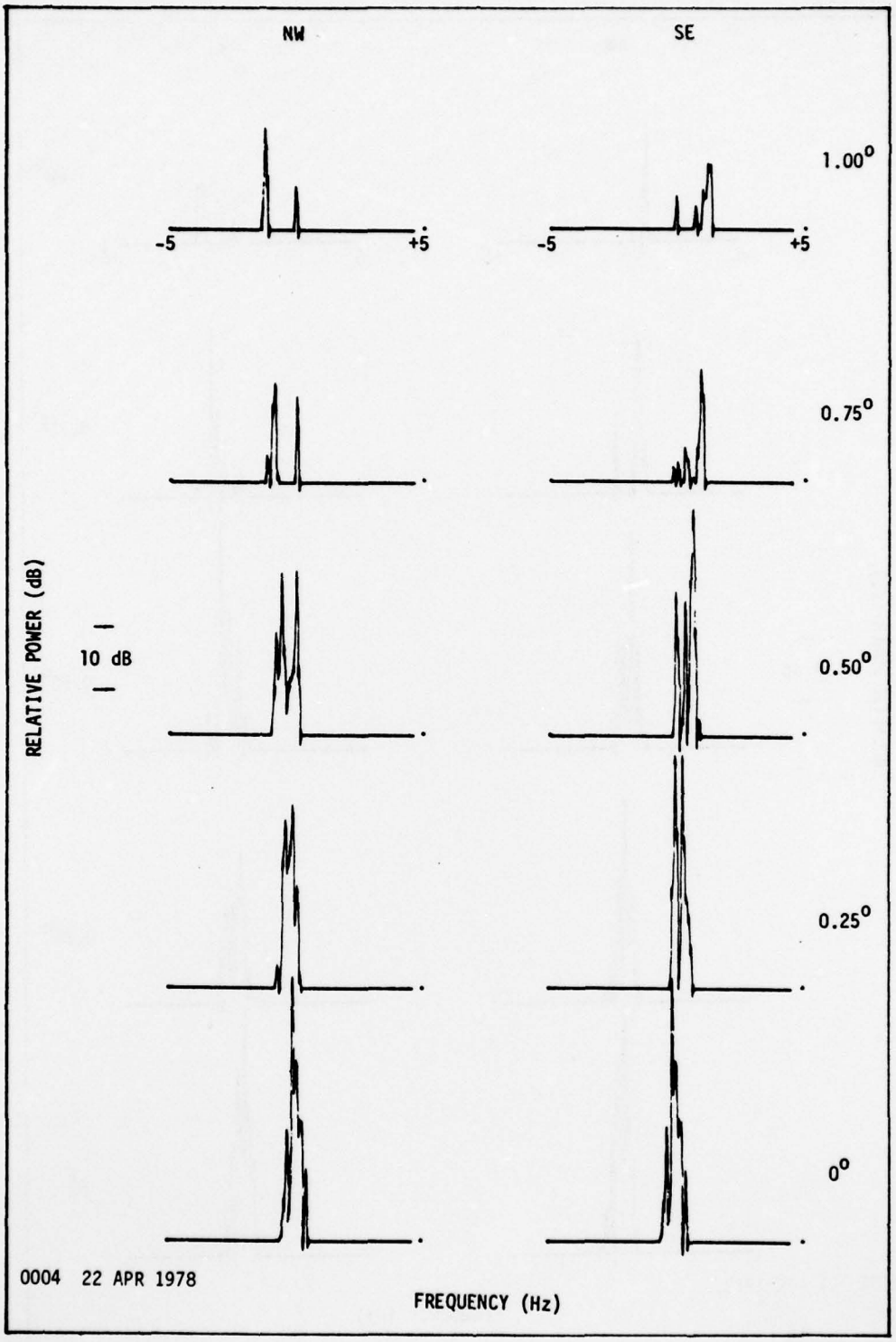

(g)

Fig. 5.4. CONTINUED.

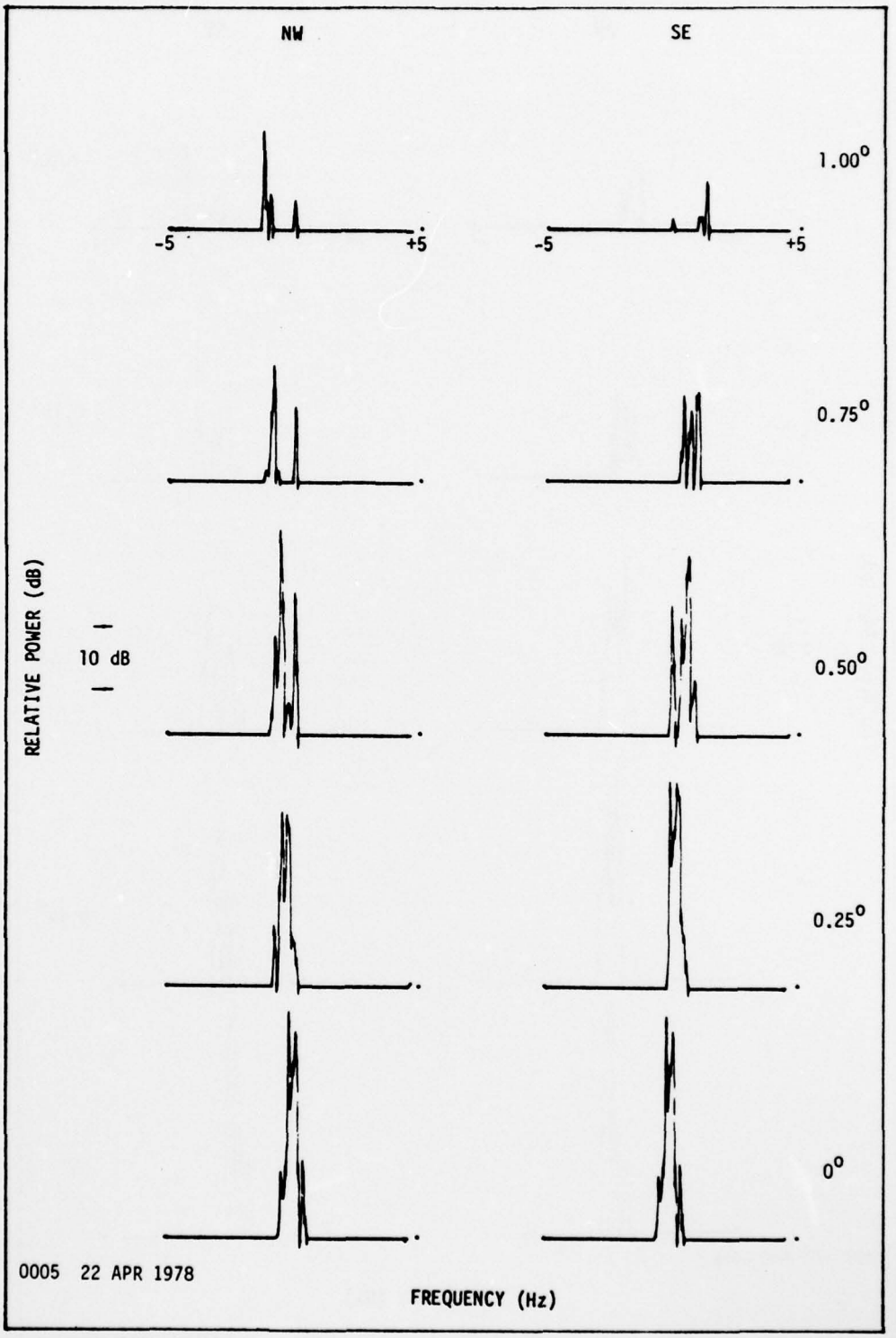

(h)

Fig. 5.4. CONTINUED.

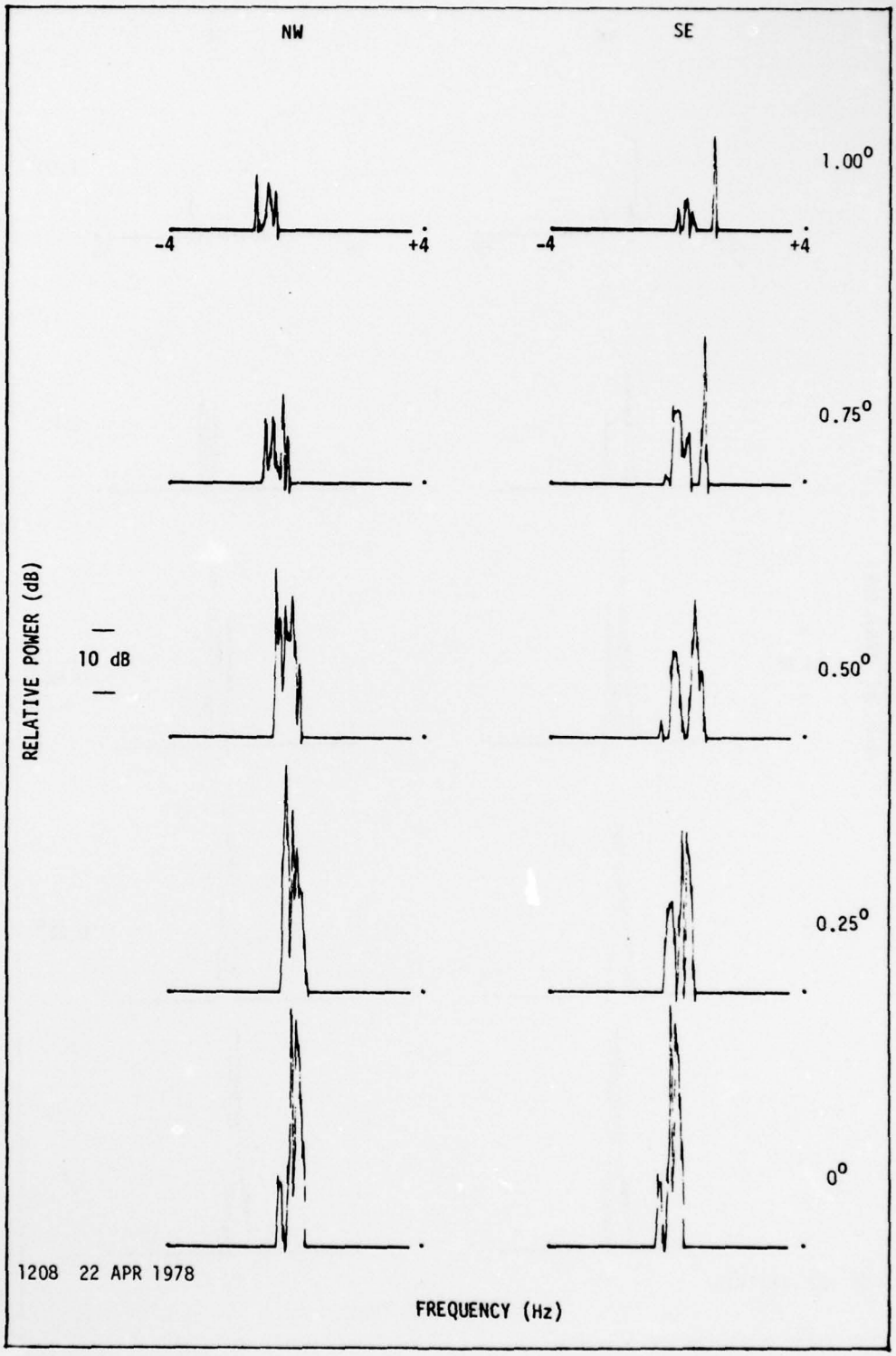

(i)

Fig. 5.4. CONTINUED.

AD-A080 592 STANFORD UNIV CALIF STANFORD ELECTRONICS LABS F/G 4/2
RAPID-SCANNING MEASUREMENTS OF WIND-PRODUCED DOPPLER ON AN ASYM--ETC(U)
JUN 79 R D FLEMING N00014-75-C-0601
UNCLASSIFIED SU-SEL-79-016 NL

1 OF 2
AD
A080592

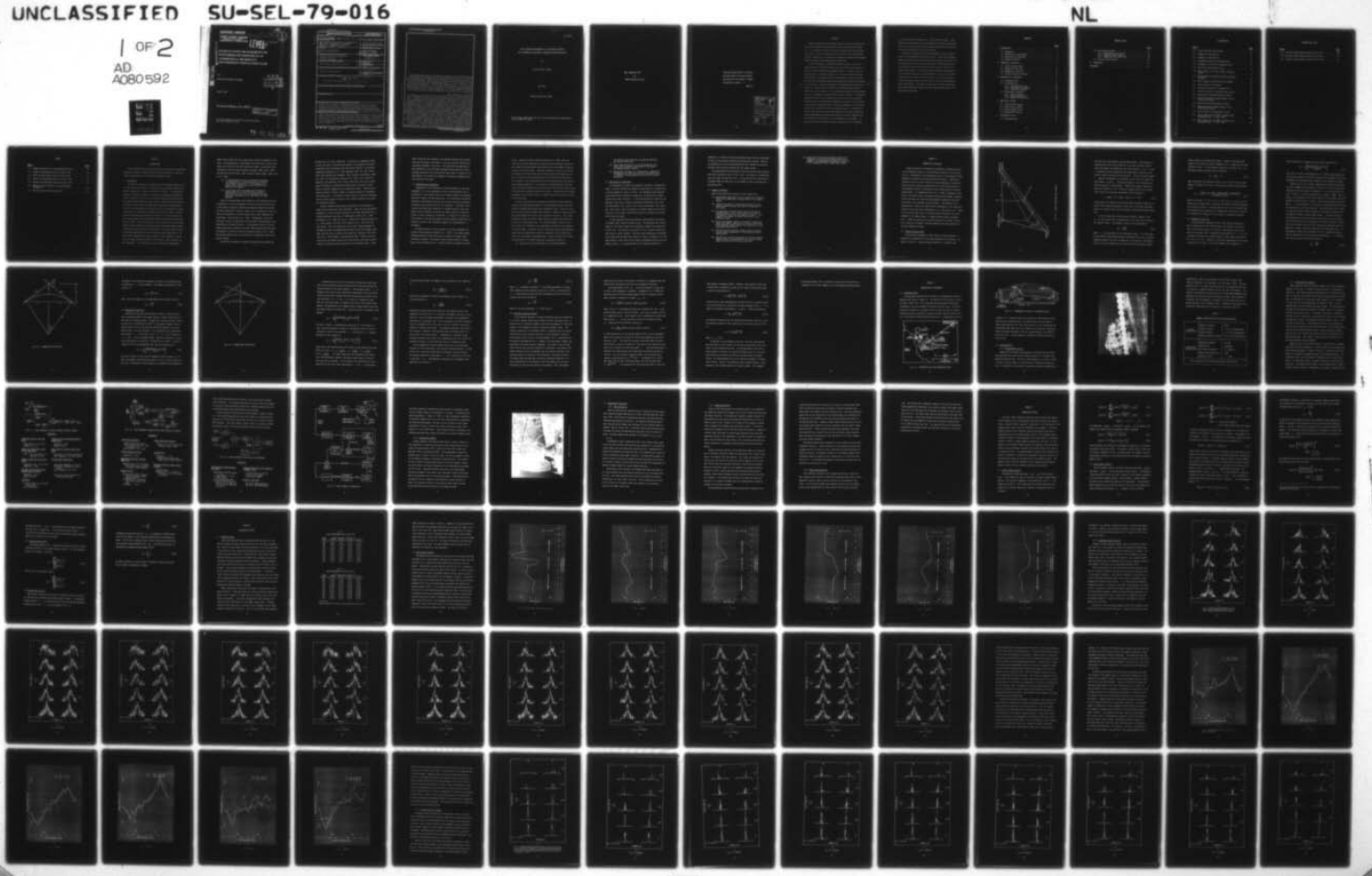

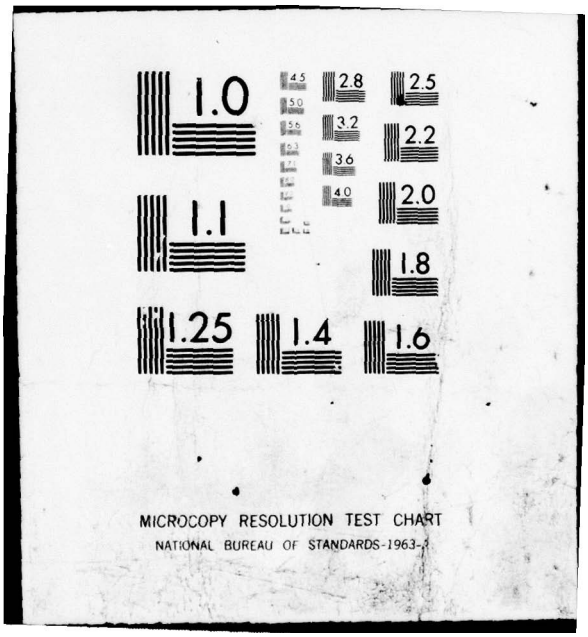
1.0
1.1
1.25
1.4
1.6
1.8
2.0
2.2
2.5
2.8
3.2
3.6
4.0
4.5
5.0
5.6
MICROCOPY RESOLUTION TEST CHART
NATIONAL BUREAU OF STANDARDS-1963-A

RADIOSCIENCE LABORATORY

STANFORD ELECTRONICS LABORATORIES
DEPARTMENT OF ELECTRICAL ENGINEERING
STANFORD UNIVERSITY · STANFORD, CA 94305

LEVEL II

SEL-79-016

RAPID-SCANNING MEASUREMENTS OF WIND-PRODUCED DOPPLER ON AN ASYMMETRICAL MICROWAVE TRANSHORIZON PROPAGATION PATH

by

Ronald Douglas Fleming

June 1979

Technical Report No. 4504-1

This work was supported by the Joint Services Electronics Program under Contract N00014-75-C-0601.

UNCLASSIFIED

SECURITY CLASSIFICATION OF THIS PAGE (When Data Entered)

REPORT DOCUMENTATION PAGE

READ INSTRUCTIONS BEFORE COMPLETING FORM

1. REPORT NUMBER: (9) Technical Report No. 4504-1

2. GOVT ACCESSION NO.

3. RECIPIENT'S CATALOG NUMBER

4. TITLE (and Subtitle): (6) RAPID-SCANNING MEASUREMENTS OF WIND-PRODUCED DOPPLER ON AN ASYMMETRICAL MICROWAVE TRANSHORIZON PROPAGATION PATH

5. TYPE OF REPORT & PERIOD COVERED: Technical Report, 6/79

6. PERFORMING ORG. REPORT NUMBER: SEL-79-016

7. AUTHOR(s): (10) Ronald Douglas/Fleming

8. CONTRACT OR GRANT NUMBER(s): JSEP Contract No. (15) N00014-75-C-0601

9. PERFORMING ORGANIZATION NAME AND ADDRESS:
Stanford Electronics Laboratories
Stanford University
Stanford, California 94305

10. PROGRAM ELEMENT, PROJECT, TASK AREA & WORK UNIT NUMBERS: (12) 143

11. CONTROLLING OFFICE NAME AND ADDRESS:
Joint Services Electronics Program

12. REPORT DATE: (11) June 1979

13. NUMBER OF PAGES: 122

14. MONITORING AGENCY NAME & ADDRESS (if different from Controlling Office):
Office of Naval Research

15. SECURITY CLASS. (of this report): Unclassified

15a. DECLASSIFICATION/DOWNGRADING SCHEDULE

16. DISTRIBUTION STATEMENT (of this Report):
Distribution Unlimited (14) SU-SEL-79-016, TR-4504-1

17. DISTRIBUTION STATEMENT (of the abstract entered in Block 20, if different from Report)

18. SUPPLEMENTARY NOTES

19. KEY WORDS (Continue on reverse side if necessary and identify by block number)
Tropospheric Propagation, Transhorizon Microwave Propagation, Doppler Spectra, Angle-of-Arrival, Phased Arrays, Aircraft Trailing Vorticies, Atmospheric Remote Probing, Wind Velocity Structure, Low-Altitude Winds, Wind-Produced Doppler, Rapid Scanning Arrays, Rapid Data-Gathering System, Spectral Signatures, Aircraft-Induced Doppler

20. ABSTRACT (Continue on reverse side if necessary and identify by block number)
Concentional methods for monitoring winds aloft have inherent spatial and/or temporal limitations that severely restrict their usefulness. An alternate solution is the use of transhorizon bistatic radio techniques. By using a phase-coherent system with some form of beam-swinging capability, it is possible to measure the wind-produced Doppler shifts associated with moving off-path scatterers.

(continued) 332400 JCB

DD FORM 1 JAN 73 1473 EDITION OF 1 NOV 65 IS OBSOLETE
S/N 0102-LF-014-6601

UNCLASSIFIED

SECURITY CLASSIFICATION OF THIS PAGE (When Data Entered)

In this experiment a rapid data-gathering system is used to remotely probe the wind-field velocity structure in the common volume region of a 164-km trans-horizon propagation path. The phase-stable system operates at 3.2 GHz and employs a 12-element horizontal receiving antenna array. The amplitudes and relative phases of the output signals from the individual elements are sequentially sampled and recorded at a 40-Hz rate. Off-line processing of the amplitude and phase data samples is used to "scan" in azimuth a 0.3° wide fan beam through a 3.88° sector and to obtain virtual simultaneous Doppler spectra measurements at a continuum of angles within the sector scanned. An algorithm developed to identify the apparent source direction of each spectral component permits an appropriate weighting to be applied to the spectra on the basis of angle-of-arrival. The average Doppler shift (spectrum centroid) as a function of the array pointing angle is interpreted in terms of the average transverse wind speed and direction. Doppler relations applicable to previous experiments are modified to account for the influence of differences in the longitudinal path geometry. An analytical expression employing a path asymmetry factor is developed for the wind-produced Doppler from a single scatterer model. Wind velocities inferred from the average Doppler shift data are compared with in situ wind observation data obtained by optically tracking pilot balloons released into the common volume.

Measurement results show the average Doppler shifts to have an almost linear dependence on angle-of-arrival. Wind-produced Doppler shifts resulting from average transverse velocities up to about 5 m/s have been measured and found consistent both in magnitude and direction with the prevailing winds observed in the lower strata of the common volume region. On numerous occasions, Doppler measurement results reflected much higher average velocities (~40 m/s) than could be attributed to normal low-altitude winds. Time-spatial analyses of these anomalous spectra are indicative of aircraft-induced atmospheric disturbances. The spectral signatures of these disturbances may provide additional insight into the generation and decay of aircraft trailing vortices.

SEL-79-016

RAPID-SCANNING MEASUREMENTS OF WIND-PRODUCED DOPPLER ON AN ASYMMETRICAL MICROWAVE TRANSHORIZON PROPAGATION PATH

by

Ronald Douglas Fleming

June 1979

Technical Report No. 4504-1

This work was supported by the Joint Services Electronics Program under Contract N00014-75-C-0601.

"The wind bloweth where it listeth,
and thou hearest the sound thereof,
but canst not tell whence it cometh,
and whither it goeth . . ."

John 3:8

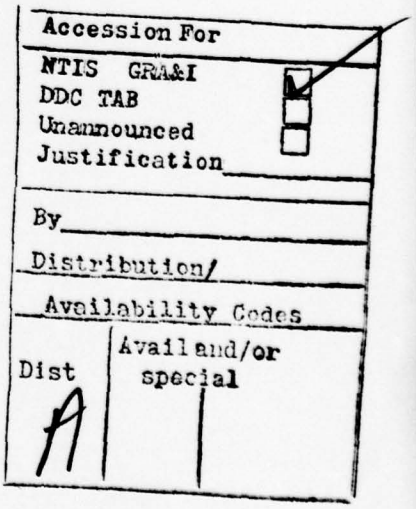

ABSTRACT

Conventional methods for monitoring winds aloft have inherent spatial and/or temporal limitations that severely restrict their usefulness. An alternate solution is the use of transhorizon bistatic radio techniques. By using a phase-coherent system with some form of beam-swinging capability, it is possible to measure the wind-produced Doppler shifts associated with moving off-path scatterers.

In this experiment a rapid data-gathering system is used to remotely probe the wind-field velocity structure in the common volume region of a 164-km transhorizon propagation path. The phase-stable system operates at 3.2 GHz and employs a 12-element horizontal receiving antenna array. The amplitudes and relative phases of the output signals from the individual elements are sequentially sampled and recorded at a 40-Hz rate. Off-line processing of the amplitude and phase data samples is used to "scan" in azimuth a 0.3° wide fan beam through a 3.88° sector and to obtain virtual simultaneous Doppler spectra measurements at a continuum of angles within the sector scanned. An algorithm developed to identify the apparent source direction of each spectral component permits an appropriate weighting to be applied to the spectra on the basis of angle-of-arrival. The average Doppler shift (spectrum centroid) as a function of the array pointing angle is interpreted in terms of the average transverse wind speed and direction. Doppler relations applicable to previous experiments are modified to account for the influence of differences in the longitudinal path geometry. An analytical expression employing a path asymmetry factor is developed

for the wind-produced Doppler from a single scatterer model. Wind velocities inferred from the average Doppler shift data are compared with in situ wind observation data obtained by optically tracking pilot balloons released into the common volume.

. Measurement results show the average Doppler shifts to have an almost linear dependence on angle-of-arrival. Wind-produced Doppler shifts resulting from average transverse velocities up to about 5 m/s have been measured and found consistent both in magnitude and direction with the prevailing winds observed in the lower strata of the common volume region. On numerous occasions Doppler measurement results reflected much higher average velocities (~40 m/s) than could be attributed to normal low-altitude winds. Time-spatial analyses of these anomalous spectra are indicative of aircraft-induced atmospheric disturbances. The spectral signatures of these disturbances may provide additional insight into the generation and decay of aircraft trailing vortices.

CONTENTS

		Page
1.	INTRODUCTION	1
	1.1 Background	1
	1.2 Significance of Experiment	4
	1.3 Description of Experiment	6
	1.4 Summary of Results	7
2.	THEORETICAL DISCUSSION	9
	2.1 Single Scatterer Model	9
	2.2 Symmetrical Path Case	12
	2.3 Asymmetrical Path Case	15
	2.4 Multiple Scattering Effects	19
3.	DESCRIPTION OF EXPERIMENT	23
	3.1 Propagation Path	23
	3.2 Instrumentation	24
	3.2.1 Data-Gathering Array	24
	3.2.2 Array-Receiver Channels	27
	3.2.3 Transmitter Assembly	31
	3.3 Experimental Procedures	34
	3.3.1 Data Collection	34
	3.3.2 System Calibration	35
	3.3.3 PIBAL Wind Monitoring	36
4.	ANALYTICAL METHODS	39
	4.1 Single Element Spectra	39
	4.2 Array Angular Spectra	40
	4.3 Average Doppler Shift	43
	4.4 Average Wind Velocity	43
5.	DISCUSSION OF DATA	45
	5.1 PIBAL Wind Data	45

CONTENTS (Cont)

	Page
5.2 Wind-Produced Doppler	47
5.2.1 Unweighted Angular Spectra	54
5.2.2 Weighted Angular Spectra	75
5.2.3 Comparisons with PIBAL Data	95
5.3 Aircraft-Induced Doppler	106
6. CONCLUSIONS	117
REFERENCES	119

ILLUSTRATIONS

Figure		Page
2.1	Single scatterer path geometry	10
2.2	Symmetrical path profile	14
2.3	Asymmetrical path profile	16
3.1	Propagation path and surrounding area	23
3.2	Topographical profile of propagation path	24
3.3	Horizontal data-gathering array	25
3.4	Block diagram of an array element receiving channel	28
3.5	Block diagram of amplitude and phase-sampling equipment	29
3.6	Block diagram of data-collection equipment	30
3.7	Block diagram of transmitter	32
3.8	Transmitting antenna and equipment van	33
5.1	Vertical profile of cross-path wind velocity	48
5.2	Unweighted wind-produced Doppler spectra	55
5.3	Measured unweighted average Doppler shift vs array pointing angle	69
5.4	Weighted wind-produced Doppler spectra	76
5.5	Measured weighted average Doppler shift vs array pointing angle	89
5.6	Hourly Doppler wind-measurement results	98
5.7	Hourly comparisons of PIBAL vs Doppler wind-measurement data - 21 April 1978	100
5.8	Hourly comparisons of PIBAL vs Doppler wind-measurement data - 22 April 1978	103

ILLUSTRATIONS (Cont)

Figure		Page
5.9	Aircraft-induced Doppler spectra at 0111:11.2	108
5.10	Aircraft-induced Doppler spectra at 0111:20.8	110
5.11	Aircraft-induced Doppler spectra at 0111:30.4	112

TABLES

Number		Page
3.1	Summary characteristics of data-gathering array	26
5.1	PIBAL wind-measurement data on 21 April 1978	46
5.2	PIBAL wind-measurement data on 22 April 1978	46
5.3	Doppler wind-measurement data on 21 April 1978	97
5.4	Doppler wind-measurement data on 22 April 1978	97
5.5	Spectral analysis results of aircraft-induced disturbance	114
5.6	Aircraft transit-time analysis data	114

Chapter 1

INTRODUCTION

This dissertation describes the results of a microwave transhorizon experiment in which a rapid data-gathering antenna array is used as a remote sensing probe of low-altitude tropospheric winds.

1.1 Background

The initial transhorizon propagation of an ultrahigh frequency signal was reported by Marconi in 1932 after he successfully transmitted a 500-MHz signal over a distance of 168 miles (270 km). The underlying physical principles involved in transhorizon propagation subsequently became a subject of discussion and some controversy among researchers. The smooth-earth diffraction theory (Watson, 1918 and 1919; Van der Pol and Bremmer, 1937, 1938, and 1939), which suggests an exponential decrease in the received power with distance, was the generally accepted explanation for transhorizon propagation in the early 1940s. With the advent of high-power transmitters and sensitive receivers during the war, signal reception far beyond the horizon became more frequent (Bullington, 1955). The received signal levels, however, were consistently found to be far above the levels predicted by the diffraction theories. Concerted efforts were made by investigators in the late 1940s to find a plausible explanation for the transhorizon signal observations. Pekeris (1947) suggested the signals, based on their appearance, were a result of some scattering process from refractive-index variations in the atmosphere. As a consequence, several theoretical propagation

models evolved that took into account the prevailing atmospheric structure. The preponderance of experimental data taken over the years supports the validity of two basic theoretical models, one derived from a turbulence scattering theory (Booker and Gordon, 1950; Staras, 1952) and the other derived from a layer reflection theory (Bauer, 1956; Friis et al., 1957):

(1) In the turbulence theory the propagation phenomena is characterized as a scattering process resulting from turbulent conditions in the atmosphere that cause random irregularities in the refractive properties of the medium.

(2) In the layer theory the propagation phenomena is characterized as a reflection process resulting from stratified layers in the atmosphere that produce sharp discontinuities in the refractive index gradient.

Much of the experimental and theoretical work conducted since the introduction of the two fundamental theories has dealt with the study of the physical mechanisms supporting propagation beyond the horizon. The early experimental research, however, was influenced to a large extent by the demands for reliable long-distance radio communications (Bullington, 1950; Mellen et al., 1955). Consequently, one of the principal concerns of researchers was the signal fading problems often experienced on transhorizon paths. The cumulative results of the numerous experiments conducted up to about 1960 provided sufficient data to establish a statistical basis for predicting (Baris et al., 1962) the average expected level of performance of transhorizon radio transmission systems.

By 1960 the tropospheric propagation characteristics beyond the

horizon were fairly well understood. Investigators subsequently began to look into ways of distinguishing between the propagation mechanisms associated with the turbulence and layer model theories. At Stanford researchers (Waterman et al., 1957; Waterman, 1958; Lee, 1961; Strohbehn, 1963; Waterman and Strohbehn, 1963; Strohbehn and Waterman, 1966; Cox, 1967; Cox and Waterman, 1969 and 1971; Cianos, 1971; Cianos and Waterman, 1973; Waterman, 1973; Cianos, 1978) have used various experimental techniques to differentiate between the two prevailing atmospheric structures suggested by the theoretical models. These empirical methods provided in effect a means of remotely probing the atmosphere with radio waves -- a technique in which analyses of specific parameters of the received signal are used to infer certain characteristics about the intervening medium.

Several important meteorological parameters can be measured remotely using transhorizon radio techniques. Among the many measureable parameters, the wind velocity structure in the lower atmosphere has received considerable attention by investigators (Atlas et al., 1968; Birkemeier et al., 1968; Atlas et al., 1969; Atlas, 1969; Birkemeier et al., 1969; Lammers and Olsen, 1973; Chadwick et al., 1975) over the past decade. Early investigations of the signal fading phenomena on transhorizon paths have demonstrated marked correlations between signal fade rates and local transverse wind conditions (Laaspere, 1958; Crawford et al., 1959; Doherty, 1959; Gjessing, 1964). Refractive structures within the common volume drift with the mean wind velocity which results in stochastic phase variations in the received signal. These

phase variations are reflected in the Doppler spectrum and are dependent upon the spatial distribution, size, and relative velocities of the moving atmospheric structures. The analytical and experimental work performed in this area have provided the motivation for the experiment described in this dissertation which seeks to further our understanding of the spatial and temporal variations of atmospheric motion produced by the wind.

1.2 Significance of Experiment

Knowledge of wind information in localized regions of the lower atmosphere is of vital importance not only to meteorologists but to researchers in such diverse areas as air-traffic safety, environmental pollution, energy, and even agriculture. The conventional rawinsonde technique of monitoring winds aloft has inherent spatial and temporal limitations that severely restrict its usefulness. Situations requiring near real-time wind information in selected regions of the atmosphere are not adequately served by the widely spaced and infrequent (every 12 hours) launches of rawinsondes. A reduction in either the time interval or the spacing between launches becomes economically prohibitive in terms of the increased manpower and instrumentation requirements.

An alternate means of wind sounding in the lower atmosphere has recently been proposed by Chadwick et al. (1975). The remote probing technique proposed involves the use of a network of bistatic radio transmission systems. The proposal stems from the results of experimental work by Birkemeier et al. (1968 and 1969) and Lammers and Olsen

(1973). Analyses by Atlas (1969) and Atlas et al. (1965, 1968, and 1969) have provided considerable insight into the elementary theory and have enabled the experimental observations to be interpreted in meteorologically significant terms. Observed systematic increases in the average Doppler shift with offset angle from the great-circle bearing have been attributed to the wind-produced drift of refractive structures in the atmosphere. By incorporating narrow-beam antennas with some form of beam-swinging capability, it is possible to remotely monitor the transverse (cross-path) component of the wind over a wide spatial extent using a bistatic phase-coherent transhorizon system. Aligning two such systems orthogonal to one another permits a complete characterization of the horizontal wind-field.

Previous experiments have employed synchronously offset steerable antennas to probe selected regions in the atmosphere and have been conducted on longitudinally symmetrical propagation paths. These are transhorizon paths where the common volume region is symmetrical about the mid-path plane between the receiver and transmitter terminals. Over highly asymmetrical paths the common volume region is skewed significantly to one side of the mid-path plane. The resultant Doppler relations must then reflect the influence of the longitudinal position of the dominant scattering region. Analytical results applicable to both longitudinally symmetrical and asymmetrical paths are presented in this dissertation along with experimental measurement data. Unique features of the experiment pertinent to the remote probing of tropospheric winds are

(1) Angle-of-arrival measurements of wind-produced Doppler

are derived from processing array-sampled amplitude and relative phase data.

(2) Rapid sampling features of the data-gathering array permit the simultaneous measurement of the upwind and downwind Doppler spectra.

(3) Measurements are made on a longitudinally asymmetrical propagation path where the principal scattering region is centrally located between the receiver and the mid-path plane.

1.3 Description of Experiment

To investigate the spatial and temporal variations of tropospheric winds, a 42-hour transhorizon propagation experiment was conducted over a 164-km asymmetrical path at 3.2 GHz. The propagation path extended from Jackson Butte, California (transmitter) to the foothills behind Stanford University (receiver). A rapid data-gathering system (Cox and Waterman, 1969) used in previous transhorizon experiments (Cox, 1967; Cox and Waterman, 1971; Cianos, 1971; Cianos and Waterman, 1973; Waterman, 1973; Cianos, 1978) was modified to remotely probe the wind-field structure in the common volume region above the Livermore Valley about 40 km from the receiver.

In this experiment the phase-coherent system employs a horizontal 12-element linear receiving antenna array. The amplitudes and relative phases of individual elements are sequentially sampled and recorded at a 40-Hz rate. An effective scan period of 5 ms is used to acquire the data from all twelve elements. Off-line signal processing is performed on the amplitude and phase data samples to "scan" in azimuth a 0.3° wide beam through a 3.88° sector and to obtain corresponding angle-of-arrival Doppler spectra. The average Doppler shift (spectrum centroid) is

computed as a function of the array pointing angle and then interpreted in terms of the average transverse wind speed and direction. Results are compared with in-situ wind observation data obtained by optically tracking pilot balloons released into the common volume.

The experimental data presented in this dissertation were obtained from tests conducted on April 21-22, 1978. Ten minutes of transhorizon radio data were recorded each hour. A pilot balloon was launched hourly between 0800 and 1800 hours in the middle of every 10-minute data recording period.

1.4 Summary of Results

Some of the significant results of this research are:

(1) Wind-Doppler measurement results compare most favorably with in-situ PIBAL data in lower strata of the common volume.

(2) Spectral broadening of wind-produced spectra are observed during afternoon hours when the atmosphere is well mixed.

(3) At symmetrical off-axis angles, measured upwind and downwind Doppler spectra are observed to be nearly antisymmetric about the zero-Doppler frequency. This suggests some degree of spatial uniformity in the transverse winds.

(4) On-axis the Doppler spectra are generally symmetrical about zero-Doppler suggesting the absence of vertical wind components and/or spatial non-uniformities in the transverse wind velocity.

(5) Aircraft trailing vorticies produce spectral broadening and spatial asymmetries in the ambient wind produced spectra.

(6) Spectral and transit-time analyses of aircraft-induced Doppler permit a determination of the spatial extent, range, and velocity of trailing vorticies.

(7) Analytical results show the Doppler shift for a scatterer at a fixed cross-path position to be greater on a longitudinally asymmetrical path vis a vis a symmetrical path of equal path length.

Chapter 2

THEORETICAL DISCUSSION

Signals received via transhorizon tropospheric scattering processes are frequently subject to rapid fading and spectral instabilities. This is a consequence of the interference nature of the Doppler-shifted components associated with moving off-path scatterers. Interference patterns are set up at the receiver by signal components scattered off refractive eddy structures transported by the wind through regions of the atmosphere mutually illuminated by the transmitting and receiving antenna beams. As suggested by Atlas et al. (1969), atmospheric structures on the upwind side of the beam produce positive Doppler frequency shifts that beat with negative-shifted Doppler components associated with eddies on the downwind side of the beam. These Doppler shifts progressively increase with the off-path displacement of the scattering region and have been shown (Birkemeier et al., 1968; Atlas et al., 1969) to be directly proportional to the cross-path wind speed in the lower segments of the common volume. A single-scatterer model (Birkemeier et al., 1968) can be used to illustrate the physical concepts involved and to show the influence of the path geometry and source position on the basic Doppler relations.

2.1 Single Scatterer Model

In the analysis presented in this section a single scatterer is assumed to be responsible for the signal observed at the receiver. As shown in Figure 2.1, the point source scatterer is located at the

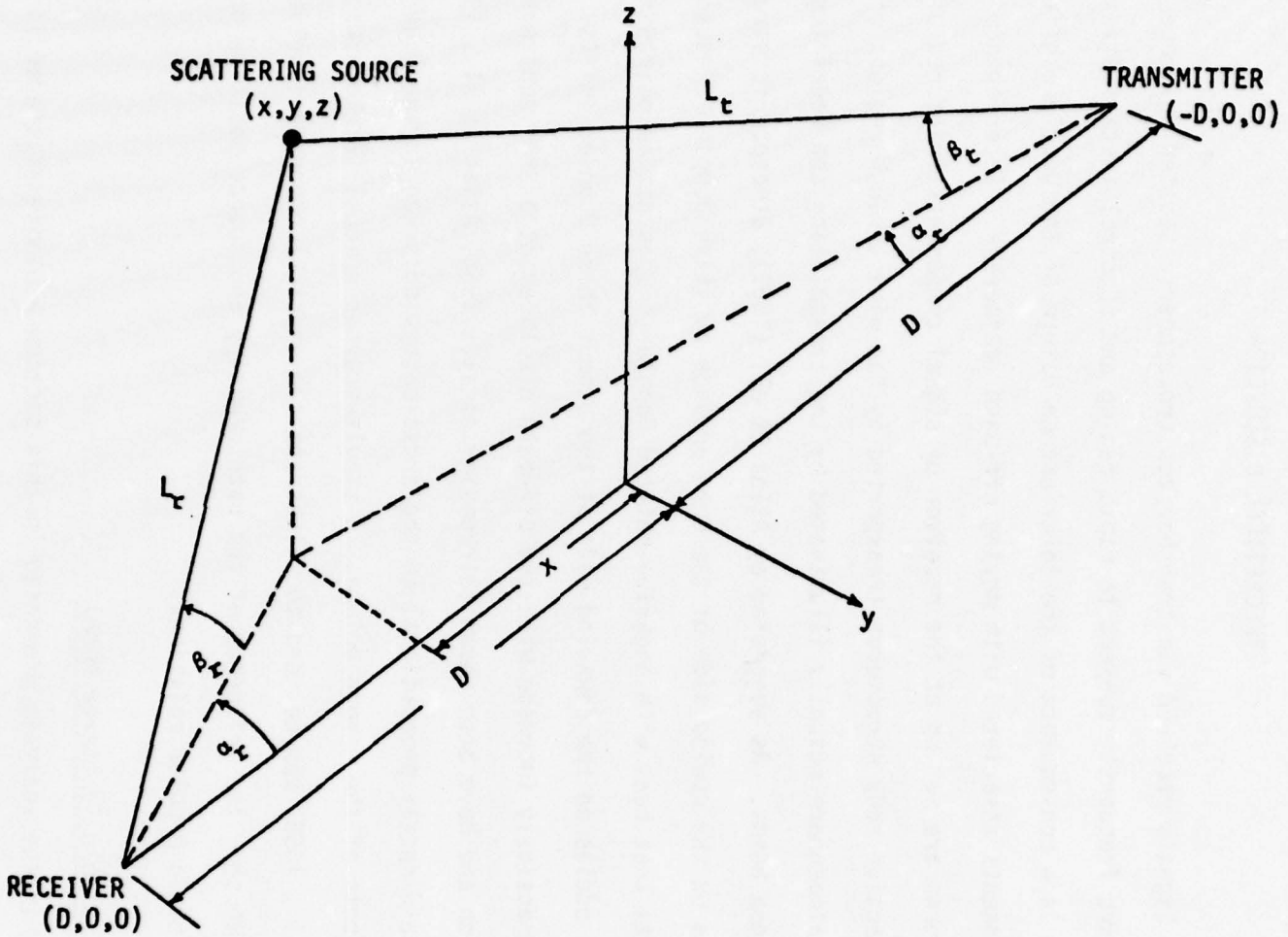

Fig. 2.1. SINGLE SCATTERER PATH GEOMETRY.

intersection of two perfectly narrow antenna beams. The Cartesian coordinate system used in this model has its origin centrally located along the chordal axis between the two radio terminals. The x, y, and z coordinates define respectively the longitudinal, transverse, and vertical spatial positions of the scatterer. The total ray-path length, L, from the transmitter to the receiver is the sum of the respective path lengths, L_t and L_r, from the transmitter to the scatterer and from the receiver to the scatterer. Denoting the chordal distance between the terminals as $2D$, the total ray-path length can be expressed in terms of the position coordinates of the scatterer as

$$L = [(D+x)^2 + y^2 + z^2]^{\frac{1}{2}} + [(D-x)^2 + y^2 + z^2]^{\frac{1}{2}} \qquad (2.1)$$

If we assume a 4/3 effective earth radius (Bean and Dutton, 1966) to account for the refractive bending of radio rays in the lower atmosphere, we may use straight lines for the ray paths in applying the above expression.

It is well known that a moving source produces a Doppler shift, f_d, at the receiver that is proportional to the time rate of change of the ray-path length. This Doppler principle can be expressed as

$$f_d = -\frac{1}{\lambda}\frac{dL}{dt} \qquad (2.2)$$

where λ is the wavelength of the transmitted signal. It is seen that if the effective path length decreases (increases) with time, a positive (negative) Doppler shift will be observed at the receiver. The Doppler shift can also be interpreted as the rate at which the scatterer moves

across surfaces of constant path length. Contours of constant path length are ellipsoidal surfaces (Birkemeier et al., 1968) with the radio terminals as foci. If the scatterer moves with a velocity, $\overline{V}_s$, an equivalent Doppler expression can be written as

$$f_d = -\frac{1}{\lambda}\overline{V}_s \cdot \nabla L \tag{2.3}$$

Upon substituting the expression given in (2.1) for the total ray-path length, the Doppler shift from a single moving scatterer becomes expressed as

$$f_d = -\frac{1}{\lambda}\left\{\frac{[ux + vy + wz]L + uD[(\gamma^2-2xD)^{\frac{1}{2}} - (\gamma^2+2xD)^{\frac{1}{2}}]}{(\gamma^2+2xD)^{\frac{1}{2}}\,(\gamma^2-2xD)^{\frac{1}{2}}}\right\} \tag{2.4}$$

where in the above $\gamma^2 = [x^2 + y^2 + z^2 + D^2]$ and u, v, and w are respectively the longitudinal, transverse, and vertical velocity components of the moving scatterer. From the general result in (2.4) specific Doppler expressions for symmetrical and asymmetrical paths will be derived to illustrate the influence of the scatterer's longitudinal position.

2.2 Symmetrical Path Case

On longitudinally symmetrical paths, the scattering regions primarily responsible for the received signal are located in close proximity of the mid-path plane. As a result, a moving point-source scatterer has relatively small longitudinal displacements, i.e. $x << D$ and is generally confined to scattering regions in the common volume where $D^2 >> [x^2 + y^2 + z^2]$. Applying a first-order approximation to the terms $(\gamma^2+2xD)^{\frac{1}{2}}$ and $(\gamma^2-2xD)^{\frac{1}{2}}$ in (2.4), the Doppler shift produced by a

moving scatterer on a symmetrical path becomes expressible as

$$f_d = -\frac{4}{\lambda L}\left[\frac{ux(1-4D^2/L^2) + vy + wz}{1 - 16x^2D^2/L^4}\right] \qquad (2.5)$$

This result arrived at by Birkemeier et al. (1968) has been applicable to previously reported transhorizon wind-sensing experiments since such experiments have heretofore been conducted on near-symmetrical paths.

Equation (2.5) can be further simplified by considering the geometry of the symmetrical path profile in Figure 2.2 and the relative contributions of the wind velocity components. It can be shown that the term $(1-4D^2/L^2)$ is small and equivalent to $4z_m^2/L^2 = 4h_m^2/D^2$ where z_m and h_m are respectively the mid-path heights of the scatterer above the chordal axis and the earth's surface. Since the longitudinal displacement, x, of the scatterer is also small, the Doppler contribution from the longitudinal wind can be neglected. the longitudinal motion produces negligible Doppler effects because of the elongated shapes of the ellipsoidal surfaces of constant path length. A scatterer moving in the longitudinal direction cuts across the surfaces at a much slower rate than one moving in the transverse or vertical directions. The effect of the vertical wind can in most instances be neglected since its magnitude is normally much less than that of the horizontal wind. It then becomes evident that the Doppler shift on a symmetrical path is linearly proportional to the cross-path displacement, y, of the moving scatterer and may be explicitly given as

$$f_d = -\frac{4vy}{\lambda L} \qquad (2.6)$$

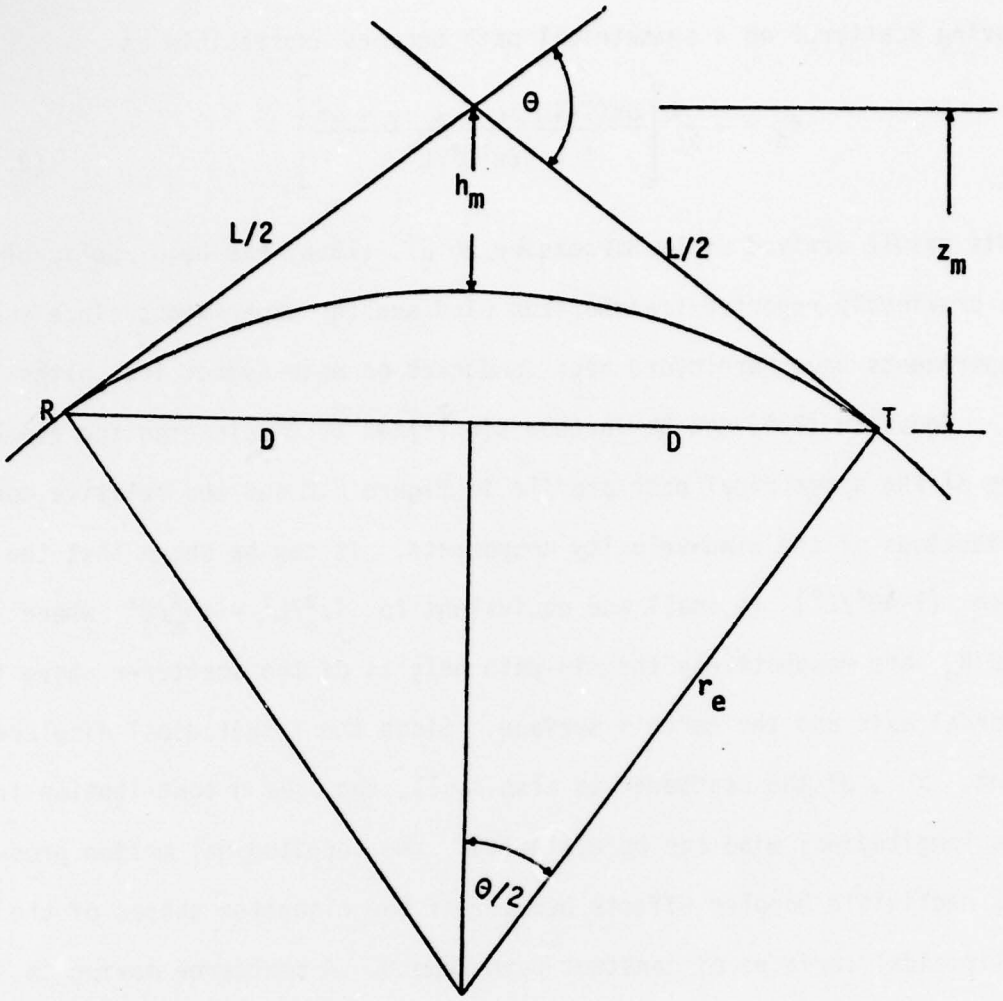

Fig. 2.2. SYMMETRICAL PATH PROFILE.

The Doppler shift may also be expressed in terms of the azimuthal angular position, α , of the scatterer. The Doppler relationship is then written as

$$f_d = - \frac{2v}{\lambda} \sin(\alpha) \tag{2.7}$$

which, for small angles, can be approximated with negligible error as

$$f_d = - \frac{2v\alpha}{\lambda} \tag{2.8}$$

2.3 Asymmetrical Path Case

Consider now the path profile shown in Figure 2.3 where the principal scattering region in the common volume is skewed significantly to one side of the mid-path plane. We begin this treatise by again looking at the terms $(\gamma^2+2xD)^{\frac{1}{2}}$ and $(\gamma^2-2xD)^{\frac{1}{2}}$ in the general Doppler shift expression given in (2.4) but view them from the standpoint of an asymmetrical path. For this situation, it is assumed that the longitudinal displacement, x , is such that $(D-x)^2 >> y^2 + z^2$ for all values of x , y , and z within the common volume. With this constraint, a first-order approximation to the terms, $(\gamma^2+2xD)^{\frac{1}{2}}$ and $(\gamma^2-2xD)^{\frac{1}{2}}$, results in a Doppler shift on an asymmetrical path that can be expressed as

$$f_d = - \frac{L}{\lambda D^2} \left[\frac{2ux(1-2D/L) + vy + wz}{1 - x^2/D^2} \right] \tag{2.9}$$

This result reduces to that for the symmetrical path case when $x << D$. Hence, the Doppler shift expression given in (2.9) is a more general result that is applicable to both symmetric and asymmetric path geometries.

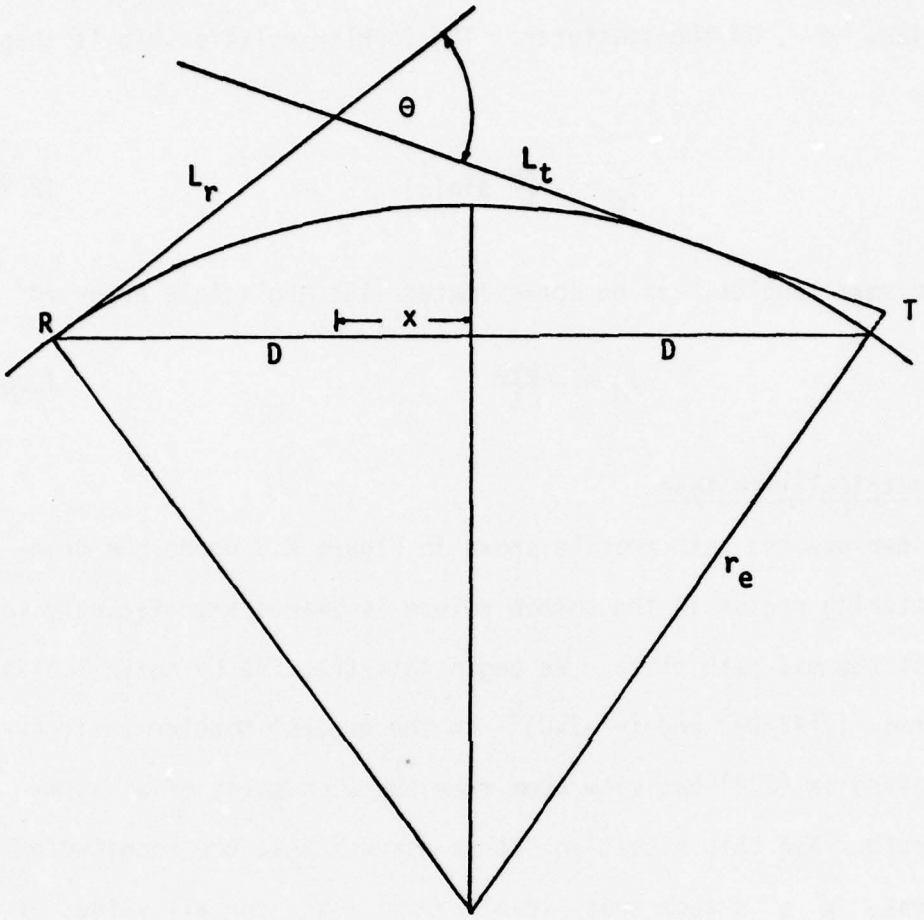

Fig. 2.3. ASYMMETRICAL PATH PROFILE

A simplification of (2.9) can be made by introducing a path asymmetry factor resulting from the terrain profile along the path and the relative heights of the radio terminals. The asymmetry factor, s, is defined as the ratio of the longitudinal displacement of the scattering source to the chordal distance from the mid-path plane to either of the radio terminals, i.e. $s \equiv x/D$. It is zero for a symmetrical path. When the scattering region is skewed to one side of the mid-path plane, however, the magnitude of the asymmetry factor becomes greater than zero but always remains less than unity. Using this factor, the Doppler shift becomes

$$f_d = -\frac{L}{\lambda D}\left[\frac{2us(1-2D/L) + vy/D + wz/D}{1 - s^2}\right] \tag{2.10}$$

The term $(1-2D/L)$ is approximately equivalent to $(y^2+z^2)/2(D^2-x^2)$. Thus, using the geometry in Figure 2.1, the Doppler shift can then be expressed in terms of the azimuthal, α, and vertical, β, angular positions of the scatterer as

$$f_d = -\frac{L}{\lambda D}\left[\frac{us(\alpha_r\alpha_t + \beta_r\beta_t)}{1 - s^2} + \frac{v\alpha_r + w\beta_r}{1 + s}\right] \tag{2.11}$$

where small angle approximations with respect to the receiver and transmitter are used, i.e. $\alpha_r \simeq \frac{y}{D(1-s)}$, $\alpha_t \simeq \frac{y}{D(1+s)}$, $\beta_r \simeq \frac{z}{D(1-s)}$, and $\beta_t \simeq \frac{z}{D(1+s)}$. For equal transverse and longitudinal wind velocities, the longitudinal Doppler contribution again remains relatively small and can be neglected. If the vertical wind contribution is also neglected and the first-order approximation, $L \simeq 2D$, is substituted

for the ray-path length, the Doppler shift expression (2.10) simplifies to

$$f_d = - \frac{2vy}{\lambda D(1-s^2)} \tag{2.12}$$

which can be rewritten in terms of the azimuthal angular offset, α_r , from the receiver as

$$f_d = - \frac{2v\alpha_r}{\lambda(1+s)} \tag{2.13}$$

Comparing the above results with those for the symmetrical path case, equations (2.6) and (2.8), it is seen that the Doppler shift for a scatterer at a given cross-path displacement is greater on an asymmetrical path than on a symmetrical path. This is consistent with the interpretation of the Doppler shift as the rate at which a scatterer cuts across surfaces of constant path length. The separation between these ellipsoidal surfaces is greatest in the mid-path plane and becomes smaller towards either of the two terminals. Consequently, a scatterer moving through the common volume region on an asymmetrical path cuts across the equiphase surfaces at a more rapid rate than on a symmetrical path.

On the asymmetrical Jackson-Stanford path used in the experiment discussed in this dissertation, the principal scattering region is in the vicinity of a transverse plane about 40 kilometers from the receiver. The average longitudinal displacement, x , of a scatterer on this path is such that $s \simeq \frac{1}{2}$. The analytical expression for the Doppler shift applicable to this path is

$$f_d = - \frac{4v\alpha_r}{3\lambda} \tag{2.14}$$

where α_r is measured in radians. If the angle measurement is converted to degrees and the numerical value (9.4×10^{-2}m) is substituted for λ, a more simplified expression for the Doppler shift on the Jackson-Stanford path can be written as

$$f_d = - \frac{v\alpha_r}{4} \tag{2.15}$$

where in the above expression v is units of m/s.

2.4 Multiple Scattering Effects

In the previous sections, a single scattering source was assumed and as a result, Doppler effects were limited to single frequency shifts. A multiplicity of scatterers randomly distributed throughout an illuminated region in the atmosphere produces a spectrum of Doppler shifts. The spectral composition of the Doppler shifts is dependent upon the spatial distribution and the relative velocities of the individual scatterers. Each scatterer gives rise to a discrete Doppler shift in accordance with the analysis developed earlier. A number of the scatterers, however, may contribute to the same spectral component. The extent of the contributions from the many off-path scatterers is reflected in the shape of the Doppler spectrum, which is dependent upon the relative strength of the received signal as a function of the scatterers' cross-path positions. The signal power received from a particular azimuthal direction is directly proportional to the product of the net antenna gain and the reflectivity or scatter cross-section of the medium. Thus, the Doppler

spectrum arising from a distribution of scatterers is dependent upon the antenna beam configuration and the basic propagation mechanism.

An average Doppler shift, $\bar{f}_d$, can be attributed to a mean flow or drift of the atmospheric scatterers. Birkemeier et al. (1968) have specified analytically the average Doppler shift for antennas synchronously aligned in azimuth at an angle, α_a , as

$$\bar{f}_d = -\frac{2v}{\lambda}\int \alpha G(\alpha-\alpha_a)W(\alpha)d\alpha \Big/ \int G(\alpha-\alpha_a)W(\alpha)d\alpha \qquad (2.16)$$

where $G(\alpha-\alpha_a)$ is the combined antenna gain function and $W(\alpha)$ is the scattered power per unit azimuthal angle. this result, however, applies to a symmetrical path. A more general result incorporates the path asymmetry factor, s , and can be given in terms of the angular offset, α_r , measured from the receiver location, as

$$\bar{f}_d = \frac{2v}{\lambda(1+s)}\int \alpha G(\alpha-\alpha_r)W(\alpha)d\alpha \Big/ \int G(\alpha-\alpha_r)W(\alpha)d\alpha \qquad (2.17)$$

In these expressions for the average Doppler shift, various atmospheric models can be applied to account for the angular-dependence scattering function, $W(\alpha)$. The classical isotropic turbulence model (Tatarski, 1961) predicts a minus 11/3 power-law variation in the scattering cross-section as a function of scattering angle, θ . The scattering angle is defined as the angle between the transmitted and received ray-path directions. For the isotropic turbulence model, the scattering cross-section is proportional to $\sin^{-\frac{11}{3}}(\theta/2)$. Birkemeier et al. (1977) have shown that for small scattering angles near the mid-path plane $\theta \simeq 2\sqrt{\alpha^2 + \beta^2}$. This expression for the scattering angle is valid for

near-symmetric propagation paths. However, a more general result that is applicable to asymmetrical paths as well shows the scattering angle to be given approximately as

$$\theta \simeq \sqrt{\alpha_r^2 + \beta_r^2} + \sqrt{\alpha_t^2 + \beta_t^2} \tag{2.18}$$

Using the small angle approximations developed earlier, the above expression can be written as a function of the path asymmetry factor, s, in terms of the angular displacements, α_r and β_r, from the receiver as

$$\theta \simeq \frac{2}{1+s} \sqrt{\alpha^2{}_r + \beta_r^2} \tag{2.19}$$

An equivalent expression for the Jackson-Stanford path, which has a minimum scattering angle of 0.84° occurring at an elevation angle of 0.25°, is

$$\theta \simeq 0.5 + \frac{4}{3} \sqrt{\alpha_r^2 + \beta_r^2} \tag{2.20}$$

where $\beta_r \geq 0.25°$.

In addition to the azimuthal variations, the above relationships show the extent of the influence of the vertical positions of the scatterers on the scattering function. The average Doppler shift from a given azimuthal direction is a spatially averaged result of the transverse motions of scatterers at various altitudes within the common volume. The wind-produced drift of the scatterers generally increases with altitude. However, the turbulence model assumed produces a rapid decrease in the scattered power with elevation angle. This suggests

the average Doppler shift is primarily associated with the motion of scatterers in the lower segments of the illuminated scattering region.

Chapter 3

DESCRIPTION OF EXPERIMENT

3.1 Propagation Path

The experiment described in this report was conducted over the propagation path shown in Figure 3.1. The 164-km (102 miles) path is aligned along a SW-NE (230° - 50°) azimuthal bearing between Jackson Butte (transmitter site) and Stanford, California (receiver site). The transmitter was situated on a 725-meter (2375 ft) peak just east of Jackson, California and the receiver was located 110 meters (360 ft) above sea level in the foothills behind Stanford University. A topographical profile

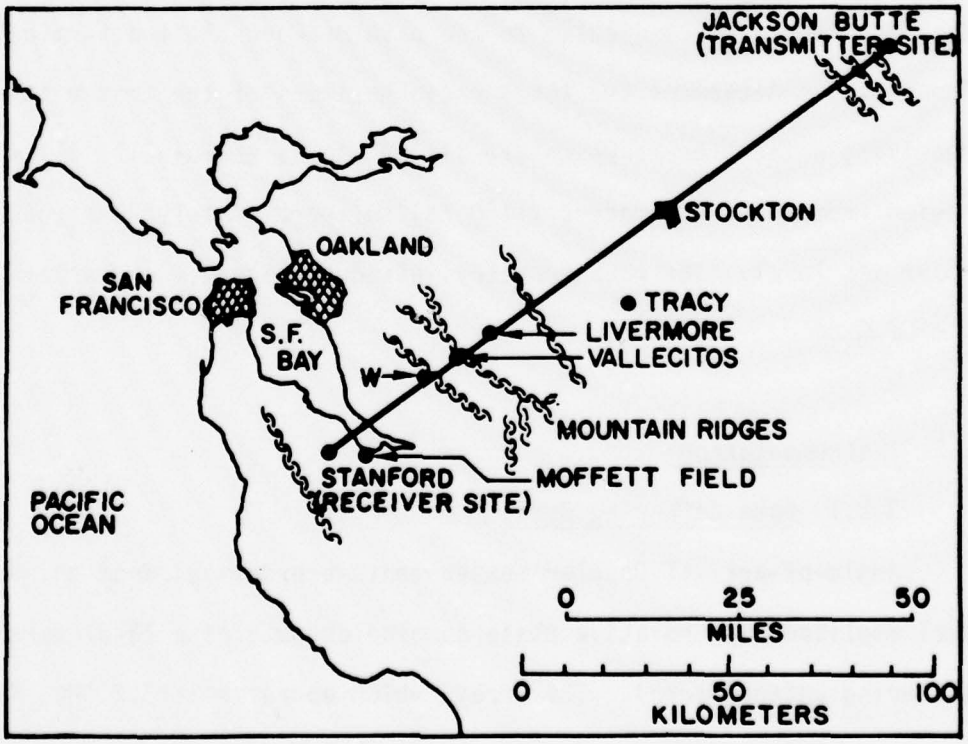

Fig. 3.1. PROPAGATION PATH AND SURROUNDING AREA.

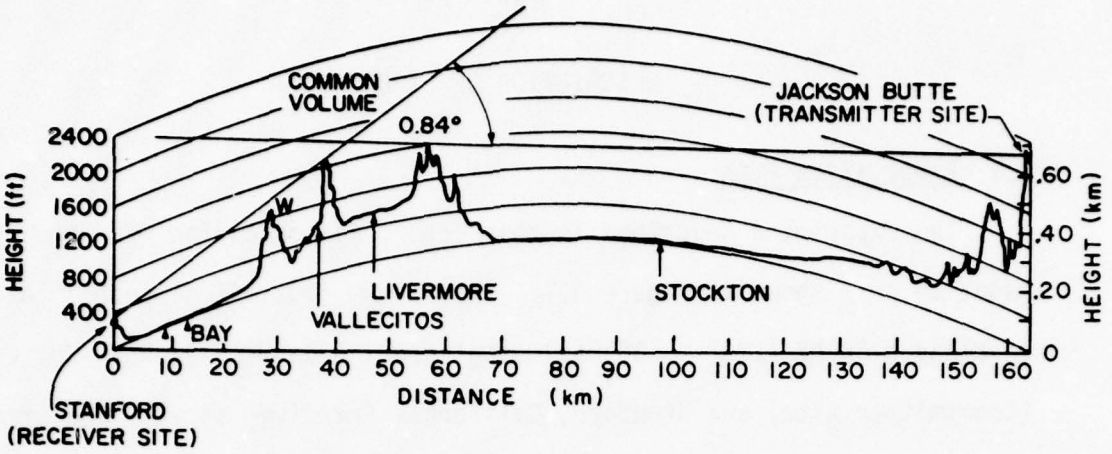

Fig. 3.2. TOPOGRAPHICAL PROFILE OF PROPAGATION PATH.

(Figure 3.2) of the path shows the existence of three mountain ridges that are nearly perpendicular to the path between the two terminals. These ridges determine the local radio horizons of the transmitting and receiving antenna beams which are aligned so as to mutually illuminate a region from about 425 meters (1400 ft) to approximately 2 km (6600 ft) above sea level. The path geometry introduces a minimum scattering angle of 0.84°

3.2 Instrumentation

3.2.1 Data-Gathering Array

Angle-of-arrival Doppler measurements are derived from the individual amplitude and relative phase sampled outputs of a 12-element data gathering antenna array. The array, which operates at 3.2 GHz, is shown in Figure 3.3 and, except for the horizontal orientation and polarization, is identical to the vertical array used in previous experiments at

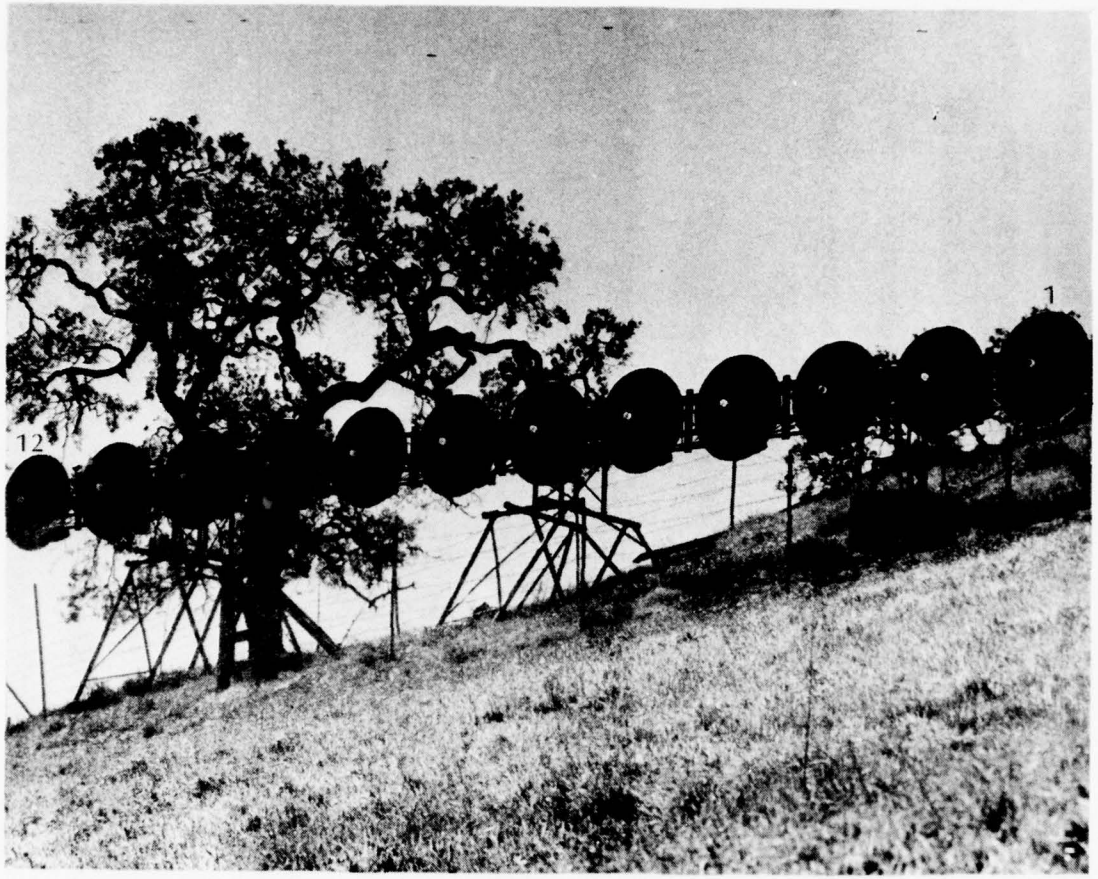

Fig. 3.3. HORIZONTAL DATA-GATHERING ARRAY.

Stanford (Cox, 1967; Cox and Waterman, 1969 and 1971; Cianos, 1971; Cianos and Waterman, 1973; Waterman, 1973; and Cianos, 1978). The data-gathering array is aligned nearly broadside to the propagation path and is structurally supported beneath the 2nd, 6th, and 10th elements. Each element is horizontally polarized and has a 5° half-power beamwidth which determines the vertical extent of the array fan beam. When uniformly illuminated, the array produces in azimuth a 0.3° wide beam which can be scanned through a 3.88° azimuthal sector. A summary of the physical and operational characteristics of the array is outlined in Table 3.1.

Table 3.1

SUMMARY CHARACTERISTICS OF DATA-GATHERING ARRAY

Physical Characteristics	Number of elements	Twelve
	Element spacing	1.4 m (14.8 wavelengths)
	Element diameter	1.2 m (13.0 wavelengths)
	Effective aperture length	15.2 m (162.5 wavelengths)
Operational Characteristics	Operating frequency	3.2 GHz
	Polarization	Horizontal
	Half-power beamwidth*	0.3° AZ/5° EL
	Grating lobe separation*	3.88°
	Sidelobe levels*	< - 13 dB
* for a uniformly illuminated conventional additive array		

3.2.2 Array-Receiver Channels

Twelve separate receiving channels connect to the twelve separate elements in the array. A typical receiving channel is illustrated in Figure 3.4. Each channel receives simultaneously the transhorizon signal at 3.2001 GHz and a stable line-of-sight reference signal at 3.2000 GHz. A 3.2300-GHz local oscillator signal (common to all 12 channels) is mixed with both the transhorizon and reference signals in mixer-preamps mounted directly behind each array element. The down-converted transhorizon (29.9-MHz) and reference (30.0-MHz) signals are separated by 2-kHz wide crystal filters. The 30-MHz IF reference is amplified and then used as a second local oscillator which mixes with the 29.9-MHz transhorizon IF signal. The resultant 100-kHz second IF signal is narrow-band filtered with a 23-Hz wide crystal filter which effectively sets the noise bandwidth of the receiving channel. After further amplification the narrow-band 100-kHz signal is passed through a variable phase shifter and a variable gain amplifier which are adjusted and set during calibration. This signal is then continuously available from each array-element receiving channel.

Sampling of the twelve 100-kHz signals is performed by a computer-controlled electronic commutator. A block diagram of the amplitude and phase sampling equipment is shown in Figure 3.5. Every 25 ms the commutator is sequentially stepped through all 12-element positions. The commutator takes five milliseconds to completely scan all twelve elements. The commutator output is bandpass filtered to reduce switching transients. The sample 100-kHz output is phase compared with a stable 100-kHz reference standard. Additionally, the signal is applied to two

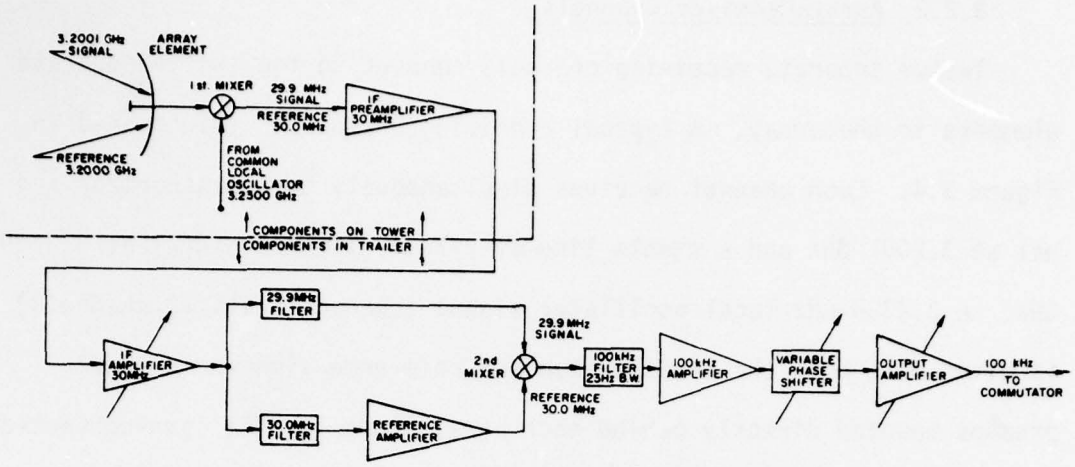

Fig. 3.4. BLOCK DIAGRAM OF AN ARRAY ELEMENT RECEIVING CHANNEL.

Parameters

1st Mixers (part of LEL type SBC-6

Noise figure: 9 to 10 dB (depends on unit)

30-MHz IF Preamplifiers (part of LEL type SBC-6)

Gain: 25 to 30 dB RF to IF (depends on unit)

30-MHz IF Amplifiers (LEL type ITA-1)

Adjustable gain: 20 to 70 dB
Bandwidth: 3 MHz

29.9-MHz and 30.0-MHz Filters (Hughes special design)

Bandwidth: 2 kHz
Quartz crystals

2nd Mixers

Balanced diodes for LO (reference signal)
Noise Suppression

100-kHz Filters (Blackhawk Networks Corporation)

Bandwidth: 23 Hz
Quartz Crystals

Phase Shifters (Nilsen V42-01 Variogon)

Adjustable 0° to 360° continuously
Loss independent of phase setting

100-kHz Output Amplifiers

Low output impedance: 5 to 10 Ω
Phase shift independent of gain setting
Gain adjustable 0 to 20 dB

All active circuit elements are solid-state devices

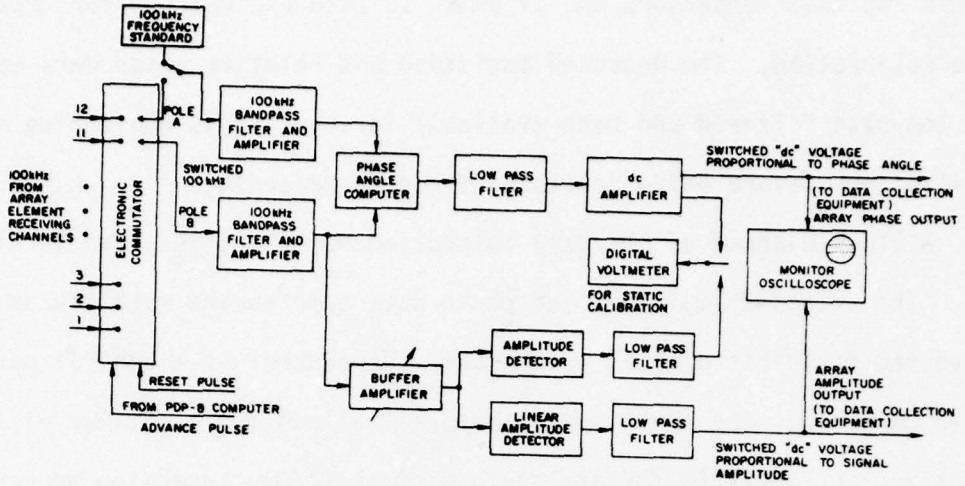

Fig. 3.5. BLOCK DIAGRAM OF AMPLITUDE AND PHASE-SAMPLING EQUIPMENT.

Parameters

Electronic Commutator

2-pole 12-position switch
Scans array at 100 scans (over 12 elements)/sec
Settling time: << 0.3 msec

100-kHz Bandpass Filters

Bandwidth: 30 kHz

Phase-Angle Computer (Wiltron Model 351)

Measures phase to 1° or better over 60 dB signal variation in either or both channels

Lowpass Filters

Active 2-pole filter using RC feedback around an operational amplifier
RC feedback set to optimize rise time at switch rate used
dc offset: < 1 mV

Linear Amplitude Detector

Linear to 1% of full scale over dynamic range > 40 dB

dc Amplifiers

dc offset: < 1 mV
Feedback around operational amplifier for good linearity

Frequency Standard (James Knight FS-1100T

100 kHz output
Aging rate of 1 to 2 parts in 10^{10}/day (1 to $2 \cdot 10^{-5}$ Hz/day at 100 kHz)

linear amplitude detectors one of which is used exclusively for amplitude calibration. The detected amplitude and relative phase data samples are low-pass filtered and made available for continuous monitoring on an oscilloscope before being processed for data recording.

A block diagram of the data collection equipment is shown in Figure 3.6. The detected amplitude and phase data samples are multiplexed and converted to 12-bit digital words under the control of a general purpose PDP-8 computer. The 12-bit digital format allows for a maximum of 4096 quantization levels in the analog-to-digital (A/D) conversion process.

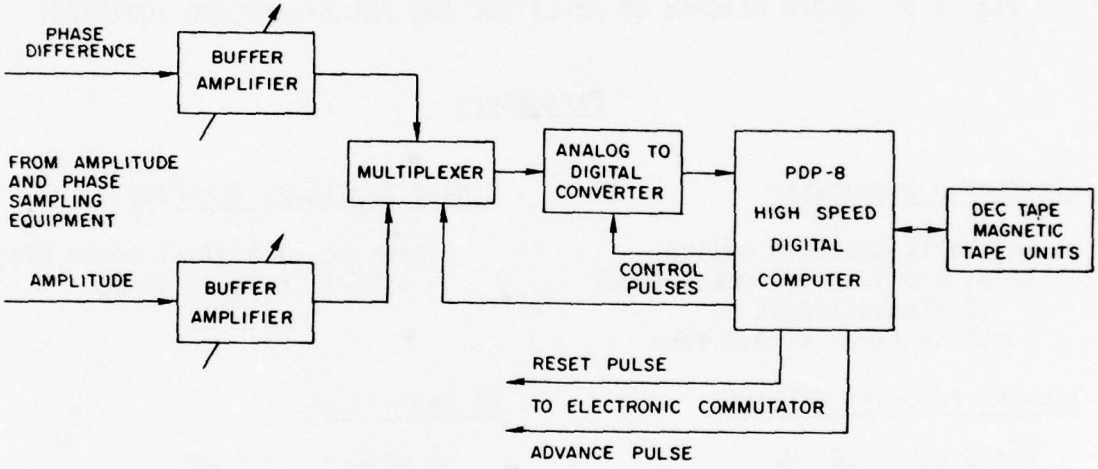

Fig. 3.6. BLOCK DIAGRAM OF DATA-COLLECTION EQUIPMENT.

Parameters

A/D Converter and Multiplexer (DEC AF01)

Multiplexer switching speed: < 2 μsec
A-D word length: 12 bits (3096 levels)
35 μsec conversion time
±0.25% max switching point error for ±1/2 least significant bit of quantization error

Computer (DEC PDP-8) with Hardware Arithmetic Unit

1.5 μsec memory cycle time
4096 word fast memory
12-bit word length

Magnetic Tape Units

DEC TU-20 (IBM Compatible)
DEC TU-55 (Program DECtape)

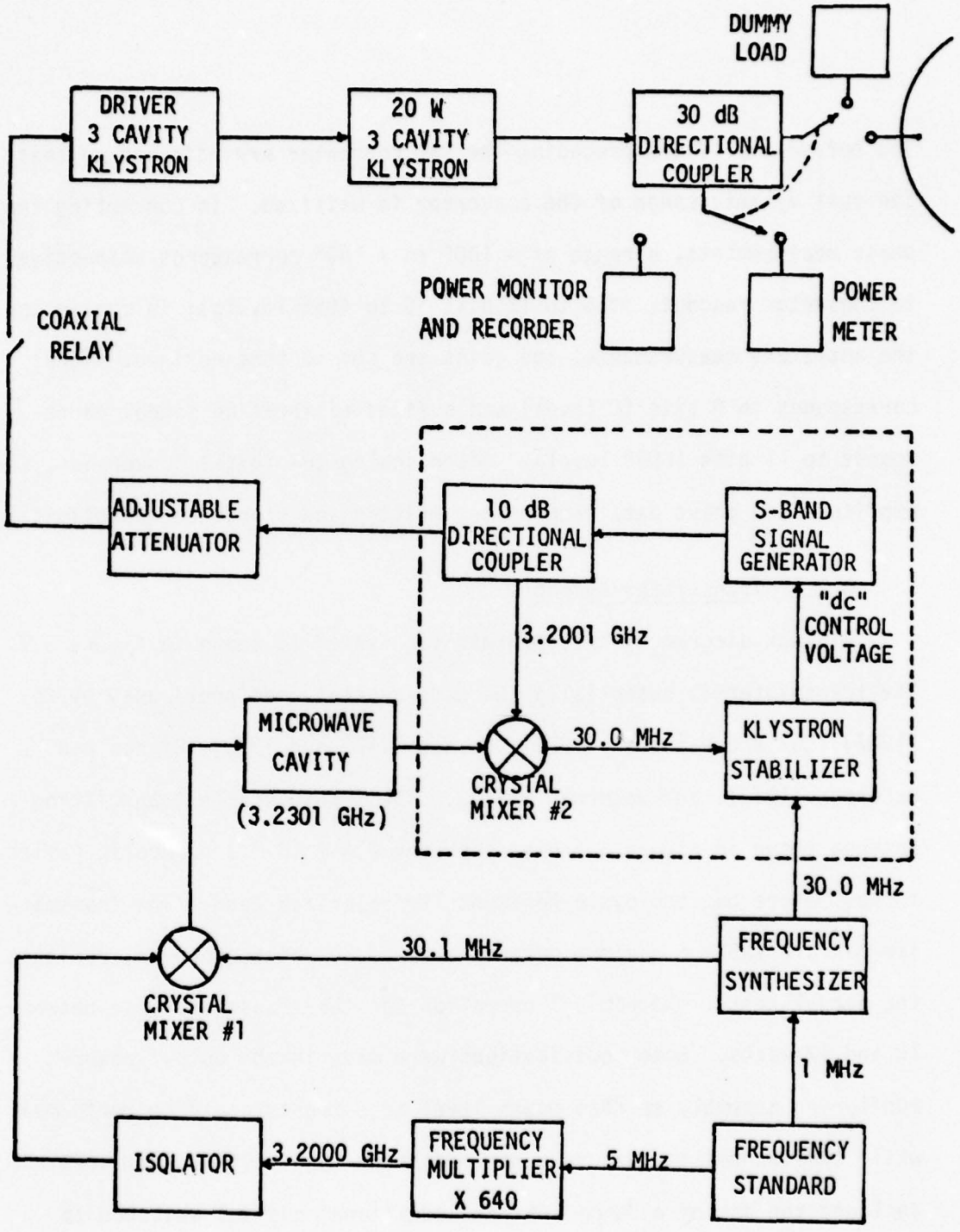

Fig. 3.7. BLOCK DIAGRAM OF TRANSMITTER

The buffer amplifiers preceding the A/D converter are adjusted so that the full dynamic range of the converter is utilized. In converting the phase measurements, a range of - 180° to + 180° corresponds respectively to converter readouts of 0 to 12 bits (0 to 4095 levels); in converting the amplitude measurements, the gains are set so that no input signal corresponds to 0 bits (0 level) and a fixed calibration signal corresponds to 11 bits (2048 level). After analog-to-digital conversion, the amplitude and phase data samples are written and stored on magnetic tape.

3.2.3 Transmitter Assembly

A block diagram of the transmitting system is shown in Figure 3.7. The transmitter is essentially the same as that used previously by Cox (1967), Cox and Waterman (1971), Cianos (1971 and 1978), Cianos and Waterman (1973), and Waterman (1973). The transportable transmitting antenna shown in Figure 3.8 uses the same 2.4-m (8-ft) parabolic reflector as before but employs a horizontally polarized feed. The transmitter has available a maximum output power of 20 watts; however, during the actual tests, the nominal operation for the transmitter was between 10 and 12 watts. Some modifications were made in the output power-monitoring assembly so that power level adjustments could be performed while the transmitter was in a non-radiating mode. These modifications included the use of a dummy load and additional coaxial switches to permit the transmitter signal to be monitored under loaded non-radiating conditions during calibration and alignment periods.

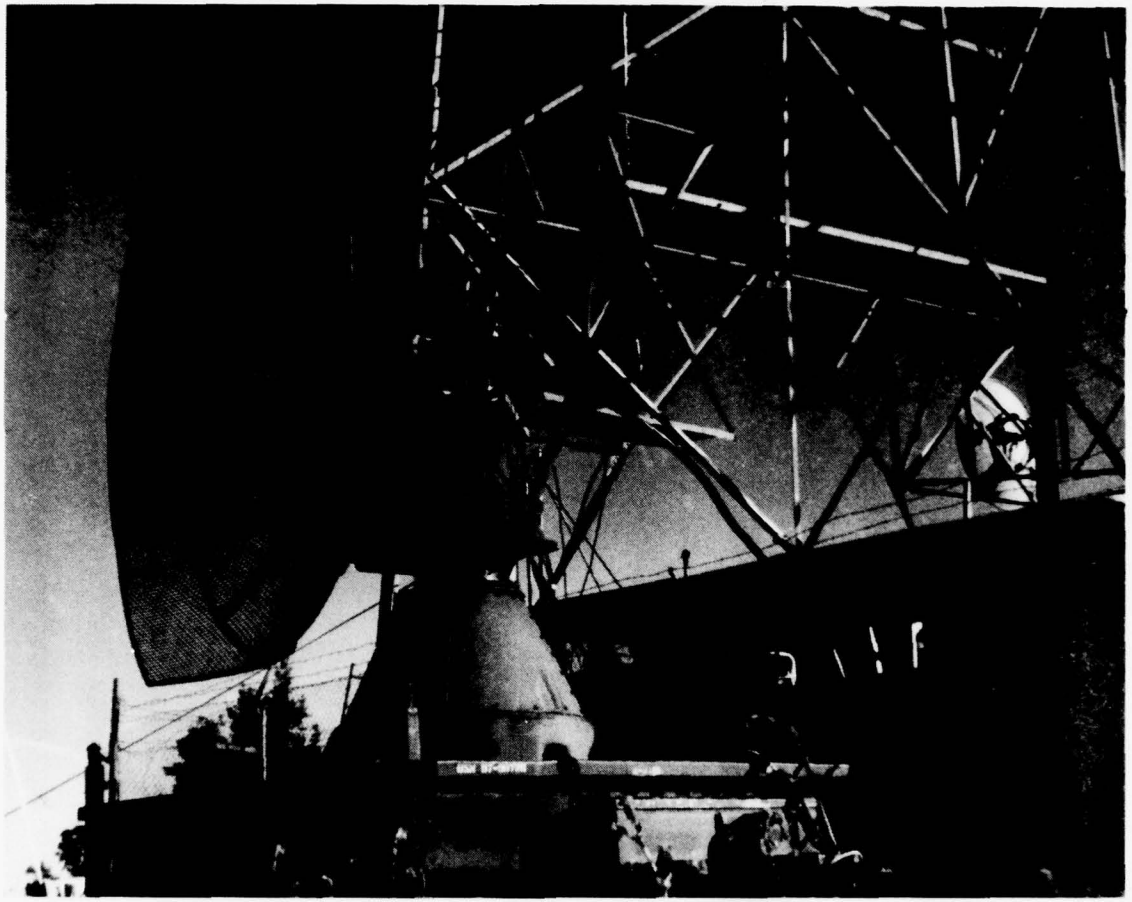

Fig. 3.8. TRANSMITTING ANTENNA AND EQUIPMENT VAN.

3.3 Experimental Procedures

3.3.1 Data Collection

Data was collected and recorded during a continuous 42-hour experiment conducted between 0000 hours on 21 April 1978 and 1830 hours on 22 April 1978. Ten minutes of transhorizon data were recorded every hour beginning approximately on the hour. The sampled amplitude and phase data from each array element were recorded in 12-bit digital format on magnetic tape at a 40-Hz rate. A five millisecond scan period was used to sample and record the amplitude and phase data from all twelve elements. The data samples were recorded in the sequence a_1,ϕ_1; a_2,ϕ_2; . . . a_{12},ϕ_{12} .

A calibration signal transmitted from a line-of-sight source about a mile from the receiver along the path was recorded for 1.6 seconds (64 scans) before every ten-minute data recording period. Immediately following the recording of transhorizon data, the transmitter was turned off and the calibration signal again turned on. The amplitude and phase calibration levels of each array element were then monitored with the digital voltmeter (Figure 3.5) and read into the log while the commutator was manually stepped through all twelve element positions.

During actual data recording, the sampled amplitudes and phases of all twelve elements were continuously monitored on an oscilloscope (Figure 3.5). Any signal anomalies that could be attributed to aircraft, interference, etc. were noted in the log. Visual sightings of aircraft in the vicinity of the common volume were logged at the transmitter, receiver, and PIBAL launch sites.

3.3.2 System Calibration

Prior to each transhorizon data recording period, the transmitter was completely checked and aligned; and all array element receiving channels were calibrated. The transmitter frequency standard (Figure 3.5) was adjusted each day during the quiet early morning hours and set to within 2 parts in 10^{11} (0.064 Hz at 3.2 GHz) of the frequency standard used to generate the reference and calibration signals. In the calibration and alignment of the individual receiving channels, a number of critical checks were made to ensure proper operation during the data-gathering portions of the experiment. The mixer currents, the amplifier gains, and the phase-lock loop status of the receiving system were routinely checked and if necessary, adjusted before each data recording period.

During calibration periods, the transhorizon signal was turned off and a 3.2001-GHz calibration signal was transmitted from a stable source about 1.6 kilometers from the receiver. This signal was remotely controlled from the receiving site and was used to properly set the variable 100-kHz amplifiers and phase-shifters in each receiving channel. With the calibration signal on, the commutator was manually advanced through all twelve element positions and the detected amplitude and adjacent element phase-difference signals were monitored with the digital voltmeter. The variable phase-shifters and amplifiers were then adjusted on an element by element basis for predetermined calibration readings on the digital voltmeter.

The predetermined phase-difference and amplitude calibration set-

tings were obtained from the results of a series of line-of-sight (LOS) tests in which the transmitter was placed at selected azimuthal positions about 15 kilometers from the receiving array. With the calibration signal off and the transmitter on (at reduced power), the individual amplitudes were set uniformly across the array by adjusting the gains of the 100-kHz amplifiers. Adjacent element phase-differences were set with the variable phase-shifters to values calculated from the signal's known angle-of-arrival. After the phase and amplitude adjustments were made, the transmitter was turned off and the LOS calibration source turned on. Phase and amplitude readings were then obtained for all twelve elements using the digital voltmeter.

The above procedures were repeated for three different line-of-sight transmitter positions. Results from two of the azimuthal positions were averaged and used to obtain the final amplitude and phase-difference calibration settings. The maximum variation in the adjacent element phase-differences observed between the two locations was 14° and the rms variation was 7°. In the amplitude readings, the maximum variation was 2 dB and the rms variation was 0.7 dB.

3.3.3 PIBAL Wind Monitoring

Pilot balloons released into the common volume from a launch site near Livermore were optically tracked during daylight hours with a single theodolite system to obtain vertical profiles of the horizontal windfield. A pilot balloon (PIBAL) was launched every hour at five minutes past the hour between 0805 and 1805 on each of the two data recording

days. The balloons were released by members of the San Jose State University Meteorology Department from a position beneath the common volume about 0.9° SE of the great-circle bearing and 165 meters (540 ft) above mean sea level. The PIBAL ascent rate was approximately 200 meters (650 ft) per minute. Azimuth and elevation position readings were taken every 30 seconds and each PIBAL was tracked to an altitude of approximately 2.4 km (7870 ft) above sea level. An algorithm used by the meteorology group reduced the PIBAL azimuth and elevation information to horizontal wind velocity profiles.

Chapter 4

ANALYTICAL METHODS

Two basic signal processing steps are used to obtain the angle-of-arrival Doppler spectra from measured amplitude and phase data samples. First, a digital Fourier transform is performed in the time domain on the sampled output signals from the individual array elements. The amplitudes and phases of the resultant spectra are preserved and used to characterize the array element output signals in the frequency domain. A spatial transform is then performed in the array plane on the element spectra to obtain an angular Doppler spectrum for the array. In this process, the individual element spectra are combined using conventional additive array techniques to maximize the output spectra for a particular angle-of-arrival. An average Doppler frequency shift (spectrum centroid) is computed as a function of the angular "pointing" direction of the array with respect to the great-circle (zero-Doppler) plane. The apparent source direction together with the computed average Doppler shift is used to infer an average transverse wind velocity.

4.1 Single Element Spectra

The measured element amplitude, $a_n(k)$, and relative phase, $\phi_n(k)$, data samples are used to construct the single element Doppler spectra. Each spectral component is evaluated from a set of K contiguous data samples. The in-phase and out-of-phase quadrature components of the element spectra are computed in accordance with the following

$$S_{XK}(n,f_i) = \sum_{k=1}^{K} a_n(k)\cos\left[\frac{2\pi f_i(k-1)}{40} - \phi_n(k)\right] \qquad (4.1)$$

$$S_{YK}(n,f_i) = \sum_{k=1}^{K} a_n(k)\sin\left[\frac{2\pi f_i(k-1)}{40} - \phi_n(k)\right] \qquad (4.2)$$

where: $n = 1, 2, \ldots, 12$

The amplitudes, $A_{nK}(f_i)$, and phases, $\Psi_{nK}(f_i)$, of the spectral components are computed from the quadrature phasor components

$$A_{nK}(f_i) = \sqrt{S_{XK}^2(n,f_i) + S_{YK}^2(n,f_i)} \qquad (4.3)$$

$$\Psi_{nK}(f_i) = \tan^{-1}\left[S_{YK}(n,f_i)/S_{XK}(n,f_i)\right] \qquad (4.4)$$

These parameters are obtained for 100 Doppler frequencies in a preselected spectral observation window. The spectral window, which is less than the receiver bandwidth (23 Hz), is centered about zero Doppler to permit simultaneous observation of the upwind (positive) and downwind (negative) Doppler shifts.

4.2 Array Angular Spectra

The array angular spectra are derived from the amplitudes, $A_{nK}(f_i)$, and phases, $\Psi_{nK}(f_i)$, of the individual element spectra. A progressive linear phase-shift across the array is applied to the spectral components of the individual element spectra. Each component is phase-shifted in accordance with conventional additive array techniques. The quadrature phasor components of the resultant angular spectra are then computed for selected beam-pointing angles, α_r , between $\pm$ 1.94° as follows

$$S_{XK}(\alpha_r, f_i) = \sum_{n=1}^{12} A_{nK}(f_i)\cos\left[\Psi_{nK}(f_i) - (n-1)\gamma\alpha_r\right] \qquad (4.5)$$

$$S_{YK}(\alpha_r, f_i) = \sum_{n=1}^{12} A_{nK}(f_i)\sin\left[\Psi_{nK}(f_i) - (n-1)\gamma\alpha_r\right] \qquad (4.6)$$

where: γ = phase shift constant

= 92.71 phase degrees/beam angle degree

A positive (negative) angular direction corresponds to a SE (NW) angle-of-arrival with respect to the great-circle bearing. The Doppler or power spectra, $P(\alpha_r, f_i)$, are computed for a particular angular direction by summing the squares of the quadrature phasor components, i.e.

$$P(\alpha_r, f_i) = S_{XK}^2(\alpha_r, f_i) + S_{YK}^2(\alpha_r, f_i) \qquad (4.7)$$

These angular spectra are essentially unweighted since each spectral component is evaluated from the same set of element amplitudes irrespective of its source direction. The Doppler spectra, however, can be weighted to account for the angle-of-arrival variations arising from the scattering mechanism and the antenna patterns. We define the direction to the source in terms of an angle, α_i , viewed from the receiver. The weighted Doppler spectra, $P_w(\alpha_r, f_i)$, are then determined by applying a normalized angular scattering function, $W_\beta(\alpha_i)$, and a combined receiver-transmitter antenna gain function, $G_c(\alpha_i - \alpha_r)$, to the unweighted spectra, i.e.

$$P_w(\alpha_r, f_i) = P(\alpha_r, f_i)\, W_\beta(\alpha_i)\, G_c(\alpha_i - \alpha_r) \qquad (4.8)$$

Each Doppler frequency is converted to an apparent angular source direction through use of the Doppler relation in (2.15), which for a uniform transverse wind velocity*, v_o , yields

$$\alpha_i = - \frac{4f_i}{v_o} \tag{4.9}$$

On the basis of the computed angular source direction, each spectral component is weighted in accordance with the classical isotropic turbulence model, a $\sin(x)/x$ receiving array pattern, and a Gaussian transmitting pattern. The normalized scattering function is evaluated for a given elevation angle, β , using the following expression with the numerator obtained from equation 2.20

$$W_\beta(\alpha_i) = \left[\frac{0.51 + \frac{4}{3}\sqrt{\alpha_i^2 + \beta^2}}{0.84} \right]^{-m} \tag{4.10}$$

where: $m = 11/3$

$\beta \geq 0.25°$

The combined antenna gain for the assumed patterns is evaluated for each source direction from the following

$$G_c(\alpha_i - \alpha_r) = \left[\frac{\sin[a(\alpha_i - \alpha_r)]}{a\pi(\alpha_i - \alpha_r)/180} \right]^2 \exp[- b\alpha_i^2] \tag{4.11}$$

where: $a = 549.900$

$b = 0.03429$

---

*The sign convention for the wind velocity is negative for a SE wind and positive for a NW wind.

The beam constants a and b are determined for half-power beamwidths of 0.29° and 3°, respectively. The transmitting beam constant, b , includes the path geometry scaling factor which permits angular measurements to be referenced to the receiver.

4.3 Average Doppler Shift

The average Doppler shift is obtained by computing the first moment (spectrum centroid) of the angular Doppler spectra. For the unweighted spectra, the average is given by

$$\bar{f} = \frac{\sum_{i=1}^{100} f_i P(\alpha_r, f_i)}{\sum_{i=1}^{100} P(\alpha_r, f_i)} \tag{4.12}$$

Similarly, for the weighted spectra

$$\bar{f}_w = \frac{\sum_{i=1}^{100} f_i P_w(\alpha_r, f_i)}{\sum_{i=1}^{100} P_w(\alpha_r, f_i)} \tag{4.13}$$

4.4 Average Wind Velocity

The average transverse wind velocity is determined using the results of averaging the unweighted and weighted Doppler spectra. An unweighted average velocity, $\bar{v}$, is obtained directly from the measured unweighted average Doppler shift, $\bar{f}$, by using equation 2.15, i.e.

$$\bar{v} = -\frac{4\bar{f}}{\alpha_r} \tag{4.14}$$

A weighted average wind velocity, $\bar{v}_w$, is computed to include corrections for the effects of the scattering mechanism and the antenna patterns. This result is obtained from a linear interpolation of the measured weighted average Doppler shift, $\bar{f}_w$, (for uniform wind v_o) and the measured unweighted average Doppler shift

$$\bar{v}_w = \frac{\bar{f}}{\bar{f}_w} v_o \tag{4.15}$$

In these expressions, the wind speed is measured in meters per second and all angles are measured in degrees.

Chapter 5

DISCUSSION OF DATA

5.1 PIBAL Wind Data

Local wind conditions were influenced during the tests by a low pressure weather system centered off the coast of the state of Washington. About six hours before the onset (0100 April 21) of the experiment, a low pressure frontal system moved through the area with slight precipitation and some gusty winds. During the two 11-hour periods between 0800 and 1800 when pilot balloons (PIBALS) were launched, the measured cross-path winds were generally from the southeast. Steady southeasterly winds prevailed at nearly all altitudes on the first day of the experiment. The winds were moderate and progressively increased during the day reaching maximum velocities in mid-afternoon. In contrast, light variable winds persisted throughout the second day when wind speeds rarely exceeded two meters per second. Typical transverse winds on this day were less than one meter per second and on occasions wind direction changes were observed between SE and NW.

PIBAL readings were taken every 30 seconds at approximately 100-m height intervals. PIBAL data above the radio horizon were averaged over 400-m vertical segments for comparison with inferred results from radio Doppler measurements. Successive averages were taken throughout the vertical extent (1600 meters) of the common volume region. Average transverse wind velocities in the four vertical segments of the common volume are tabulated in Tables 5.1 and 5.2 for the PIBAL wind soundings

Table 5.1

PIBAL WIND-MEASUREMENT DATA ON 21 APRIL 1978*

PIBAL Release	Average Transverse Wind Velocity (m/s) 1st 400-m	2nd 400-m	3rd 400-m	4th 400-m
0805	1.93 SE	3.58 SE	5.69 SE	7.12 SE
0905	1.06 SE	3.37 SE	5.61 SE	6.85 SE
1005	1.16 SE	2.73 SE	5.19 SE	5.86 SE
1105	1.84 SE	1.96 SE	3.96 SE	5.12 SE
1205	4.10 SE	4.49 SE	1.68 SE	4.19 SE
1305	3.95 SE	4.18 SE	4.55 SE	4.02 SE
1405	3.21 SE	3.95 SE	4.81 SE	4.01 SE
1505	1.98 SE	1.08 SE	3.51 SE	4.51 SE
1605	3.52 SE	4.32 SE	4.74 SE	4.65 SE
1705	4.96 SE	4.65 SE	2.51 SE	3.55 SE
1805	3.15 SE	2.40 SE	2.92 SE	3.69 SE

Table 5.2

PIBAL WIND-MEASUREMENT DATA ON 22 APRIL 1978*

PIBAL Release	Average Transverse Wind Velocity (m/s) 1st 400-m	2nd 400-m	3rd 400-m	4th 400-m
0805	0.10 NW	0.92 NW	0.48 SE	2.82 SE
0905	0.12 NW	1.49 NW	0.14 SE	1.76 SE
1005	0.34 SE	0.09 SE	0.53 NW	0.98 SE
1105	0.54 NW	0.14 NW	1.00 NW	0.08 SE
1205	0.43 NW	0.78 SE	0.99 NW	1.13 NW
1305	0.09 SE	0.29 SE	2.17 NW	0.40 NW
1405	0.53 SE	1.88 SE	0.56 NW	2.25 NW
1505	1.45 SE	0.73 SE	1.07 NW	0.09 NW
1605	1.01 SE	0.72 SE	0.98 NW	0.52 NW
1705	0.45 SE	0.22 SE	0.70 NW	2.72 NW
1805	0.89 NW	0.18 NW	2.17 NW	1.02 NW

*Average transverse wind in 400-m vertical segments above radio horizon.

taken respectively on April 21 and 22. Examples of vertical profiles of the cross-path wind component observed on the two days are shown in Figure 5.1 [(a) thru (f)]. Data from the 0805 launch on April 21 (Figure 5.1a) reflected a fairly strong wind shear between the 1300 and 1600-meter elevations. Within this 300-meter vertical range, the wind changed from 0.8 m/s NW to 12 m/s SE. This shear dissipated by the next wind sounding one hour later. No other anomalous wind conditions were observed for the duration of the experiment.

5.2 Wind-Produced Doppler

The Doppler spectra presented in this section are computed from 600 contiguous sets of data samples representing 15 seconds of real-time data. Each data set is comprised of twelve amplitudes and twelve relative phases. Computations are made from the same data sets for a sequence of array pointing angles about the great-circle bearing. In order to simultaneously measure upwind and downwind Doppler shifts, spectral observation windows are centered about the zero-Doppler frequency. Observation windows used in the spectrum analysis are narrower than the system noise bandwidth (23 Hz) but are broad enough to encompass the ambient wind-produced Doppler shifts. For the wind conditions experienced during the tests, an 8 to 10-Hz wide observation window was found to be sufficient to completely envelop the wind-produced Doppler spectrum. Outside the selected observation windows, the Doppler spectra have relatively low power spectral densities. Each computed spectrum contains 100 Doppler frequencies spaced from about 0.08 to 0.10 Hz apart depending upon the width of the spectral observation window. The spectral resolution

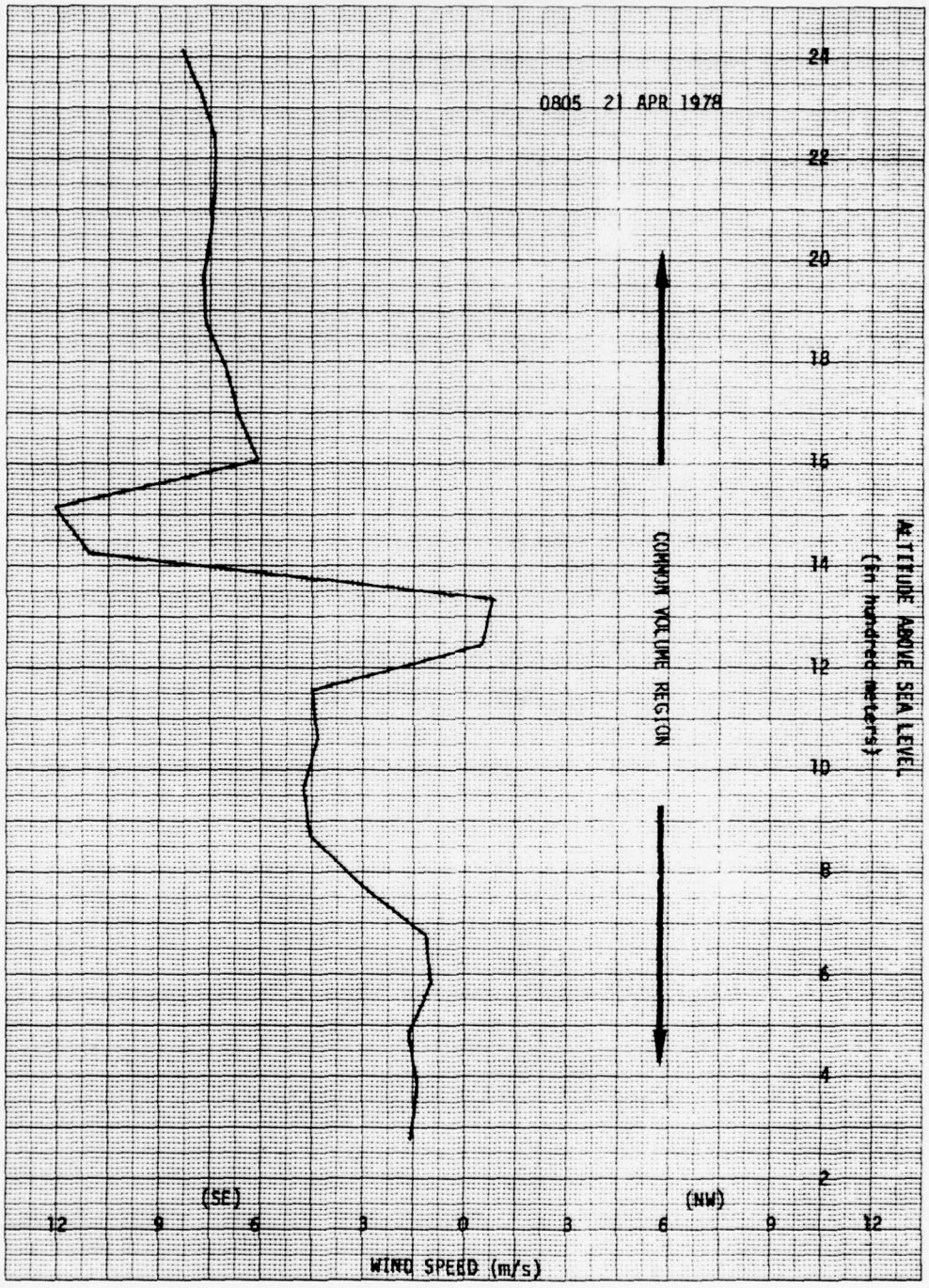

(a)

Fig. 5.1. VERTICAL PROFILE OF CROSS-PATH WIND VELOCITY

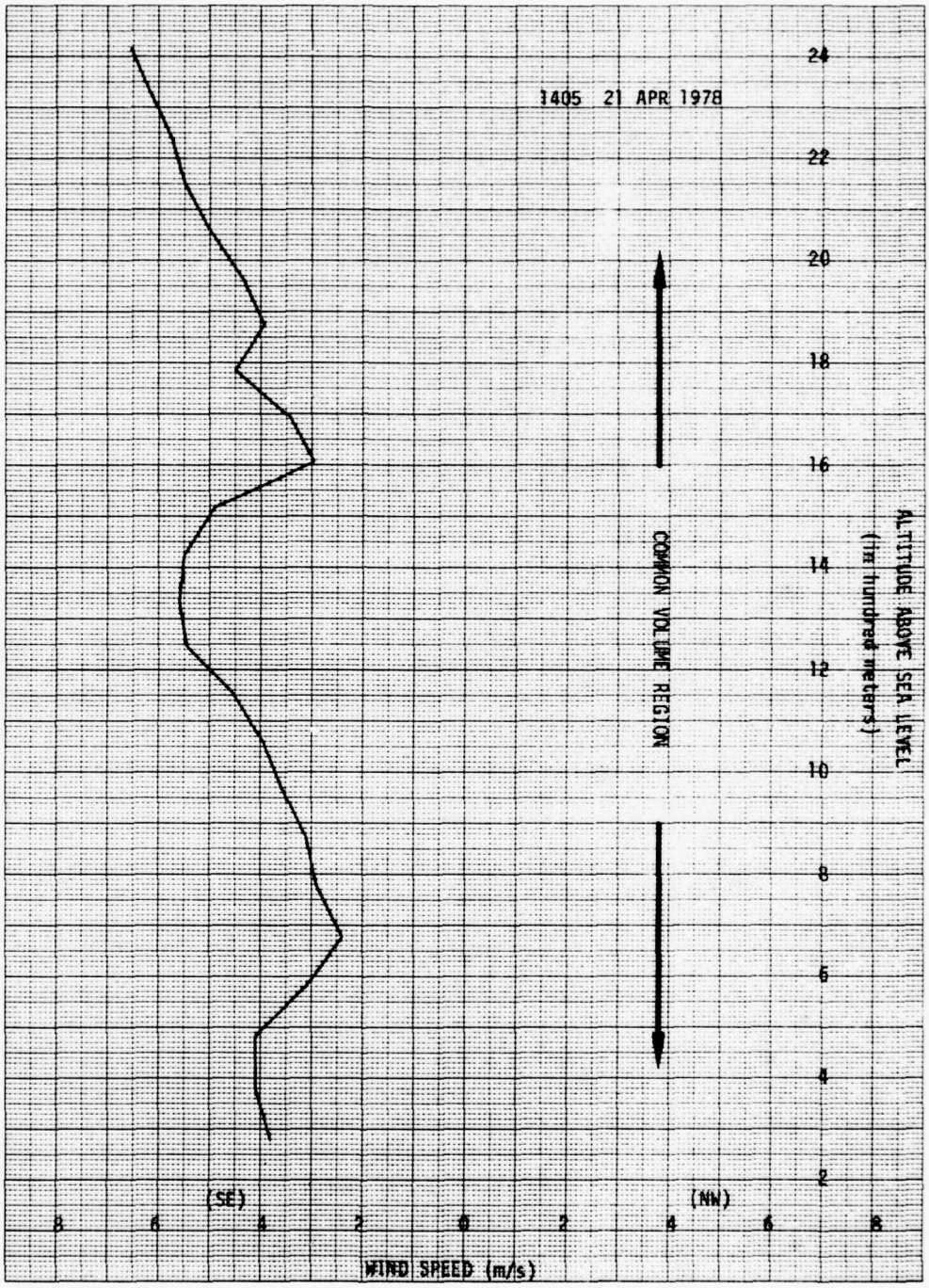

(b)

Fig. 5.1. CONTINUED.

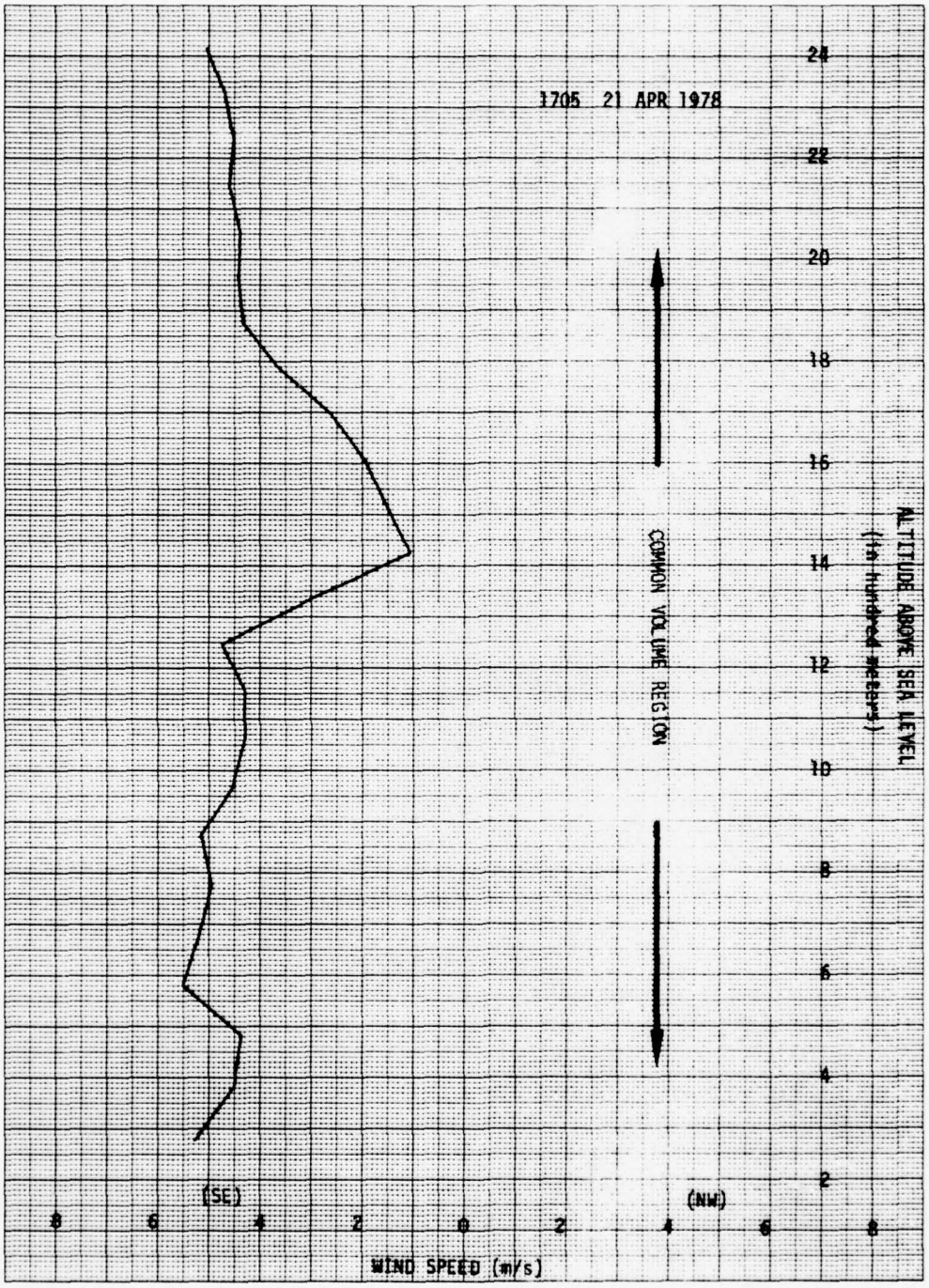

(c)

Fig. 5.1. CONTINUED.

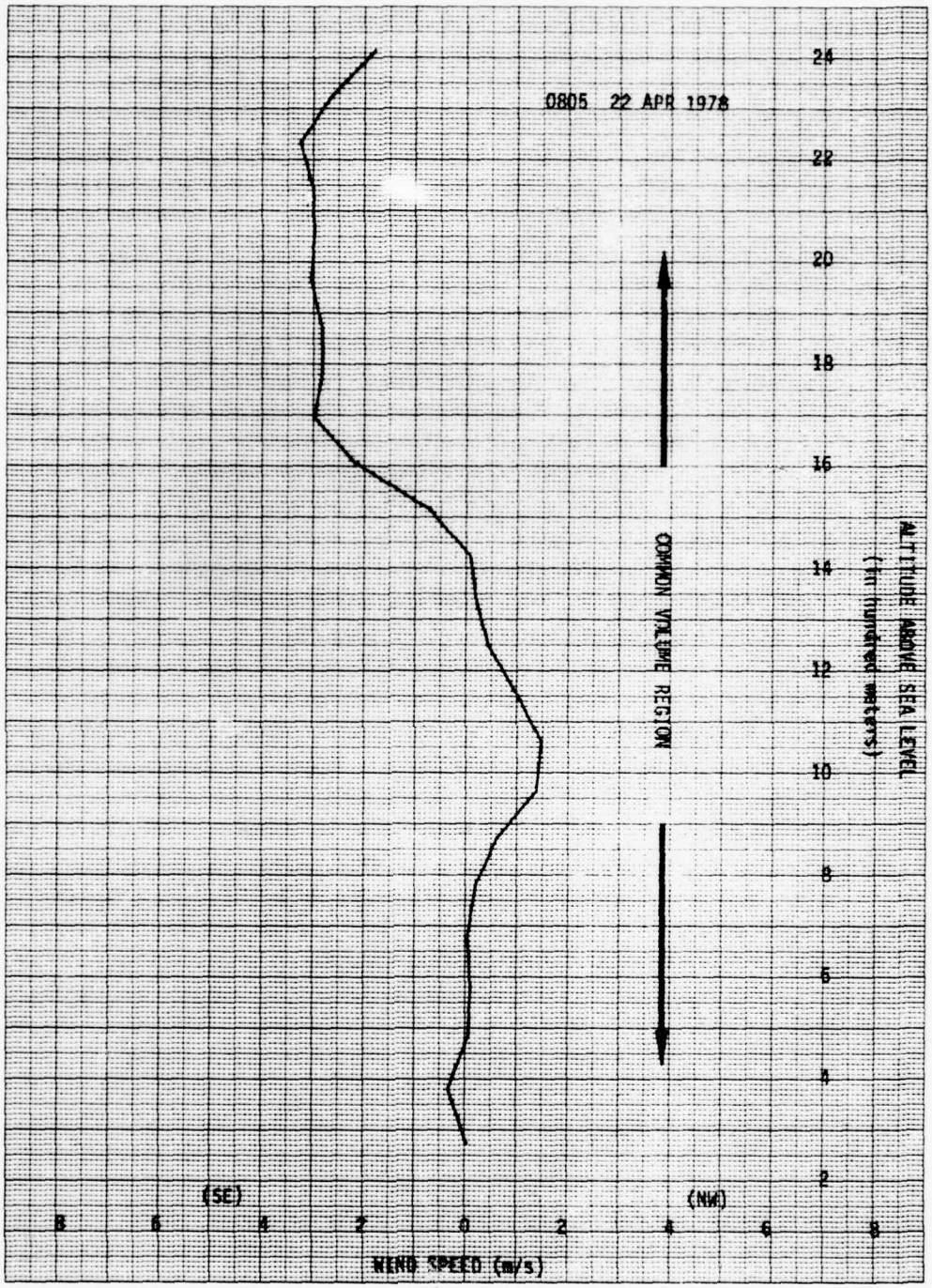

(d)

Fig. 5.1. CONTINUED.

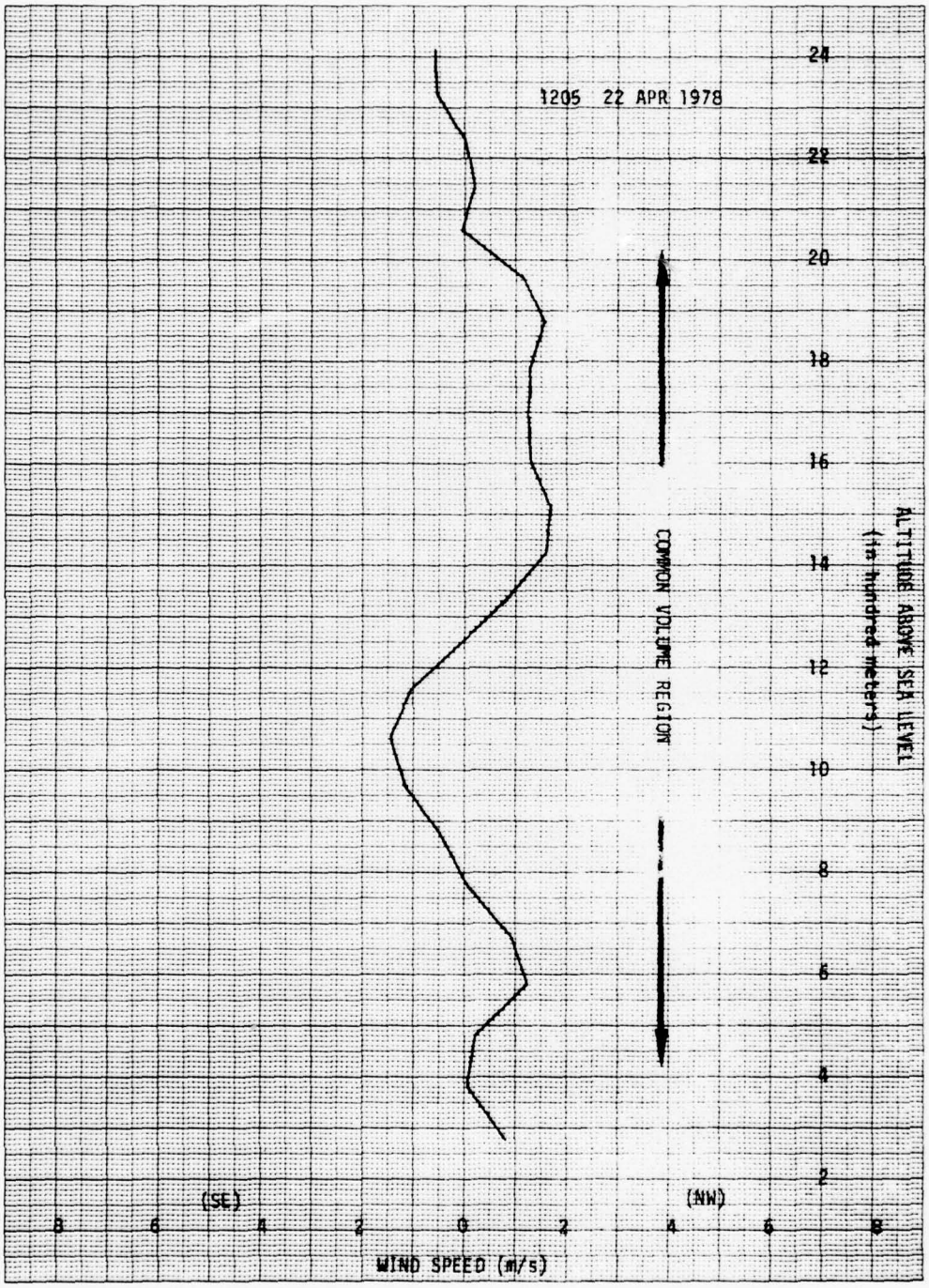

(e)

Fig. 5.1. CONTINUED.

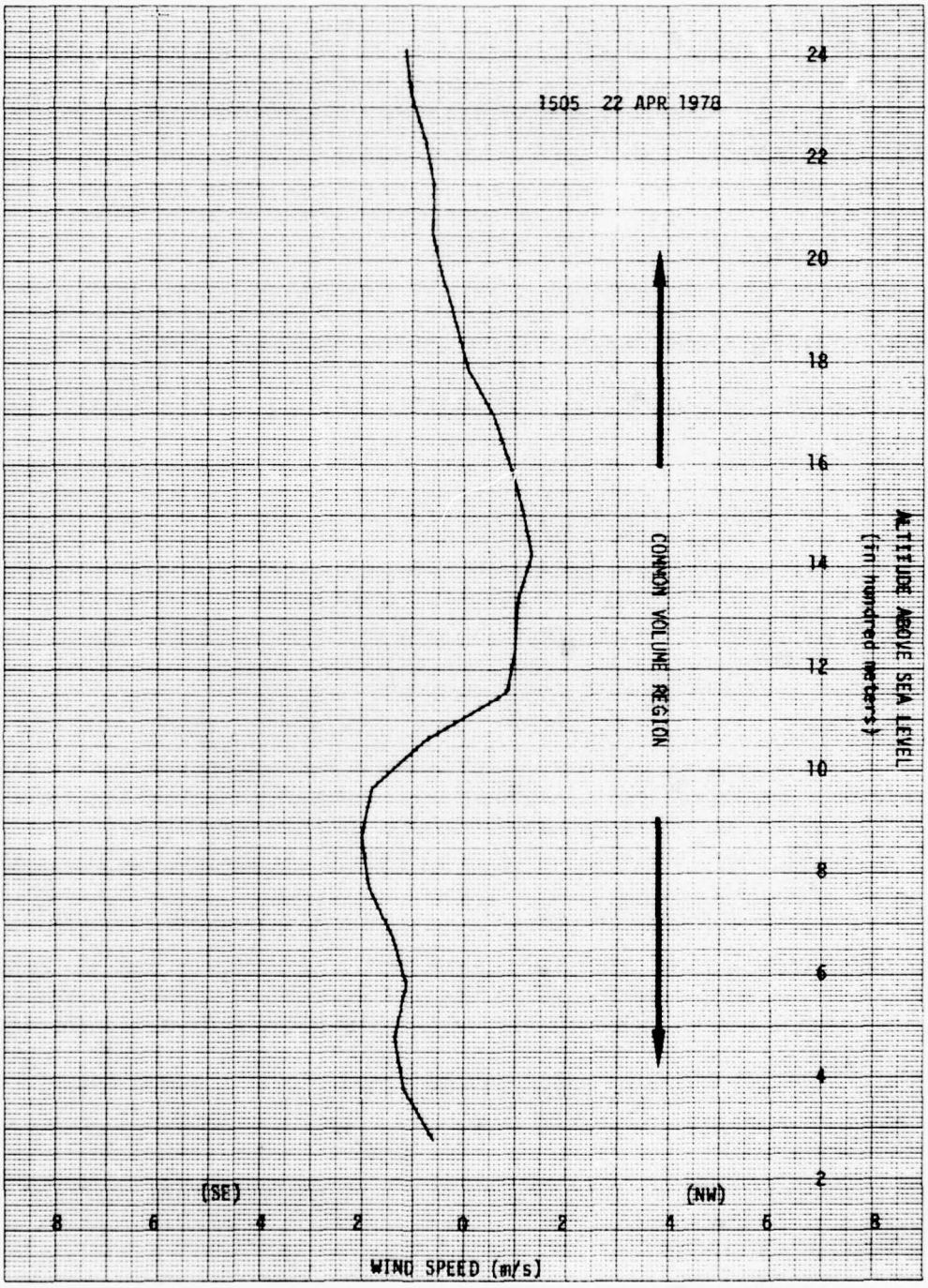

(f)

Fig. 5.1. CONTINUED.

attainable in the coherent integration process of the 600 data samples is 0.07 Hz. However, the realizable resolution is more on the order of 0.1 Hz due to the short-term instabilities (1.5 parts in 10^{11}) of the quartz oscillators.

5.2.1 Unweighted Angular Spectra

Examples of some unweighted Doppler spectra are shown in Figure 5.2 [(a) thru (1)]. These spectra are taken for symmetrical (NW/SE) beam pointing directions about the great-circle bearing at 0° azimuth. The spectra are plotted over a 40-dB range in 0.25° increments out to one degree either side of the great-circle bearing. Two 15-second samples taken one minute apart are presented for each hourly example in order to show temporal variations in the wind-produced Doppler shifts.

Initial observations of the high-resolution spectra show the presence of a coherent stationary source with a very narrow spectral width at zero-Doppler frequency. This spectral component is most likely a result of knife-edge diffraction over one or more of the mountain ridges between the transmitter and receiver. It is seen that the diffracted component increases in intensity as the array scan approaches the great-circle. Occasionally, when the array beam is pointed on-axis, the level of the diffracted component exceeds the 40-dB plotting range and a linear foldover (overshoot) occurs. Aside from its intensity level, the diffraction component is totally invariant to the azimuthal pointing direction of the array.

In contrast, the wind-produced Doppler shifts show systematic variations with the array pointing direction. A qualitative analysis of the

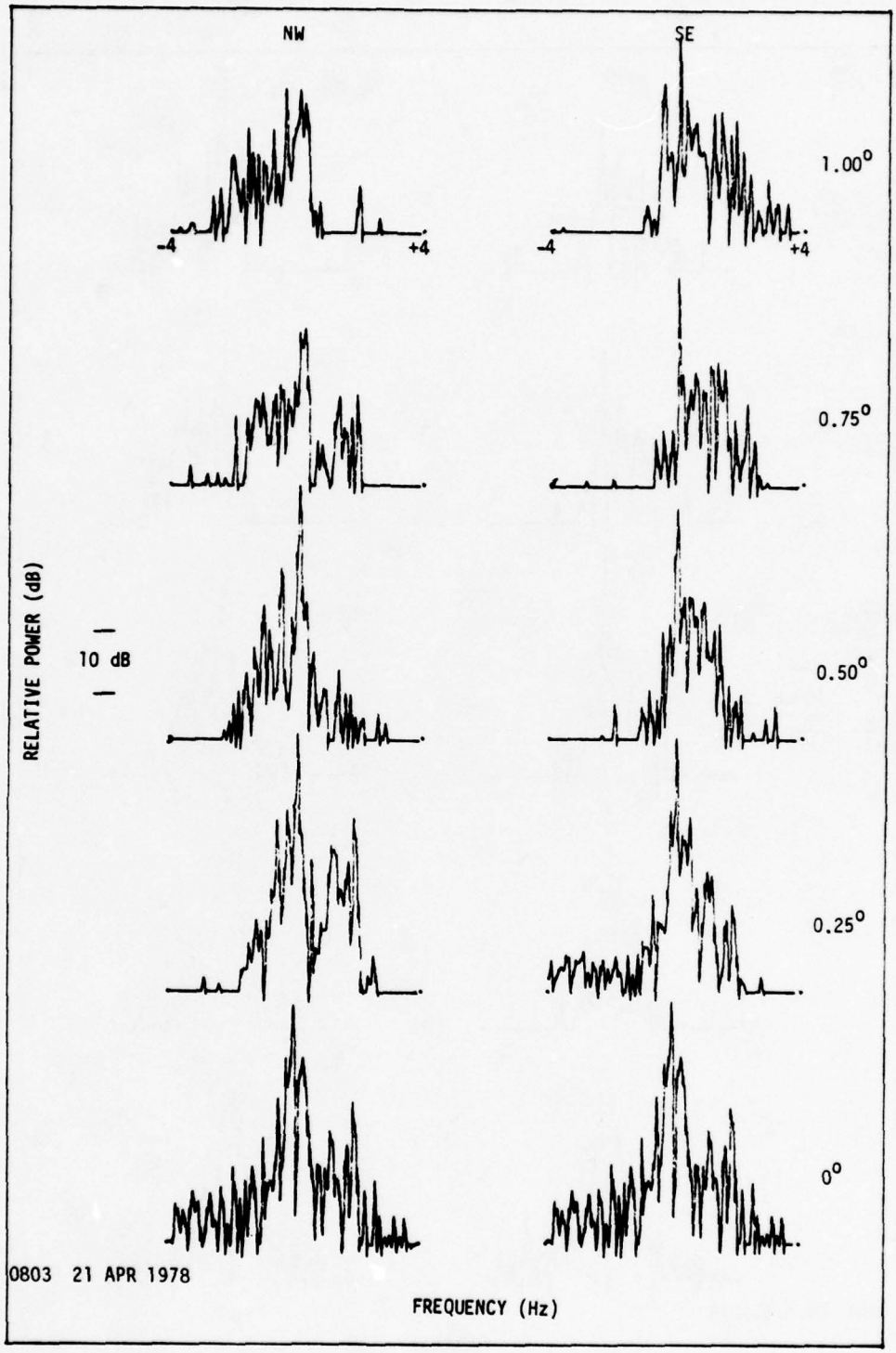

(a)

Fig. 5.2. UNWEIGHTED WIND-PRODUCED DOPPLER SPECTRA. Angle-of-arrival spectra are computed from the coherent integration of 600 (15-sec) data samples.

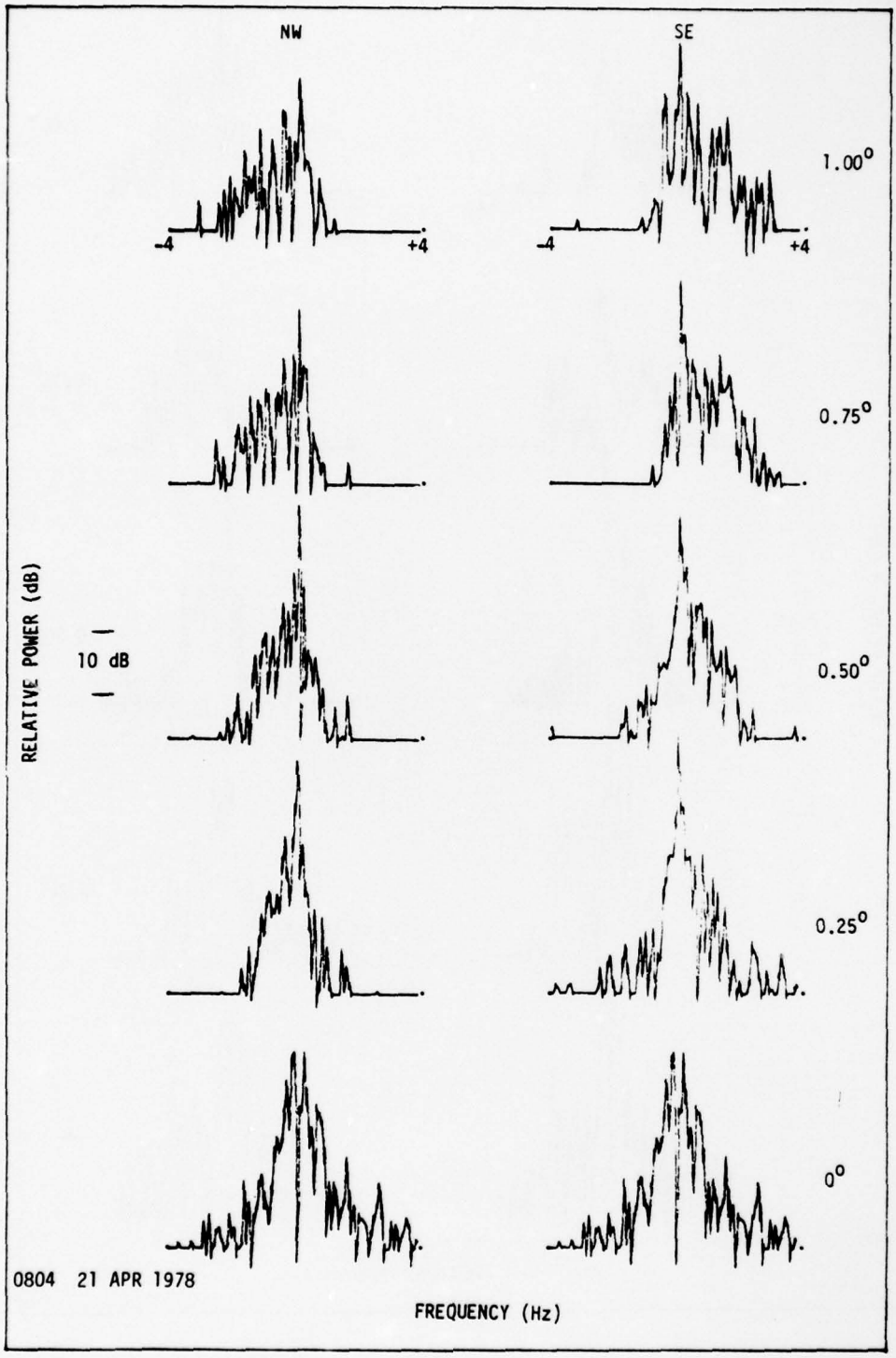

(b)

Fig. 5.2. CONTINUED.

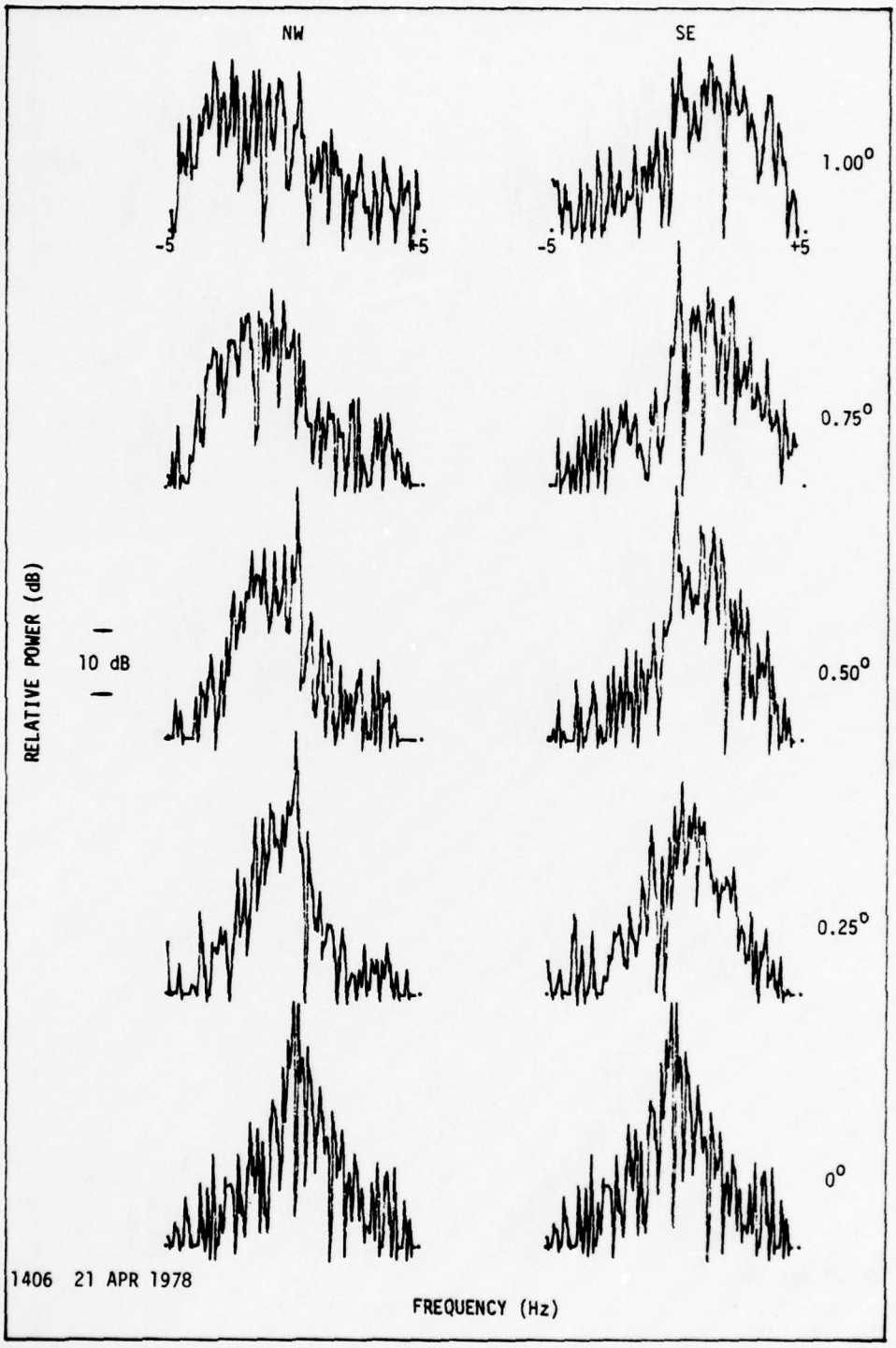

(c)

Fig. 5.2. CONTINUED.

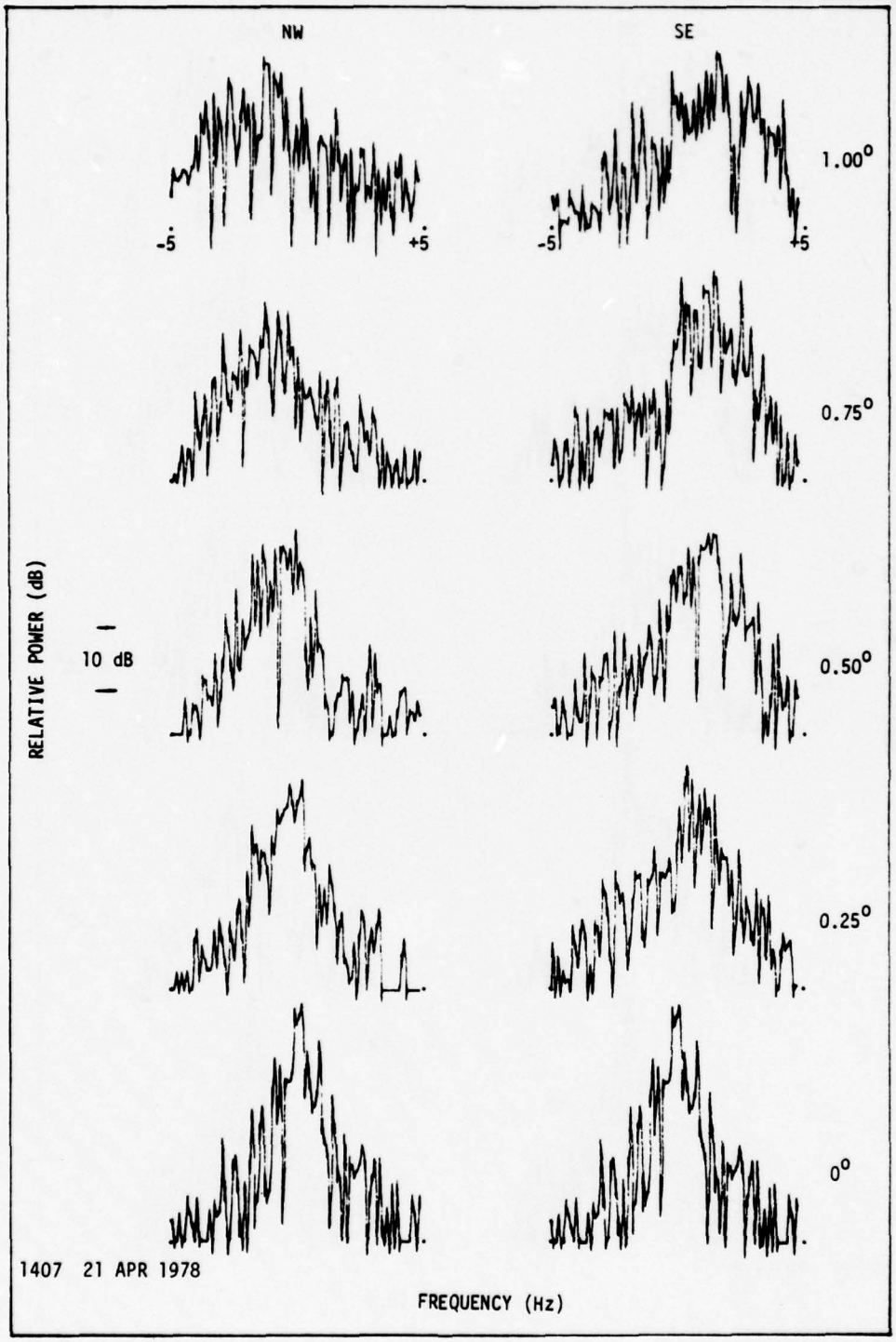

(d)

Fig. 5.2. CONTINUED.

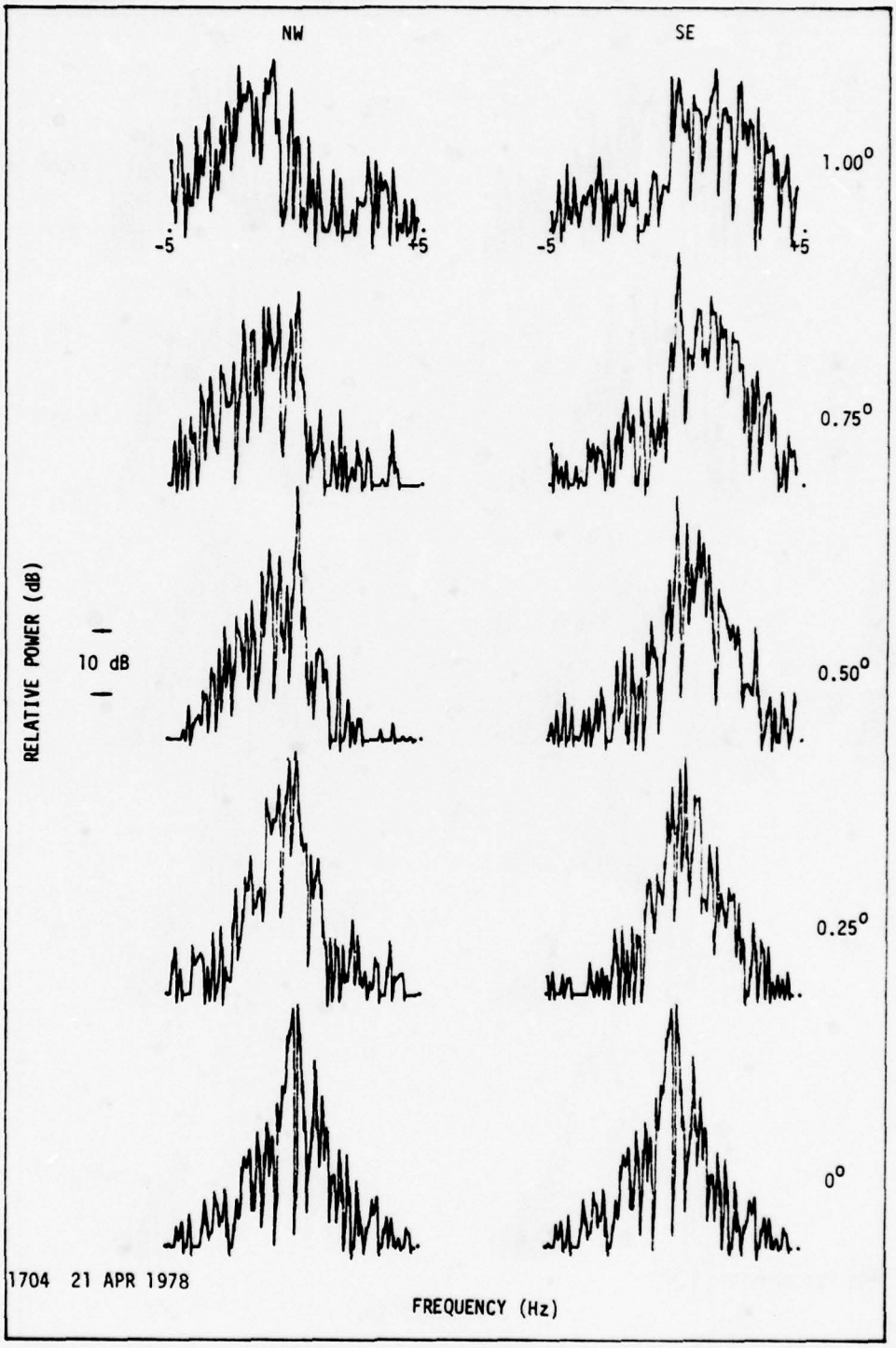

(e)

Fig. 5.2. CONTINUED.

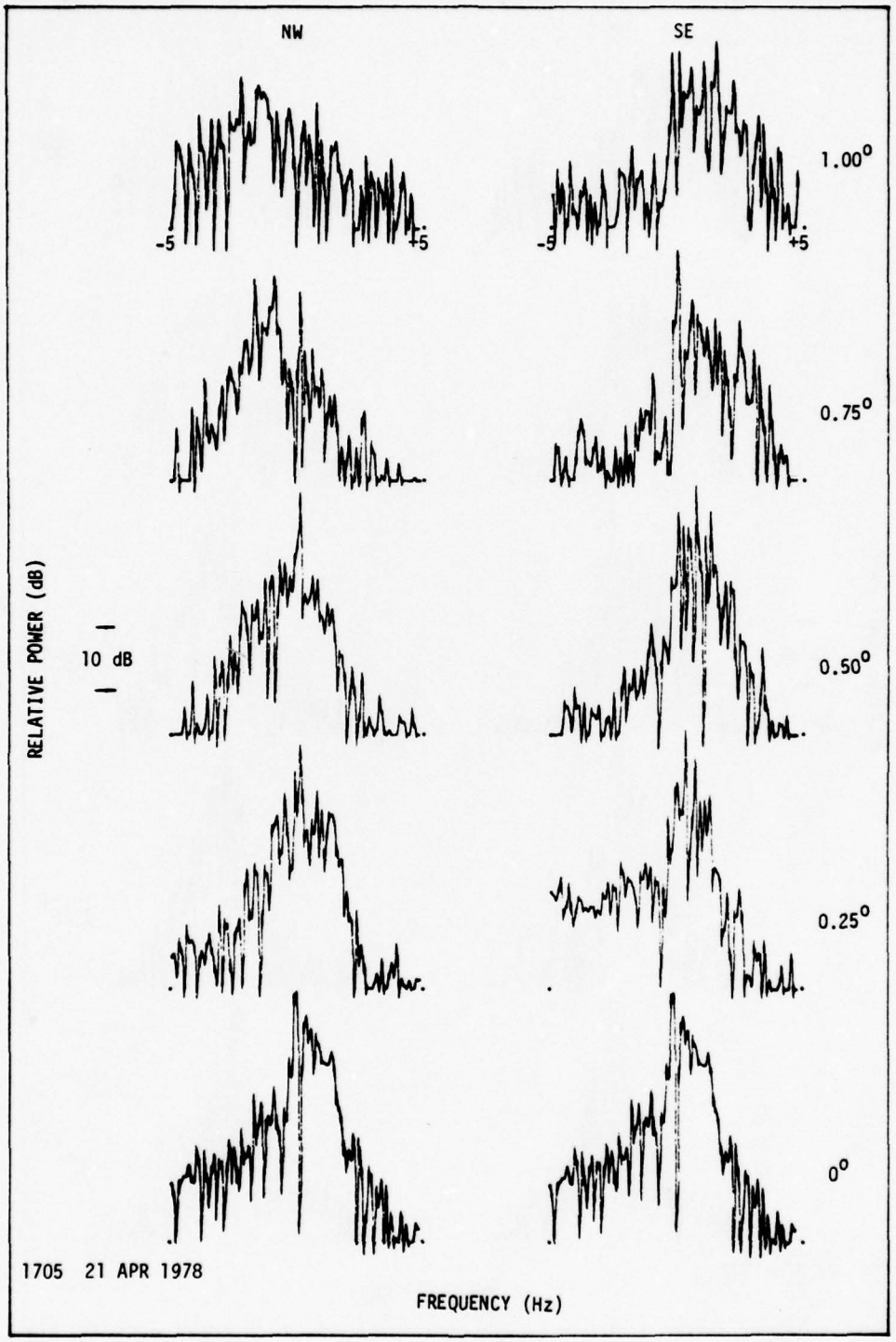

(f)

Fig. 5.2. CONTINUED.

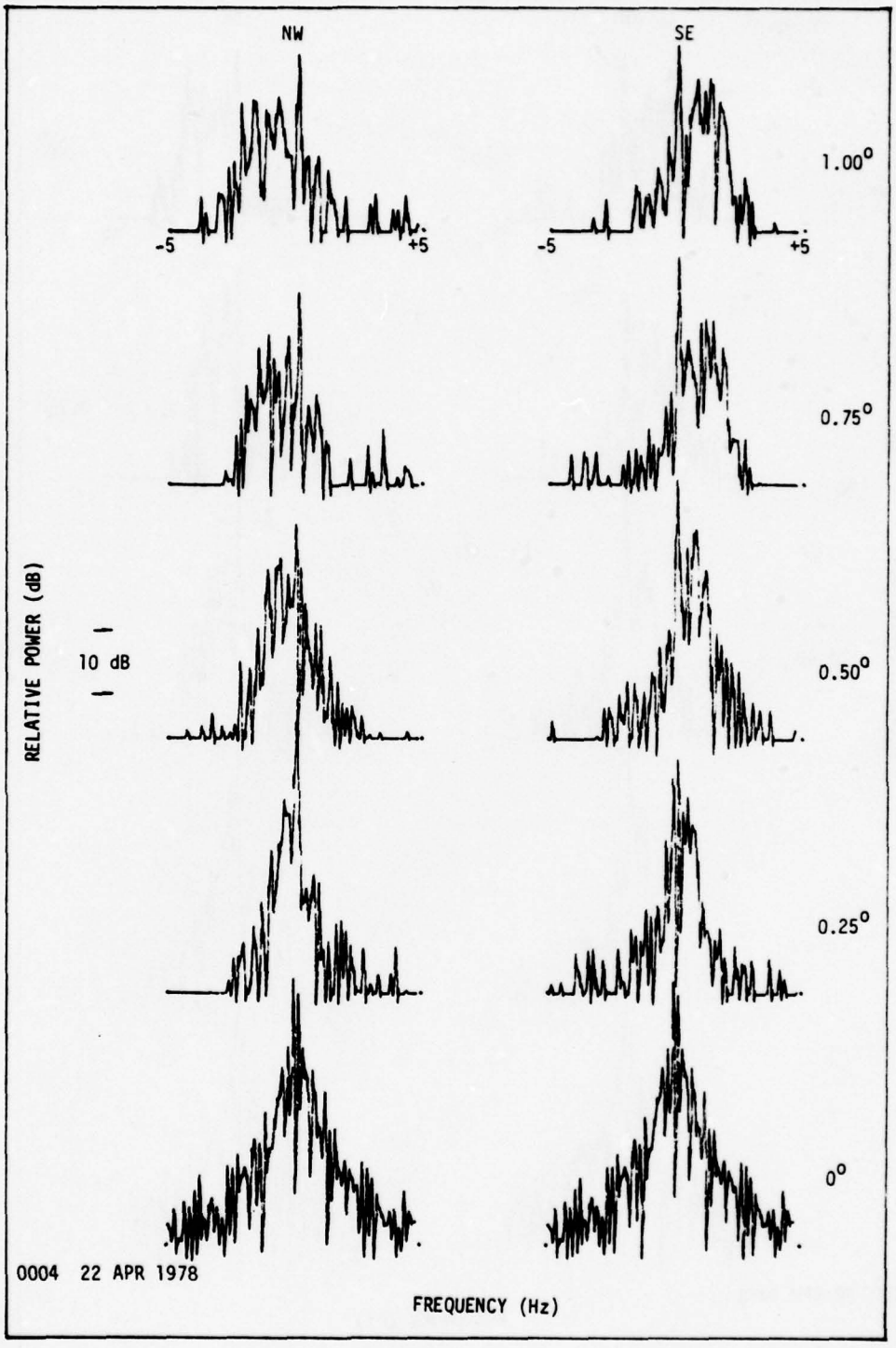

(g)

Fig. 5.2. CONTINUED.

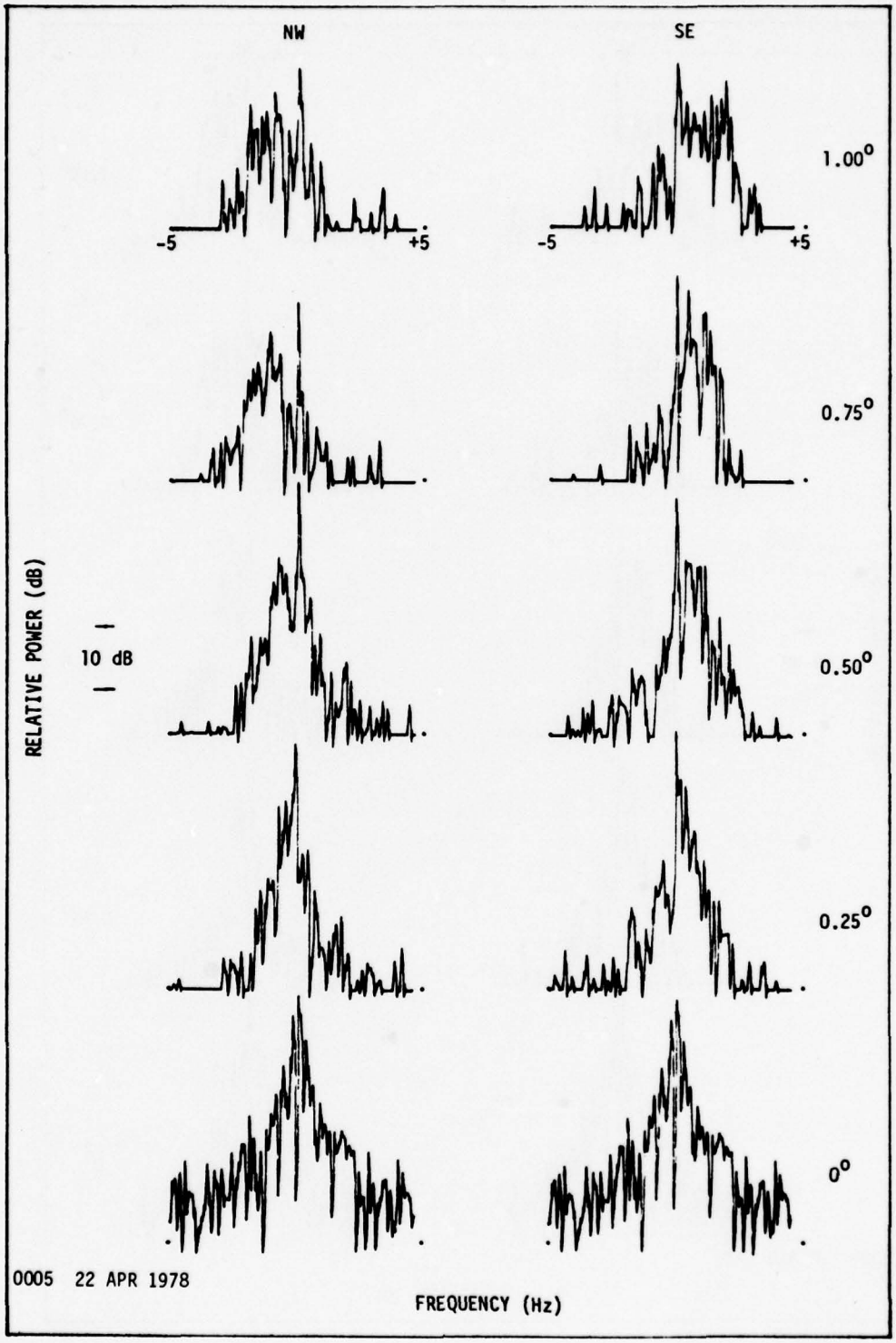

(h)

Fig. 5.2. CONTINUED.

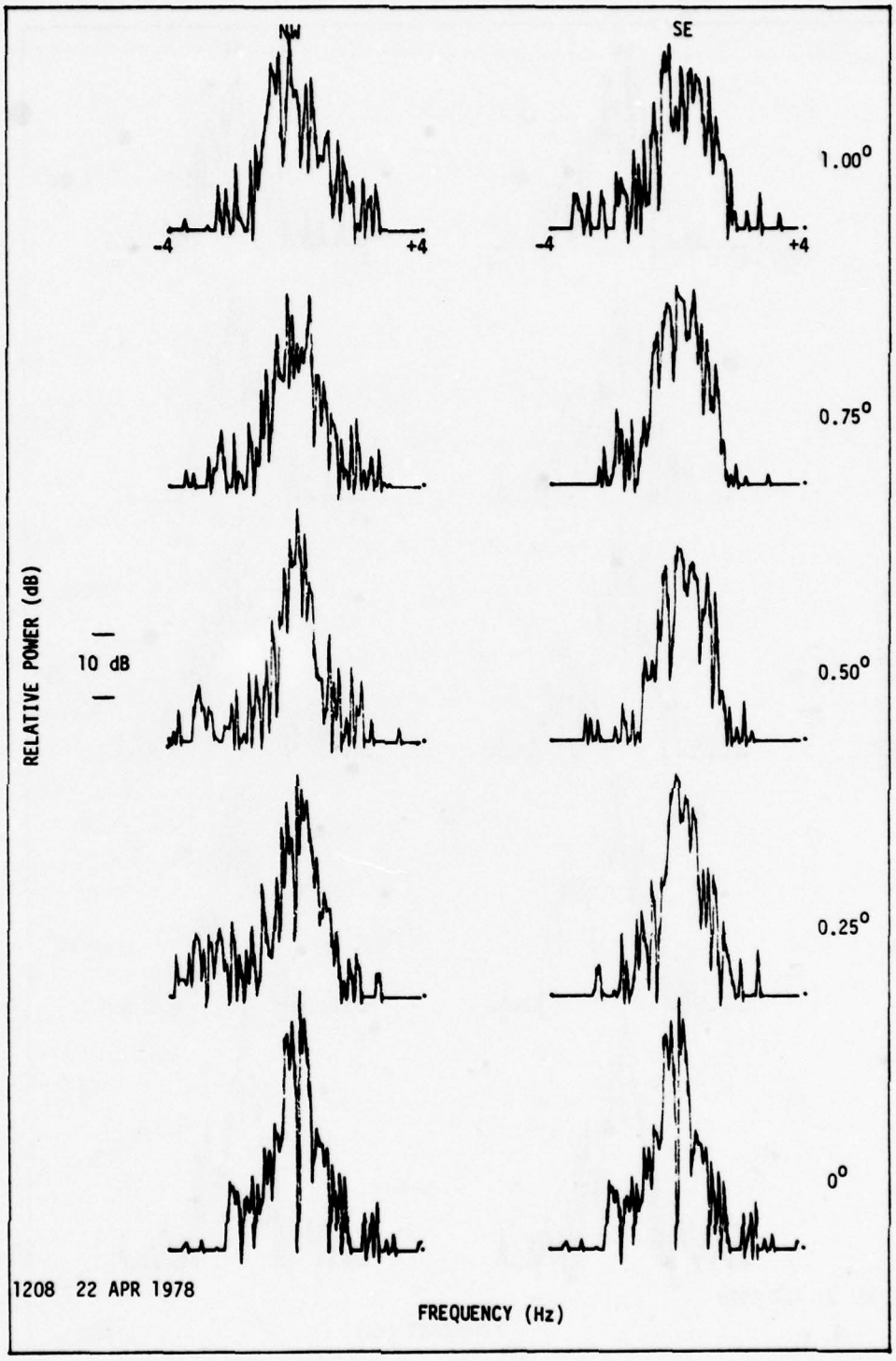

(i)

Fig. 5.2. CONTINUED.

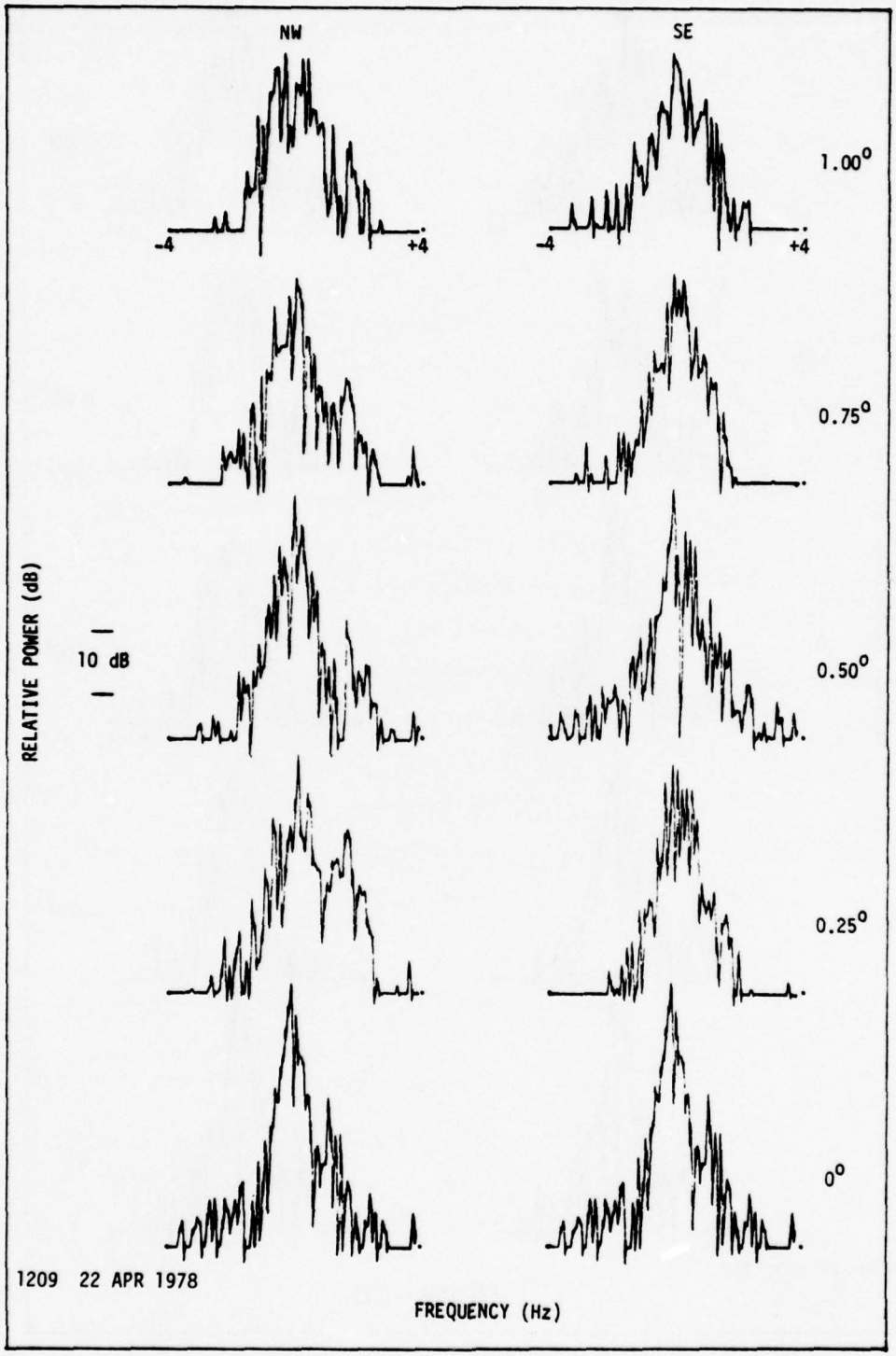

(j)

Fig. 5.2. CONTINUED.

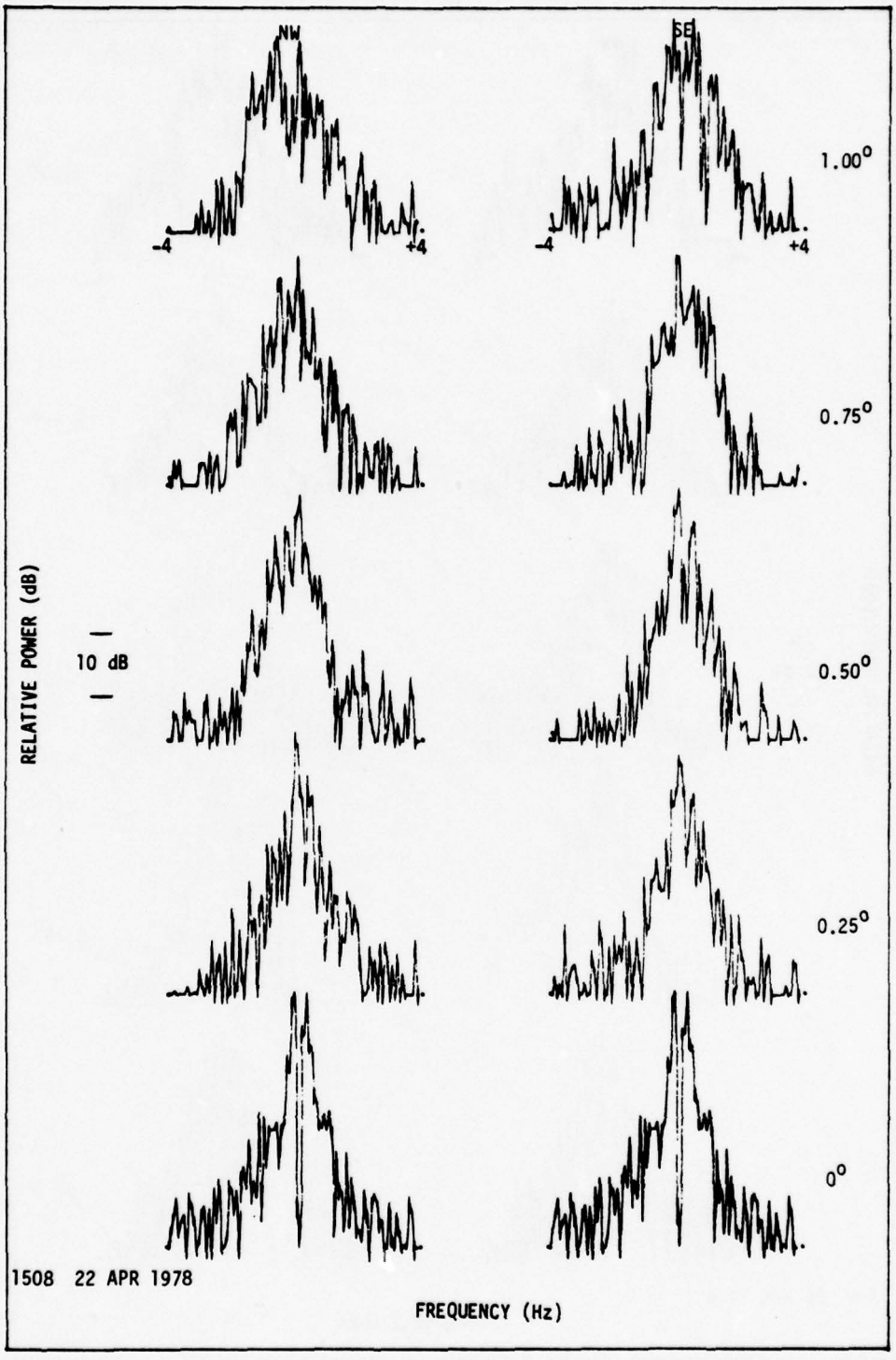

(k)

Fig. 5.2. CONTINUED.

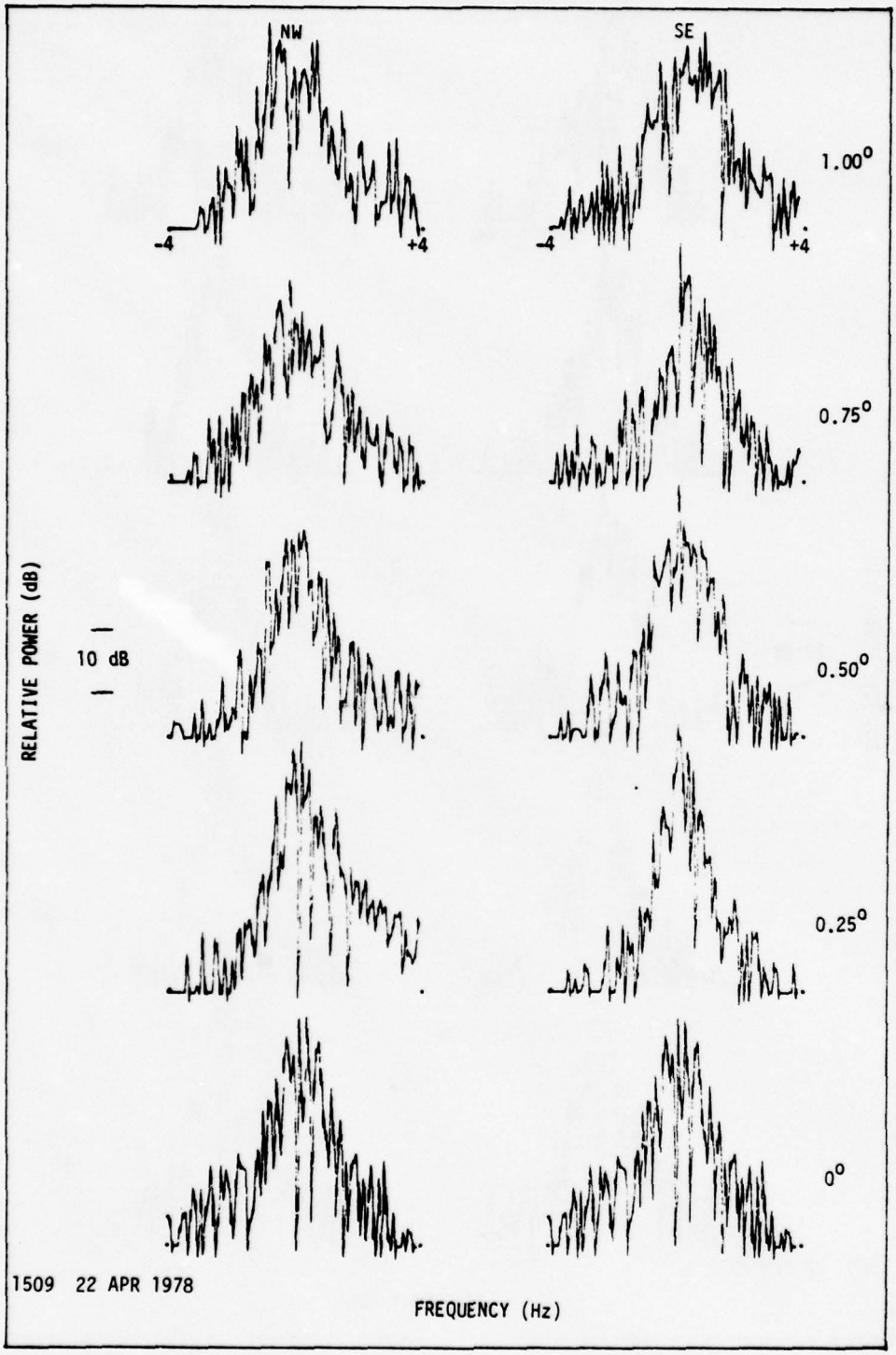

(1)

Fig. 5.2. CONTINUED.

wind-produced spectra shows progressive increases in the average Doppler shift as the array is pointed off-axis. For the examples shown in Figure 5.2, SE winds are apparent at all angles. Doppler shifts are generally positive for array pointing angles in the SE (upwind) direction and negative for angles in the NW (downwind) direction. At most off-axis angles, the upwind and downwind Doppler spectra are nearly antisymmetric about the zero-Doppler frequency which suggests some degree of spatial uniformity in the transverse winds. On-axis the Doppler spectra are generally symmetrical about zero Doppler. Any asymmetries appearing in the spectra when the array beam is aligned along the great-circle can either be attributed to a vertical wind component or to spatial non-uniformities in the transverse wind. Birkemeier et al (1977) point out that such spectral asymmetries also result from the misalignment of the transmitting and receiving antennas. Misalignment errors, however, are eliminated when using a phased-array.

Although no quantitative analysis is presented, other observations from Figure 5.2 reveal definite spectral broadening during afternoon periods when the atmosphere is fairly well mixed. This is a logical consequence of diffuse (turbulent) scattering processes which produce wide variations in the signal's angle-of-arrival. On the other hand, in the morning hours, the atmosphere is relatively stable and is more likely to be partially stratified. In such situations, a quasi-coherent signal is received that arrives via a number of specular reflection points distributed over a small angular region near the great-circle

bearing. As a result of the narrow range of angles-of-arrival, the signal spectra are not nearly as broad as the spectra produced by signals propagating through a turbulent atmosphere. The spectra are also seen to be somewhat broader on the first day [Figure 5.2 (a) thru (f)] of the experiment than on the second day [Figure 5.2 (g) thru (l)]. This variance appears directly attributable to the contrasting wind conditions on the two days.

The short-term variability of the wind can be observed from temporal changes in the Doppler spectra. Of particular importance in this regard are the temporal changes in the average Doppler shift as a function of the array pointing angle. Figure 5.3 [(a) thru (f)] shows the measured average Doppler shifts for the spectra given in Figure 5.2. Average Doppler shifts are computed in accordance with equation 4.12 for 21 equally-spaced (0.15°) pointing angles between 1.5° NW and 1.5° SE. The slopes of these curves are directly proportional to the prevailing wind speeds. Averages taken one minute apart are shown on the same plot for comparative analysis of short-term variations. The 15-second samples are generally in close agreement from one minute to the next. This suggests reasonably good correlation of wind conditions within one minute intervals. As evidenced by the near linearity of the Doppler shift curves, there is some apparent uniformity in the wind structure over the spatial regions probed. Occasionally, however, there are noticeable departures from this linear trend that may be attributable to variable wind conditions. For example, in Figure 5.3a at 0803 on 21 April a definite change in the polarity of the average Doppler shift is

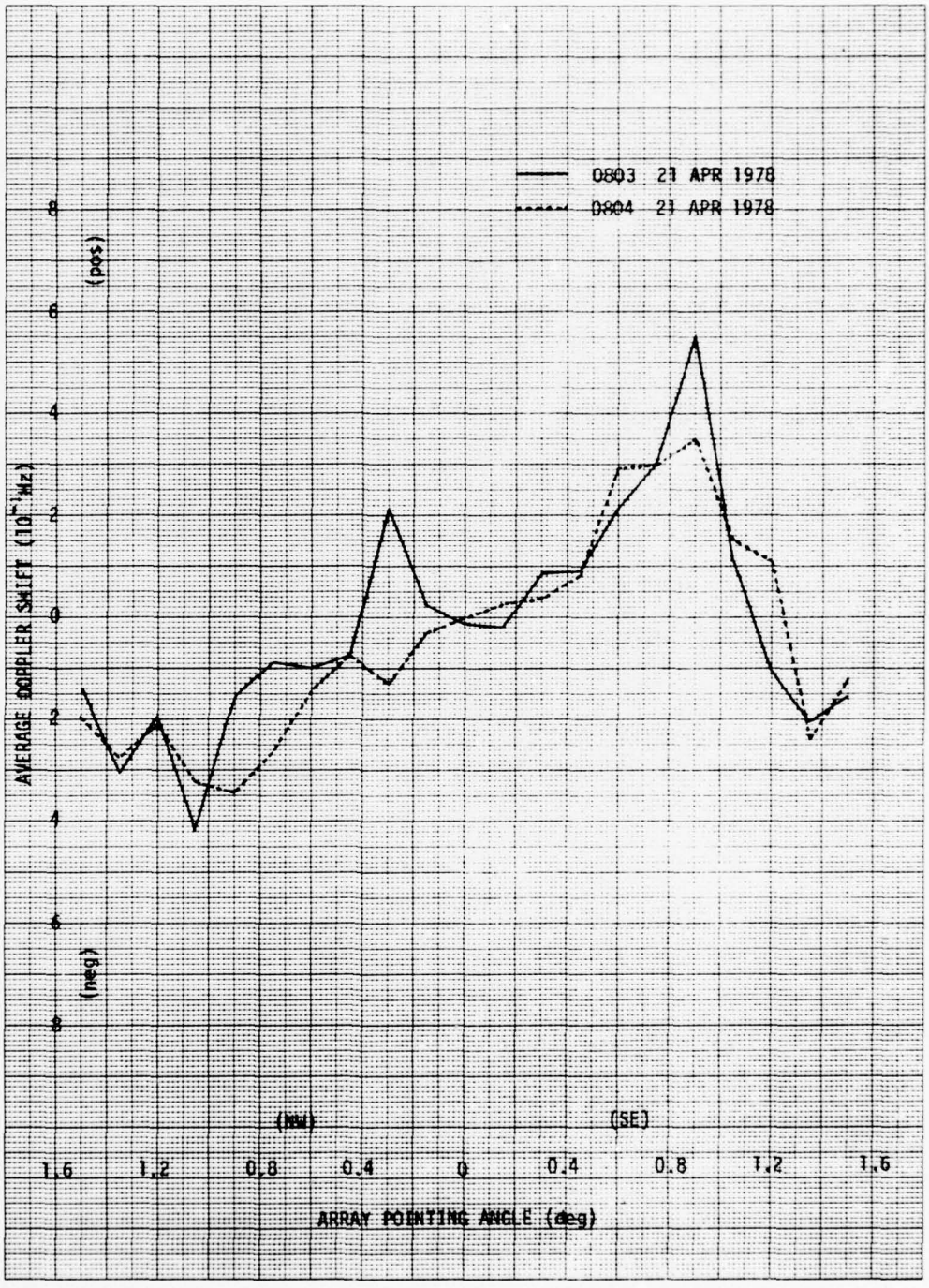

(a)

Fig. 5.3. MEASURED UNWEIGHTED AVERAGE DOPPLER SHIFT VS ARRAY POINTING ANGLE.

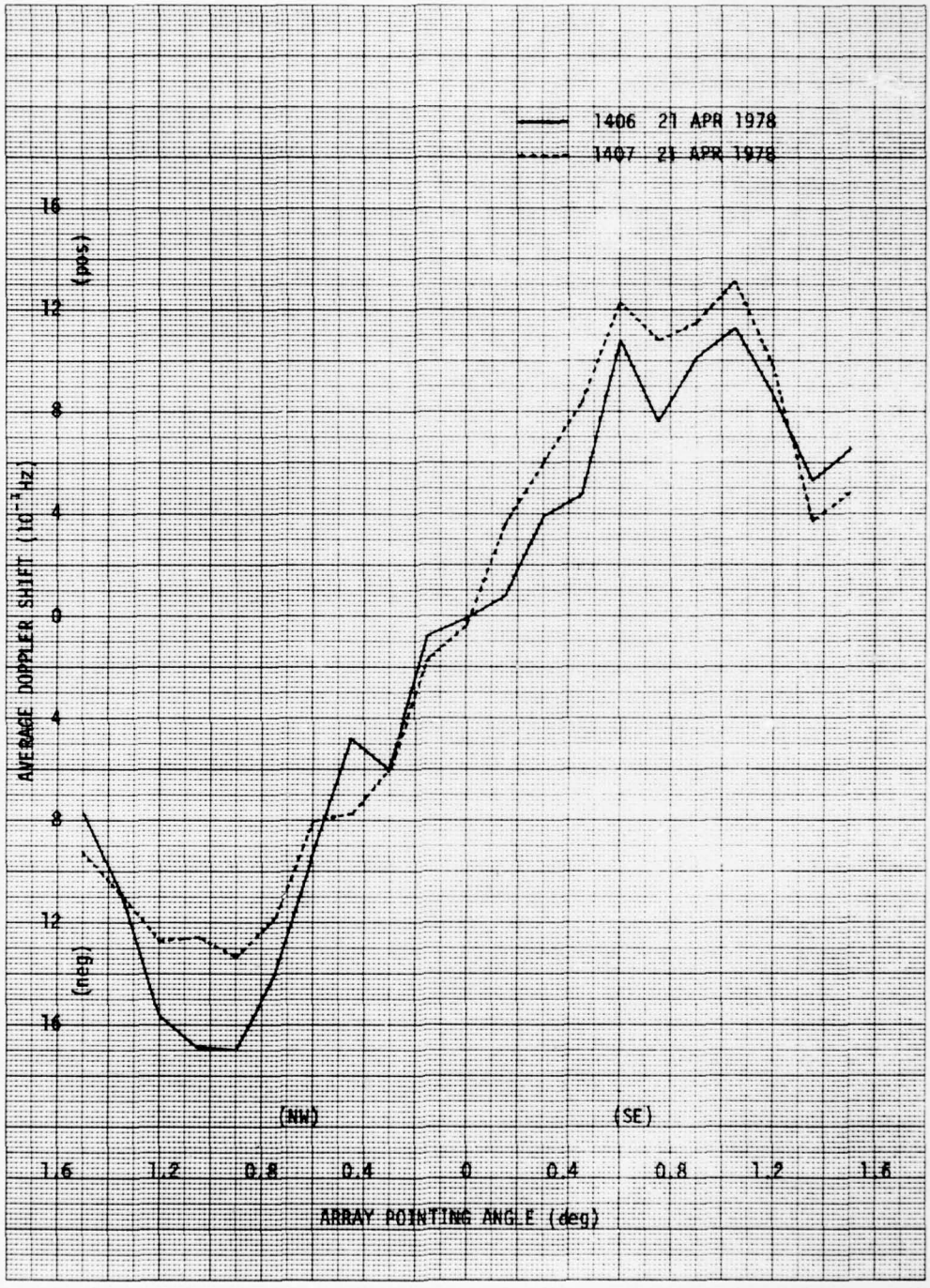

(b)

Fig. 5.3. CONTINUED.

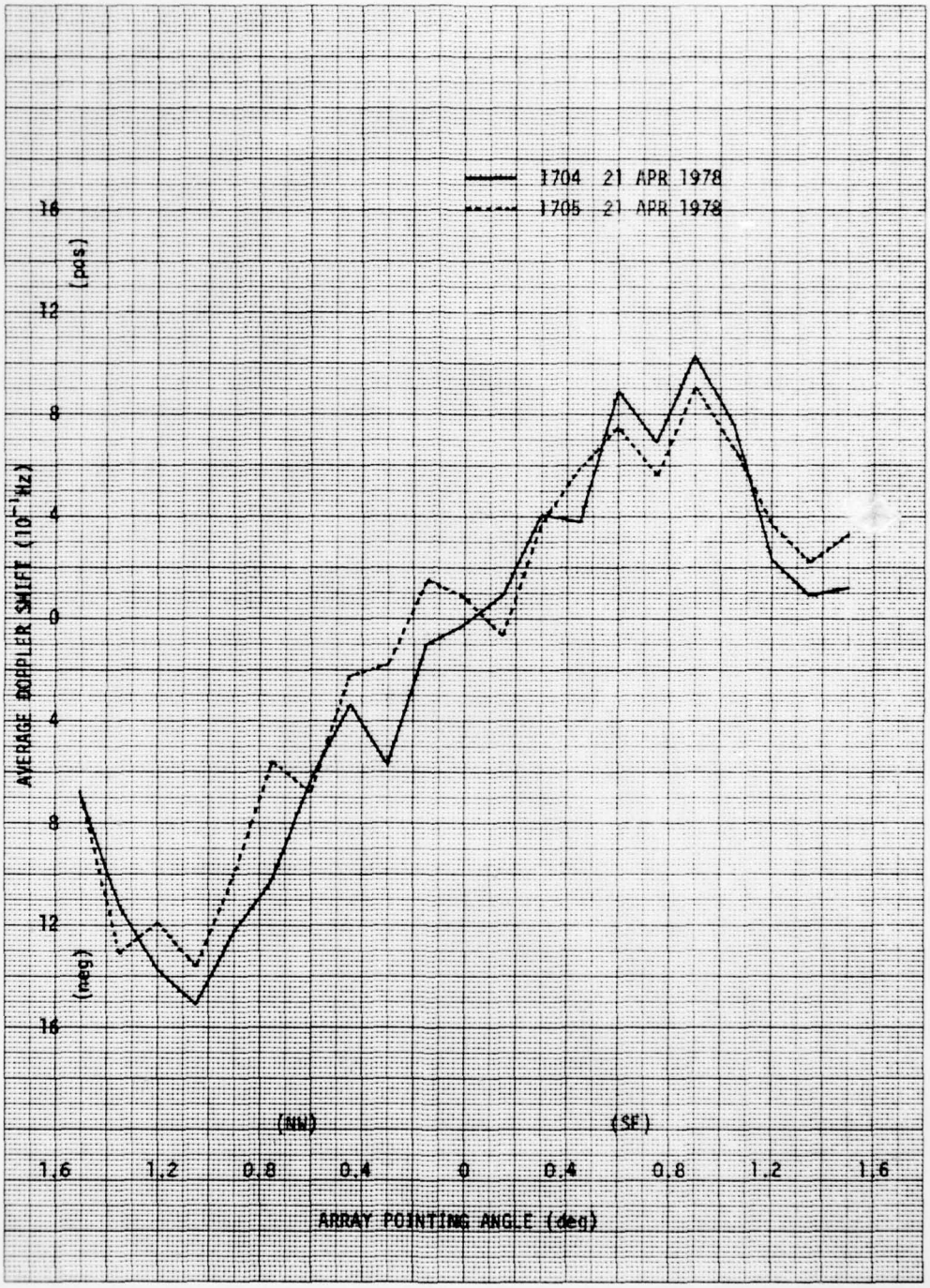

(c)

Fig. 5.3. CONTINUED.

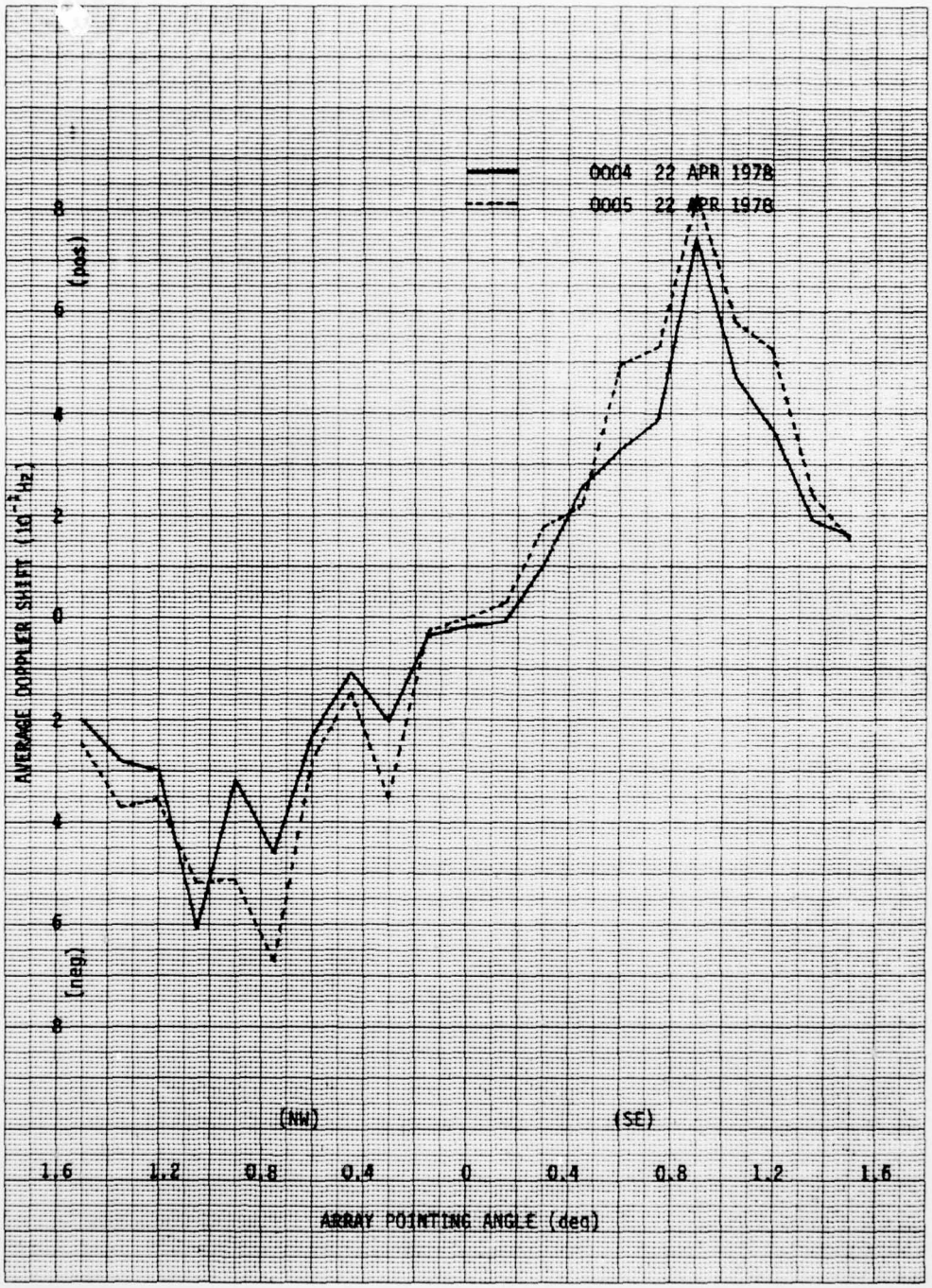

(d)

Fig. 5.3. CONTINUED.

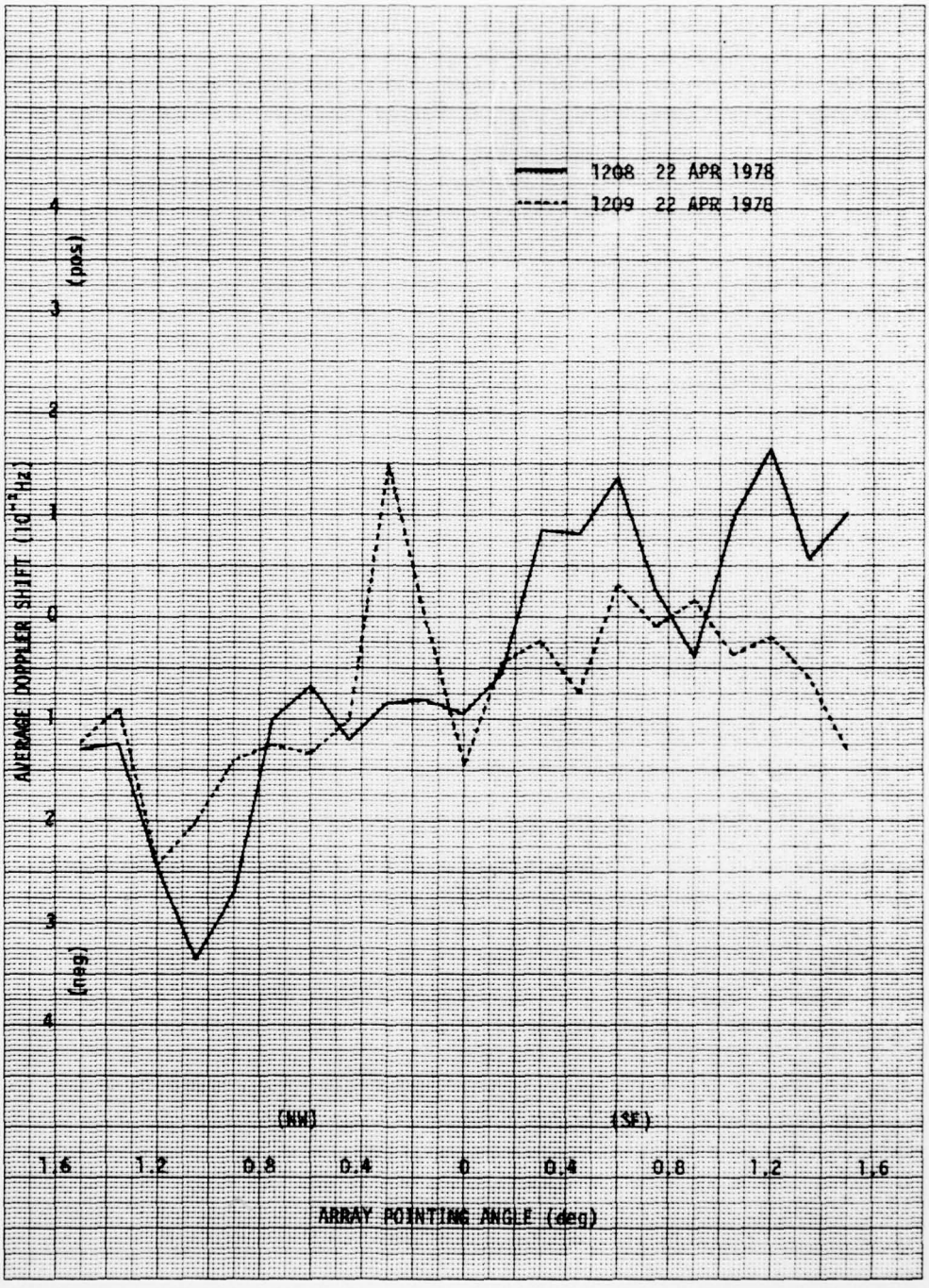

(e)

Fig. 5.3. CONTINUED.

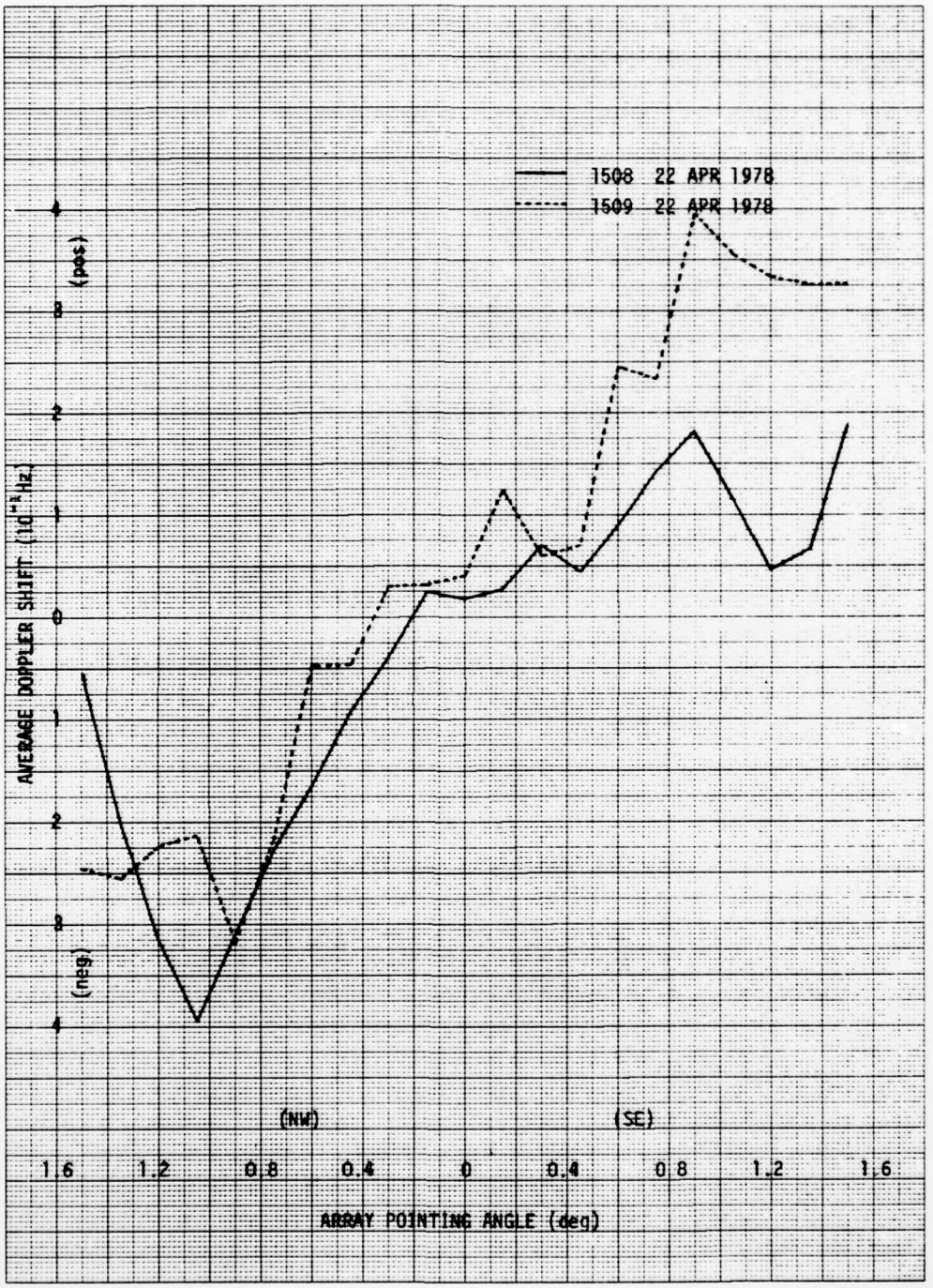

(f)

Fig. 5.3. CONTINUED.

observed when the array is pointed in the vicinity of 0.3° NW. An off-axis polarity change such as this is reflective of a corresponding wind direction change. Supporting this are the wind-shear conditions reflected in the PIBAL measurement data (Figure 5.1a) at the same hour. There are nonlinearities in the average Doppler shift curves that are not necessarily associated with the wind. These nonlinearities occur near the extremities of the array sector scan and are most likely due to the combined off-axis effects of atmospheric scattering and secondary grating lobes. Effects of the scattering mechanism can be taken into account by weighting the Doppler spectra in accordance with an appropriate atmospheric scattering model. The data results from this effort are discussed in the following section.

5.2.2 Weighted Angular Spectra

The Doppler spectra presented in the previous section are essentially unweighted in that the spectral components are derived from data samples that are uniformly weighted over the angular range scanned by the array. Here we take into account the apparent source direction of each spectral component and the angular scattering properties of the atmosphere. Weighting factors based on angle-of-arrival scattering variations are then applied to the individual spectral components in accordance with procedures outlined in section 4.2.

Figure 5.4 [(a) thru (l)] shows the results of applying a normalized Tatarski scattering model to the unweighted spectral data in Figure 5.2. These spectra are obtained for an assumed uniform wind and a turbulent scattering region situated at an elevation angle of 0.25°.

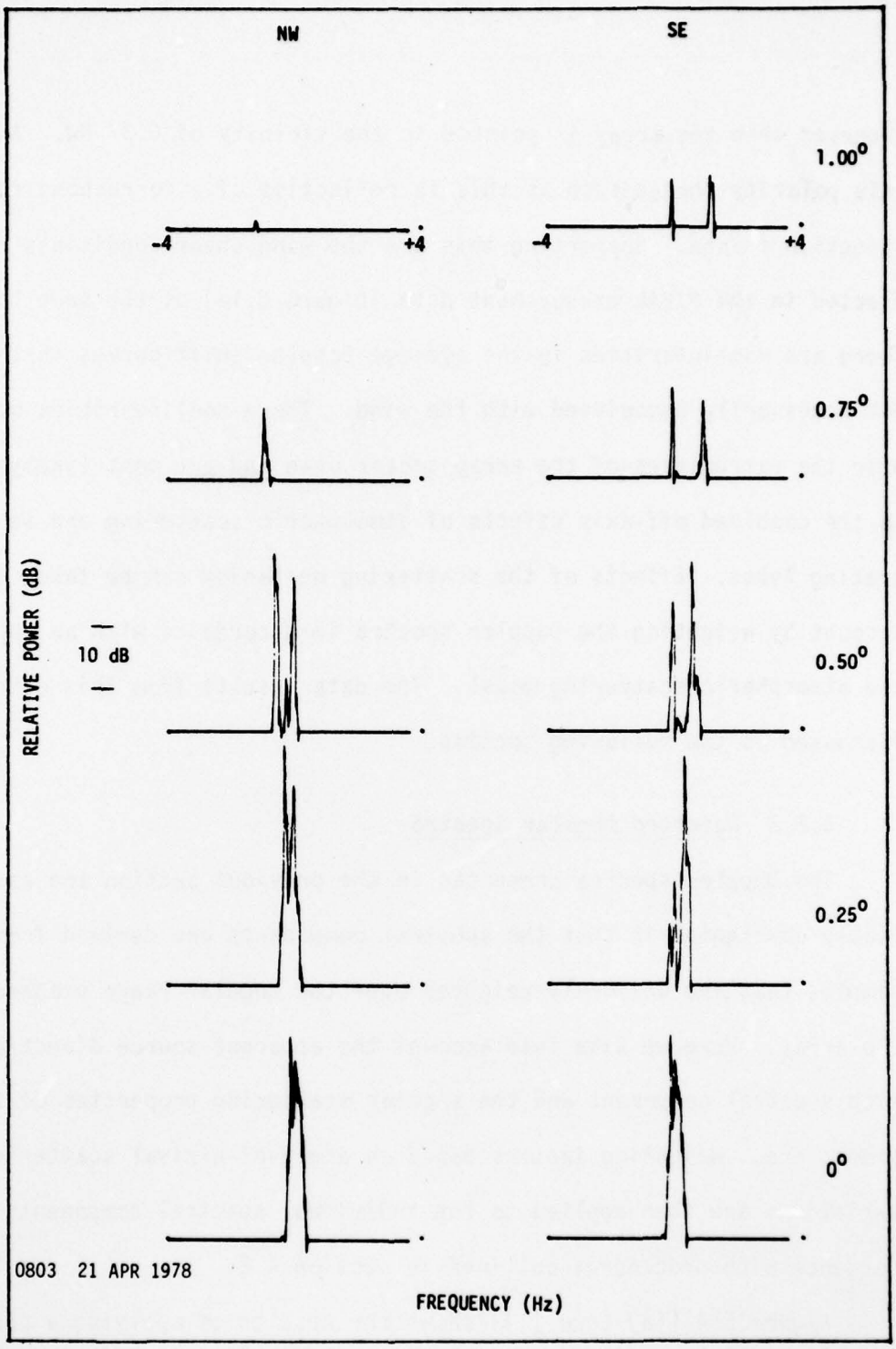

(a)

Fig. 5.4. WEIGHTED WIND-PRODUCED DOPPLER SPECTRA. Angle-of-arrival spectra are weighted in accordance with (1) a normalized Tatarski scattering model, (2) a sin(x)/x receiving array pattern, and (3) a Gaussian transmitting pattern under the assumption of a uniform wind and a source elevation angle, $\beta = 0.25°$.

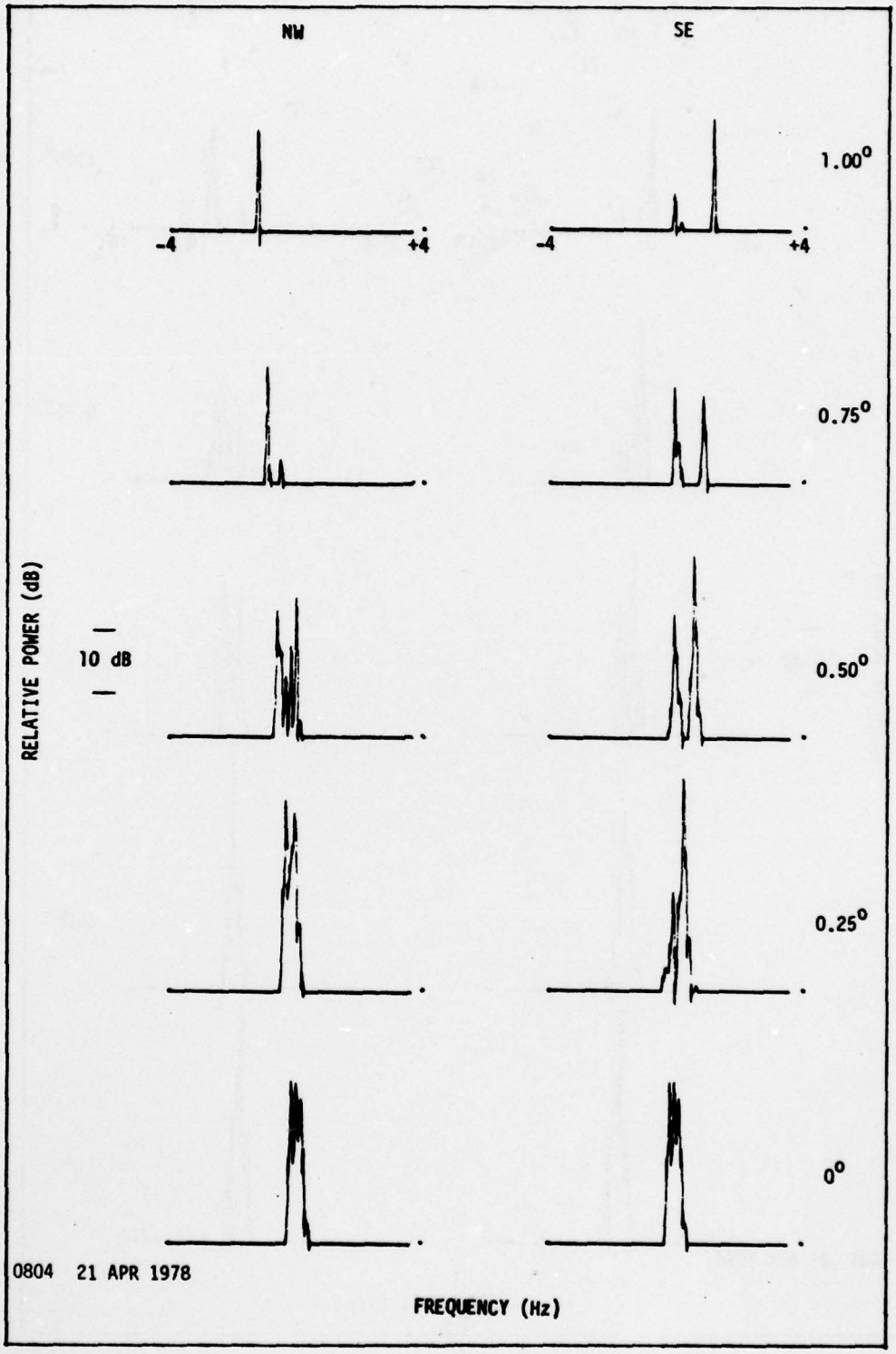

(b)

Fig. 5.4. CONTINUED.

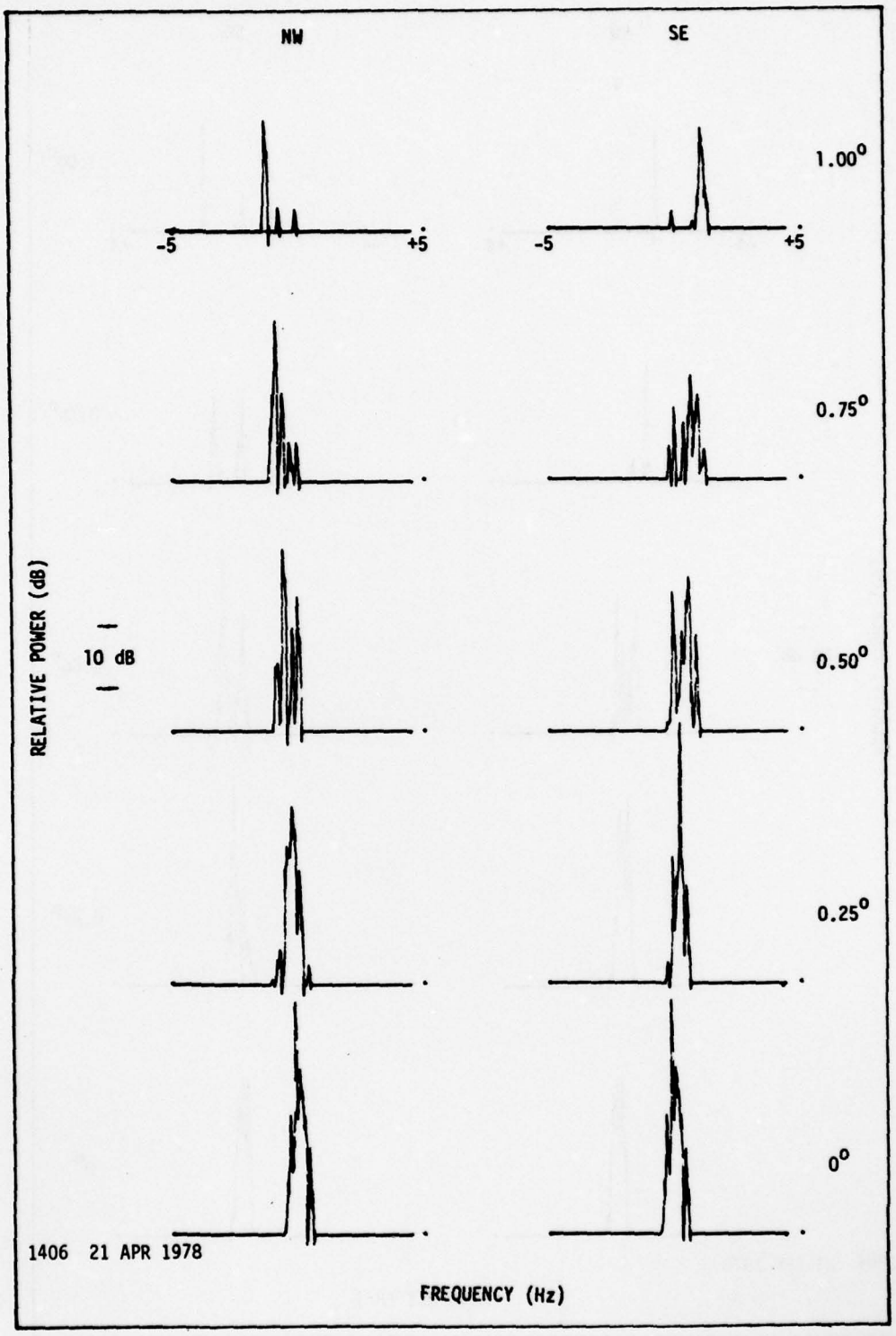

(c)

Fig. 5.4. CONTINUED.

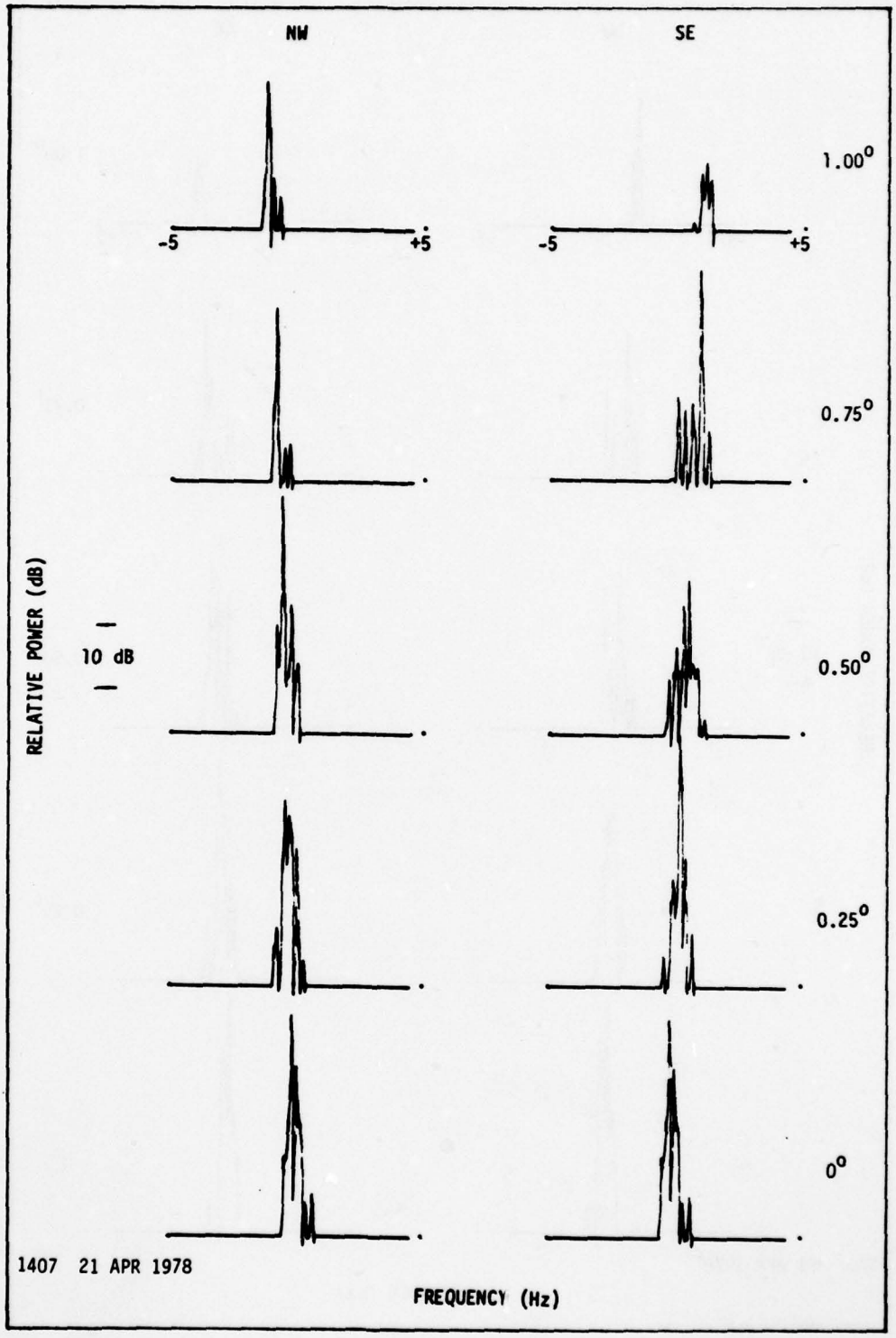

(d)

Fig. 5.4. CONTINUED.

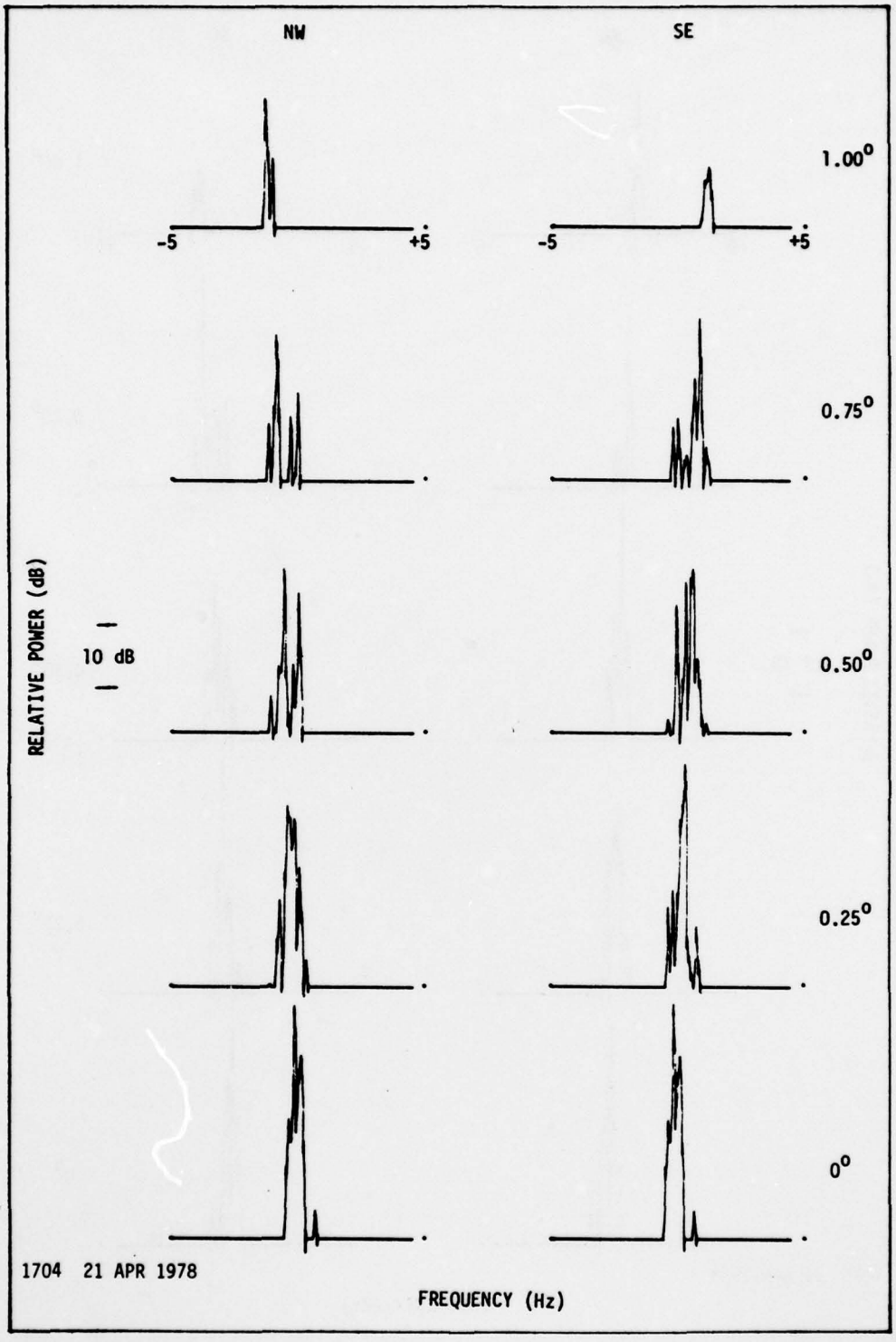

(e)

Fig. 5.4. CONTINUED.

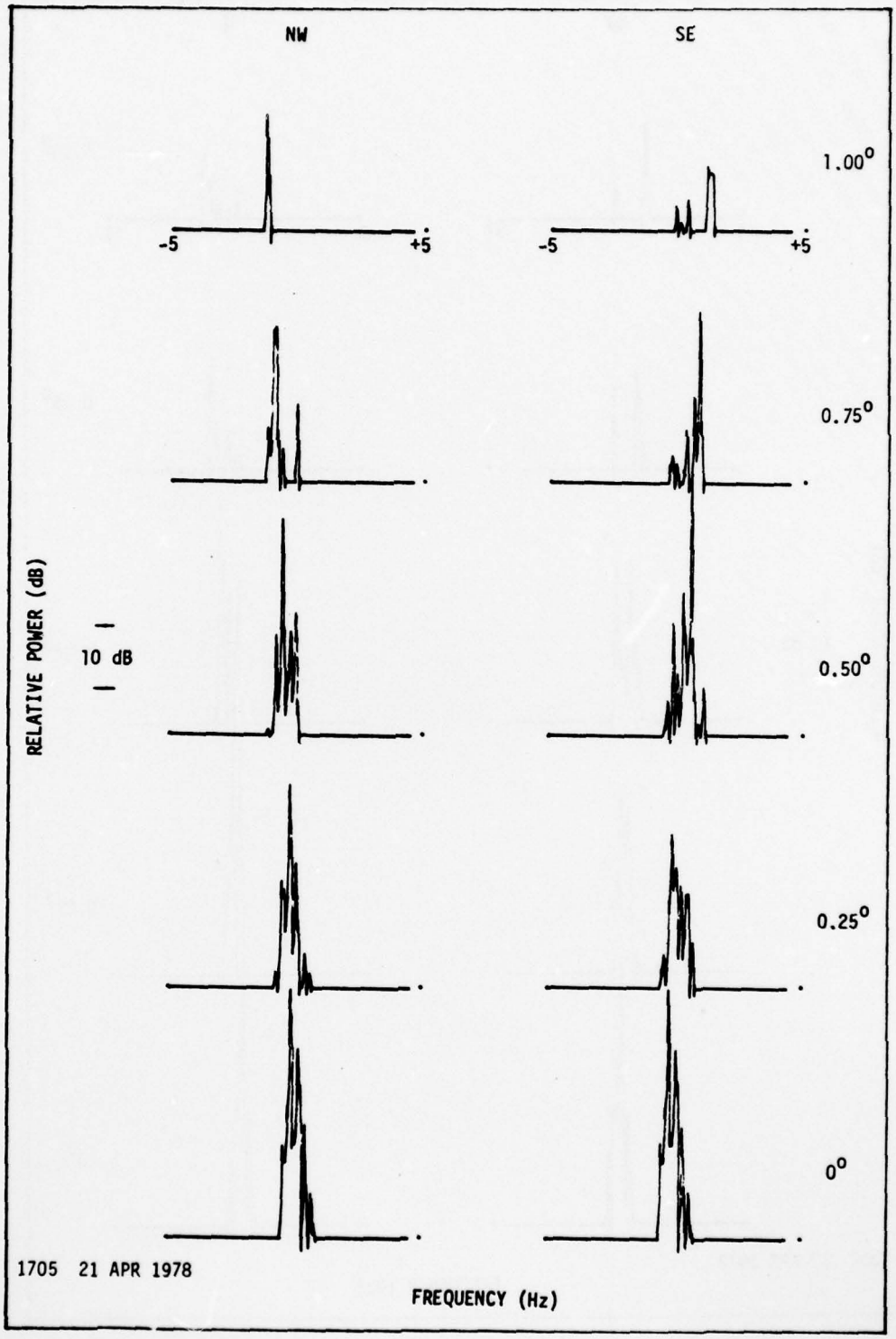

(f)

Fig. 5.4. CONTINUED.

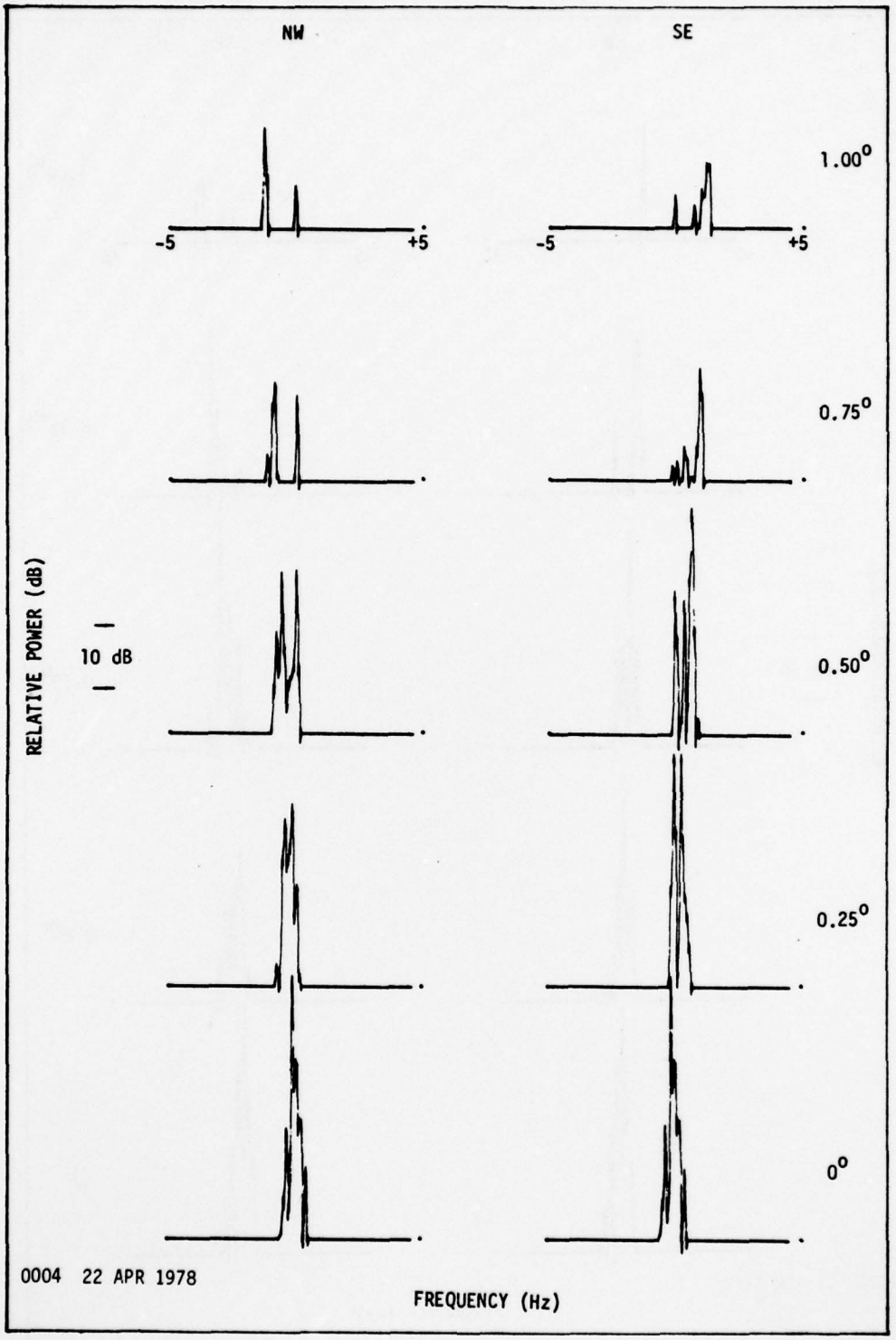

(g)

Fig. 5.4. CONTINUED.

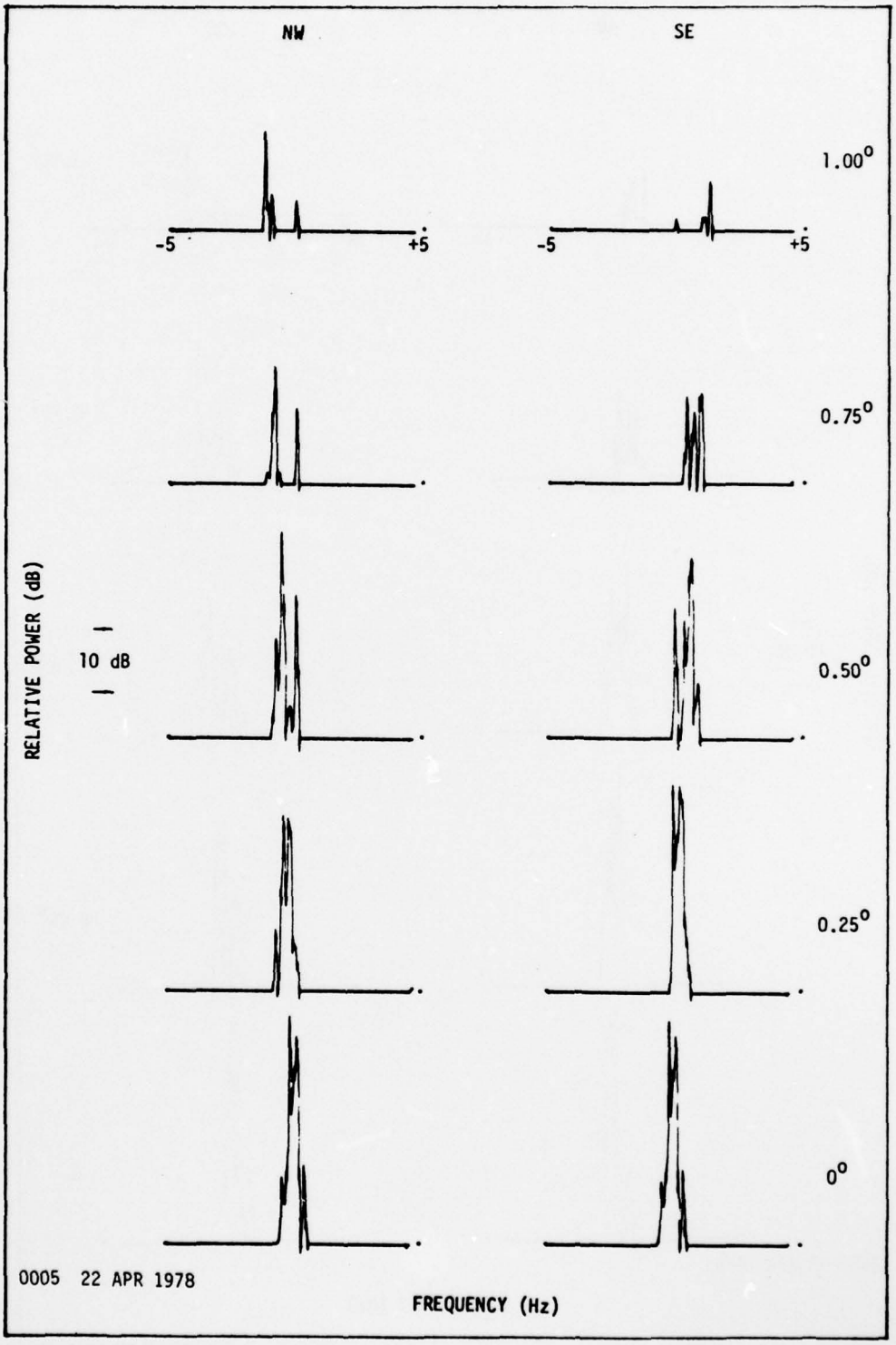

(h)

Fig. 5.4. CONTINUED.

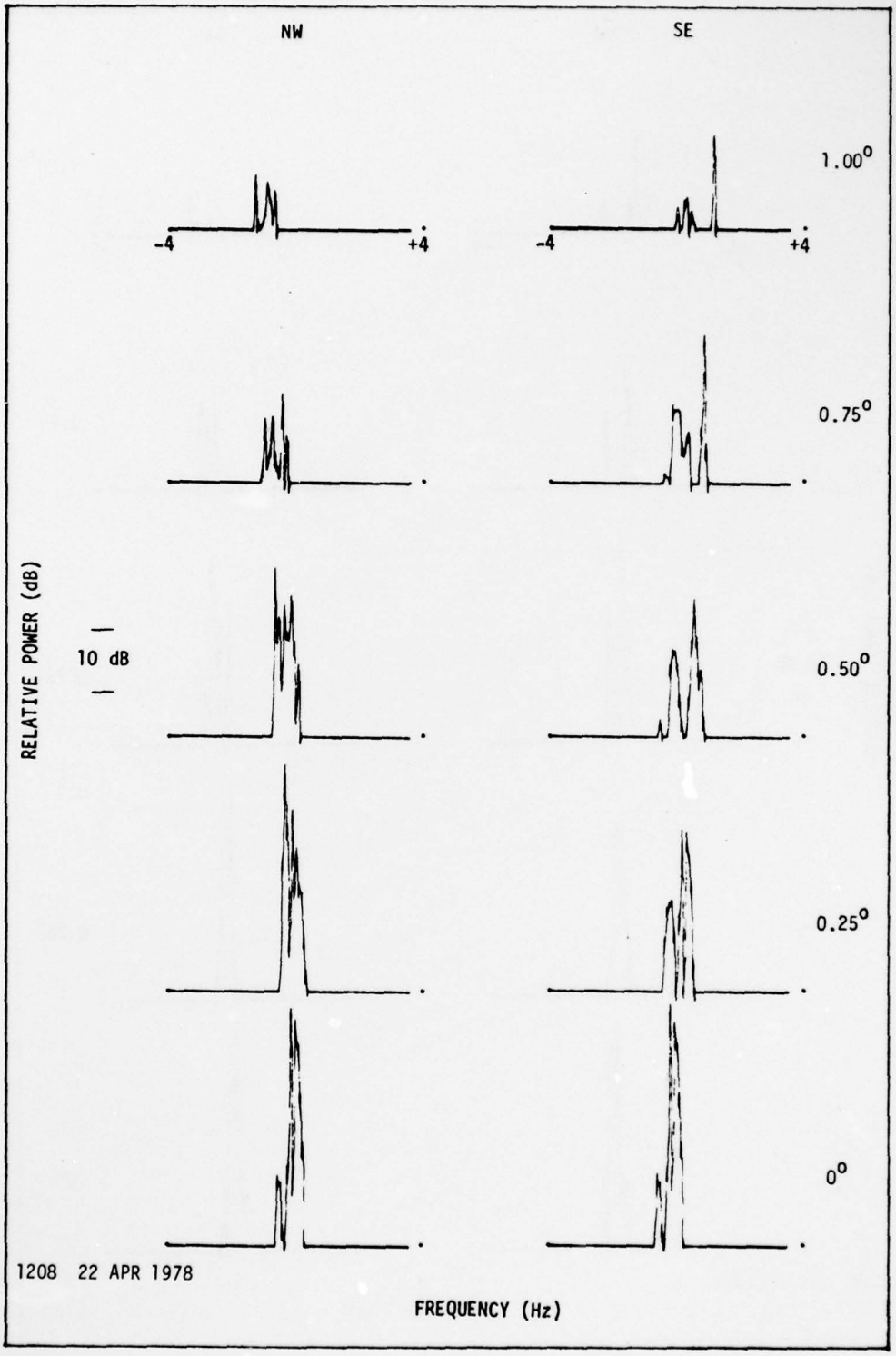

(i)

Fig. 5.4. CONTINUED.